Investigation of surface film formation on $LiNi_{0.5}Mn_{1.5}O_4$ cathodes in carbonate based liquid electrolytes using the secondary ion mass spectrometry

---

Aufklärung der Oberflächenfilmbildung auf $LiNi_{0.5}Mn_{1.5}O_4$ Kathoden in flüssigen carbonatbasierten Elektrolyten mittels Sekundärionen-Massenspektrometrie

---

dem Fachbereich Biologie und Chemie
der Justus-Liebig-Universität Gießen

vorgelegte Dissertation zur Erlangung des Grades
Doktor der Naturwissenschaften
- Dr. rer. nat. -

Eingereicht von

Mareike Falk

Gießen 2014

1. Reviewer / Gutachter: Prof. Dr. Jürgen Janek

2. Reviewer / Gutachter: Prof. Dr. Bernd Smarsly

submitted / eingereicht: May 2014

The present thesis was prepared at the Institute of Physical Chemistry of the Justus-Liebig University Giessen in the period of October - May 2014 under the supervision and guidance of Prof. Dr. Jürgen Janek and Dr. Joachim Sann. Hereby I declare the preparation of this Ph.D. thesis, experimentally and theoretically, as my own work. Expect the advices in the context of supervision I did not use other sources or assistances than those referred to.

Die vorliegende Arbeit wurde im Institut für Physikalische Chemie der Justus-Liebig-Universiät Gießen in der Zeit vom 04.10.2010 - 2014 unter der Betreuung von Prof. Dr. Jürgen Janek und Dr. Joachim Sann angefertigt. Hiermit erkläre ich die vorgelegte Dissertation, sowohl im experimentellen, als auch im theoretischen Teil, als meine selbstständig verfasste Arbeit, in der außer den Ratschlägen im Rahmen der Betreuung und den in der Arbeit angegebenen Quellen und Hilfsmitteln keine weiteren verwendet wurden.

Giessen, 2014

Mareike Falk

Zusammenfassung

Im Rahmen der vorliegenden Arbeit wurde die Grenzschicht zwischen $LiNi_{0.5}Mn_{1.5}O_4$, einem Kathodenmaterial für Lithiumionenbatterien, und flüssigen, carbonat-basierten Elektrolyten untersucht. Die Hauptanalytik wurde dabei mittels Sekundärionen- Massenspektrometrie durchgeführt. Es wurden Dünnfilm-Modellelektroden, die im Gegensatz zu technischen Elektroden keine Leitfähigkeitszusätze und Binder enthalten, untersucht, um den Einfluss dieser Zusätze auf die Grenzschichtbildung auszuschließen und das System zu vereinfachen. Außerdem konnte so die Rauigkeit der Elektroden deutlich reduziert werden, wodurch sich die Tiefenauflösung der Sekundärionen-Massenspektrometrie signifikant verbesserte. Hauptziel der Dünnfilmoptimierung war somit die Reduzierung der Rauigkeit der Elektrode. Vor allem durch Erhöhung der Abscheidetemperatur wurden Werte unter 10 nm erreicht. Es konnte gezeigt werden, dass die Grenzschicht einen schichtartigen Aufbau aufweist. Vorwiegend organische Spezies befinden sich auf der Elektrolytseite der Schicht, während im Bereich nahe der Kathodenoberfläche vor allem anorganische vorliegen. Die Dicke der Schicht wächst mit Zyklenzahl, Lagerungzeit und Temperatur. Beide im Kathodenmaterial enthaltenen Übergangsmetalle zeigen zudem signifikante Löslichkeit im Elektrolyten und diffundieren durch diesen bis zur Anode. Weiterhin wurde ein Modell zur Ausbildung der Grenzschicht aufgestellt.

Abstract

The scope of the present work was the investigation of the interface film formed between $LiNi_{0.5}Mn_{1.5}O_4$, a cathode material for lithium ion batteries, and liquid carbonate based electrolytes. Main characterization tool was the secondary ion mass spectrometry. Thin film model electrodes, which are in contrast to technical electrodes free of conductive carbon and binder, were studied in order to exclude the influence of these additives on the surface film formation and to simplify the system. By usage of thin film electrodes in addition the electrode roughness could be distinctly reduced. This in turn increases the depth resolution of the secondary ion mass spectrometry. Main aim during thin film optimization was the reduction of the electrode roughness. Mainly by increasing the deposition temperature values of less than 10 nm could be reached. It could be revealed that the interface film shows a stacked structure. The region close to the electrolyte is mainly composed of organic species, while mainly inorganic ones are located close to the cathode surface. The thickness of the interface film increases with cycle number, storage time and temperature. Both transition metals contained in the cathode show significant dissolution in the electrolyte and diffuse through the electrolyte towards the anode. A model concerning the surface film formation was developed.

Contents

List of Figures

List of Tables

List of abbreviations

AFM	atomic force microscopy ... 47
ALD	atomic layer deposition ... 166
BASF	Badische Anilin- und Sodafabriken
BMP-TFSI	1-butyl-1-methylpyrrolidinium bis(trifluoromethylsulfonyl)imide ... VII
CA	chronoamperometry ... 32
CEI	cathode electrolyte interface ... 2
cc	constant-current ... 32
CP	chronopotentiometry ... 32
CV	cyclic voltammetry ... III
CVD	chemical vapor deposition ... 48
DC	direct current ... 51
DEC	diethyl carbonate ... 63
DMC	dimethyl carbonate ... 14
DOD	depth of discharge ... 1
EC	ethylene carbonate ... 57
EMC	ethyl methyl carbonate
EXAFS	extended X-ray absorption fine structure ... 15
FEC	fluoroethylene carbonate ... 54
FTIR	Fourier-transformed infrared spectroscopy ... 54
GITT	galvanostatic intermittent titration technique
HOMO	highest occupied molecular orbital ... 12
HOPG	highly ordered pyrolytic graphite ... 69
ICP-OES	inductively coupled plasma-optical emission spectroscopy ... 2
IR	infrared ... 68
KIT	Karlsruher Institut für Technologie ... IX
LATP	$Li_{1+x}Al_xTi_{2-x}(PO_4)_3$ ... 50
LiB	lithium ion battery ... 1
LiBOB	lithium bisoxalatoborate ... 68
LiPON	lithium phosphorus oxynitride ... 19
LiTFSI	lithium bis(trifluoromethylsulfonyl)imide ... VII
LMO	$LiMn_2O_4$ ... 9
LNMO	$LiNi_{0.5}Mn_{1.5}O_4$ ... 2
LSM	lanthanum strontium manganese oxide
LTO	$Li_4Ti_5O_{12}$ ... 19
LUMO	lowest unoccupied molecular orbital
NCM	$LiNi_{1/3}Co_{1/3}Mn_{1/3}O_2$ ... 70
NMP	N-methyl-2-pyrrolidon ... 79
OCV	open circuit voltage ... 57
PC	propylene carbonate ... 57
PCA	principle component analysis ... 163
PDF	powder diffraction ... 76

PEIS	(potential-controlled) electrochemical impedance spectroscopy	32
PLD	pulsed laser deposition	III
PVDF	polyvinylidene fluoride	79
RDS	rate determining step	57
RF	radio frequency	50
SEI	solid electrolyte interphase	57
SEM	scanning electron microscope	49
SIMS	secondary ion mass spectrometry	2
SOC	state of charge	65
TEM	transmission electron microscopy	96
ToF	time-of-flight	21
UHV	ultra-high vacuum	
VC	vinylene carbonate	54
WE	working electrode	32
XANES	X-ray absorption near edge spectroscopy	146
XPS	X-ray photoelectron spectroscopy	2
XRD	X-ray diffraction	2
YAG	yttrium aluminum garnet	30
YSZ	yttria-stabilized zirconia	

1. Introduction - Thin film model electrodes for the study of interface reactions with liquid electrolytes

Limited oil reserves together with an increasing effort by the governments of many countries, as stated for example in the Kyoto protocol, to reduce the amount of exhausted CO_2, cause not only a shift in electric energy production towards renewable energies, but also result in search for alternative engines in the automotive industry. Moreover, increasing demand for durable high power storage media in consumer electronic as well as in biomedicine, telecommunication and automotive industry promotes both the improvement of existing and the development of new energy storage systems with main focus on efficiency, cost reduction and safety.[1] Since many sources of regenerative energies like wind and solar ones produce energy discontinuously, storage media saving it during periods of high production and delivering it during high demand are needed. Due to its high gravimetric energy storage capability[2] the lithium ion battery (LiB) is a promising system not only for today and future energy storage, but also for use in automobiles and in a large variety of other special applications. However, to compete with today's engines based on gasoline, the United States Advanced Battery Council made special demands on the LiB, like a calendar life-time of 15 years for both 42 V battery systems and hybrid electrical vehicles as well as ten years for electrical vehicles, so that a life-time of up to 1000 cycles at 80 % depth of discharge (DOD) needs to be reached.[3] Especially in these mobile applications systems with increased storage capacity and higher operating voltage are desired to reduce both the space occupied by the storage medium and the number of single cells in the battery stack, which in turn simplifies its control and heat management since for instance thermal conditions for single cells in the outer part of the battery stack are completely different to those in its inner region.[4,5]

The first commercialized LiB was produced by Sony in 1991 based on $LiCoO_2$ as positive and graphite as negative electrode,[6] delivering a potential of 4.0 V vs. Li/Li^+. However, since cobalt is both comparatively expensive and toxic, the search for alternative cathode materials proceeds and an increasing number of other material combinations are tested and partially commercialized.[7] One possibility to increase the energy density of the LiB

is raising the operating voltage of the cells since the energy density W increases with the square of the cell voltage E ($W = 1/2CE^2$, where C is the capacity of the battery).[8] This could be achieved by usage of cathode materials with higher electrode potential like the $LiNi_{0.5}Mn_{1.5}O_4$ (LNMO) spinel, delivering a voltage of 4.7 V vs. Li/Li^+.[4,9] Thus a member of the high voltage manganese spinel family is already applied as cathode in the Chevrolet Volt's car engine.[10,11] Energy and power density of cells with LNMO cathodes is about 20 % higher than those using $LiCoO_2$.[12]

However, besides several battery systems to date running stable over several hundreds and thousands of cycles in a large number of applications, there are still severe problems concerning aging, capacity fading especially at high temperatures, stability under extreme conditions like heat and cold or safety issues, that need deeper insight in the processes occurring in the lithium ion cell during charge, discharge and even storage. These problems become even more severe for high voltage materials because in this potential range oxidation of common carbonate based electrolytes takes place as investigations by the research group of Lucht show, in which the electrolyte solvents ethylene carbonate, dimethyl carbonate and diethyl carbonate decompose in a cell using LNMO as cathode above 4.85 V, participating in the formation of a surface layer on this electrode, often being called cathode electrolyte interface (CEI).[9]

Surface film formation due to reactions between the electrode material and the electrolyte also takes place on the anode side of the LiB, acting on the one hand as protection layer, but on the other hand being detrimental for the cell because it leads to performance losses.[13] Since the power of the LiB depends on the mobility of the lithium ions in both electrodes and the electrolyte, knowledge about the characteristics of these surface layers, especially concerning its transport properties for Li^+ as active species in the lithium ion battery, are of great importance. However, whereas the surface film formed on the anode is by now comparably well characterized, to date there is little knowledge about the exact structure, composition and formation mechanism of the one formed on the cathode. Its thickness is in the range of several tens of nanometers and therefore important analytical tools like X-ray diffraction (XRD) or inductively coupled plasma-optical emission spectroscopy (ICP-OES) fail in studying it, because its signals are superimposed by those coming from the bulk of the cathode material. In contrast to this, for several methods using electron or ion beam probes like X-ray photoelectron spectroscopy (XPS) or secondary ion mass spectrometry (SIMS) information only comes from the uppermost monolayers of the sample under investigation. The latter of them is very sensitive to lithium together with an outstanding depth resolution of about 2 nm, therefore turning out as well suitable method for CEI investigation.[14] However, this technique requires flat samples, since with increasing roughness the mass definition as well as the depth resolution decrease. There-

fore, thin film samples are needed instead of technical electrodes like those employed in commercial cells, which are deposited on metal foils by a doctor blade, as will be reviewed in chapter 4.2, but possess a significant roughness and can hardy be used for surface studies.

Moreover, since even a single cell in a battery stack is a complex system comprised of at least three different compartments, namely the positive and the negative electrode together with an electrolyte containing the separator, simplified model systems are needed to resolve the influence of single parameters on the cell performance that otherwise would diminish in the large number of additional effects. Since technical composite electrodes themselves comprise not only the electrochemically active material, but also conductive carbon and binder, a first step towards simplification is the use of thin films being composed of 100 % active material deposited on sufficient flat and conductive substrates. In a first attempt, these systems may be seen as ideally flat and therefore may overcome several drawbacks of technical electrodes, although the latter ones would mimic the commercial ones even better. In this respect, the study of electrode interfaces suffers from a "materials gap" like the study of complex heterogeneous catalysts.[15]

Thin film electrodes have a well-defined contact area to the electrolyte, thus allowing direct calculation of local current densities. In technical electrodes the electrolyte permeates via open porosity; carbon and binder also cover parts of the active surfaces, turning the exact determination of the total contact area into impossible.[16] Moreover, by a proper choice of the substrate, differently orientated films can be generated, enabling the study of lithium ion intercalation into selected crystal planes. In addition, more subtle effects caused by e.g. different types of carbon with slightly varying graphitic ratio or different amounts of binder in technical electrodes are avoided by using thin films of pure active material. Thin films can be fabricated of 100 % active material, and once they are thin enough even for rather poor conducting electrode materials no addition of conducting agents is needed. In this case intrinsic properties of the material under investigation like the lithium diffusion coefficient can be determined.[17] For further simplification lithium counter electrodes are usually applied instead of e.g. graphite ones used in commerical systems. Lithium electrodes deliver lithium ions in excess and therefore no further balancing is needed. However, as discussed later, the choice of the anode may influence the CEI formation. Unfortunately, additional complexity is added to the thin film model systems because the typical thin film substrates are often either electrical insulating or adhesion of the active material is insufficient. Therefore additional inter-layers are required on the substrate to guarantee sufficient electric contact or grip.

Goal of the PhD project was the characterization of the surface film formation on LNMO cathodes during cell operation using a thin film model system. Secondary ion mass

spectrometry was employed as main analytical tool due to its sensitivity to lithium together with its outstanding depth resolution, thus enabling the study of even very thin films deposited on the electrode surface. Primary aspects were the composition and structure of the deposited layers in dependence of parameters like temperature, electrolyte and storage time. In addition, protection of the cathode by deposition of thin metal oxide layers was studied. Since SIMS does not deliver any information about the oxidation state of the elements under investigation, additional analytic techniques were employed as well as electrochemical methods like constant-current chronopotentiometry and impedance spectroscopy. In a second step the gained results were used to develop a model of the surface layer formation on this type of cathode using liquid electrolytes as well as for concepts to improve the long term stability of LNMO electrodes.

2. The Basics - Methods and material

2.1. The lithium ion battery

Batteries are energy storage systems that convert the chemical energy contained in its pairs of active materials directly into electric energy by means of an electrochemical redox reaction.[18] They are comprised of at least three components, namely two electrodes or active masses immersed in an ion conducting, but electronic insulating electrolyte and are only connected by an external circuit containing an appliance, thus electron and ion transport are separated.[2] The term battery is commonly used but misleading, since the smallest compartment composed of the two electrodes and electrolyte is called cell, whereas a battery contains several single cells connected in series to reach higher voltage. The two electrodes are either constructed from two different materials or contain different concentrations of the same redox-active species, thus establishing a potential difference between them. The electrode with the lower potential during discharge reaction, at which therefore an oxidation reaction takes place, is called anode or negative electrode, whereas the other one, at which reduction occurs during discharge, is named cathode or positive electrode. During battery operation, driven by the potential difference, electrons flow in the external circuit, able to perform electric work. Charge balance occurs through charged species which travel across the electrolyte from one electrode to the other. The species carrying the ion current inside the cell is called active species. In most cases the electrolyte is liquid, but ceramic or polymer electrolytes are also applied. For physical separation of the electrodes in liquid based systems, thus preventing direct contact and therefore short-circuit between them, a porous membrane - called separator - soaked with electrolyte enables diffusion of the electro-active species. Whereas in most battery systems the electro-active species itself is reduced or oxidized, in the case of the LiB, lithium ions are the active species migrating through the electrolyte. They keep their charge and redox activity is achieved by immobile redox centers in the electrodes, thus, Li^+ is incorporated or released only for charge balancing reasons ("rocking chair battery").

We distinguish between primary and secondary cells. Whereas the former ones can only be discharged one time, secondary systems are rechargeable. By application of an extern current the reverse reaction takes place, so that oxidation occurs at the positive

and reduction at the negative electrode. A schematic sketch of the LiB together with the ionic and electronic flow during both charge and discharge reaction is shown in figure 2.1 with graphite and a transition-metal oxide as anode and cathode, respectively. In contrast to chemical redox reactions, where the transfer of electrons occurs directly and where only heat is dissipated, for battery systems the limitation of the Carnot cycles dictated by the second law of thermodynamics[i] does not hold and thus they can have higher energy conversion efficiencies.[18]

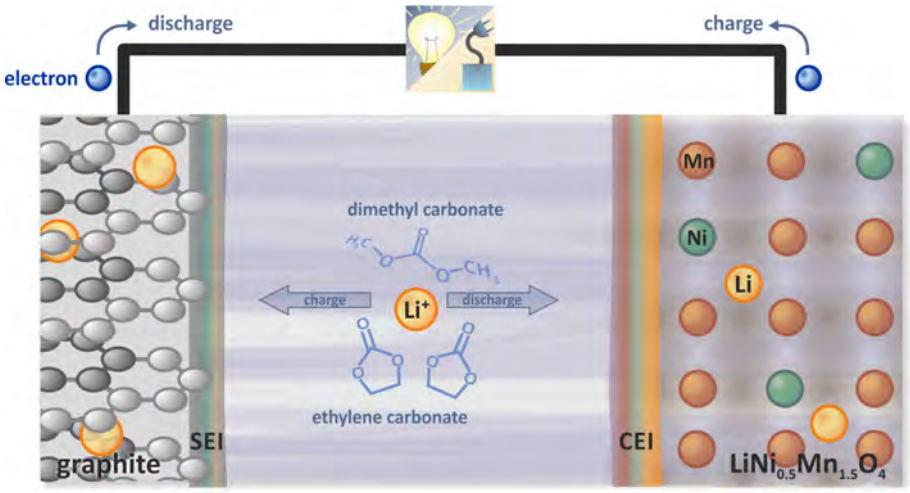

Fig. 2.1.: *Schematic sketch of a lithium ion battery together with the ionic and electronic flow during both charge and discharge reaction. As anode and cathode graphite and a transition-metal oxide, respectively, are displayed.*

In a cell, reactions take place at both electrode/electrolyte interfaces, thus the generalized reactions can be written as stated in equation 2.1 where o molecules of O take up n electrons e to form r molecules of R. The same holds for O' and R', and forward direction means the thermodynamically spontaneously occurring reaction:[18]

$$\begin{aligned} o\mathrm{O} + ne &\rightleftharpoons r\mathrm{R} \text{ (electrode, where reduction in forward reaction takes place)} \\ r\text{'R'} - ne &\rightleftharpoons o\text{'O'} \text{ (electrode, where oxidation in forward reaction takes place)} \end{aligned} \tag{2.1}$$

thus delivering the overall reaction

$$o\mathrm{O} + r\text{'R'} \rightleftharpoons r\mathrm{R} + o\text{'O'} \tag{2.2}$$

[i] The second law of thermodynamics places constraints upon the efficiency of heat engines and states, that there exists no periodic working machine that transforms an amount of heat completely into mechanic work.[19]

The change in the standard free energy ΔG^0 of a cell reaction is the driving force, thus enabling the electrochemical system under investigation to deliver electrical energy to an external circuit:[18]

$$\Delta G^0 = -nFE \tag{2.3}$$

Here, n is the number of electrons transferred in the reaction, F is the Faraday constant and E the voltage of the cell.[18] For conditions different frrom the standard state, the voltage of a cell in which the reaction stated in equation 2.2 takes place is given by the Nernst equation, where a_i is the activity of species i, R the gas constant, T the temperature and E^0 is the standard electromotive force. It corresponds to the reversible cell voltage if a_i of all components i is one:[18,19]

$$E = E^0 - \frac{RT}{nF} ln \left(\frac{\alpha_{\mathrm{R}}^{r} \alpha_{\mathrm{O}}^{o'}}{\alpha_{\mathrm{O}}^{o} \alpha_{\mathrm{R}}^{r'}} \right) \tag{2.4}$$

However, the actual voltage of an operating cell is somewhat lower due to activation polarization and charge-transfer polarization over-voltage at anode and cathode as well as concentration polarization at both electrodes.[18] Technical electrodes used in commercial batteries show however a porosity of about 30 %.[2] Their actual surface area is much larger than the geometric area, which in turn reduces the polarization of the electrode.[2]

To date lithium ion batteries offer the highest energy density available for rechargeable batteries, therefore being promising energy supplies for e.g. mobile applications where volume and size should be minimized.[20] Research on lithium batteries started already in the 1950s with the observation of the kinetic stability of lithium in a number of non-aqueous electrolytes.[21] Commercialization of primary lithium batteries took place soon after in the late 1960s and early 1970s.[21] However, commercial breakthrough of rechargeable lithium based batteries succeeded not until 1991 since systems using metallic lithium as anode failed due to dendritic lithium deposition during charge, leading to short-circuit and therefore failure of the cell.[21] Several approaches like adding scavengers to the electrolyte, dissolving lithium dendrites, have been pursued to improve cycle life, but most successful was the replacement of the metallic lithium anode by insertion electrode materials like graphite in which Li^+ is only incorporated in its ionized form.[21] Thus, redox activity takes place solely on the graphite host.[21] Intercalation, i.e. uptake between the graphene sheets, of lithium ions into graphite occurs via the following reversible reaction in which Li^+ from the electrolyte penetrates into the graphite host material and is placed between its carbon layers, leading to a moderate increase of the interlayer distance between the graphene sheets of 10.3 %:[21]

$$\mathrm{Li}_x\mathrm{C}_n \underset{charge}{\overset{discharge}{\rightleftharpoons}} x\mathrm{Li}^+ + xe^- + \mathrm{C}_n \tag{2.5}$$

At maximum, one lithium ion per six carbon atoms can be stored.[21] Since graphite shows a potential of about 0.1 V vs. $\mathrm{Li/Li^+}$ in its completely lithiated state the cell voltage is reduced by this value.[21]

As cathode materials in the LiB mostly inorganic transition-metal oxides or sulfides capable to incorporate lithium ions are used.[21] Their specific charges are based on a reversible range Δx of the lithium content during charging/discharging process according to the following equation in which X = oxide or chalcogenide and $x \geq 0$:[21]

$$\Delta x\mathrm{Li}^+ + \Delta xe^- + \mathrm{Li}_x\mathrm{MX} \underset{charge}{\overset{discharge}{\rightleftharpoons}} \mathrm{Li}_{x+\Delta x}\mathrm{MX} \tag{2.6}$$

The previous paragraph is only intended to give a short overview of the basic function of a lithium ion battery. Further information is provided by numerous books and reviews. See for example texts by of Winter et al. or Winter and Besenhard.[21,22] The next chapter will give a deeper insight in the cathode material studied in the PhD project. Further information on operation characteristics of the LiB like the change of the cell voltage during charge and discharge reaction and its correlation with the state of the storage phases in the electrode material are summarized in chapter 2.5.2.

2.2. The cathode material - lithium nickel manganese oxide

This section delivers a deeper insight into $\mathrm{LiNi_{0.5}Mn_{1.5}O_4}$ - the cathode material investigated during the PhD project. It summarizes its benefits in comparison to other cathode materials and its "parent" compound $\mathrm{LiMn_2O_4}$ as well as its general electrochemical response. The two different crystal structures of LNMO are discussed and a short overview of the current research dealing with this cathode material is given.

2.2.1. The spinel structure - from LMO to LNMO

In 1991 the lithium ion battery was commercialized by Sony using lithium cobalt(III) oxide ($\mathrm{LiCoO_2}$) as cathode material.[23] However, due to its toxicity and the comparably high costs of cobalt, its replacement is desired.[7] Besides the delivered capacity and voltage, another important factor for the choice of materials in the LiB is the abundance of their components in the earth crust securing long term availability and cost reduction, due to which iron and manganese based materials are of great interest.[24] Moreover, for a sustainable establishment of the LiB on the market, in addition to a cheaper production, increased energy density as well as improved safety are needed to compete against other energy

storage systems. A promising group of cathode materials are the manganese oxides since manganese is a low priced and non-toxic element.[25] In addition, manganese oxides have a rather high electronic conductivity together with a suitable electrode potential.[21] Among the lithium manganese oxides the layered $LiMnO_2$ and the spinel type $LiMn_2O_4$ (LMO) are the most prominent ternary phases. Advantages of the latter one in comparison to the layered phase are a higher potential of about 4.0 V against Li/Li^+, whereas $LiMnO_2$ delivers only 3.0 V. The $LiMn_2O_4$ lattice offers three dimensional lithium diffusion, resulting in faster uptake and release of this ion.[26,27] Lithium diffusion channels are shown in figure 2.2. In addition, the non-layered structure prevents the insertion of large solvent molecules, also showing only small contraction and expansion during lithium (de)intercalation.[28]

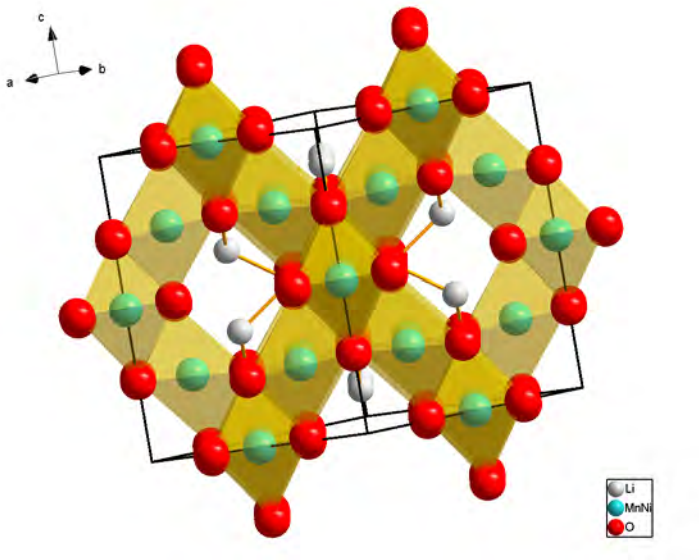

Fig. 2.2.: *Lithium diffusion channels in $LiMn_2O_4$.*

The $LiMn_2O_4$ spinel structure is composed of a cubic close-packed oxygen lattice on the crystallographic $32e$ sites of the $Fd\bar{3}m$ space group in which half of the octahedral ($16d$) and one eighth of the tetrahedral ($8a$) interstitial sites are filled by manganese and lithium ions, respectively, thus forming a diamond-type network of tetrahedral $8a$ sites and surrounding octahedral $16c$ ones.[21,27,28] Empty octahedra and tetrahedra are interconnected with one another by common faces and edges, enabling 3D diffusion of lithium ions, which move via adjacent $16c$ sites from one $8a$ position to the neighboring.[21,29] The structure of this material, highlighting both lithium tetrahedra and manganese octahedra, is shown in figure 2.3.

Lithium incorporation/release at 4.0 V in $LiMn_2O_4$ proceeds in a two-step process visible in e.g. cyclic voltammetry experiments by two peaks in this potential range. The diamond

lattice formed by the tetrahedral a sites consists of two interpenetrating face-centered cubic arrays, thus stabilizing an ordered phase at half Li^+ filling in which lithium ions occupy only one of them.[30] Detailed information about the cycling behavior of this material and relation to its crystal phases are give in chapter 2.5.2.

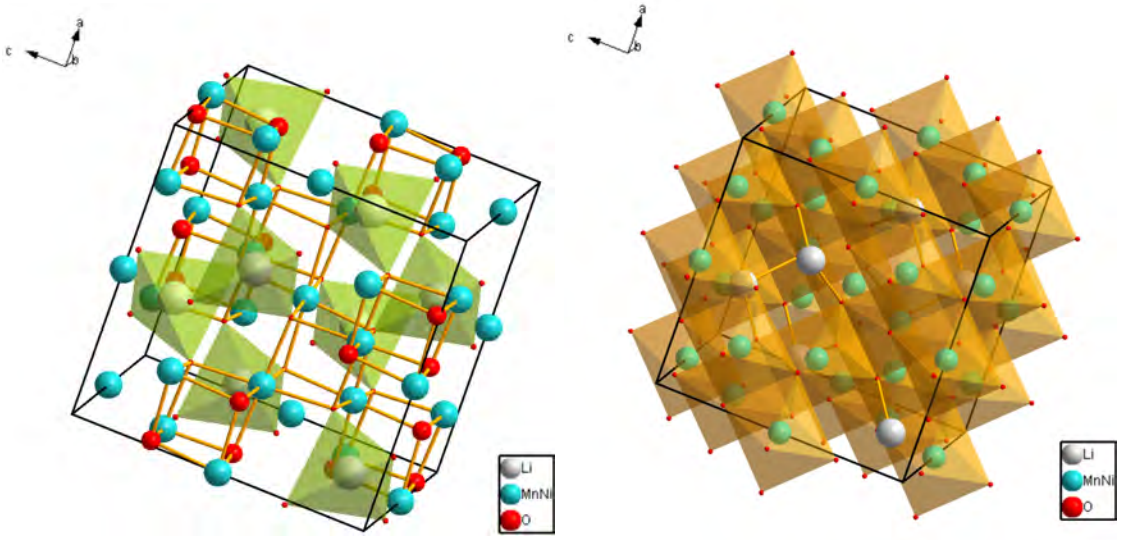

Fig. 2.3.: *Crystal structure of $LiMn_2O_4$ highlighting lithium tetrahedra on the left and manganese octahedra on the right side.*

Excess lithium ions are incorporated at about 3.0 V in the 16c sites. Since they share planes with 8a tetrahedra, there are electrostatic interactions between lithium ions on these two places, leading to a shift of the latter ones in neighboring empty 16c sites, which goes along with a Jahn-Teller distortion of the $Mn^{3+}O_6$ octahedra and as consequence the crystal symmetry reduces from cubic to tetragonal.[31,32] This transition goes along with an anisotropic contraction of 5.6 %, thus leading to capacity losses during repeated charge-discharge cycles, and occurs if the mean oxidation state of manganese falls below 3.5.[30,32–34] This phenomenon is explained by the crystal field theory:[35] for a single, gasesous metal ion its five d-orbitals are degenerated. If however a field of negative charges surrounds this ion, e.g. caused by anions like O^{2-}, the orbital energy of the (central) ion is increased due to repulsion between the negative field and the negatively charged electrons in the orbitals.[35] In addition, the degeneracy disappears. For octahedral complexes, i.e. a metal ion surrounded by six anions in the shape of an octahedron, the energy of the orbitals located on the axes - the d_{z^2} and the $d_{x^2-y^2}$ orbital - is a bit higher in comparison to that of a spherically symmetric field, since they are closer to the anions than the orbitals situated between the axes. The energy of the latter orbitals - the d_{xy}, d_{xz} and d_{yz} orbital

- is a bit lowered. These orbitals are called t_{2g}, while the former ones are named e_g. For octahedral complexes exhibiting an non-uniform occupation of the e_g or t_{2g} orbitals, a distortion of the octahedra could be energetical favourable. Stretching along the z-axis lowers the energy of the obtials having a z-component (d_{z^2}, d_{xz} and d_{yz} orbital), since they are situated further away from the negative charge. They are thus stabilized, as visualized in figure 2.4.[35] The energy of the other orbitals is raised by this deformation, so that the sum of their energies equals that before the stretching. If after this streching more electrons are in orbitals that are lowered in enery, this deformation is stabilized and the metal ion shows Jahn-Teller distortion like the Mn^{3+} ion. Since Mn^{4+} has no electron in the e_g orbital, the deformation would not result in a stabilization. This ion is thus Jahn-Teller inactive. Whereas in the fully charged, lithium free structure all manganese ions are in their tetravalent state, during discharge due to lithium ion uptake, they are reduced to the trivalent form for charge balance. Theoretically, even in the completely discharged state ($x = 1$ in $Li_xMn_2O_4$) the average oxidation state of manganese is 3.5 and therefore Jahn-Teller distortion should be suppressed. But if the insertion rate of Li^+ is higher than its diffusion rate from the surface in the volume, there is a surface enrichment of the electrode particles with lithium ions, resulting in a local decrease of the average manganese oxidation state below 3.5 and therefore in the occurance of local Jahn-Teller distortion.[36]

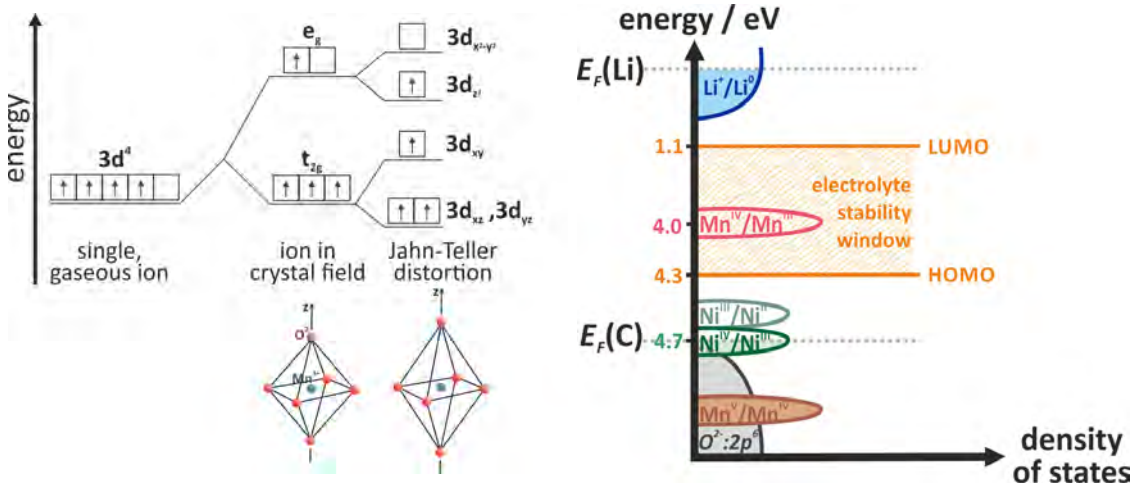

Fig. 2.4.: *Left: energy diagram of Mn^{3+} in an octahedral field with and without Jahn-Teller distortion. Right: density of states and Fermi energies for a LNMO electrode referred to the Fermi energy of the lithium anode E_F (Li). The stability window of common carbonate based electrolytes is also given. Here, LUMO denotes the lowest unoccupied molecular orbital, which lies for electrolytes based on dimethylene carbonate or diethyl carbonate approx.* 1.1 eV *above the E_{FA}.*[30] *Modified and redrawn from*[17,30,35,37]

An additional problem is the tendency of trivalent manganese ions to disproportionate into the tetra- and divalent form according to Hunter's reaction:[3,38–40]

$$2\mathrm{LiMn_2O_4}(s) \rightarrow 3\lambda\text{-}\mathrm{MnO_2}(s) + \mathrm{MnO}(s) + \mathrm{Li_2O}(s) \tag{2.7}$$

Since MnO is soluble in organic electrolytes, partial dissolution of the cathode material results.[3,39] Therefore there are attempts to reduce the content of trivalent manganese in the spinel structure in the discharged state by partial replacement of this element with aluminum, lithium or transition metals to increase the stability of the material.[34,41] This substitution reduces the capacity from the redox reaction of manganese. Its replacement with other transition metals however results in additional redox activity at, in mosts cases, higher voltages.[42] This voltage shift is, regarding substitution by nickel, caused by a $0.5 - 0.6\,\mathrm{eV}$ higher binding energy of the Ni d-electrons in the e_g level in comparison to those of manganese, resulting in the rise of the cathode potential by $0.5 - 0.6\,\mathrm{V}$.[43] Figure 2.4 shows a schematic sketch of the density of states and Fermi energies for $\mathrm{LiNi_{0.5}Mn_{1.5}O_4}$, a nickel substituted form of the LMO spinel, and a common carbonate based electrolyte explaining the discharge potentials at 4.0 V and 4.7 V, respectively. The $\mathrm{Ni^{2+}/Ni^{4+}}$ and $\mathrm{Mn^{3+}/Mn^{4+}}$ couples in LNMO lie about 4.7 eV and 4.0 eV, respectively, below the Fermi energy $E_F(\mathrm{Li})$ of a lithium metal anode.[17] The top of the O $2p$ bands of LNMO is placed a little over 5 eV below $E_F(\mathrm{Li})$.[17] The maximum voltage vs. lithium of a cathode material is constrained by either the decomposition voltage of the electrolyte or the intrinsic limit of a host transition metal compound, which is the voltage at which the Fermi energy E_{FC} of the cathode material approaches the top of its anion (i.e. oxygen) bands.[17] Above this energy oxidation of the anion starts, leading to destruction of the cathode material. Since the $\mathrm{Mn^{4+}/Mn^{5+}}$ couple lies well below the top of the O $2p$ bands, the $\mathrm{Ni^{3+}}$ and $\mathrm{Ni^{4+}}$ valence states are the highest accessible ones and LNMO cathodes show thus a voltage of approx. 4.7 V vs. lithium.[17] However, formation of a passivating, $\mathrm{Li^+}$ permeable surface layer on their active particles is required, because $E_F(\mathrm{C})$ of the cathode falls below the HOMO of the electrolyte.[17] The highest occupied molecular orbital (HOMO) of a liquid carbonate electrolyte is 4.3 eV and its decomposition voltage about 5 eV below the Fermi energy of a lithium electrode.[17,30]

Among the transition metal doped $\mathrm{LiMn_2O_4}$ spinel electrodes LNMO is a very promising material: It has an additional capacity at a relatively high voltage of 4.7 V vs. $\mathrm{Li/Li^+}$ due to the electrochemical activity of the $\mathrm{Ni^{2+}/Ni^{4+}}$ redox couple. It moreover shows both good cycling behavior and rate capability, as well as a specific capacity of 147 mAh/g and an energy density of about 700 Wh per kg active material, referring to lithium metal.[1,44–47] By replacing 25 % of the manganese ions with nickel, there is no $\mathrm{Mn^{3+}}$ left in the structure.

For charge balance reasons the Ni^{2+} incorporation forces all manganese ions to in their tetravalent state.[48] An even higher nickel content would on the one hand increase the capacity of the 4.7 V plateau, but on the other hand would reduce the electric conductivity of the material, which occurs by electron hopping between tri- and tetravalent manganese ions.[49,50]

In comparison to the chromium- or iron-doped form, the nickel-substituted $LiMn_2O_4$ spinel shows higher discharge capacity and drastic reduced degradation at higher temperatures.[51] The reason for its outstanding performance is the unique surface chemistry of this material, caused by the nickel content and resulting in the development of a stable cathode-electrolyte interface in aprotic electrolytes.[20] This will be discussed in detail in chapter 3.2.2. Doping with nickel moreover strengthens and shortens the binding between the 2p orbitals of oxygen with those of the two transitions metals, and leads to a different filling of the manganese and nickel 3d orbitals, thereby improving the discharge capacity as well as the structural stability of the material.[52,53] The material shows in addition a very small change of lattice parameters between the fully lithiated and the completely lithium free LNMO of only 2.1 %, resulting only in minor structural changes and thus being one reason for the good cycling behaviour of the material.[54] The lithium ion diffusion coefficient in LNMO increases with the electrode potential and is in the range of $10^{-11} - 10^{-9}\,cm^2/s$, partially even reaching values in the range of $10^{-8}\,cm^2/s$.[55–57] For thin film electrodes, values of $10^{-12} - 10^{-10}\,cm^2/s$, thus being an order of magnitude lower, have been reported.[29] Lower values for thin film electrodes in comparison to technical ones could be caused by different surface areas A assumed for calculation of the lithium diffusion coefficient D_{Li}, see equation 4.1. Whereas for thin film electrodes the actual surface area is close its geometric one, technical electrodes posssess distinctly higher porosity and thus higher surface areas. If for the latter type of electrodes the geometric area is used for calculation of D_{Li}, this value is overestimated.

Despite these promising properties, especially at high temperatures significant capacity fading occurs, which is critical for the application of this material in the automotive industry.[1] Therefore ways to stabilize this material under extreme conditions are needed. However, to date a modification of the lithium nickel manganese spinel is already implemented in the battery of the Chevrolet Volt by GM.[10] Another reason for the capacity fading of LNMO is the loss of active material caused by the disproportionation of trivalent manganese ions with the subsequent dissolution of the divalent ion into the electrolyte. Therefore, deep discharge, i.e. incorporation of more than one lithium per $LiNi_{0.5}Mn_{1.5}O_4$, thus generating Mn^{3+}, has to be prevented. The suppression of Mn^{2+} formation is not only important on the cathode side of the LiB to prevent its capacity fading. As Mn^{2+} diffuses through the electrolyte to the anode surface it is incorporated in the anode SEI,

resulting in an increased electrolyte decomposition as well as in self-discharge of the cell.[3] An additional problem of the high discharge potential of LNMO of 4.7 V is the electrolyte decomposition at such high potentials, also resulting in degradation of the cell. However, by variation of the electrolyte components a widening of the electrochemical window is possible, and dimethyl carbonate (DMC) containing electrolytes are reported to be stable up to 5.1 V.[58]

2.2.2. Crystal phases of LNMO

LNMO exists in two different crystallographic modifications. On the one hand, there is an ordered spinel phase (space group $P4_332$), in which Mn^{4+} and Ni^{2+} ions are located on distinct crystallographic $12d$ and $4a$ sites, respectively, and Mn^{3+} is completely absent. On the other hand exists a phase ($Fd\bar{3}m$ space group), in which Mn^{4+} and Ni^{2+} ions are randomly distributed on the $16d$ sites.[55,59,60] In the latter form Li and O ions are located on $8a$ and $32e$ positions, respectively, whereas in the $P4_332$ phase Li ions occupy $8c$ sites and O ions are located on $8c$ and $24e$ positions.[60] In contrast to the ordered form of LNMO, containing a stoichiometric amount of oxygen, in the $Fd\bar{3}m$ phase there is a deficit δ of this element, leading to the formula $LiNi_{0.5}Mn_{1.5}O_{4-\delta}$ with some of the manganese ions reduced to its trivalent state for charge balance.[60]

$$Li[Ni^{2+}_{4a}]_{0.5}[Mn^{4+}_{12d}]_{1.5}O_4 \overset{-\frac{\delta}{2}O_2}{\rightarrow} Li[Ni^{2+}_{16d}]_{0.5}[Mn^{4+}_{16d}]1.5-2\delta[Mn^{3+}_{16d}]_{2\delta}O_{4-\delta} \tag{2.8}$$

The Mn^{3+} ions are responsible for the disorder of the transition metal ions in the latter crystal structure since Mn^{3+} and Ni^{2+} have approximately the same ionic radii of 65 and 69 pm, therefore easing mixing of cations on the octahedral sites.[61] The crystal structure of the two different phases is shown in figure 2.5. Since tetravalent manganese ions possess smaller ion radii than trivalent ones, the ordered $P4_332$ phase shows a smaller lattice constant than the oxygen deficient $Fd\bar{3}m$ one.[62]

Distinction between these two phases is for example possible by electrochemical investigations. The ordered type shows due to lack of trivalent manganese ions no electrochemical activity in the 4.0 V region, where redox reactions of the Mn^{3+}/Mn^{4+} couple occur. The different electrochemical behavior of the two phases is schematically sketched in figure 2.6. Still under discussion is the question, whether a distinction is also possible by the electrochemical behavior in the high voltage range. Some authors report two separate plateaus for the nickel oxidation at about 4.7 V only for the disordered spinel, whereas the ordered form shows just one at approx. 4.75 V.[63] This difference possibly arises from a vacancy and lithium ion ordering at half lithium filling in the $Fd\bar{3}$m structure, which is less commensurate with the manganese and nickel distribution in the ordered phase.[64] Thus,

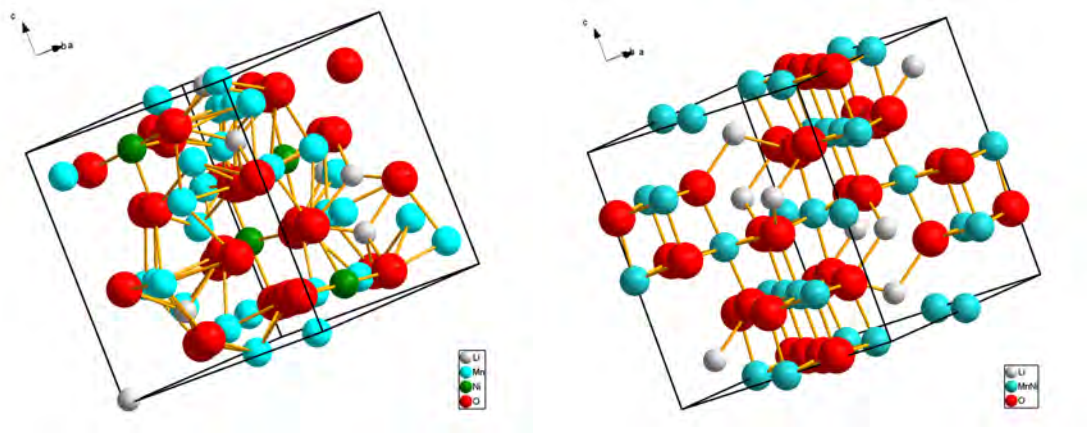

Fig. 2.5.: *Crystal structure of the two different crystallographic modifications of LNMO: The ordered $P4_332$ phase on the left and the disordered $Fd\bar{3}m$ phase on the right side.*

for the ordered phase there exists only one two-phase region for lithium content x between 0 and 0.5, whereas the disordered structure possesses an additional two-phase region at $x = 0.5 - 1$.[64] The relation between the number of phases in equilibrium and voltage evolution will be given in greater detail in section 2.5.2. In contrast to this, other groups report for the $P4_332$ phase also a two-step mechanism in this high voltage range, but with very small voltage variation, since the first of the two reactions in this voltage range, that appears at slightly lower voltages, shifts to bit higher potential.[60,65] This phenomenon is presumably caused by the development of a different structure - domain formation was reported for $Fd\bar{3}m$ - so that the lithium ions need more energy to be incorporated in or released from the host material.[60,62] Thus the marginal potential difference for the two redox couples in the $P4_332$ phase is possibly seen in other investigations just as one plateau or peak. Reasons for this effect could be peak broadening caused by imperfect material or too fast voltage scan rates in CV measurements, that do not allow the system to react completely due to sluggish kinetics resulting in partially overlap of the two processes.[59,60]

The origin for the voltage step in LNMO at about 4.7 V is also controversially discussed. On the one hand, it could result from a vacancy and lithium ion ordering at half filling, and on the other hand it is possibly caused by the two-step oxidation of divalent nickel to the tetravalent form via Ni^{3+}.[64,67] Thus, the electrochemical activity located at a bit more positive potential in this high voltage range results from the Ni^{2+}/Ni^{3+} redox couple, whereas the second one at slightly higher voltage is caused by the Ni^{3+}/Ni^{4+} couple. This hypothesis was supported by *in situ* extended X-ray absorption fine structure (EXAFS) studies by Terada et al., reporting a peculiar variation of the Ni-O peak height with lithium insertion and thereby showing a minimum at $x = 0.6$ in $Li_{1-x}Ni_{0.32}Mn_{1.69}O_4$ which can be ascribed to the distorted Ni^{3+}-O octahedron due to the Jahn-Teller effect.[68]

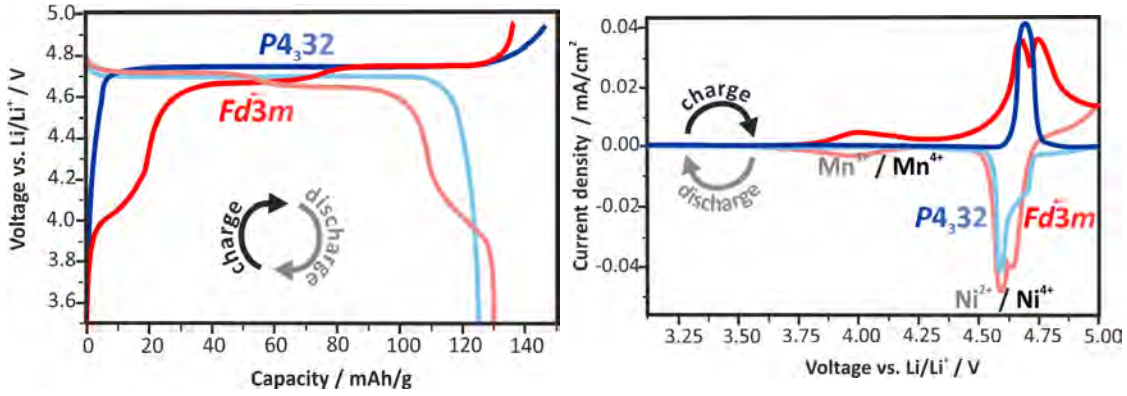

Fig. 2.6.: *Sketch to illustrate the different electrochemical behavior of the two LNMO phases during constant-current cycling on the left and cyclic voltammetry on the right side with the $P4_332$ phase in dark and light blue and the $Fd\bar{3}m$ one in red and rose, respectively. In each case, the light color symbols the charge and the darker ones the discharge behavior. Modified and redrawn from*[63,66]

However, assuming that the two-stage mechanism in this voltage range only holds for the disordered form, the former explanation seems to be more likely since nickel oxidation via its trivalent form presumably should take place or not for both crystal phases in the same manner. Another argument for the vacancy and lithium ion ordering at half filling as reason for the voltage step at about 4.7 V is given by theoretical calculations by Kim et al. concerning the thermodynamic analysis of LNMO.[69] All preferable sites in a bulk are occupied before any of the more undesirable ones.[69] Due to the electrostatic repulsion between lithium ions it is energetically favorable for them to be positioned as far apart as possible, resulting in an vacancy and lithium ion ordering. Their calculations reveal only three stable compositions for $Li_xNi_{0.5}Mn_{1.5}O_4$, namely $Ni_{0.5}Mn_{1.5}O_4$, $Li_{0.5}Ni_{0.5}Mn_{1.5}O_4$ and $Li_{1.0}Ni_{0.5}Mn_{1.5}O_4$; thus, for lithium occupation x of $0 < x < 0.5$ $Li_xNi_{0.5}Mn_{1.5}O_4$ should decompose to $Ni_{0.5}Mn_{1.5}O_4$ and $Li_{0.5}Ni_{0.5}Mn_{1.5}O_4$, whereas for $0.5 < x < 1.0$ $Li_{0.5}Ni_{0.5}Mn_{1.5}O_4$ and $Li_{1.0}Ni_{1.0}Mn_{1.5}O_4$ are present.[69] Since in the latter structure all lithium sites are occupied and thus electrostatic repulsion is greater than for half lithium filling, this form is energetic less favorable, thus leading to the observed voltage step.

The oxygen stoichiometric structure shows lower electronic conductivity and therefore worse electrochemical performance especially at high rates, since, as already mentioned, electron transfer occurs mainly by electron hopping between tri- and tetravalent manganese ions.[59,61,70] In addition to the lack of Mn^{3+} in the $P4_332$ phase, there is an ordering of the transition metals, so that the electron transfer is dominated by $Ni^{2+/3+} \rightarrow Ni^{3+/4+}$, whereas electron hopping between Mn^{3+} and Ni^{2+} is suppressed.[61] Therefore, a certain amount of trivalent manganese in the spinel is beneficial despite its tendency to dispro-

portionate with the concomitant Jahn-Teller distortion, but its amount should be kept below the critical value for the latter effect. This for example can be achieved by partial substitution of Mn and/or Ni ions, as will be described in the next section.[59]

By variation of preparation parameters a distinction and even a reversible transformation between the two crystal phases of LNMO is possible. Since high temperatures are "reducing", i.e. result in loss of oxygen from the material, the disordered spinel forms during annealing at temperatures of more than 750 °C with concomitant quenching, whereas the ordered spinel builds up either by long annealing in a narrow temperature interval of $600 - 700\,°C$ or by slow cooling of higher calcined material.[44,60,63,71] The loss of oxygen loss goes along with the introduction of interstitial cations in a cation-deficient rock salt second phase.[30,61,65]

All these structural changes are induced by oxygen loss from the $8c$ sites of the ordered spinel structure, starting at $650 - 680\,°C$, thereby taking place solely from MnO_6 octahedra at $12d$ positions and Mn-O-Mn bonds.[72] As a consequence, the metal-oxygen bond lengths elongate as well as the metal-metal distances at $12d$ sites due to reduced shielding and therefore increased cation-cation repulsion. Moreover, disorder of Mn and Ni on octahedral sites occurs due to reduction of Mn^{4+} to Mn^{3+} with concomitant increase in its atomic radius as already mentioned earlier in this chapter.[61,72] Increased M($12d$)-O bond lengths are also caused by substitution of larger Ni^{2+} ions on these octahedral sites as well as by the greater radius of Mn^{3+}. Thus, the M($12d$) octahedra become less distorted until all six bond lengths are equal at the phase transition from $P4_332$ to $Fd\bar{3}m$, with the transition metal mixing at $12d$ positions as main reason.[72] In conclusion, the $P4_332$ phase exists only for a very low oxygen deficit δ of 0 to 0.05, whereas for $0.05 \leq \delta \leq 0.18$ single-phase $Fd\bar{3}m$ prevails. Further oxygen loss of $0.18 \leq \delta \leq 0.7$ above $750 - 800\,°C$ causes formation of a second phase in addition to the $Fd\bar{3}m$ phase with cubic rock salt structure.[72] Above an oxygen deficit of 0.7 the rock salt phase is the main one, but a second spinel phase of unidentified composition moreover persists in small amounts between 950 to 1100 °C. Thus, LNMO is essentially single-phase below $\approx 750 - 800\,°C$ and above $\approx 1000 - 1050\,°C$, whereas in the intermediate range the fraction of the spinel phase decreases with increasing temperature, while that of the rock salt one augments.[72] Above 1100 °C irreversible lithium loss sets in.[72] A summary of the presence of the different phases of LNMO as function of temperature and oxygen deficit is given in figure 2.7.

Due to similarity of atomic scattering factors of the two transition metals in XRD investigations, their exact lattice positions cannot be obtained by this method.[72] Thus no information is available, if nickel and manganese or just one metal is present in the rock salt phase. Diverging models exist in literature, and in some publications this phase is supposed to consist of either NiO or $Li_xNi_{1-x}O$, whereas in others it is assumed that both

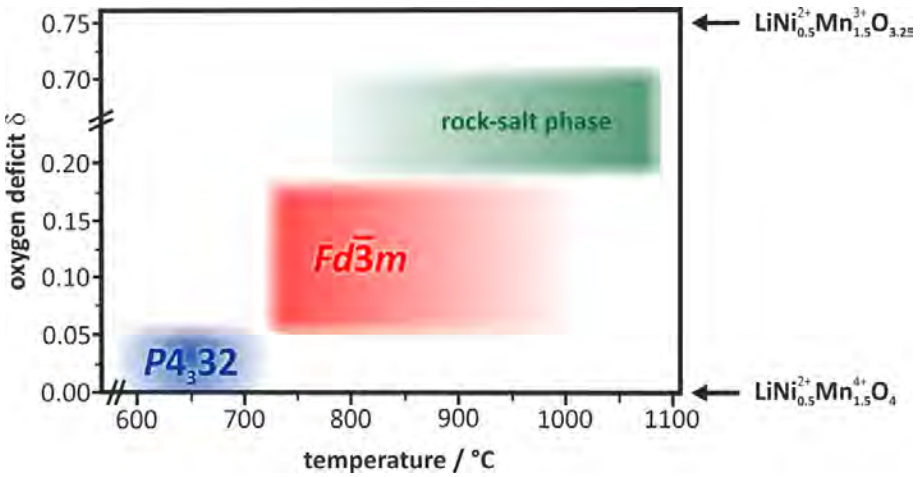

Fig. 2.7.: *Presence of the different phases of LNMO in dependence of temperature and oxygen deficit δ.*

transition metals are present.[72,73] Thereby either the stoichiometry of the starting spinel phase is maintained or it contains a lower ratio of manganese to nickel of 2:1 in comparison to the ratio of 3:1 of the spinel phase, since the rock salt phase formation occurs through preferential extrusion of nickel ions out of the spinel particles.[72,73] Formation of the rock salt phase does not occur at temperatures below 700 °C since the transition metal ion mobility must be high enough for their transfer to interstitial octahedral 16*c* sites.[63] In principle the transition from spinel to rock salt phase is reversible via reinsertion of oxygen upon slow cooling to 700 °C. However, too short dwell time at this temperature does not permit long-range ordering of the transition metals so that oxygen vacancies and with them trivalent manganese ions are retained in the structure.[63]

Both spinel modifications show a structural transformation during lithium extraction, which is presumably caused by the movement of the transition metal ions, but the stoichiometric phase displays an additional intermediate $Fd\bar{3}m$ phase.[60] This two-stage transformation results in a lower structural reversibility especial at high discharge rates in comparison to the oxygen deficit one.[60]

2.2.3. Surface modification and doping

One still unresolved problem of LNMO is its rather poor capacity retention especial at elevated temperatures and high discharge rates.[74] However, investigations by the group of Aurbach showed that a possible fading during prolonged cycling is rather caused by sluggish kinetics than by pronounced degradation of the active material.[67] Other problems of this material are its loss of oxygen, accompanied by the formation of $Li_xNi_{1-x}O$ or NiO, thereby reducing the capacity of the material, when it is heated above 650 °C, and at least

to some extent the presence of trivalent manganese.[74,75] Replacement of some of the Mn and/or Ni ions in LNMO with other metals leads - virtually without any exception - to improved performance due to e.g. avoidance of phase transitions with concomitant stabilization of the spinel structure,[12] prevention of the Jahn-Teller distortion by substituting some of the high spin Mn^{3+} ions with chromium, since the latter ion does not show this effect, as well as suppression of the manganese dissolution in the electrolyte[76] or improvement of the capacity retention and performance at high rates.[77,78] As dopant ions mainly transition metals like chromium, titanium and iron, but also magnesium, aluminum or even ruthenium are used.[76,78–82] Iron doping does not only stabilize the cation-disordered structure, but also suppresses the formation of thick CEI layers due to enrichment of this ion with concomitant deficiency of nickel at the electrode surface.[81]

One possibility to increase the capacity retention is by coating of the active material with protecting layers, preventing both transition metal dissolution and reactions between the active material and the electrolyte.[83] Besides mainly used metal oxide coatings like MgO and Al_2O_3,[20,84] organic, e.g. polyimide based ones also show promising effects since they form very thin, dense layers, so that the additional ionic resistivity caused by an about 10 nm thick coating does not seriously affect the resistance of the cell, but decreases the transition metal dissolution by about 23 %.[85] As coatings also solid electrolytes like lithium phosphorus oxynitride (LiPON) or even the anode material $Li_4Ti_5O_{12}$ (LTO) have been tested.[69,86] An overview of commonly employed coatings on LNMO electrodes and the benefit gained with them is given in table 2.1.

2.2.4. Powder preparation

Besides investigations concerning coatings and dopand ions stabilizing the performance of LNMO, the third main focus in current research activity on this cathode material deals with the optimization of the powder. It is after synthesis either mixed with graphite as conducting agent and a binder in a slurry for deposition by doctor blade to achieve porous, "technical" electrodes or deposited as thin film by various techniques further reviewed in chapter 3.1. An important aspect in the powder preparation is the achievement of single-phase spinel, since impurity phases like $Li_xNi_{1-x}O$ reduce the cell performance.[44] In most cases powder preparation occurs either via solid-state or sol-gel based synthesis.[44,91–93] Some more exotic methods like the formation of core-shell particles[94] or self-combustion reactions[95] were also applied. However, the sol-gel route appears to be superior due to prevention of impurity phases, lower synthesis temperature, more homogeneous mixing at atomic or molecular level and uniform particle distribution.[23,44] However, this method results in higher surface area compared to the solid-state route, thus leading to increased electrolyte oxidation.[44]

Tab. 2.1.: *Overview of commonly employed coatings on LNMO electrodes and the benefit gained with them. The reason for the improvement is also reported if mentioned in literature.*

coating	**benefit**	**reason for better performance**
polyimide[85]	mitigation of electrolyte decomposition and avoidance of highly resistive species like LiF in the CEI	-
$AlPO_4$[87]	reduction of both surface and charge-transfer resistance, resulting in enhanced electrochemical reversibility and stability at elevated temperatures together with higher lithium diffusion rates	reduction of the contact area between electrode and electrolyte and suppression of undesirable solid electrolyte interface films
$FePO_4$[88]	better capacity retention	reduction of the contact area between electrode and electrolyte; suppression of undesirable thick CEI layers
ZnO, LTO[8,89]	reduction of manganese dissolution into the electrolyte	trapping of HF from the electrolyte
LTO, anatase TiO_2[86]	suppression of the formation of undesired impurity phases and loss in crystallinity at elevated temperature cycling	maintenance of the structural integrity
graphene[90]	enhanced cycling performance	increased conductivity, protection of the cathode surface from undesired reactions with the electrolyte
LiPON[69]	reduction of manganese dissolution, improvement of rate performance and capacity retention	deceleration of resistance increase at the cathode/electrolyte interface due to slightly thinner reaction product layer

An important parameter for stable cycling performance and good rate capability is the particle size of the powder, typically being in the range of tens of nm to few μm.[96,97] Smaller particles show enhanced storage kinetics and faster lithium diffusion into the material, therefore showing better performance at high cycling rates.[60,98,99] Smaller particles lead to reduced over-voltages, but on the other hand cause more electrolyte oxidation and worse capacity retention at lower cycling rates.[60,98,99] Combination of the advantages of small and big particles is either possible by mixing equal amounts of both sizes or by usage of sub-μm particles.[99,100] These are small enough to possess short lithium diffusion distances, but also show high crystallinity. The latter aspect raises like particle size with increasing temperature and enhances the electrode capacity.[100]

2.3. Secondary ion mass spectrometry

Secondary ion mass spectrometry is an analytical technique suitable for characterization of both the surface and the local volume of solid matter using high energetic ions, named primary ions, that bombard the sample surface. Due to this impact, ions of the sample, the so called secondary ions, are released and subsequently analyzed using mass spectrometry.[101] Advantage of this analytical tool is its capability of detecting all elements with high spatial resolution of a few hundred nanometers and trace level sensitivity.[14] Moreover, it possesses outstanding depth resolution in the sub-nanometer range and even differentiation between isotopes is possible.[14] This chapter only gives a short overview of this technique, thereby highlighting aspects and problems important for the investigations done in this thesis. However, for deeper insight into the SIMS mechanism the reader is referred to a paper by De Souza and Martin or the textbook by Vickerman and Briggs.[101,102]

In the SIMS technique as primary ions mainly Cs^+, ${O_2}^+$, Ar^+, Xe^+ or cluster ions like ${Bi_n}^{z+}$ and ${C_{60}}^+$ with energies in the range of $0.25 - 30\,\mathrm{keV}$ are used.[14] The latter two are suitable for analysis of polymers and biomolecules since they improve yields of higher molecular weight fragments. The choice of the primary ion energy depends on the requirements of the measurement since a higher energy on the one hand results in an increased sputter yield and thus higher sensitivity as well as better focused ion beams, but on the other hand reduces the depth resolution.[14] Moreover, there has to be always a compromise between good mass and spatial resolution, since the shape of the primary ion beam greatly varies with these two parameters.[103] By impact on the solid, the primary ions transfer their energy in binary collisions to sample atoms, which in turn bump at others with this cascade going on until the energy transfer is insufficient to cause further atom displacement. If such a cascade reaches the sample surface and its energy is sufficient to overcome the binding energy of sample species, matter is ejected, occurring typically from the top two to three monolayers. Most of the released species are neutral, but some are either positively or negatively charged, with their polarity being independent of their charge in the sample. These secondary ions are emitted in a range of energies that peaks around $10\,\mathrm{eV}$, thereby being independent of the primary ion energy.[14] They are collected in the analyzer, which electric polarity decides whether positive or negative ions are analyzed and sorted in it according to their mass-to-charge ratio (m/q). The choice of polarity depends on the matter under investigation, since some elements, mainly electropositive ones from the first two groups of the periodic table or metals, tend to form cations, whereas others are mainly emitted as negative ions since they are more electronegative like halogens or oxides.[101] Different constructions of SIMS machines exist, mainly different by the detector, i.e. quadrupole, double focusing magnetic sector and time-of-flight (ToF)

spectrometers. Each has specific advantages and disadvantages regarding resolution, mass detection, complexity of operation or costs.[14] As exclusively a ToF-SIMS was used in the present study, in the following only this spectrometer is explained in detail. A major advantage of ToF-SIMS is its capability to measure all masses simultaneously for each sample point under investigation, thereby archiving an entire mass spectrum so that later on additional species can be analyzed. In contrast to this, quadrupole or magnetic sensor instruments cannot register more than one element at a time and only selected elements are analyzed. A schematic sketch of the main parts of a ToF-SIMS together with the three different kinds of information gained in a SIMS measurement, which will be discussed later in this chapter, is shown in figure 2.8.

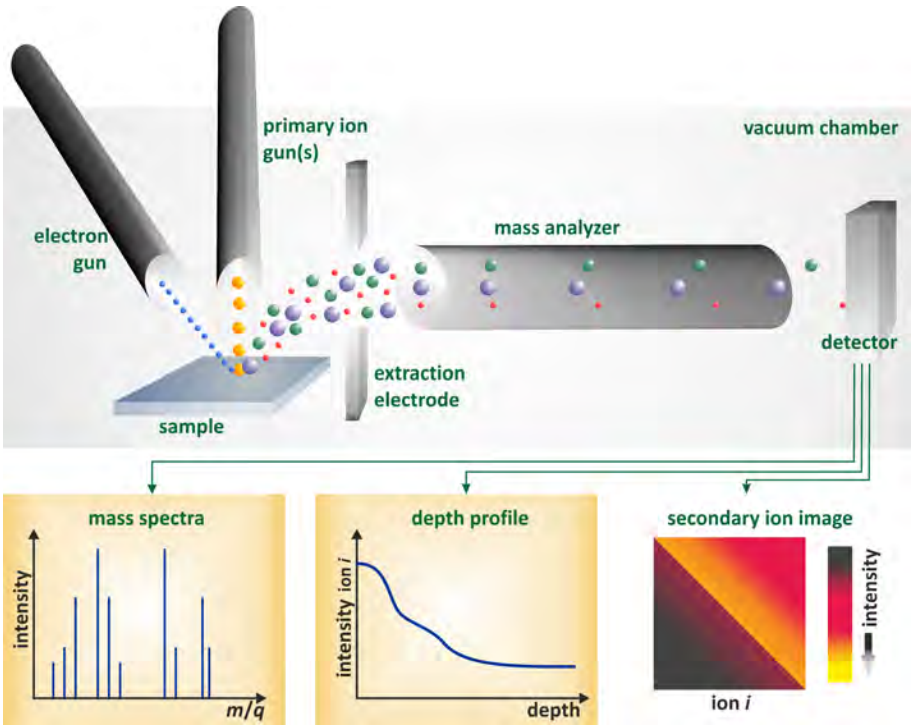

Fig. 2.8.: *Schematic sketch of the main parts of a ToF-SIMS together with the three different kinds of information gained in a SIMS measurement. The whole equipment is housed in an UHV chamber. Modified and redrawn from*[101]

The secondary ions of selected polarity are accelerated by a potential U_{ex} to the analyzer entrance, thus all having the same kinetic energy at the beginning of the so called flight tube, a field-free space where the ions are sorted by their m/q ratio. This region is passed faster by lighter ions, which therefore reach the detector at the other end of the tube first, followed by increasingly heavier species, according to equation 2.9, with v being the velocity of the secondary ions:[101]

$$E_{kin} = 1/2mv^2 = U_{ex} \cdot q \tag{2.9}$$

The flight time of a specific secondary ion thus only depends on the fixed instrumental parameters U_{ex} and the length of the flight tube l_f together with its mass-to-charge ratio:[101]

$$t = \frac{l_f}{v} = \sqrt{\frac{l_f^2}{2U_{ex}} \frac{m}{q}} \tag{2.10}$$

Since all ions necessarily have to start their flight at the same time, the primary gun is operated in a pulsed mode with the pulse length below 1 ns for high mass resolution.[101] To achieve both, longer flight times, which in turn results in greater differences in arrival times at the detector for the different species, as well as better mass resolution, often no linear mass analyzer, but one equipped with a reflector is employed. The latter component is an electric field at the other end of the flight tube that slows the secondary ions down and accelerates them in the reverse direction. Thus they fly two times through the field-free space. Better mass resolution is achieved, since secondary ions with a bit higher kinetic energy than others of the same type, which therefore would reach the end of the flight tube a little earlier, fly a bit deeper into the reflector. In consequence they travel a little longer way and as a result are bundled together with the slower ones and arrive together at the detector.[104] A schematic sketch of the reflector setup and function is shown in figure 2.9. Normally, the trajectory of the secondary ions before and after passage of the reflector is constructed in that way, that there is a small angle between them.[104] Therefore, in a SIMS machine equipped with a reflector, the detector is positioned next to the ion entrance in the flight tube. For those having a linear setup without this feature, it is located at the opposite end of this tube as it holds for the setup in figure 2.8.

Besides at least one primary ion gun and the mass analyzing system with flight-tube and detector, most machines are also equipped with an electron-floodgun for charge compensation building up especially during ion bombardment of poorly conducting samples.[14]

The SIMS machine can be operated in two different modes, called static and dynamic mode. In the former mode, only the surface of the sample is investigated. The results can be afterwards displayed either as mass spectrum, i.e. secondary ion intensity against m/q ratio, or as ion image, in which the lateral variation of secondary ion intensity is displayed for selected ions. In the static mode only a very low dose of primary ions of less than 10^{12} ions per cm^2 is used.[14] In consequence, during the analysis secondary ions are statistically emitted from regions that had not yet been irradiated.[14] This enables the investigation of the true surface, since its damage is minimized and ions are predominantly emitted from the uppermost monolayer. In contrast to this, in the dynamic mode progressive

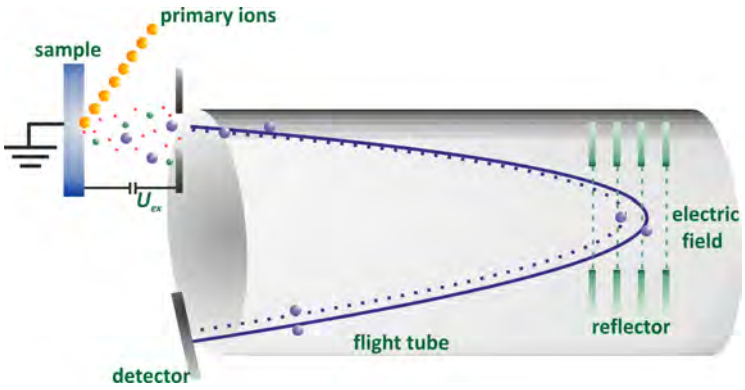

Fig. 2.9.: *Schematic sketch of the setup and function of the reflector in a ToF-SIMS analyzer. Modified and redrawn from*[104]

erosion, called sputtering, of a defined sample region by a high current primary ion beam occurs with concomitant analysis of this area.[14] Thereby, the secondary ion intensity of selected ions as function of depth is achieved, the so called depth profile.[14] In contrast to SIMS machines using other analyzers, a ToF-SIMS requires separate primary ion guns for analysis and sputtering. Since primary ion beams usually show Gaussian-type profiles, the use of stationary beams would lead to rapid loss of depth resolution because secondary ions coming from various depths would be collected. To overcome this problem, named crater-wall effect, the sputter ion beam is raster scanned over a greater area, but secondary ions are collected only from the central, flat area, being typically 1/9 or even smaller than the sputtered area.[14] A schematic sketch showing the recording of a SIMS depth profile is given in figure 2.10. In the depth profile first no depth, but the sputter time is displayed on the abscissa, since the sputter yield depends to a large extent on the material under investigation. Therefore, the depth of the sputtered crater has to be determined separately e.g. with a profilometer. It raster scans the sample surface with a fine needle, thereby delivering information about hight differences between two regions of the sample or its roughness. By knowledge of the lateral crater size and the energy of the sputter gun together with the external determined crater depth, the sputter yield for the given material can be calculated. This in turn can be used to determine the crater depth of another SIMS depth profile in the same material if the lateral crater size and the energy of the sputter gun used for this measurement are known. This could be beneficial for samples with irregular coloring, thus complicating the detection of the crater in the profilometer camera and therefore its depth determination in this machine.

The whole SIMS process takes place under UHV conditions of $10^{-7} - 10^{-10}$ Pa to increase the mean free path of the primary and the secondary ions as well as to increase the

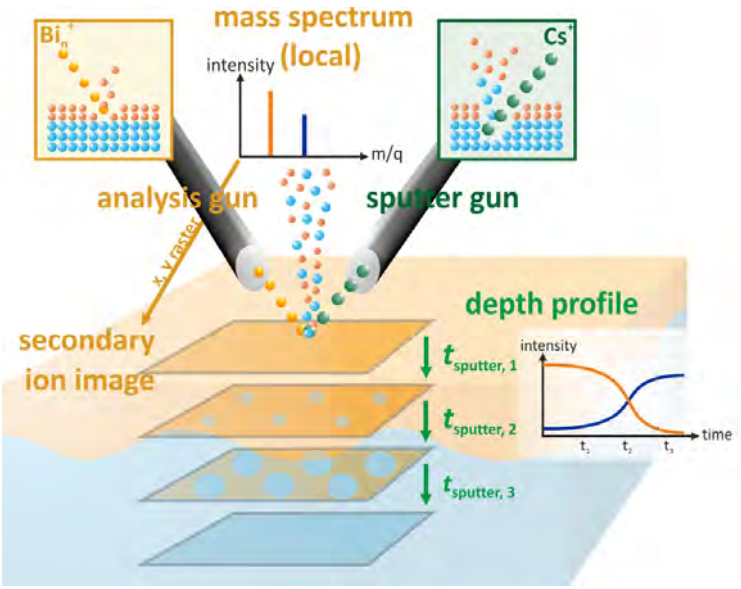

Fig. 2.10.: *Schematic sketch showing the recording of a SIMS depth profile.*

time required to contaminate the surface with a monolayer of residual gas molecules. In consequence, only vacuum stable samples, mainly solids, but in special applications also frozen liquids with sufficient low partial pressure, can be analyzed.[101] Another drawback of the SIMS is the formation of the so called "altered layer" due to ion beam erosion of the sample surface, which is schematically sketched in figure 2.11. As a result, it is impossible to analyze the same position twice together with a homogenization of the composition and alteration of the structure of this layer. This is caused by ion beam mixing, i.e. a continuous redistribution of surface and sub-surface species either directly by the primary ions or within the collision cascade. Occurrence of this altered layer firstly means that intensity variations with sputter time do not necessarily reflect changes in the sample composition. Secondly, the actual depth resolution is not the maximum depth from which secondary ions are emitted, which is in the range of a few monolayers, but due to redistribution in the altered layer by its thickness, thus being approximately in the range of the primary ion penetration depth, which is in the range of nanometers to tens of nanometers.[14] The altered layer also reduces the lateral resolution, which is theoretically limited by the diameter of the primary ion beam. It is, however, actually given by the size of the collision cascade, since secondary ions will be emitted up to several nanometers away from the exact point of primary ion impact.[14] Moreover, preferential sputter may occur, leading to the depletion of one or more species in compound samples. Implantation of primary ions also may happen in the altered layer, which is not only a drawback, since they can enhance the ionization probabilities of the sample species by several orders of magnitude. In this

regard, electronegative O_2^+ primary ions in comparison to noble gas ones increase the ionization probability for species tending to form cations, whereas usage of electropositive Cs^+ ions enlarge the ionization probability for species which are more likely to be emitted as anions.[14]

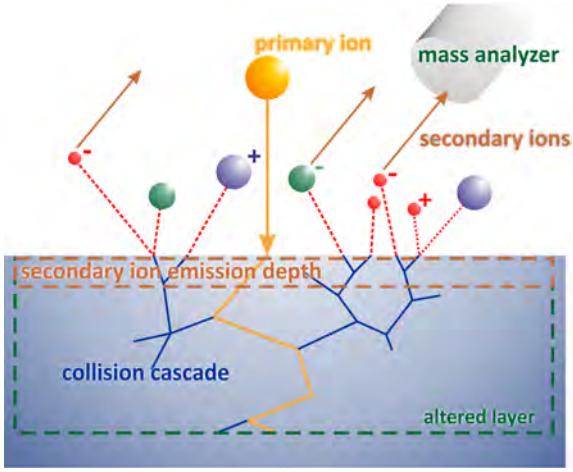

Fig. 2.11.: *Schematic sketch of the altered layer formed in the sample due to primary ion impact. In this example negative secondary ions are collected which are therefore accelerated towards the entrance of the analyzer. Modified and redrawn from*[101]

Another disadvantage of SIMS investigations which also holds for other techniques using mass spectrometers is the possibility of mass interferences. They result from the occurrence of two or more secondary ions with the same nominal m/q like e.g. $^{56}Fe^+$ ($m = 55.934939$) and $^{28}Si_2^+$ ($m = 2 \cdot 27.976927 = 55.953854$), which are only separated by a very small mass difference Δm of 0.018915.[14] If the mass resolution of the SIMS is not sufficient, the peak visible in the mass spectra will be an overlay of both species. This results in misleading information about the lateral and in-depth variation of both species, since contributions of both ions are contained in the detected signal. For this example a mass resolution $m/\Delta m$ of $55.934939/(2 \cdot 27.976927 - 55.934939) \approx 2.9 \cdot 10^3$ is required. Moving from elemental semiconductors to compounds and especially oxides, the number of possible interferences increases drastically. This problem becomes even more severe since mass interferences result not only from components in the sample, but also from residual gas in the analysis chamber, the primary ions or combinations of the various species.[14]

Main difficulty of SIMS is the quantification of the measured intensities since these depend on a number of parameters like the background pressure in the chamber, the element of interest, A, and, most problematic, on the matrix M in which it is located. Relation of the measured secondary ion intensity i_A to the atomic fraction x_A of element A in the sample is achieved by the following equation, where I^P is the primary ion intensity in ions

per second, Y the sputter yield, $\alpha_A^{+/-}$ the ionization probability for positive and negative secondary ions, respectively, η_A the combined transmission efficiency of the extraction optics, the mass spectrometer and the detector and Θ_A the isotopic abundance:[14]

$$i_A = I^P \cdot Y \cdot \alpha_A \cdot \eta_A \cdot \Theta_A \cdot x_A \tag{2.11}$$

Whereas I^P and Y can be measured separately and Θ_A is tabulated, this does not hold for η_A and $\alpha_A^{+/-}$. The latter parameter moreover varies by orders of magnitude depending on several factors like the secondary ion and the matrix under consideration. As a result, quantification is mainly done by analyzing a known concentration of the species of interest in a matrix close to the one of the sample with the unknown concentration under identical measurement conditions with concomitant comparison of the intensities.[14] Since separate standards are required for each element under investigation and every different matrix, it is clear that this procedure is very time-consuming.

Drawback of the SIMS in comparison to XPS is the lack of information about the oxidation state of the ions in the sample. However, whereas in SIMS measurements lithium delivers high intensity and even small amounts can be properly investigated, in XPS it shows only a small peak, which often diminishes in the background signal or overlaps with the line of Mn(3p).[105] SIMS measurements moreover may yield more useful information especially during study of organic molecules than those obtained form XPS, since e.g. fragmentation patterns of related species obtained by ToF-SIMS could show large differences, whereas the spectra recorded by XPS are similar.[103] Therefore, both techniques offer own, partially opposed, advantages and disadvantages so that combination of both using the strength of each tool is recommended for sufficient sample characterization.

Proper peak selection is another problem in the evaluation of SIMS measurements. On the one hand, narrow peak widths are advantageous, since mass interferences are avoided, but on the other hand, small areas will result in reduced intensity and even severe, some information could be lost. This could be caused by large height differences in the sample, so that secondary ions coming from deeper areas have slightly longer flight times. They therefore reach the detector a little later, thus resulting in peak broadening. The same effect is also caused by areas of different polarity or electric conductivity being investigated in the same measurement, so that the reflector potential cannot be optimized for both regions at the same time. This in turn causes varying trajectories in the reflector and thus different flight times for secondary ions of the same sort, but from different regions. The latter aspect holds for the example in figure 2.12 showing the secondary ion images of a sample consisting of an YSZ single crystal being half covered with LSM, a cathode material for solid oxide fuel cells. Whereas the latter one is electronically conductive, this

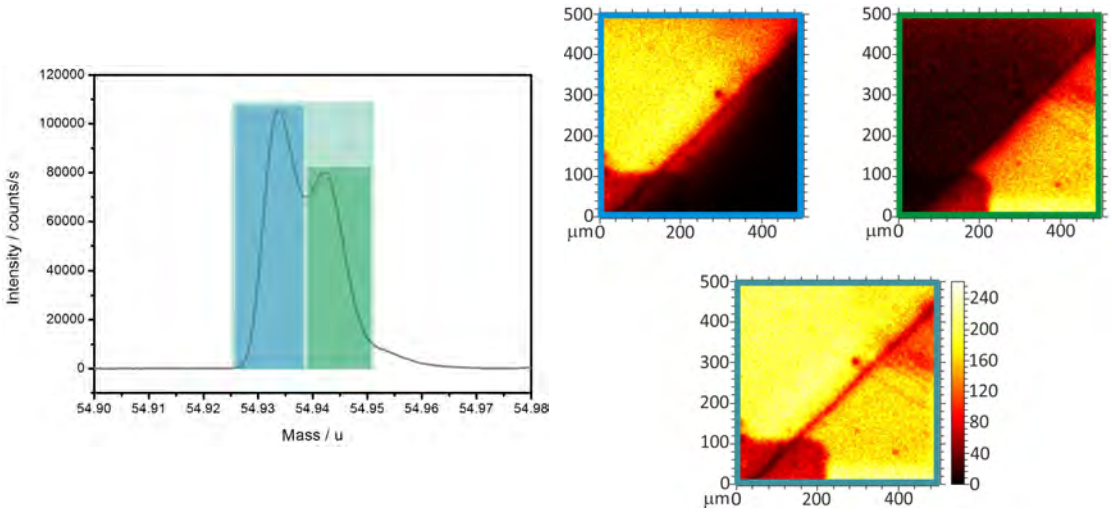

Fig. 2.12.: *SIMS spectrum of Mn^+ on the left and corresponding secondary ion images on the right side of a LSM electrode deposited on a YSZ single crystal showing the influence of the peak selection in the mass spectra on the resulting secondary ion image. In the image, the LSM electrode is located in the lower right corner and the free YSZ crystal in the upper left one. The blue framed image belongs to the left part of the Mn^+ peak in the spectra, the green framed one to the right part and in the turquoise one the sum of them was evaluated.*

does not hold for the substrate, which is used as electrolyte in this application. High temperature treatment of this material combination results in diffusion of the metal ions of the cathode into and onto the electrolyte, so that afterwards e.g. manganese is found in both regions. Recording a secondary ion image of this ion along the cathode/electrolyte interface results in the SIMS spectra and images shown in figure 2.12. In the spectra, the left, blue colored part of the peak belongs to the blue framed secondary ion image, the right, green colored one to the green framed one and the turquoise image shows the sum of the two peak areas. Since this peak splitting occurs also for a number of other species in this sample, it is obvious that these double peaks do not arise from different masses, but result from varying states of charge in the two different sample areas. Thus, the signals coming from one region are shifted compared to those from the other one, but belong to the same mass. Evaluation of only one part of the peak in the mass spectrum in consequence would result in a completely wrong ion distribution for this sample.

Besides vacuum stability, another sample requirement for SIMS investigations is sufficient flatness of the sample. In the case of too large roughness the whole region under investigation cannot be focused simultaneously. From areas out of focus less ions reach the detector, resulting in lateral variation of the secondary ion intensity and therefore apparent concentration gradients in the sample that do not exist in reality. Surface topography also can influence the ultimate mass resolution obtainable, arising from slight differences

in the extraction field seen.[103] Electric conductivity of the sample is also beneficial, but this problem can be overcome to large extend by usage of the charge compensating flood-gun. Besides these, there are no other sample requirements and furthermore, no sample pretreatment is required.

2.4. Pulsed laser deposition

Pulsed laser deposition (PLD) is a thin film preparation technique feasible to a variety of materials and substrates. Advantages of this method with respect to other thin film deposition techniques are its effective evaporation and therefore deposition of matter with high melting points or low vapor pressures as well as its ability to deposit both electrical conducting and insulating material.[106] In this section only a short overview of this technique is given, emphasizing the aspects important for the thin film deposition of LNMO cathodes used in this thesis. For deeper insight see the textbook "Pulsed Laser Deposition of Thin Films" by Chrisey and Hubler[107] or papers by Beckel et al.[108] and Schönig et al.[109]

In the PLD process, a high energetic, pulsed laser beam is directed onto the material to be ablated and deposited, named target, which evaporates in a expanding plasma plume normal to its surface and redeposits onto the so called substrate which is placed at a distance of a few cm away from the target with their surfaces faced to each other. Heating of the substrate is possible, which results in better homogeneity of the deposited films. Typical wavelengths used for irradiation are in the range of $200 - 400\,\mathrm{nm}$ and with an appropriate choice of the laser energy any material can be deposited.[108] Since PLD is a non-equilibrium process, deposition of stoichiometric layers of even complex, multi-component systems using just one target with the desired composition is possible.[107–109] Also deposition of material combinations which could not be deposited by other methods due to e.g. too large differences in melting points or of metastable compositions succeed.[106] This is possible due to the high heating rate induced by the laser. This results in concomitant evaporation of all target components instantaneously during irradiation, thereby circumventing the thermodynamic equilibrium.[107] The resulting particle cloud is approximately of the same composition like the target material.[107] Another advantage of this technique is the wide variety of background gases, either reactive or not, which could be used. Pressures from ultra high vacuum to up to six orders of magnitude higher values are possible.[106,110]

The PLD setup, which is schematically sketched in figure 2.13, consists of a vacuum chamber containing substrate and target holders together with a UV-transparent window, through which the laser beam enters the chamber, and a gas inlet to vary the atmosphere

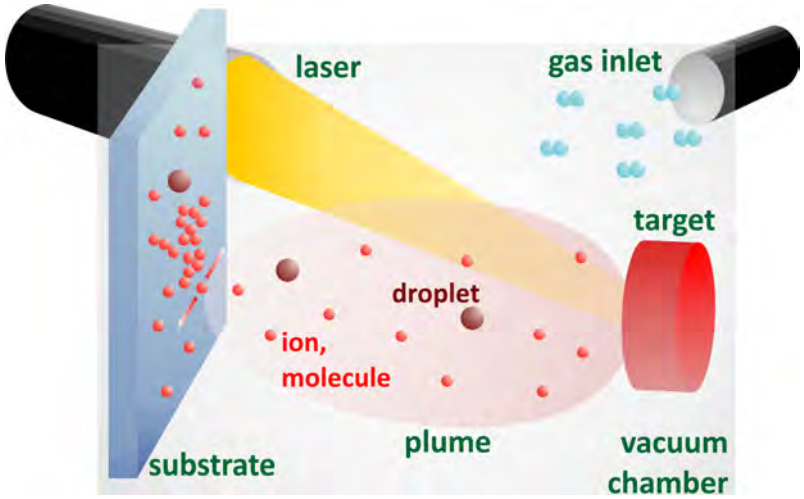

Fig. 2.13.: *Schematic sketch of the main components of a PLD chamber together with the plume which forms during irradiation of the target material and contains species evaporated from it like ions, molecules or larger particle agglomerates called droplets. Due to their residual kinetic energy, species deposited on the substrate are still mobile. Modified and redrawn from*[110]

during the deposition. The laser/target interaction is schematically sketched in figure 2.14: During the PLD process, the laser light is absorbed by the solid surface of the target material, then converted first into electronic excitations and afterwards in thermal, chemical and mechanic energy causing immediate local melting of the target surface. Thereafter, evaporation of the target material occurs as atoms, molecules, electrons, ions and clusters with energies ranging from 10 to over 100 eV depending on the material, together called plume.[106,108] Inside the plume a plasma forms due to photon absorption of the vaporized species and rapidly expands normal to the target material in a jet, remaining narrow and relatively anisotropic, thus allowing coverage of only small areas.[108,110] This spatial restriction is the main drawback for the application of this thin film preparation technique in industrial production since scaling-up is rather difficult.[108] The typical laser energy is in the range of $1 - 10$ J and effective pulse durations are several 10 ns in which energy densities of 10^8 W/cm^2 are reached.[106,110] At the end of the pulse, the system returns to its initial state.[110] However, since components with higher melting point resolidify first, those melting at lower temperatures enrich at the surface.[107] In consequence, homogeneity of the target is lost after prolonged laser irradiation together with an increase in roughness of the target surface.[107] Since effective evaporation of the target material is ensured if the absorption of the pulse energy occurs near its surface, light sources operating in the UV spectrum are applied, because for most materials decreasing wavelengths go along with a drastic reduction of their optical penetration depth.[110] Therefore, PLD chambers are normally equipped with either Nd:YAG (yttrium aluminum garnet (YAG)) or excimer

lasers.[110] Adjusting the laser energy to the material to be deposited is important since it mainly influences the area of the melting zone.[109] Energy distribution beyond the evaporated volume should be avoided to the minimize destruction of the residual target as well as the segregation of the different components.[108]

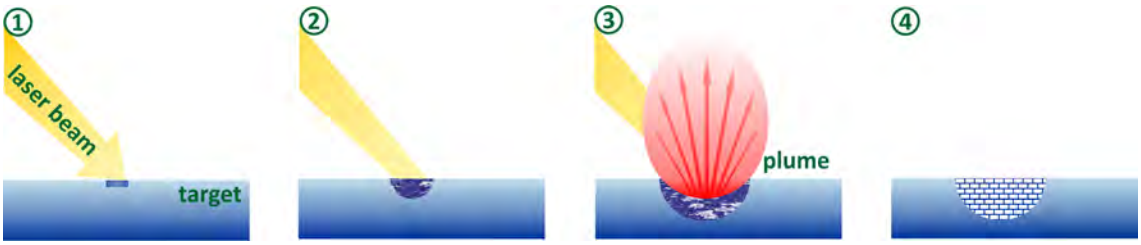

Fig. 2.14.: *Schematic sketch of the laser/target interaction during the PLD process: 1) absorbance of the laser light by the solid target surface; 2) local melting of the surface; 3) evaporation of the target material in a plume; 4) resolidification of the target material after end of the laser pulse. Modified and redrawn from*[106,107]

After deposition on the substrate, the surface atoms diffuse along the surface due to their residual kinetic energy and aggregate, thereby forming dense layers.[111] This process is influenced by both the substrate temperature and the pulse repetition rate. With increasing temperature the surface atoms are more mobile and therefore can lead to growth in energetically more favorable directions. At low repetition rates, the formed islands have more time to ripen, thus their number reduces and the film morphology turns into a compact structure, whereas at high pulse rates, there are more and dispersed or dendritic shaped aggregates.[111] The already formed film is moreover influenced by the bombardment of further particles, resulting in e.g. desorption, demixing, point defect generation or chemical reactions.[106]

An important drawback of the PLD process is the formation of larger particles in the range of one μm named droplets that also deposit on the substrate and therefore deteriorate the film quality. Their occurrence results e.g. from phase transformations at the solid/liquid interface with concomitant density variation between these two regions, thermal expansion of the matter in the irradiated region, over-heating of the liquid surface or by recoil pressure pulse on the molten surface generated by the vaporised species.[110,112] The latter aspect results from surface wrinkling during prolonged laser irradiation which leads to discontinuities of the molten film. Thus, the recoil pulse pressure might be locally destabilizing, causing the ejection of molten material, thereby leading to large droplets.[110]

The background pressure and the distance between target and substrate are also important parameters influencing the quality of the deposited film: for small spaces between target and substrate the energy of the impacting particles could be so high, that the

already formed film is destroyed and defect formation is likely.[113] Too large distances however drastically reduce the deposition rate, since only particles with very high energy reach the substrate.[113] Too high background pressures on the one hand lower the velocity of the particles in the plume, thus reducing their diffusion on the substrate and therefore bearing the fear of increased film roughness. On the other hand, a certain amount of oxygen background pressure is often needed during the deposition of oxides to avoid oxygen deficit in the film.

2.5. Electrochemical techniques

For the electrochemical investigation of batteries basically two different strategies are applied: Either sweeping the applied potential and measuring the responding current in the so called cyclic voltammetry (CV) or controlling the latter parameter and measuring the potential needed to maintain it, named chronopotentiometry (CP). In CP experiments of galvanic cells usually a constant current is applied to the cell under investigation, thus called constant-current chronopotentiometry. Less usual, chronoamperometry (CA), i.e. setting the potential at a defined value and measuring the resulting current, is used as well as pulsed forms of the latter two techniques with subsequent relaxation times between the single steps. Another investigation tool is the (potential-controlled) electrochemical impedance spectroscopy (PEIS), in which an alternating potential of varying frequency is applied to the sample and the frequency dependent current of the sample is measured. The resulting impedance spectra can be assigned to electronic devices like resistors or capacitors as well as to combinations of them. These in turn correlate to processes occurring in the sample, thus delivering e.g. information about reaction mechanisms like the rate determining step or values of the charge transfer resistance and double-layer capacity.[114] Since both CV and constant-current (cc) experiments were used for the electrochemical characterization of cells studied for this thesis, the next two sections focus on these techniques. However, in each case only a short overview is given, emphasizing the aspects important for the present investigations. For deeper insight in these methods the reader is referred to "Understanding voltammetry" by Compton and Banks[115] concerning cyclic voltammetry and for constant-current chronopotentiometry to "Electrochemical Methods: Fundamentals and Applications" by Bard and Faulkner,[116] see especially chapter 8.

2.5.1. Cyclic voltammetry

In CV experiments a triangular voltage, i.e. a voltage ramp with linear potential variation with time, is applied to the sample between two defined potentials. The current flowing through the working electrode (WE) is monitored and plotted as function of the applied

potential. Peaks, i.e. high current flow, in the cyclic voltammogram are correlated to reduction and oxidation reactions in the sample. Usually, the starting potential E_S is selected so positive, that no reaction takes place and thus negligible, only nonfaradaic current flows.[115,116] The voltage is than linear swept to the second potential E_F, at which the potential applied to the electrode is reversed and scanned to its original value. E_F is selected such, that the redox reaction of interest, occurring at potential E_f^0, occurs in the interval between these two potentials. Thereby, E_f^0 is the formal potential of the redox couple under investigation, defined as[115]

$$E_f^0(\mathrm{A,B,.../X,Y,...}) = E^0(\mathrm{A,B,.../X,Y,...}) + \frac{RT}{F} ln\left(\frac{a_A^{\nu_A} a_B^{\nu_B} ...}{a_X^{\nu_X} a_Y^{\nu_Y} ...}\right) \tag{2.12}$$

where a_i and ν_i are the activity coefficient and the stoichiometric factor of species i, respectively, concerning the reaction $\nu_A\mathrm{A} + \nu_B\mathrm{B} + ... + e^- \rightleftharpoons \nu_X\mathrm{X} + \nu_Y\mathrm{Y} + ...$ and E_0 is the standard electrode potential of the A,B,.../X,Y,... couple.[115] E_f^0 is independent of $[\mathrm{A}]^{\nu_A}$, $[\mathrm{B}]^{\nu_B}$, $[\mathrm{X}]^{\nu_X}$, $[\mathrm{Y}]^{\nu_Y}$, ... i.e. the concentration of species A, B, X, Y, ... Thus, the Nernst equation (see equation 2.4) rewrites to:[115]

$$E = E_f^0(\mathrm{A,B,.../X,Y,...}) + \frac{RT}{F} ln\left(\frac{[\mathrm{A}]^{\nu_A}[\mathrm{B}]^{\nu_B} ...}{[\mathrm{X}]^{\nu_X}[\mathrm{Y}]^{\nu_Y} ...}\right) \tag{2.13}$$

Since E_f^0 depends on electrolyte concentrations, it loses the thermodynamic generality of E_0 being only applicable to very specific conditions.[115] A schematic sketch of the voltage evolution with time for CV measurements is given in figure 2.15 together with the current response. Also depicted is the concentration developing with time for the species being reduced, O, as well as for R, the one formed in the reaction, regarding electrode processes during CV experiments in its simplest manner according to the following equation:[115,116]

$$\mathrm{O} + e \rightleftharpoons \mathrm{R} \tag{2.14}$$

Peaks in the voltammogram arise since the current increases when the electrode potential reaches the vicinity of E_f^0, where reduction of species O to R begins. As the potential moves in anodic direction, the surface concentration of O drops due to its consumption in the reaction, hence its flux to the surface and thus the current increases. As the potential moves past E_f^0, its surface concentration decreases to nearly zero, its mass transfer to the surface reaches a maximum rate and then declines since depletion sets in.[116] During reverse potential scan, the oxidation of R to O, thus the back reaction, takes place if the process is reversible and the reversal current has a shape much like that of the forward one.[116]

The exact form of the CV wave depends on the scan rate as well as on the reversibility

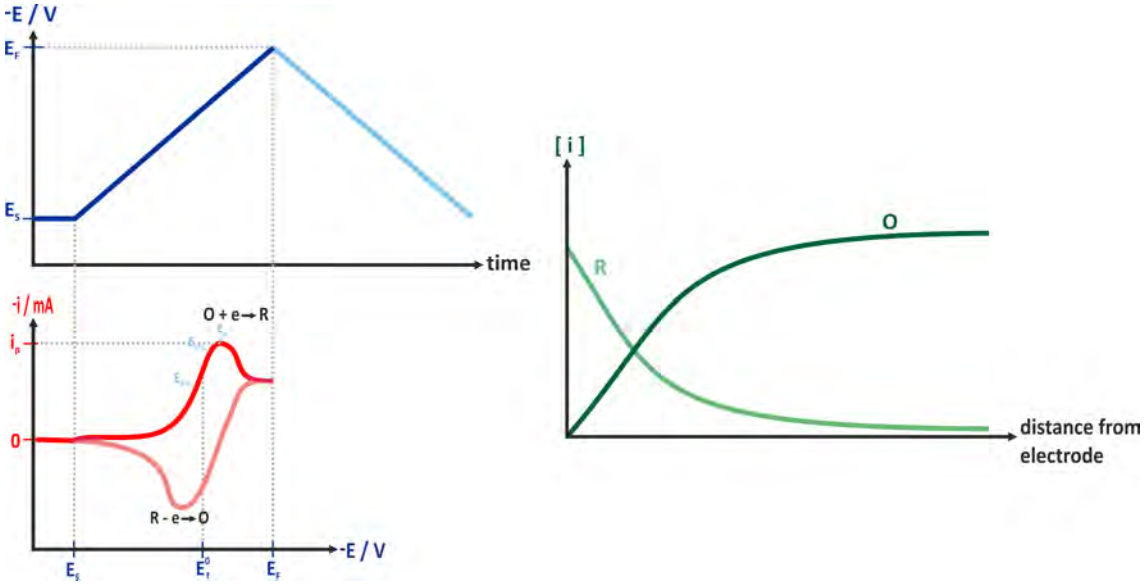

Fig. 2.15.: *Schematic sketch of the voltage evolution with time for a CV measurement in the left upper row and in the lower one the current response together with the definition of the different potentials characterizing the peak form. On the right side the concentration developing with time for O, the species being reduced, as well as for R, the one formed in this reaction, is given. Modified and redrawn from*[116]

of the underlying processes. Reversible voltammetry occurs for fast electrode kinetics, while slow kinetics result in irreversible behavior.[115] Decision between these two cases is possible by regarding the rate of electron transfer kinetics, measured by the standard electrochemical rate constant k^0[ii] in relation to the rate of mass transport to the electrode m_T, which is defined as:[115]

$$m_T = \frac{D}{\delta} \approx \sqrt{\frac{D}{(RT/F\nu)}} \tag{2.15}$$

$$\begin{aligned} reversible &: k^0 \gg m_T \\ quasi-reversible &: k^0 \approx m_T \\ irreversible &: k^0 \ll m_T \end{aligned} \tag{2.16}$$

where D is the Diffusion coefficient of the species under investigation, δ the thickness of the diffusion layer, i.e. the region surrounding the electrode in which the concentration of

[ii] The standard electrochemical rate constant k^0 is a measure of the kinetic dynamics of a redox couple, i.e. a system with large k^0 will reach equilibrium on a short time scale, whereas a system with small k^0 will be sluggish.[116] In equilibrium, k^0 is defined as $k^0 = \frac{i_0}{FA[\mathrm{O}]_{bulk} e^{-\alpha \frac{F}{RT}(E-E_f^0)}}$ where i_0 is the exchange current, A is the electrode surface, $[\mathrm{O}]_{bulk}$ the volume concentration of species O and α is the transfer coefficient of the reaction.[116]

the electroactive species is different to its bulk value, and ν the voltage scan rate.[115] All equations in this chapter are given without derivation, but they can be retraced e.g. in chapter 4 of the textbook "Understanding voltammetry" and chapter 6 of "Electrochemical Methods: Fundamentals and Applications".[115,116] The relationship given in equation 2.16 shows that the reversibility of a system is not a fixed property, but depends on the scan rate employed in the experiment. The appearance of kinetic effects depends on the time needed to traverse the wave in CV measurements: at small scan rates or long times, systems may yield reversible behavior, while at high scan rates it turns into irreversible one.[116] However, for sufficiently fast scan rates, at least in principle, all processes can appear to be electrochemically irreversible.[115] This is caused by the diffusion layer surrounding the electrode during CV experiment and widens while sweeping from E_S to E_F. The longer the time takes to scan the voltammogram, the thicker is this region. Conversely, the faster the sweep rate, the thinner is this layer. The thickness of the diffusion layer controls the rate of mass transport to the electrode as parameterized in m_T and reflecting Fick's 1^{st} law[iii] predicting greater fluxes for a given concentration drop over a thinner diffusion layer. Since electrochemical reversibility reflects the competition between electrode kinetics and mass transport, faster scan rates enforce greater irreversibility.[115]

In the irreversible case, negligible current flows for potentials close to the formal potential E_f^0.[115] Thus, more negative potentials in cathodic and more positive ones in anodic direction, called overpotentials, must be applied in order to drive the electrode process due to small value of k^0.[115] Thus, the peak-to-peak separation ΔE_{pp} between the forward and reverse peak in voltammograms also depends on the reversibility of the system. Whereas in the reversible limit, this value is approx. 57 mV at 298 K and is independent of the scan rate, under quasi- and irreversible conditions ΔE_{pp} is defined by

$$\Delta E_{pp} = \frac{59.4}{\alpha} log_{10}\nu + constant \tag{2.17}$$

at 298 K, thus depending on the voltage scan rate.[115] In the reversible case, the peak potential E_p is also independent of scan rate and given by equation 2.18, where $E_{1/2}$[iv] is the potential just about midway between E_p and $E_{p/2}$, the potential at half peak current:[116]

$$E_p = E_{1/2} - 1.109\frac{RT}{nF} \tag{2.18}$$

Since the peaks are somewhat broad, thus complicating the determination of the peak

[iii] $j = -D\frac{\delta c}{\delta x}$, where j is the flux corresponding to the number of moles passing through unit area in unit time and $\frac{\delta c}{\delta x}$ is the local concentration gradient at point x.

[iv] $E_{1/2} = E_f^0 + \frac{RT}{nF} ln(\frac{D_R}{D_O})^{1/2}$ where n is the number of electrons transferred and D_R, D_O are the diffusion coefficients of the two species R and O[116]

potential, it is sometimes convenient to report $E_{p/2}$, which is defined regarding the electrochemical reversible case as follows:[116]

$$E_{p/2} = E_{1/2} + 1.09\frac{RT}{nF} \tag{2.19}$$

In contrast to this, for the irreversible case the potentials at both peak current and half peak current are a function of scan rate, shifting for a reduction to more negative values with increasing ν:[116]

$$E_p = E_{1/2} - \frac{RT}{\alpha F}\left[0.780 + ln(\frac{D_O^{1/2}}{k^0}) + ln(\frac{\alpha F\nu}{RT})^{1/2}\right] \tag{2.20}$$

$$E_{p/2} = E_{1/2} - \frac{RT}{\alpha F}\left[-1.077 + ln(\frac{D_O^{1/2}}{k^0}) + ln(\frac{\alpha F\nu}{RT})^{1/2}\right] \tag{2.21}$$

A summary of the definition of the different potentials in a cyclovoltammogram is given in figure 2.15. In the reversible as well as in the irreversible limit, the peak current i_p varies with the square root of voltage scan rate, thus indicating diffusion control, but with different coefficients of proportionality:[115,116]

$$reversible: i_p = 0.446FA[\mathrm{O}]_{bulk}\sqrt{\frac{FD\nu}{RT}} \tag{2.22}$$

$$irreversible: i_p = 0.496\sqrt{\alpha}FA[\mathrm{O}]_{bulk}\sqrt{\frac{FD\nu}{RT}} \tag{2.23}$$

In contrast to this, for quasi-reversible systems the square-root dependence of the peak current on the voltage scan rate does not hold.[115]

Concerning Fick's first law, it is obvious that higher scan rates result in larger i_p, again due to greater fluxes. However, as already seen in figure 2.15 before and after a peak in the cyclovoltammogram, the current does not decay to zero, but rather shows steady increase during voltage scan from E_S to E_F. Thus, i_p must not be measured from zero current to the maximum value, but from a baseline, constructed as shown in figure 2.16 by extrapolation of the current gradient at the bottom of the peak.

The third difference between reversible and irreversible systems is the lineshape of the forward peak, being characterized by the distance between E_p and $E_{1/2}$.[115] While for a reversible system

$$\left|E_p - E_{1/2}\right| = 2.218\frac{RT}{F} \tag{2.24}$$

holds, for a irreversible one, there is a difference between reduction and oxidation:[115]

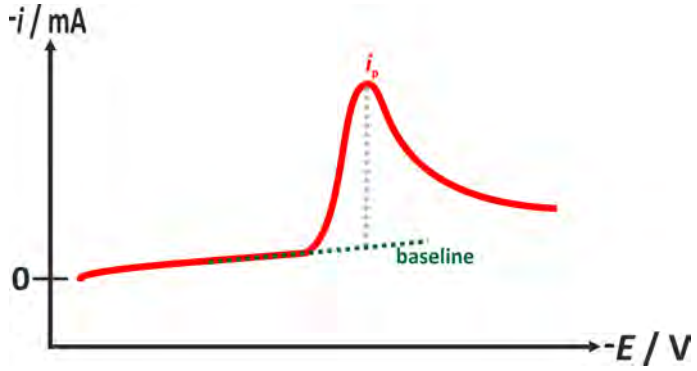

Fig. 2.16.: *Schematic sketch showing the construction of the baseline in a CV.*

$$\begin{aligned} reduction: \left|E_p - E_{1/2}\right| &= 1.857\frac{RT}{\alpha F} \\ oxidation: \left|E_p - E_{1/2}\right| &= 1.857\frac{RT}{(1-\alpha)F} \end{aligned} \tag{2.25}$$

A schematic sketch showing the influence of the electrochemical reversibility on the peak shape and position is given in figure 2.17. However, independent of the reversibility, the formal potential $E_f^0(\mathrm{O/R})$ is located at the potential midway between the peaks of forward and back reaction, if the diffusion coefficients of species O and R are equal. In contrast to this, if e.g. $D_\mathrm{R} \gg D_\mathrm{O}$, the reductive process in the CV occurs at less negative potential in comparison to the case when $D_\mathrm{R} = D_\mathrm{O}$.[115] Thus, E_f^0 is more negative than in the latter case and therefore located closer to the reduction peak.

It is worth noting, that the criteria stated above only hold for the first cycle since the concentration of the electroactive species close to the electrode changes due to previous cycles, thus variation of the peak current for forward and reverse scan as well as of the peak potential occurs.[115] To overcome this problem, the solution could be stirred between the single scans to reconstitute homogeneous concentrations.

Additional complexity arises, if in the voltage range under investigation not only one redox reaction, but multi-step charge transfer occurs, either independent according to[116]

$$\begin{aligned} \mathrm{O} + e &\rightarrow \mathrm{R} \\ \mathrm{O'} + e &\rightarrow \mathrm{R'} \end{aligned} \tag{2.26}$$

or consecutive as

$$\begin{aligned} \mathrm{O} + e &\rightarrow \mathrm{R_1} \\ \mathrm{R_1} + e &\rightarrow \mathrm{R_2} \end{aligned} \tag{2.27}$$

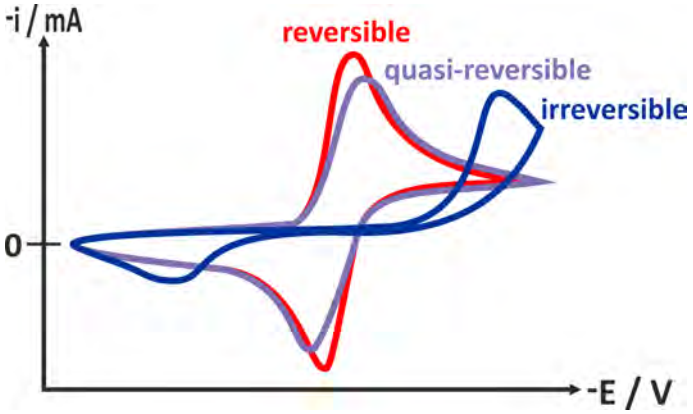

Fig. 2.17.: *Schematic sketch showing the influence of the electrochemical reversibility on the peak shape by varying only the electrochemical rate constant over five orders of magnitude with the red curve showing the highest value, the blue one the lowest and the violet one an intermediate one, but keeping all other variables constant. Modified and redrawn from*[115]

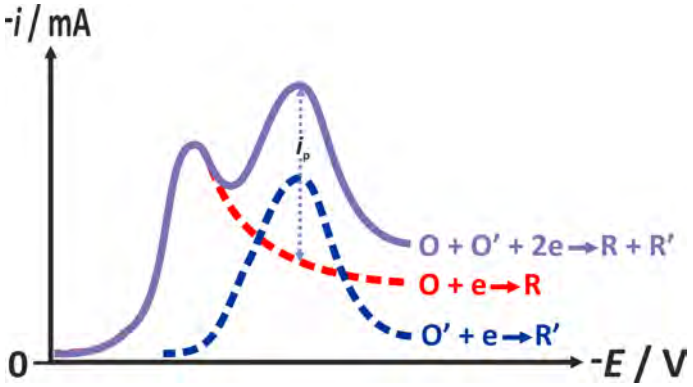

Fig. 2.18.: *Schematic sketch showing the determination of the peak current of the second process in multistep charge transfers. Modified and redrawn from*[116]

In the first case, here only considering reversible reactions, if the diffusion of the two educts O and O' is independent, the fluxes are additive and the *i-E* curve for the mixture is thus a sum of the individual ones of the two processes.[116] However, for calculation of the peak current of the second process the decaying current of the first one has to be used as baseline.[116] It is obtained assuming that the current past the peak potential decays as $t^{-1/2}$, being sketched in figure 2.18.[116]

For stepwise reduction of a single substance, again considering only the reversible case, the situation is similar to the two-component case. Additional complexity however arises since the product of the first process, R_1, is the educt of the second one. The progress of the first reaction thus influences not only the concentration of R_1, but as consequence also

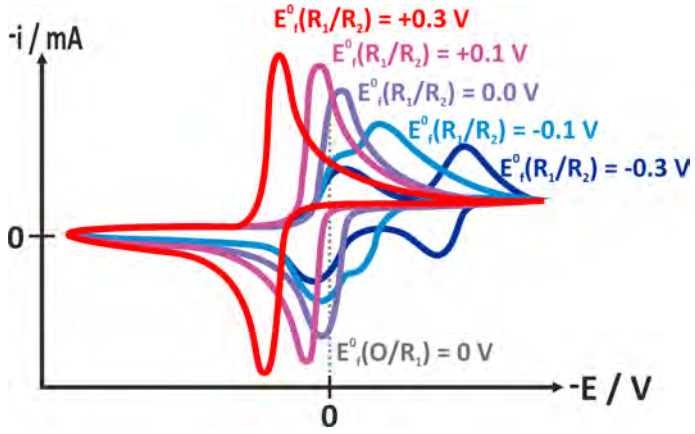

Fig. 2.19.: *Schematic sketch showing the influence of the separation ΔE^0 of the peaks and their relative magnitude for two consecutive reactions $O + e \rightarrow R_1 + e \rightarrow R_2$. Modified and redrawn from*[115]

the second reaction. These two processes result in principle in two distinct peaks in the CV. After the first one is traversed the formed product R_1 diffuses into the solution, until the potential of the second wave is reached, at which it travels back to the electrode to be reduced to R_2.[116] Moreover, additional R_1 is formed since O continues to be reduced, either directly at the electrode or by reaction with R_2 diffusing away from the electrode: $O + R_2 \rightarrow 2R_1$.[116] The shape of the CV depends, besides the reversibility of the two processes, on the separation ΔE_f^0 of their formal potentials and the relative magnitude of the latter parameter.[115,116] Considering the case of two consecutive reactions which electrode kinetics are sufficient fast compared to mass transport, thus operating in the reversible limit, and prior to the experiment only educt O is present in the solution. Then in principle three different cases have to be considered, which are schematically sketched in figure 2.19: If the product of the first step, R_1 is more easily reduced than O ($E_f^0(R_1/R_2) \gg E_f^0(O/R_1)$), the reduction of O to R_1 occurs at a potential well negative of that required to reduce R_1 to R_2.[115] Accordingly, only a single voltammetric wave is seen, corresponding to the net conversion of O to R_2, thus being an overall two-electron process. In the opposite case ($E_f^0(R_1/R_2) \ll E_f^0(O/R_1)$) two voltammetric waves will be seen, the first at relative positive potential corresponding to the reduction of O to R_1 and the second at relative negative one due to the reaction of R_1 to R_2. The potential of the first step is insufficient negative for the reduction of R_1 and thus only after the potential has been scanned further negative in the vicinity of $E_f^0(R_1/R_2)$ the second wave will be seen. The latter two cases are only visible, if ΔE^0 is greater than 180 mV, whereas in the third case, when ΔE^0 is between 0 and 100 mV, there is only one wave, which is rather broad in contrast to the distinct one arising in the first case.[116]

2.5.2. Constant-current chronopotentiometry

Using constant-current chronopotentiometry, a steady current is applied to an electrode, thereby recording the the voltage needed to maintain it constant. It is thus an indicator to changes in the electrode processes occurring at its interface.[18] The current causes species O to be reduced to R at a constant rate and the potential of the electrode moves to the value characteristic of this redox couple.[116] Thus, the concentration of O decreases in the vicinity of the electrode and it therefore diffuses from the bulk solution into the depleted layer. This causes growth of a concentration gradient from the electrode surface into the solution, which extends further as the electrode process continues.[18] The potential of the electrode varies with time as the O/R concentration ratio changes at its surface and can be regarded as titration of species O in the vicinity of the electrode by the continuous flux of electrons, resulting in $E-t$ curves similar to those obtained by acid/base titration experiments.[116] When the surface concentration of O falls to zero, the flux of this species to the surface is insufficient to accept all of the electrons being forced across the electrode/solution interface. The electrode potential will rapidly shift towards more negative values until a new, second reduction process can start.[116] The time between commencement of the reduction and the sudden potential shift is called transition time τ.[18] It is related to the concentration and diffusion coefficient of the species under investigation, thus being the chronopotentiometric analogue to the peak current in potential-controlled experiments.[18,116] Its definition is depicted in equation 2.28 where C_{O}^{0} is the starting concentration of species O and i is the applied current:[18]

$$\tau^{1/2} = \frac{nFAD_{\mathrm{O}}^{1/2}\pi^{1/2}C_{\mathrm{O}}^{0}}{2i} \tag{2.28}$$

Shape and location of the $E-t$ curve are determined by the reversibility of the electrode reaction.[116] For a reversible reduction, where O and R are free to diffuse to and from the electrode surface, the relationship stated in equation 2.29 holds, where $E_{\tau/4}$ is the quarter-wave potential at 1/4 transition time[v], thus being the chronopotentiometric equivalent of the voltammetric $E_{1/2}$ and t is any time between zero and τ:[18,116]

$$E = E_{\tau/4} + \frac{RT}{nF} ln \frac{\tau^{1/2} - t^{1/2}}{t^{1/2}} \tag{2.29}$$

The corresponding equation for an irreversible process is given by

$$E = E_f^0 + \frac{RT}{\alpha F} ln \frac{FAC_{\mathrm{O}}^{0}k^0}{i} + \frac{RT}{\alpha F} ln \left[1 - \left(\frac{t}{\tau}\right)^{1/2}\right] \tag{2.30}$$

[v] $E_{\tau/4} = E_f^0 - \frac{RT}{2nF} ln \frac{D_{\mathrm{O}}}{D_{\mathrm{R}}}$ [116]

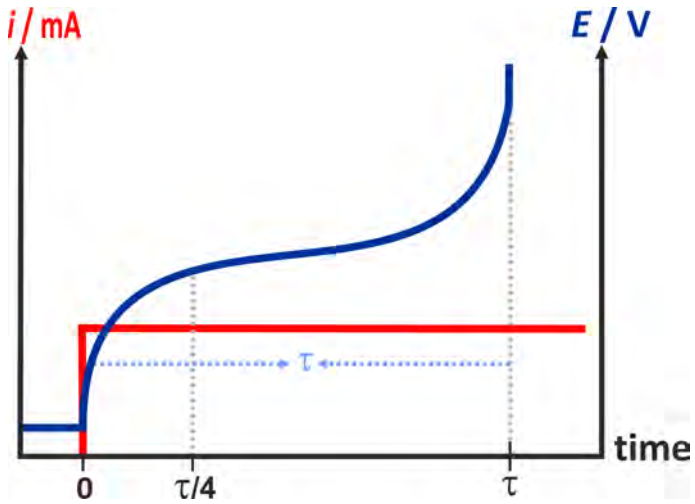

Fig. 2.20.: *Schematic sketch showing an $E-t$ curve together with the excitatory current and the relevant times during constant-current chronopotentiometry. Modified and redrawn from*[18,116]

Thus, for a totally irreversible reduction wave the whole $E-t$ curve shifts towards more negative potentials with increasing current, resulting in a shift of $2.3RT/\alpha F$ for a tenfold increase in current.[116] Reversibility of a system can be tested by plotting E vs. $log[(\tau^{1/2}-t^{1/2})/t^{1/2}]$ delivering a linear dependence with slope of $59n$ mV, or a value of $\left|E_{\tau/4}-E_{3\tau/4}\right| = 47.9/n$ mV at 25 °C.[116] In contrast to this for totally irreversible systems $\left|E_{\tau/4}-E_{3\tau/4}\right| = 33.8/\alpha$ mV at 25 °C.[116] A schematic sketch of an $E-t$ curve together with the relevant times is given in figure 2.20.

During cycling of a LiB, there exist in principle two different potential progresses: it either steadily raises and decreases until complete lithium release or filling, respectively, or stays constant over a wide range of lithium content. Combinations of both behaviors are also possible. The difference in potential development arises due to varying number of phases being in equilibrium during lithium (de)intercalation. For a given redox couple, the potential of an intercalation electrode, is given by the thermodynamic relation $\Delta G = -zFE$, thus leading to[17]

$$\frac{\delta E(x)}{\delta x} = -\frac{1}{zF}\frac{\delta(\Delta G(x))}{\delta x} + constant \tag{2.31}$$

where ΔG denotes the variation in Gibbs energy of the system, x the composition, i.e. the fraction of guest species in the host lattice, and z the number of electrons involved in the uptake of the latter species. Thereby, an intercalation electrode is considered as solution of a guest species - Li^+ in the case of the lithium ion battery - in the host lattice $< H >$. Thus, $E(x)$ is the electrode potential as a function of the composition x in

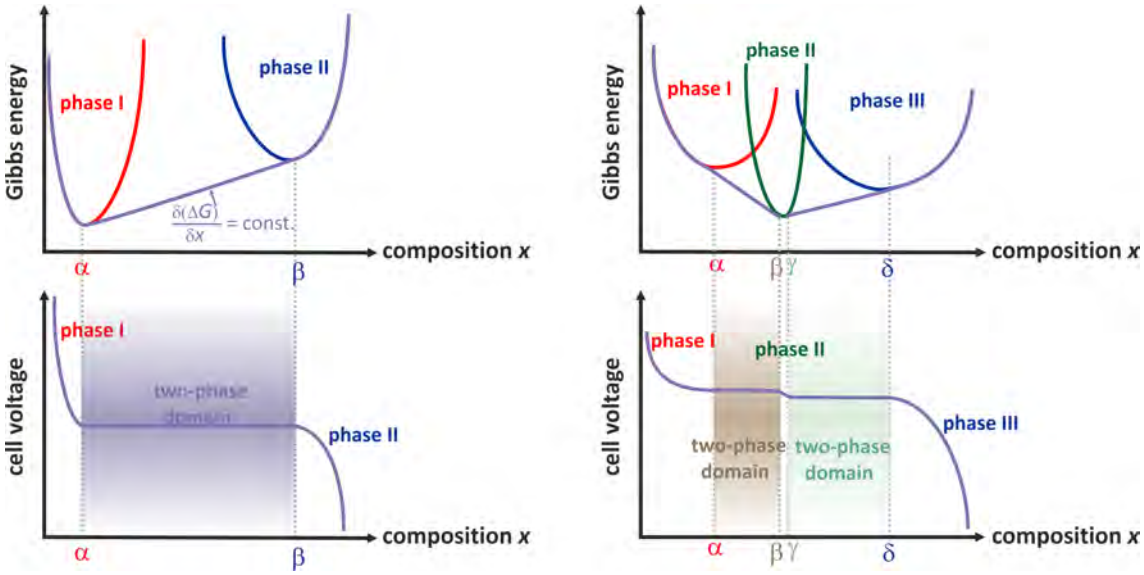

Fig. 2.21.: *Schematic sketch of the two different types of potential evolution with composition. Modified and redrawn from*[17]

$< Li_xH >$.[17] At equilibrium in a closed system, Gibb's phase rule delivers the relation between the number of degrees of freedom, f, the number of phases involved in the reaction, p, and the number of independent components, c, as:[17]

$$f = c - p + 2 \tag{2.32}$$

Considering LNMO or LMO as host material of interest, the cathode can be treated as quasi-binary system ($c = 2$) consisting of Li and $Ni_{0.5}Mn_{1.5}O_4$ or Mn_2O_4, respectively. Since temperature and pressure are usually kept constant during experiments, the degrees of freedom reduce to $f = (2 - p + 2) - 2 = 2 - p$.[17] If only one phase exists in a cathode particle, $p = 1$ and thus $f = 1$. Thus the potential has one degree of freedom and as consequence varies with the lithium concentration, resulting in a sloped potential development with time.[17] On the other hand, if there are two phases present, there is no degree of freedom left and thus the cell potential cannot change, thus delivering a constant voltage until one of these phases is consumed.[17]

A schematic sketch of the two different types of potential evolution with composition is given in figure 2.21. Potential progress of a $LiMn_2O_4$ half cell together with the corresponding Gibbs energy curves and the evolution of the c-axis parameter are given in figure 2.22. This cathode material was chosen as example since it shows both one- and two-phase reactions during lithium (de)intercalation. In this material, lithium uptake or release occurs in three steps. During discharge, reduction takes place first as two-phase

reaction by transformation from one cubic phase into another with greater lattice constant characterized by a constant potential of 4.1 V for $0.27 < x < 0.6$ in $Li_xMn_2O_4$. The occurrence of the second cubic phase is presumably due to lithium ion ordering in the $Li_xMn_2O_4$ matrix.[32] Thereafter, a one-phase reduction shown by an S-shaped curve for $0.6 < x < 1.0$ occurs. It is followed by another two-phase reduction from a cubic to a tetragonal one, characterized by a an additional plateau at 3.0 V for $1.0 < x < 2.0$.[32] The latter transformation results from a change in the local symmetry of the MnO_6-octahedra due to Jahn-Teller distortion, since the average manganese oxidation state in this region lies below 3.5.[32] It is accompanied by large anisotropic change in unit cell dimension of about 12 % expansion and 3 % shrinkage of the *c*- and *a*-axis, respectively, during lithium uptake. The other two-phase transition and the one-phase reaction result both in a volume change of 1.2 %.[32]

Evidence for these results are e.g. given by *in situ* XRD measurements by Ohzuku et al. and Eriksson et al.[32,117] The latter of them monitored the shift of the (111) reflex, calculating changes in the atomic cell parameters with it, and related them to features in the constant-current cycling between 3.5 and 4.3 V vs. Li/Li^+.[117] From 0 to 11 % DOD cell parameters increase linearly due to lithium uptake and concomittant reduction of manganese from the tetravalent to the trivalent state. Therby, the latter ion possesses a bigger radius in comparison the tetravalent one. Subsequent to this region two instead of just one (111) reflexes develop, thus showing a two-phase region for $11 - 34$ % DOD. Thereafter, again only one is present and lattice parameters show linear increase up to 100 % DOD, i.e. composition of $Li_1Mn_2O_4$. Since the lower potential was limited to 3.5 V, the second plateau, occuring for over-lithiated $Li_xMn_2O_4$ with $x > 1.0$, was not investigated.

To get a brief overview of the phases involved in the (de)lithiation of $LiMn_2O_4$, a schematic sketch of the ternary phase diagram of this material highlighting important phases is shown in figure 2.23. Detailed information about the variety of phases of the lithium manganese oxide spinel are given e.g. in the papers by Gummow et al.[38] or Thackeray.[118] The phases of interest for the LiB lie in the tie triangle defined by the $LiMn_2O_4$, $Li_2Mn_4O_9$ and $Li_4Mn_5O_{12}$ phases.[38] Lithium excess compounds $Li_{1+\delta}Mn_{2-\delta}O_4$ with $(0 \leq \delta \leq 0.33)$ are located on the tie-line between $LiMn_2O_4$ ($\delta = 0$) and $Li_4Mn_5O_{12}$ ($\delta = 0.33$). Lithium insertion into or extraction from the tetrahedral sites of the spinel at 4.0 V vs. Li/Li^+, occurs in the region within the $LiMn_2O_4$ - λ-MnO_2 - $Li_4Mn_5O_{12}$ tie-triangle and the over-lithiated structure, in which lithium is placed in the octahedral sites at 3.0 V, is located within the $LiMnO_2$ - $LiMn_2O_4$ - $Li_4Mn_5O_{12}$ - Li_2MnO_3 tie-quadrilateral.[38] Jahn-Teller distortion sets in during lithiation of the spinel, if the average manganese oxidation state reaches 3.5, being represented in the figure by the broken line.

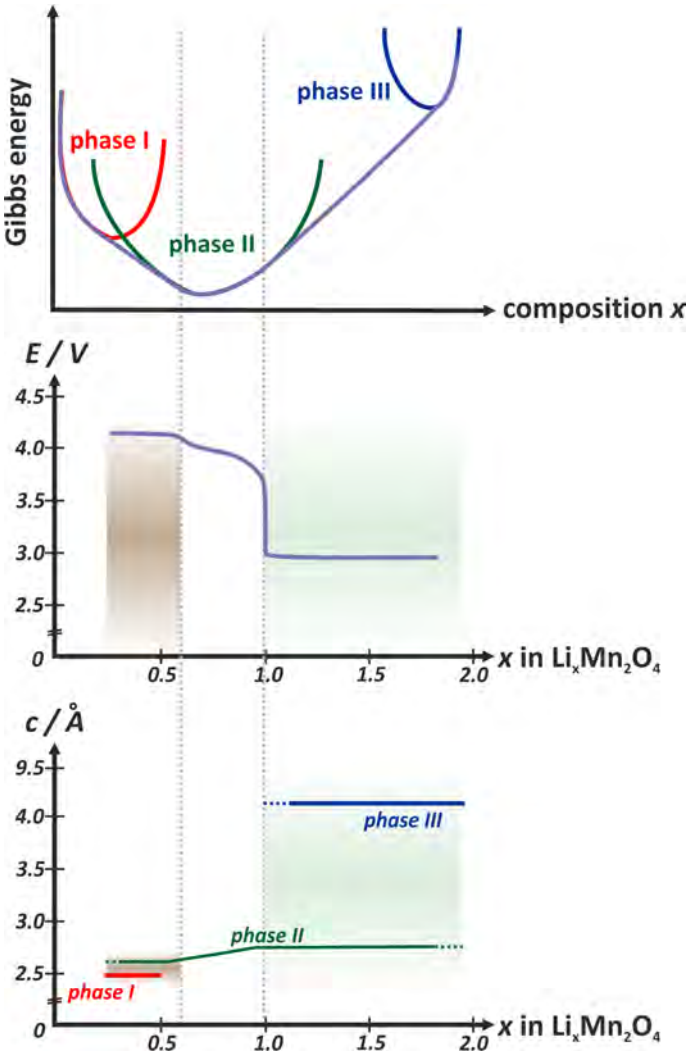

Fig. 2.22.: *Schematic sketch of the different potential progresses together with the evolution of c-axis parameter for $LiMn_2O_4$. Modified and redrawn from.*[117]

Therefore it becomes clear that 4 V-electrode materials that can be discharged through the stoichiometric $LiMn_2O_4$ - $Li_4Mn_5O_{12}$ tie-line into a cubic, 3 V region, in which the Jahn-Teller distortion is suppressed, will be more stable.[38]

The information given in the last three paragraphs deals with $LiMn_2O_4$ and not with the cathode material investigated in this thesis, LNMO, since to the author's best knowledge, up to date there is no detailed investigation of its ternary phase diagram reported. In consequence, unfortunately the relation between the different phases and the processes during lithium uptake or release cannot be sketched. However, investigations by Wang et al. reveal a reaction mechanism comparable to LMO during (de)intercalation with one

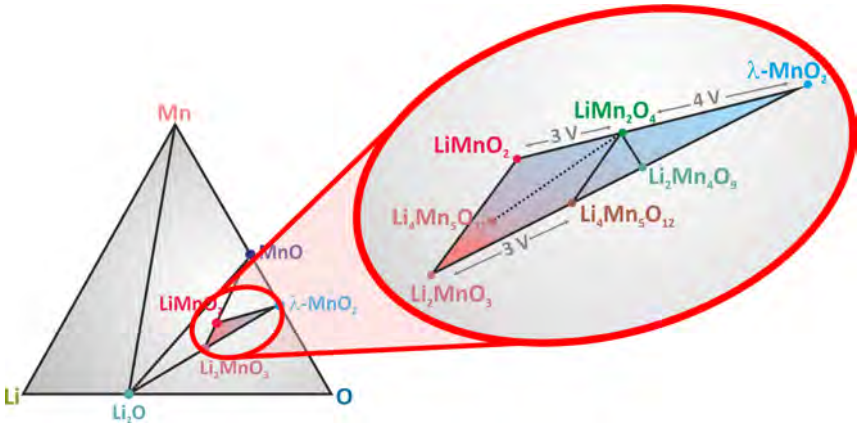

Fig. 2.23.: *Schematic sketch of the ternary phase diagram of the phases involved in the (de)lithiation of $LiMn_2O_4$ highlighting important phases. Modified and redrawn from.*[38]

single- and two two-phase regimes during constant-current cycling with concomitant *in situ* XRD.[65] Regarding the $Fd\bar{3}m$ phase, for $1 \geq x \geq 0.6$ in $Li_xNi_{0.5}Mn_{1.5}O_4$ continuous voltage increase occurs together with a steady enlargement of the cell parameters within the same cubic symmetry due to the existence of a single-phase solid solution. For $0.6 \geq x \geq 0.5$ in addition to the first phase a second one, also of cubic structure, but with a smaller lattice constant, evolves. This is consistent with the first voltage plateau of this material in the range of 4.7 V. Finally, for $x \leq 0.5$ occurrence of the second plateau goes along with the transformation from the second phase to a third cubic one with even smaller lattice constant.[65] The same also holds in principle for the $P4_332$ phase, but with slightly varying values for lithium content x. For this structure moreover all three phases appear together for $x \leq 0.55$, thus in the regime of the second plateau. The latter phenomenon is presumably caused by the kinetic limitation of the ordered spinel.[65] It possibly originates from its lower electronic conductivity and higher activation energy in comparison to the disordered form, thus resulting in larger polarization.[65]

2.5.3. Differential capacity

Transformation of the data gained by constant-current cycling to compare them to those received in a CV experiment is possible by calculation of the differential capacity $\mathrm{d}(Q - Q_0)/\mathrm{d}E$. Here, Q_0 is the charge at the beginning of the experiment, which is usually set to zero. There are however small, but important differences. First of all, in the differential capacity plot, there are discontinuities at the extrema. At these points the derivation of the charge Q as function of the potential E is undefined, because they correspond to the plateaus appearing in cc experiments in the two-phase regime, meaning zero change in the

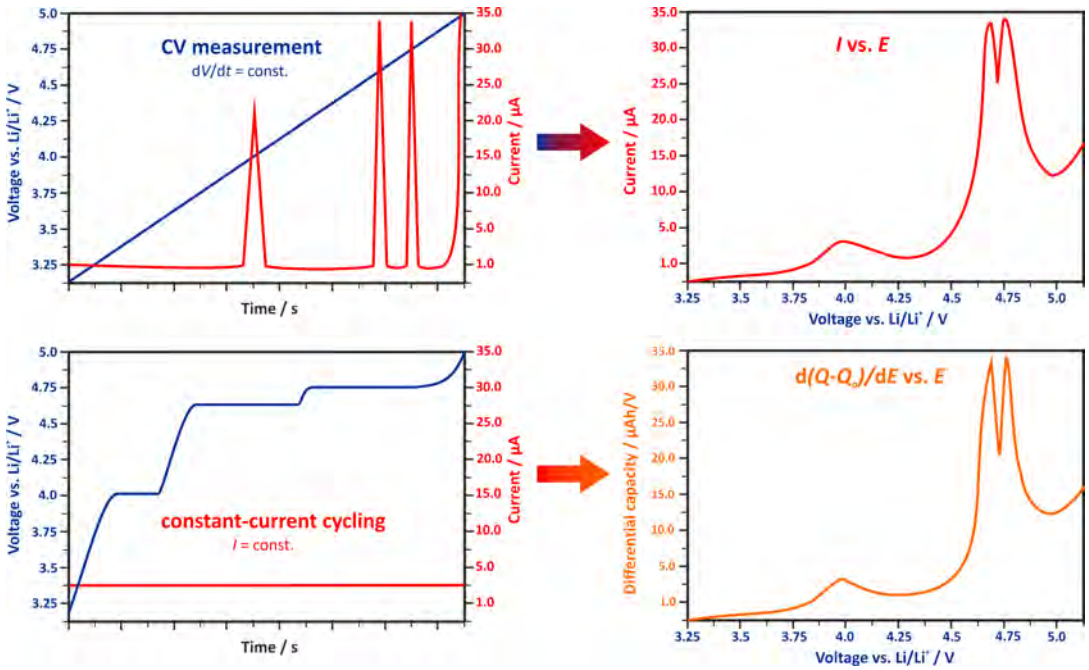

Fig. 2.24.: *Schematic sketch showing the differences in data recording and representation comparing a cyclic voltammogram with a differential capacity plot.*

voltage. As a consequence, these missing values have to be extrapolated by the evaluation software. However, these calculations can be performed in different ways, for instance using a fitting procedure, trace interpolation or simply a connection line across missing data, thus resulting in slightly varying curves. Moreover, since the potential variations on the verge both before and after the plateau become very small, the derivation of the charge as function of the potential increases distinctly, thus resulting in sharper tips of the peaks in comparison to those measured in CV experiments. Secondly, in the differential capacity plot the peaks are smaller than those in cyclic voltammograms, since during constant-current cycling the voltage only changes, if the reaction in the vicinity of the electrode has been completed due to consumption of the starting material in a certain area around the electrode. Thus, in this experiment the systems is closer to equilibrium conditions, whereas during CV measurements the voltage is raised at a constant rate.[119] The redox reaction in consequence has not necessary completely ended and proceeds at higher voltages, thus causing peak broadening. The differences in data recording and representation comparing a cyclic voltammogram with a differential capacity plot are schematic sketched in figure 2.24. However, main aspects like position of the peak potentials are the same in both representations so that at least to some extent comparability is ensured.

3. State of the art - literature overview

This chapter summarizes knowledge on state of the art thin film cathodes, on SEI/CEI formation and their investigation by SIMS. Thereby, focus is set on LNMO electrodes, the material studied in this thesis, and its nickel free counter part, since only few investigations deal with the former one. Results gained on other cathode thin films are also briefly summarized, but with an exclusive focus on surface-analytical studies.

3.1. Thin film cathodes used in the LiB

Thin film electrodes are often used as geometrically simplified model systems to study reaction mechanisms during charge and discharge, surface film formation or lithium diffusivity by excluding other detrimental influences coming from additives like binder and conductive carbon. They show a reduced roughness in comparison to technical electrodes being deposited by the doctor blade process, thus enabling characterization by analytical techniques that require flat surfaces like XPS, SIMS or the bending beam method, which enables *in situ* strain measurements.[36,120,121] The thin films are either used as positive or negative electrode together with lithium metal as half cell, partially even in combination as full cell with liquid electrolyte or as all-solid state cell comprising a solid electrolyte. The resulting knowledge on e.g. the optimization of deposition parameters is not only meaningful for the improvement of the model system,[120,122,123] but also for further application in all-solid state cells. These have several advantages over cells using liquid electrolytes like high energy density, very good safety due to lack of organic components and long life time, making them interesting for application e.g. as energy source for smart cards.[12]

The combination of theoretical and practical work allows the evaluation of the influence of geometry, kinetics and mechanics of the electrode material on the stress-strain state and therefore on the structural stability of the material. The use of oriented films simplifies for instance diffusion models and mathematical calculations.[124] Park et al. for example used a theoretic model to describe their *in situ* atomic force microscopy (AFM) measurements achieved on $LiCoO_2$ thin films concerning volume changes during electrochemical cycling, revealing a good agreement between simulation and experimental.[125] Whereas technical electrodes contain not only active material, but also binder and conductive carbon, thin

film cathodes can be produced of 100 % active material, because they are thin enough that no conducting agent is needed, even for poor conducting materials like $LiFePO_4$. Well defined composition and geometry of the thin film sample enables the exclusion of the impact of secondary, non-active material like conductive carbon and binder that may affect the stress level in the electrochemical active electrode particles as well as of some uncertainty due to the irregular shape of particles. A well-defined geometry allows easier correction for instance during modeling of AFM data.[125] Thanks to their reduced roughness, thin films can be modeled as 2D system. Due to their well defined geometry employment of thin films is beneficial during studies investigating electrode size effects on the small µm scale, since estimation of the surface area is simplified.[123] For the same reason, usage of grids to achieve a patterned electrode structure is easier with thin films electrodes.[123] Application of GITT and PEIS measurements lead to wrong results for materials exhibiting a two-phase region in which the dE/dx term used in both methods for calculation of D_{Li} becomes zero.[126] Since the electrode area is needed in the latter technique for determination of the diffusion coefficient, thin films are advantageous over technical electrodes due to their well-defined surface area.

There is a large variety of different techniques for thin film preparation on either conducting or non-conducting substrates of sufficient flatness. On the one hand there are liquid based methods in which the material to be deposited is dissolved and either spread over the substrate like e.g. in the spin-coating process. Here the substrate is rotated with high speed to distribute the solution homogeneously over the whole area. The obtained roughness is typically in the range of tens of nm.[127,128] Another possibility is the so called dip coating, in which the substrate is dipped into the solution and removed sufficiently slow so that some of the material sticks to it. After a drying step the procedure is repeated until the desired thickness is reached. This process enables the instantaneous deposition on both substrate sides. On the other hand, thin film deposition is possible by evaporation of the material which should be deposited, either induced by simply heating or by exposure to high energetic light beams like e.g. in the sputtering or pulsed laser deposition process. The material to be deposited exists either pure as powder as well as pressed in pellet form or in a precursor connected to ligands that facilitate the deposition of the desired species called chemical vapor deposition (CVD).

Also there is a large number of studies using thin film cathodes, the actual benefit by employment of this electrode type instead of the more commonly used technical ones is often unclear, see for example Yu et al.[129] Unfortunately, often important information about the thin films like thickness, roughness, porosity or phase purity lack. These however are important for classification of the presented results. The exact surface area is for example needed for calculation of D_{Li}, see equation 2.22, which differs for rough samples

distinctly from its geometric one. However, for apparently smooth thin films often simply the latter value is employed. If the surface is not as flat as expected, D_{Li} is overestimated and comparison to other values reported in literature is difficult without any information about sample roughness.

On the cathode side of the LiB $LiCoO_2$ is still the most investigated model system. $LiFePO_4$ and other olivine type $LiMPO_4$ (M = Fe, Co, Mn) thin films are of interest both for fundamental studies as well as for their application in micro-batteries or sensors.[123] Due to its high voltage of 4.0 V vs. Li/Li^+, low prices and low toxicity, $LiMn_2O_4$ is also a well-studied thin film cathode material. Whereas its high voltage is favorable for application in e.g. batteries for electric vehicles, common carbonate based electrolytes are unstable in the high potential region especially in the presence of catalytically active surfaces in the cathode material. Therefore, surface film formation at the interface between cathode and electrolyte is needed to prevent the direct contact between cathode and electrolyte and in consequence the reactivity between these two phases. Thus, surface film formation on $LiMn_2O_4$ is one major issue investigated on thin film electrodes since they are free of binder and conductive carbon to exclude their suspected influence on the reaction.[130] Further advantage of thin film electrodes is their flat surface, so that roughnesses as low as approximately 1 nm can be reached. Thus, surface reactions can be easier studied. Simmen et al. emphasized the importance of sufficiently flat films during SEI/CEI studies, because these surface layers appear to be very thin and could be detected by scanning electron microscope (SEM) only on the smoothest thin film electrodes.[130] Since thin films often possess preferred orientation, information about anisotropic reaction mechanisms can be achieved.[131] Besides commonly employed cathode materials like Li_xCoO_2, $LiFePO_4$ and the manganese spinel, with and without nickel substitution, also some less used cathode materials like V_2O_5, $Li[Li_{0.2}Mn_{0.56}Ni_{0.13}Co_{0.13}]O_2$, NiOH, Li_2RuO_3, layered $LiNi_{0.5}Mn_{0.5}O_2$ and MoS_2 were studied as thin film.[16,124,132–135]

Comparative studies between technical and thin film electrodes concerning their electrochemical properties deliver in most cases comparable results.[124,130,136–138] For very thin films - the exact value thereby depends largely on the thin film-substrate system - partially diverging behavior from the bulk material was reported.[124] This discrepancy probably results from a different film orientation or composition near the substrate that becomes significant at low thicknesses. Partially stronger capacity fading is reported for thin films due to removal of active material caused by the weak adhesion to the substrate.[130] Care has to be taken during the deposition of layered electrode materials. If the Li diffusion channels are orientated in parallel to the substrate, hardly any lithium can be incorporated/released during cycling, resulting in a drastically reduced capacity. Impact of the thin film orientation on its electrochemical properties was also proven by Bouwman et

al.[122] Whereas $LiCoO_2$ thin films deposited by radio frequency (RF) sputtering are oriented along the (110) axis, which is active for lithium ion uptake, films deposited by PLD are aligned along the inactive *c*-axis and therefore employ only 3 % of their theoretical capacity at a scan rate of 0.1 mV/s.[122] The reason for this difference is that the close-packed (00l) planes of $LiCoO_2$ possess the highest density as well as the lowest surface energy and are therefore preferentially formed parallel to the substrate surface in the kinetic growth regime at high deposition rates which holds for the PLD process. Due to its pulsed character this technique indeed possesses high growth rates, whereas the RF deposition employs a continuous plasma at low power. Here, *a*-axis orientation results, since the (110) alignment is thermodynamically stable. Using higher deposition rates, with RF sputtering also the adverse *c*-axis orientation is achieved. The apparent lithium diffusion coefficient of the films deposited by RF sputtering is ten orders of magnitude higher than that of the PLD films due to the more favorable orientation and shows with approx. $10^{-4}\,cm^2/s$ an even higher value than reported for composite electrodes.[139]

Although comparative impedance and CV studies between thin film and technical $LiMn_2O_4$ electrodes by Hjelm et al. and Striebel et al. in principle reveal good comparability between both types of electrodes, a closer look reveals some distinct differences.[136,138] Thus, the question remains, whether thin films are sufficiently close in structure to bulk oxides that one can expect to measure properties similar to those of the bulk material. According to Hirayama et al. a diverging behavior with respect to structural changes between bulk and thin film electrodes during cycling may be caused by binding of the $LiMn_2O_4$ lattice to the substrate, which is thus to some extend mechanically constrained.[131] Therefore, lattice expansion and shrinkage during lithium uptake and release, respectively, is hindered and no phase transition occurs during these reactions. In addition, there may be nano-scale effects related to the short diffusion length of the lithium ions. An enhanced surface reactivity caused by the larger contact area between electrode and electrolyte together with lower physical strains during lithium (de)intercalation is also possible.[131]

3.1.1. Lithium nickel manganese oxide cathodes

Thin film electrodes of $LiNi_{0.5}Mn_{1.5}O_4$, the electrode material studied for this thesis, were prepared by electrostatic spray deposition, PLD, sputtering, spin-coating and a sol-gel process.[4,140–143] Using the latter technique, approx. 0.5 μm thick LNMO films were deposited on $Li_{1+x}Al_xTi_{2-x}(PO_4)_3$ (LATP), a solid electrolyte in LiBs.[143] They delivered a remarkable capacity of 145 mAh/g, i.e. 98 % of its theoretical value of 148 mAh/g. SEM images however reveal a rather porous structure with roughness of several hundred nm, thus being no "real" thin film.[143]

To best of my knowledge to date only seven reports on LNMO thin films prepared by

PLD have been published from mainly two groups.[29,142,144–148] Roughnesses of less than 5 nm were achieved by Konishi et al., who deposited LNMO on $SrTiO_3$ single crystals, thereby reaching capacities of $80 - 130\,mAh/g$.[144] Xia et al. prepared LNMO thin film electrodes on both silicon wafers and stainless steel by PLD to study intrinsic properties of the electrode material such as lithium diffusivity without the presence of binder and conductive carbon.[142,146] The authors determined D_{Li} in LNMO as $10^{-12} - 10^{-10}\,cm^2/s$.[142] Since the initial capacity as well as the capacity retention highly depends on the thin film crystallinity and purity, Xia et a. and Wang et al. optimized the PLD parameters of LNMO.[29,148] Below $550 - 600\,°C$ no sufficiently flat, but rather flake-like thin films with insufficient crystallinity were deposited.[29,148] With increasing oxygen pressure in the deposition chamber both crystallinity and purity were improved.[29] An increased oxygen partial pressure led to morphology evolution with more defined, but larger particles and therefore higher roughness.[147] A lower oxygen partial pressure during the film deposition causes higher oxygen non-stoichiometry, thereby leading to an increase in impurities like the rock salt phase, thus reducing the capacity.

The role of interface degradation has been studied by comparison of the coulombic efficiencies of $350 - 1100\,nm$ thick LNMO films.[147]The thicker electrodes deliver higher efficiencies, since the volume fraction of near-surface material is smaller. Therefore, coating of the active material to hinder a direct contact with the electrolyte is a promising way to improve the electrochemical performance of the LNMO. The authors also investigated the electrochemical activity of the two metals used as substrates, namely stainless steel and platinum. While the latter one hardly showed any activity in the voltage range used for cycling of LNMO, stainless steel showed an irreversible capacity in the first cycle at about 3.4 and 4.1 V vs. Li/Li^+ after heating at conditions used for the film deposition. Thus platinum can be considered as suitable current collector for LNMO thin films.

Baggetto et al. used $LiNi_{0.5}Mn_{1.5}O_4$ thin films to study the beneficial effect of surface coating of the cathode material concerning cycling stability.[4,84] The advantage of using thin films for this investigation is the ability to prepare uniform coatings with controlled thickness. The LNMO films were deposited on platinum covered Al_2O_3 substrates by RF magnetron sputtering. Either metal oxides, namely ZnO, ZrO_2 and Al_2O_3, each 2 nm in thickness, or 40 nm thick LiPON coatings were subsequently deposited by direct current (DC) magnetron or reactive sputtering. TThe irreversible capacity of the bare cathode material was high in the first and following cycles. This is caused by continued electrolyte oxidation above potentials of 4.6 V and even more severe above 4.7 V vs. Li/Li^+. Coating of the cathode indeed decreased its irreversible capacity, but also worsened the rate performance. The latter aspect presumably results from changes in the surface kinetics. Due to the protecting layer the transfer of lithium ions no longer takes place from the

electrolyte into the electrode, but into the coating. The Al_2O_3 coating delivered the best performance of all metal oxides and significantly reduced the irreversible capacity.[84]

3.1.2. *in situ* investigations

Results reported so far rely on post mortem investigations, i.e. the cell under investigation was disassembled after the electrochemical experiment and the electrode was afterwards transferred into the analysis chamber to examine morphological and/or compositional changes. However, by applying this procedure, it is difficult to relate e.g. a specific electrochemical reaction to a distinct sample feature. This problem can be overcome partially by stepwise cycling and analysis, but repeated transfer between the cell housing and the analysis chamber is often difficult to manage. Moreover, due to typical inhomogeneities of the sample, it is better to investigate always the same region, which is often difficult to be found again. Additional problems arise concerning CEI analysis since the removal out of the cell may change it. Firstly, in many studies the sample is washed prior to the analysis to remove any residual electrolyte salt, thereby possibly damaging the surface film and even remove some parts of it. Secondly, it is dried and often exposed to UHV conditions. In consequence, not its real physical extension, which exists in the cell, is measured, but instead only a compact, dry layer.[149] *In situ* studies can overcome these drawbacks. An electrochemical technique is applied in parallel with an analytical method and changes are directly observed during cycling of the cell.

However, additional difficulties arise in designing a suitable electrochemical cell which enables *in situ* investigations with the desired method. Many analytical techniques like XPS and SIMS operate under UHV conditions so that cells based on liquid based electrolytes are not suitable. Moreover, if rather thin films like the CEI are of interest, surface sensitive techniques are required. Raman spectroscopy as well as XRD are bulk-sensitive and give only small intensities for surface signals. However, since they operate with light, they do not require UHV and are suitable to study cells containing liquid electrolytes. For this purpose the cell housings need a window transparent for the wavelength used for excitation and analysis. In figure 3.1 for instance the schematically sketch of a setup equipped with a quartz window for Raman studies is depicted.

Ionic liquids instead of common carbonate based ones can be employed as alternative, because they show vapor pressure. However, it is still under discussion whether ionic liquids form an interface film like carbonate based electrolytes. This problem can be overcome to some extent by addition of some percent of the liquid carbonate based electrolyte to form the common SEI- or CEI-like surface film. It would evaporate upon exposure to vacuum, but it must be assured that the formation process is sufficient fast so that it is immediately consumed. The required amount of the carbon based electrolyte is very

difficult to estimate, since an excess would evaporate, thus damaging the UHV, and a too small amount is insufficient to build up the complete surface film. In addition, it is not assured, that all reactions occur in the same manner like in the cells comprised completely of carbonate based electrolytes. Especially dissolution and transport phenomena should be drastically influenced due to completely different concentrations of the species like EC and the higher viscosity of the ionic liquid.

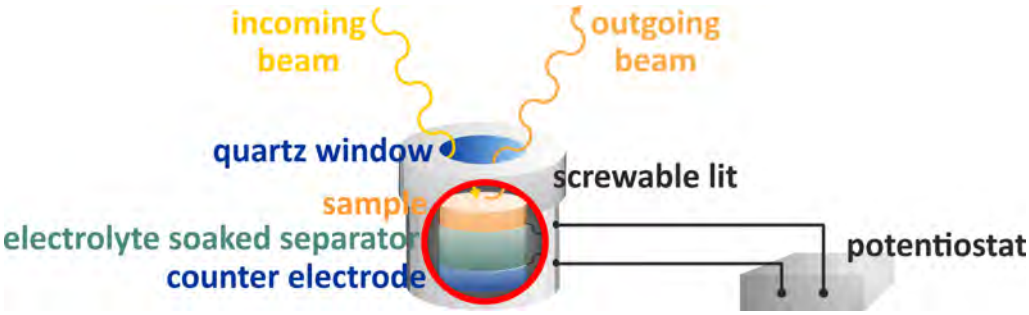

Fig. 3.1.: *Schematic sketch of an in situ cell suitable for e.g. Raman measurements.*

An interesting attempt concerning quasi *in situ* XPS experiments using liquid electrolyte has been developed by the group of Jaegermann. They employ a cannula containing both lithium reference and counter electrode as well as the liquid electrolyte, which is in contact to the cathode thin film sample, in this case V_2O_5 and $LiCoO_2$. The cathode can be washed and dried after the electrochemical experiment and transferred without air contact to the XPS chamber and back for further cycling. This assembly thus enables e.g. CEI studies in dependence of the applied potential without surface contamination due to repeated air contact.[156] The setup is schematically sketched in figure 3.2.

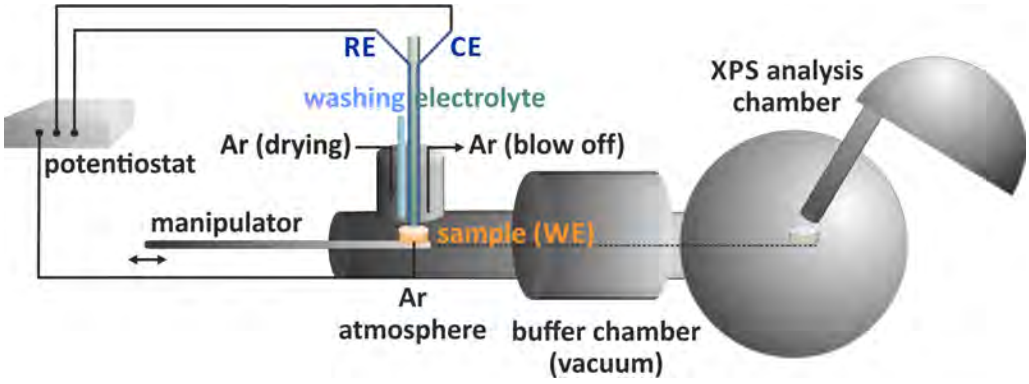

Fig. 3.2.: *Principle setup of the quasi in situ XPS experiment using liquid electrolyte by the group of Jaegermann. Modified and redrawn from.*[156]

Tab. 3.1.: *Summary of in situ studies mainly dealing with CEI investigation on LMO and LNMO electrodes.*

system	method	main results
$LiNi_xMn_{2-x}O_4$ thin film, liquid electrolyte[150]	combined CV and Raman spectroscopy	resolution of the reactions responsible for the two peaks in the CV at about 4.7 V vs. Li/Li^+ as two step oxidation of nickel
LNMO thin films, liquid electrolyte[145]	X-ray absorption spectroscopy	CEI formation occurs in the high voltage range without irreversible change of the surface states of LNMO, i.e. formation of a protective surface layer
LMO and LNMO thin films, carbonate based electrolyte[151]	*in situ* Fourier-transformed infrared spectroscopy (FTIR)	CEI formation during anodic polarization, but is not stable and strips off during cathodic polarization; CEI mainly forms for LMO at $4.0-4.3$ V (Mn^{3+}/Mn^{4+} redox couple) and for LNMO at $4.0-4.3$ V and $4.6-4.8$ V (Ni^{2+}/Ni^{4+}); additional CEI formation and stripping off for LMO at low potentials of $2.9-3.2$ V, i.e. CEI forms simultaneously at electrolyte contact
spin-coated $LiMn_2O_4$[152]	*in situ* spectroscopic ellipsometry	CEI thickened during storage in electrolyte and cycling; cathode film thickness decreased during both treatments, i.e. incomplete protection by the CEI; during cycling thickness increase/decrease is higher than during storage drawback: possible oversimplification of the system, since cathode roughness and porosity was without verification neglected
TiN thin film, carbonate based electrolyte[149]	*in situ* spectroscopic ellipsometry	SEI thickness is $10-30$ nm, but it partially dissolves at higher potentials; it thickens by presence of additives vinylene carbonate (VC) or fluoroethylene carbonate (FEC) drawback: assumption, that SEI optical constants do not change by additives, which is called into question by XPS results
Au and Cu cathodes, carbonate based electrolyte[153]	*in situ* vibrational sum-frequency generation spectroscopy	CEI thickness varies with the applied potential and is thinnest in the charged state for Cu; CEI on Au is thicker, possibly since metallic lithium deposits only on Au; EC deposits as lithium ethylene dicarbonate on the Au, its content remains approx. unchanged although the CEI thickens and thins during cycling
$LiMn_2O_4$ thin films[154]	*in situ* AFM	storage at 25 % SOC at 80 °C and cycling in the low potential range of $3.81-4.07$ V at 60 °C result in coverage of the entire surface with round-shaped, amorpous particles of about 20 nm; these morphological changes should be responsible for the capacity fade; loss of crystallinity occurred by formation of small $LiMn_2O_4$ particles on the electrode surface, which accelerates by electrolyte contact at 25 % SOC at elevated temperatures
$LiMn_2O_4$ thin films, 2 nm rough[131]	*in situ* surface X-ray diffraction	CEI formation in dependence of the crystal plane; thin films, since the growth of films with restricted lattice planes is possible; CEI formed during electrolyte soaking only on (111) plane; Mn dissolution was more intense on the unprotected (110) plane; during cycling CEI formed also on this plane; differences possibly due to varying surface energies and ion arrangements
Li_xCoO_2 thin films[155]	*in situ* X-ray reflectivity	method requires flat samples with a roughness of about one nm; CEI formation occurs only on the intercalation active (110) crystal plane; it forms already by soaking into the electrolyte

Whereas there are a some *in situ* studies on layered $LiNi_xMn_{1-x}O_2$ electrodes, only very few deal with the manganese spinel, both with and without nickel content. These are summarized in table 3.1, thereby focusing on CEI investigation. Since a relation between the applied voltage and the reactions occurring inside the cell is of special interest to gain further knowledge about its formation mechanism, *in situ* studies are of special interest.

3.1.3. Conclusion

The information about thin films and their properties, as summarized in the former paragraphs, is often incomplete, since in most cases no details on film roughness and thickness are given. The comparison to the corresponding volume material used in technical electrodes often lacks and it is therefore often questionable, whether thin films can indeed be employed as model for technical electrodes. Specific differences between films and technical electrodes, e.g. by different mechanical boundary conditions are not addressed. Another difference is their different composition, since in thin film electrodes in contrast to technical ones no binder and conductive carbon are used. Dimensions of the particles of the active material in technical electrodes are completely different compared to the geometry of the films. Therefore, the results of electrochemical experiments are not necessarily comparable on quantitative basis. For thin film electrodes the deposited masses are often so low that the exact amount of material cannot be determined by simply weighing the sample. Thus, calculation of the exact specific capacity is nearly impossible. However, an estimation can be achieved by knowledge of the film thickness together with its porosity and the theoretical density of the electrode material, leading to typical area capacities of only approx. $65\,\mu Ah/cm^2$.[84,136]

Nevertheless, in most cases thin films are suitable systems for the modeling of more complex technical electrodes, since they mimic the main features of them. However, a closer look often reveals some small differences. These are e.g. caused by restriction of the thin film deformation during lithium (de)intercalation due to rigid substrates or the presence of small extra peaks in the CVs of technical electrodes indicating side reactions which are not apparent in thin films.[136] Therefore, care has to be taken, that a well-matching thin film model system is selected and comparison to real electrodes is necessary to secure that the main features are similar, before in more sophisticated experiments using the model system detailed reaction mechanisms are investigated.

3.2. The electrode/electrolyte interface

On both the negative and the positive electrode of a LiB surface film formation takes place. LiB cells with non-aqueous electrolytes often work beyond the electrochemical stability limit of the electrolyte and reaction products between electrolyte components and the active material as well as of electrolyte decomposition species form complex interphases. Reduction occurs if the negative electrode takes a potential close to that of metallic lithium of about −3.0 V vs. the standard hydrogen electrode. The electrolyte is oxidized on the cathode side, since e.g. the redox potential of the Ni^{2+}/Ni^{4+} couple in LNMO lies with approx. 4.75 V above the HOMO of common liquid carbonate-based electrolytes at 4.0 − 4.3 V, which was already sketched in figure 2.4.[21,30] If the formed products adhere to the electrode, direct contact between the active electrode material and the electrolyte and therefore further reactions like the corrosion of the electrode materials are prevented. The formed interface films lower and rise the potentials of the cathode and anode, respectively. Thus, the resulting potentials lie within the electrochemical window of the electrolyte. Its decomposition is thus suppressed and cycling of the LiB is nevertheless possible.

Despite the fact that the LiB could not be operated without these interface layers, their formation degrades the cell performance. Capacity is lost and the electrode resistance rises.[20,26] To minimize the latter effect, these films should show a high lithium ion conductivity, to maintain the ion transport during charge and discharge and to block electrons. The current through the interface film is maintained by both anionic and cationic defects, but ideally shows a transfer number of one for the lithium ions. If there is a contribution of negative ions to the current during the discharge of the battery, anions from the solution are injected into the surface layer and subsequent reach the electrode-layer interface, resulting in its growth together with an increased polarization.[157] In the worst case the anode is thus blocked already after a short discharge time.[157] Since mass and charge transfer occur at this interface layer between electrode and electrolyte, its properties determine the kinetics of the electrochemical reactions and therefore the power capability of the entire cell.[5] Whereas the interface film formed on the anode has been investigated in a large number of studies and is up to date well characterized, there is comparatively little knowledge about the films formed on the cathode.[21]

3.2.1. The solid electrolyte interphase on the anode

On the anode of a LiB a surface film of insoluble reaction products between electrode material and electrolyte builds up, when the chemical potential of lithium becomes high enough. This layer shows characteristics of a solid electrolyte and is therefore called solid electrolyte interphase (SEI).[157] In the case of lithium metal anodes this interphase

forms instantaneously upon contact between the electrolyte and the active material, since virtually no solvent or salt is thermodynamically stable vs. lithium metal.[5,157] The SEI on lithium anodes has the additional advantage of acting as "ionic sieve" being only permeable for Li^+ ions, but not for other electrolyte components.[21] Its morphology and composition depends on the used electrolyte solvent and salt together with impurities present in the cell. In organic solvent-based electrolytes a stacked structure with thick, porous, electrolyte permeable organic layers in the μm range on the electrolyte side of the interface layer is formed. A thin, compact, electrolyte impermeable inorganic layer in the nm range forms close to the electrode surface.[21,158] This composition gradient with more inorganic species like LiF and Li_2CO_3 close to the anode surface and organic species like semi-carbonates being located further away from it arises from the decreasing chemical potential of lithium along the film.[5] Likewise, the thickness of the freshly formed SEI also depends on the electron tunneling range.[157] In the extreme case, the heterogeneous surface film consists of a mosaic of numerous individual microphases of different chemical composition.[158,159] Whereas LiF forms with fluorine containing electrolyte salts like PF_6^- or BF_6^- in the SEI, LiCl and Li_2O are expected with $LiClO_4$. The use of ethylene carbonate (EC) or propylene carbonate (PC) as solvents results in Li_2CO_3 crystals as main constituents of this surface layer.[157,158] Phosphorus and oxygen are also enriched in it, as well as components dissolved from the cathode.[3,160,161] These diffuse through the electrolyte, redeposit on the anode surface and thus are incorporated in its SEI like e.g. iron in the case of $LiFePO_4$ cathodes or manganese from the $LiMn_2O_4$ spinel.[3,161] Peled et al. reported that at least near the open circuit voltage (OCV) the Li^+ transport in the SEI is the rate determining step (RDS) for the deposition-dissolution process.[158]

The SEI formation on graphite does not take place instantaneously upon electrolyte contact, but nearly completely during the first cycle, starting at about 0.8 V vs. Li/Li^+.[21] This is clearly visible by a large irreversible capacity during the first charge so that only $80 - 90\,\%$ of the specific energy is used.[21] Another difference between the solid electrolyte interphases (SEIs) formed on lithium and graphite is the dimension in which layer formation takes place: for lithium with its non-intercalating, flat surface the decomposition products deposit only on the electrode surface and passivate it. Thus, more or less a two-dimensional film forms. In the case of graphite anodes the electrolyte solvents can be intercalated at potentials far higher than the standard chemical potential of lithium $\mu^0(\mathrm{Li})$, so that rather a three-dimensional surface layer builts up.[5] This leads to another important feature of the SEI on graphite anodes: the intercalation of solvated lithium ions into the graphite structure results in an extreme expansion of about 150 % of the matrix, frequently leading to its deterioration (exfoliation) and therefore additional capacity fading.[21] This holds especially for low lithium contents of $x \leq 0.33$ in Li_xC_6. At

this stage of Li^+ intercalation the coulombic interaction between the lithium guest layer and the balancing negative charge distributed over the graphene sheets is weak. Thus space to accommodate large solvent molecules is still available. The solvated intercalation compounds are thermodynamically favoured over the corresponding lithium-graphite compounds, i.e. the potential of their electrochemical formation is more positive.[21] To avoid this source of fading, an effective surface film formation in early stages of the first reduction is needed, so that no excessive solvent co-intercalation takes place. EC turned out to be an electrolyte component to fulfill these requirements and to date, there is an agreement in literature, that the presence of EC is required to form a stable anode SEI.[21,160] A schematic sketch of the SEI formation, also highlighting the differences between lithium and graphite anodes, is given in figure 3.3.

The SEI formation results in an increased impedance of the electrode, since especially LiF, being nearly always present in this surface phase, is highly resistive.[162,163] However, despite these drawbacks, formation of the SEI is necessary, since the LiB otherwise would not work. Longterm stability is only possible, if at least one of the SEI components is insoluble and deposits instantaneously on the electrode surface so that a dense, electronically well insulating film forms. However, even in this case there is a slow increase in its thickness with storage time due to residual reactions of lithium with thermodynamically unstable anions or impurities.[157,158]

In conclusion, the SEI formation has both positive and negative effects. It is on the one hand required to protect electrolyte and anode from detrimental reactions, but on the other hand slows down mass and charge transfer across the interface, so that stability of the cell comes at the expense of its kinetics.[5] There are attempts to reduce this kinetic barrier by tailoring the electrolyte by additives. These are preferentially decomposed before other electrolyte components, thus leading to unique features of the deposited interface film. Since they are only added in trace amounts, they are mostly consumed in the SEI and have thus hardly any impact on the bulk properties of the electrolyte.[5] To date, the most employed additive is VC, which leads to a more flexible and/or denser interface film. It protects the electrode by preventing the penetration of liquid electrolyte species and minimizes the amount of SEI products even for Si electrodes, which undergo large volume changes of up to 300 % during cycling.[164] This results in cracks in the electrode, in which new SEI formation takes place. Electrolyte solvents are required, which on the one hand effectively solvate the ions of the lithium salt in its bulk to provide sufficient conduction, but on the other hand should not bind to Li^+ too strong, so that it could easily strip off its solvent molecules at the electrode/electrolyte interface prior to its intercalation into the electrode. This behavior is reported for many enzymes, referred as "allosteric effect".[5] Adoption of this concept in LiB cells could drastically increase their performance.[5]

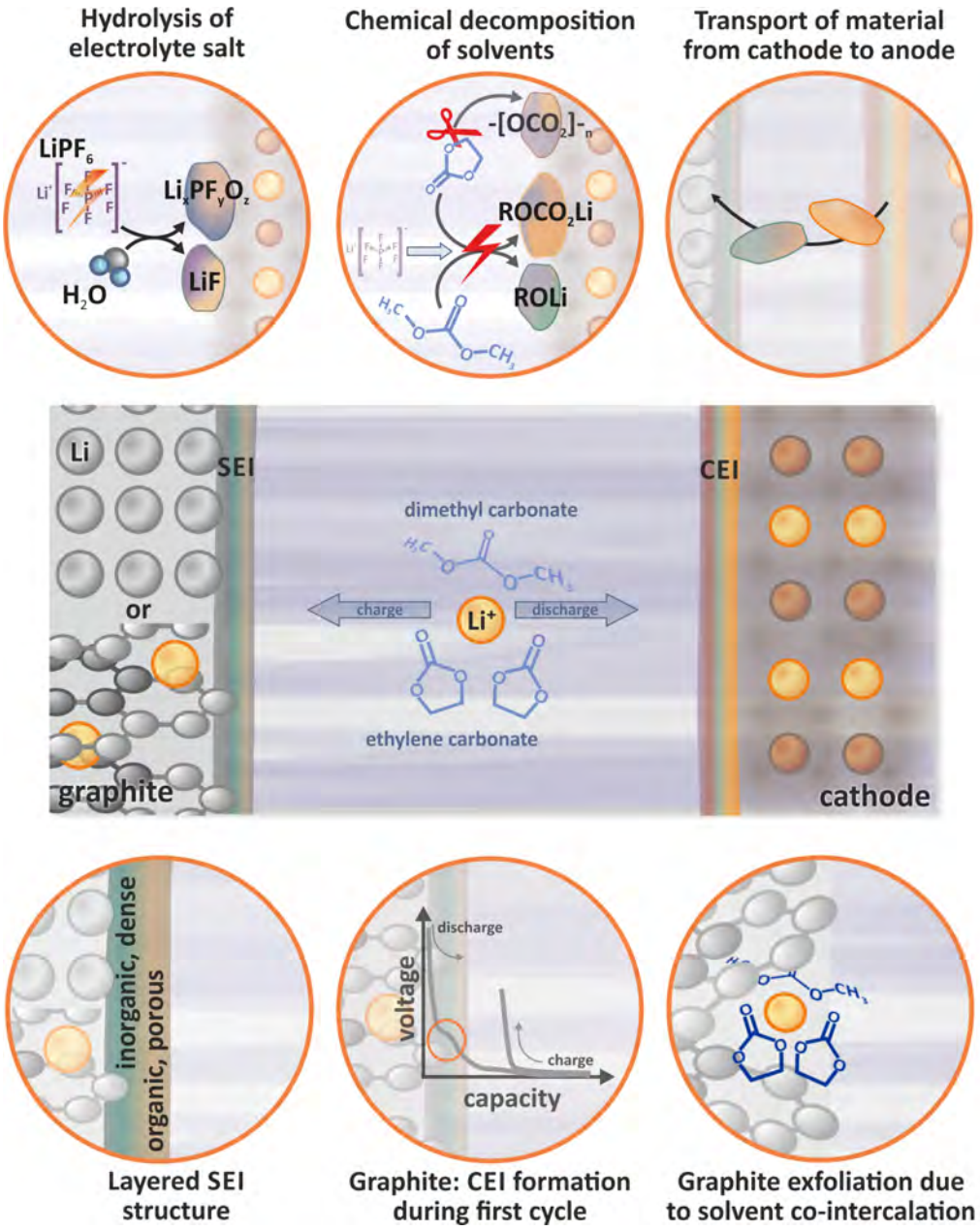

Fig. 3.3.: *Schematic sketch of the SEI formation on lithium and graphite anodes. In the upper row presence of species in the SEI due to electrolyte salt and solvent decomposition as well as components coming from the anode are depicted. In the lower row micro structure of the SEI and phenomena occurring solely at graphite anodes are sketched. The graph visualizes results by Peled et al. and Winter et al.*[21,157–159]

3.2.2. The cathode/electrolyte interface

In comparison to the SEI on the anode, there is little knowledge about the surface film formed on different cathodes. There is a wide variety of cathode materials and therefore generalization is less straightforward. LNMO is of special interest as cathode material for surface film investigations, since this material can be charged to a high voltage of 4.7 V vs. Li/Li^+ and therefore operates close to the oxidation potential of common electrolytes.[165]

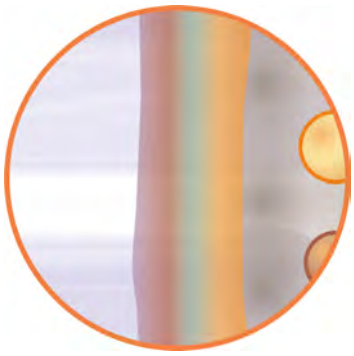

Stacked setup of the CEI: organic species close to the electrode and inorganic ones on top.

Like the SEI on the anode side of the LiB the interface film formed between cathode and electrolyte is comprised of organic and inorganic species like polycarbonates (-[-OCO_2-]-$_n$), alkyl carbonates ($ROCO_2Li$), alkoxides (ROLi), LiF, $Li_xPF_yO_z$ and, due to their partial dissolution in the electrolyte, MF_x compounds with M = Mn and/or Ni.[20,39,165,166,168] However, the exact surface chemistry of the cathode, the film thickness as well as the stability of the surface layer depend on the used electrolyte. Thus, employment of e.g. $LiAsF_6$ instead of $LiPF_6$ as electrolyte salt results in a more stable surface chemistry and therefore in a lower cell impedance, presumably because the formation of HF together with its subsequent detrimental reactions are more severe for the latter one.[67,160,168] The occurrence of LiF in the CEI results from the reaction of the active material with the unavoidable HF if $LiPF_6$ is used as electrolyte salt.[169] Its presence is detrimental to the cell performance due to its high resistivity.[169] An overview of the CEI formation entailing the models that were proposed by several groups is given in figure 3.4. The different phenomena will be reported in the following paragraphs.

The group of Edström and Eriksson proposes a stacked microstructure of the CEI with P-O species like $Li_xPO_yF_z$ in the outer region, followed by LiF and thereafter layers of organic polymers and polycarbonate products in the inner region close to the electrode.[166,167] They used XPS depth profiling as analytical tool. Thus the CEI has the reverse structure of the SEI, in which inorganic compounds are located close to the electrode and the organic components on top of them at the electrolyte side of the interphase (see chapter 3.2.1).

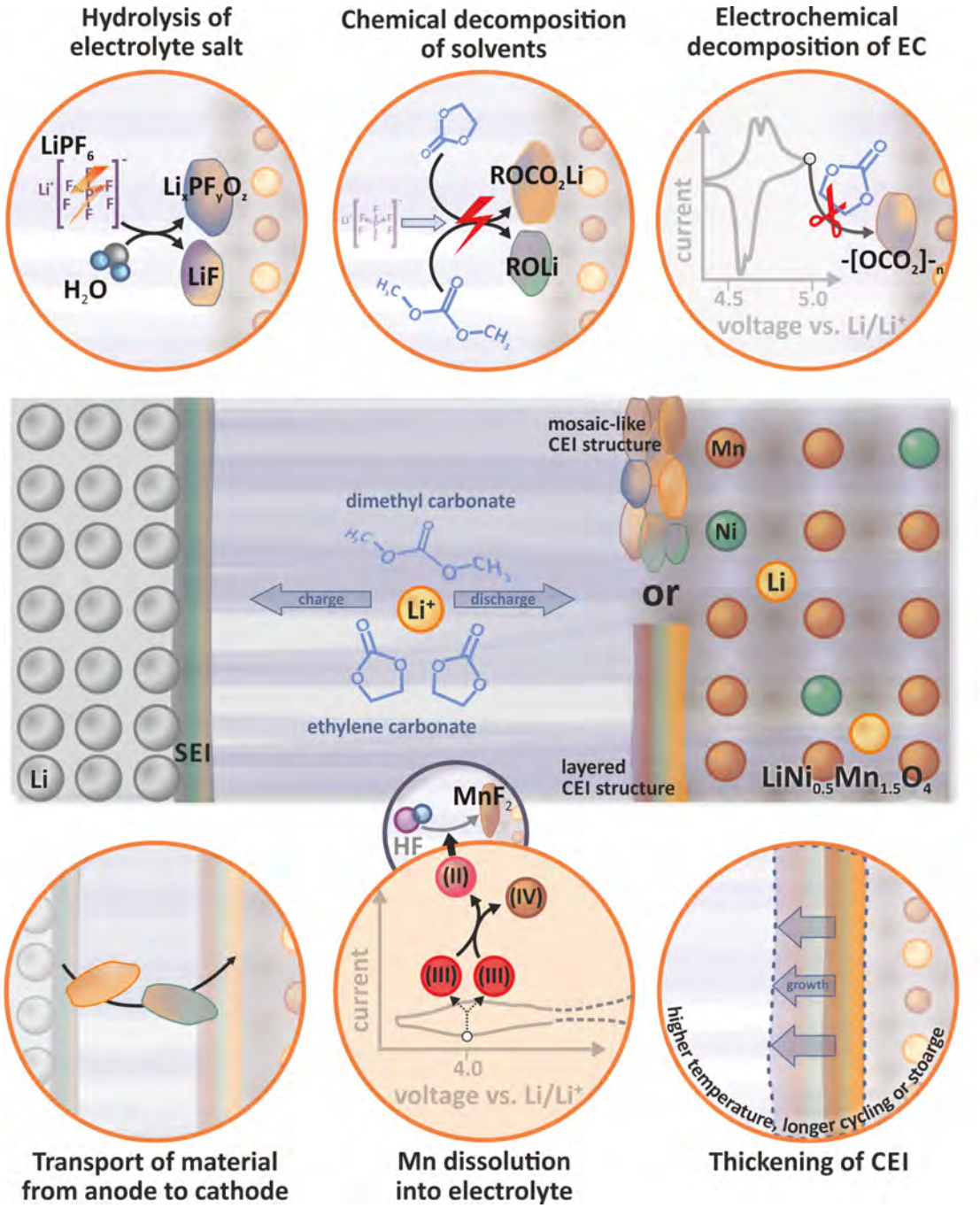

Fig. 3.4.: *Overview of the CEI formation visualizing effects proposed by several groups. In the upper row presence of species in the CEI due to electrolyte salt and solvent decomposition is sketched. In the lower row CEI species coming from the anode and those due to transition metal dissolution are depicted. Impact of different treatment on the CEI thickness is also presented. The model was constructed using results mainly reported by the groups of Aurbach, Edström and Eriksson as well as Duncan et al..*[20,165–168]

a. CEI components formed by electrolyte decomposition

During the first cycle in electrochemical experiments using $LiMn_2O_4$ electrodes an irreversible capacity between 3.8 and 4.3 V vs. Li/Li^+ is observed.[170] It is assumed that it arises from the electrochemical oxidation of the electrolyte solvents, since carbonates can be oxidized already at potentials as low as 2.1 V vs. Li/Li^+. Above 3.5 V their rate of oxidation substantially increases.

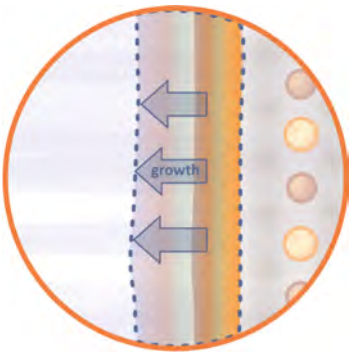

Increase of the CEI thickness with temperature, storage time and cycle number; after storage at elevated temperatures additional organic species form.

XPS studies by the group of Edström and Eriksson[39,166,167] on $LiMn_2O_4$ cathodes using both surface analysis and depth profiling with Ar sputter ions reveal essentially identical surface films for both electrochemically cycled and stored films at a given temperature. Therefore, the reactions occurring at the cathode surface seem to be of chemical and/or electrochemical origin and take place both under storage and cycling. Minimal differences between both treatments are found, since the kinetics for the surface film formation may be accelerated during cycling due to enhanced mass transport in the electrolyte.[167] The deposited material thickens with temperature, storage time and cycle number.[166] The increase in temperature primarily enhances the reaction kinetics rather than promoting new reactions.[167]

At room temperature the surface layer only partially covers LMO cathodes and does not passivate it like the SEI on the anode side.[166] It rather enables continuous transport of fresh electrolyte to the electrode surface, thus maintaining electrolyte oxidation.[166] Therefore the term "solid permeable interface" is frequently used for the film formed on the cathode.[166] In consequence, fresh electrolyte can reach it and is continuously oxidized there, resulting in organic rather than inorganic degradation products. In contrast, at 60 °C a more complete coverage exists.[166] At this temperature, additional and more resistive polymeric components are present in the CEI, which result from the polymerization of the electrolyte solvent ethylene carbonate.[165–167] It is either initiated by the oxidation of this molecule due to the high potential close to the cathode surface or by strong Lewis acids like e.g. PF_5, formed by the decomposition of the electrolyte salt $LiPF_6$ according to the following reaction:[39,166,167]

$$\begin{aligned} LiPF_6(sol.) &\rightarrow LiF(s) + PF_5(g) \\ PF_5(g) + H_2O(l) &\rightarrow 2HF(sol.) + POF_3(g) \\ 2POF_3(g) + 3Li_2O(s) &\rightarrow P_2O_5(s) + 6LiF(s) \end{aligned} \tag{3.1}$$

Acidic contaminants in the electrolyte may catalyze the polymerization of EC.[169] This reaction is not blocked by the growth of the surface film, because it does not propagate by electron transfer from the cathode material, but by the reaction of partially polymerized species with solvent molecules.[169] The fraction of $Li_xPF_yO_z$ and Li_xPF_y being present in the CEI remains constant independent of the storage voltage, again suggesting that the reaction between the electrolyte salt and the cathode material is mainly thermal and not electrochemically induced.[9] The commonly used electrolyte salt $LiPF_6$ shows worse temperature stability, so that its decomposition reaction takes place already at $60 - 85\,°C$, subsequently mediating solvent destruction.[171] This problem becomes even more severe in the presence of water. Commercial LiBs electrolytes contain below tens of ppm of this impurity, but these traces are sufficient to accelerate the decomposition of $LiPF_6$ either at elevated temperatures of more than $40\,°C$ or at potentials higher than $4.0\,V$ vs. Li/Li^+.[172] Thereby, HF is formed, which reacts with the cathode, thus creating new water molecules and therefore continuously decomposing the electrolyte salt, until the water molecules completely disappear.[172] However, since other salts are even worse concerning e.g. conductivity or costs, to date there is no alternative to $LiPF_6$.[171]

Despite the fact that the other electrolyte solvents diethyl carbonate (DEC) and DMC also decompose, the main source of the polymer species is EC, because this molecule is more likely to be oxidized at the positive electrode.[9,173] PF_6^- anions will be preferentially solvated by this species.[173] By application of a positive potential these anions and thus the EC molecules will enrich in the double layer at the cathode, where the strong electric field close to its surface will serve to align the polar EC molecules, thus facilitating its oxidation. Moreover, due to its higher polarity, EC will be the preferred target of electrophilic and nucleophilic attacks by contaminants in the electrolyte solution.[173] XPS investigations in addition reveal the existence of ethers and carbonates in the CEI at elevated temperature of $60\,°C$, resulting from EC and DMC decomposition:[167]

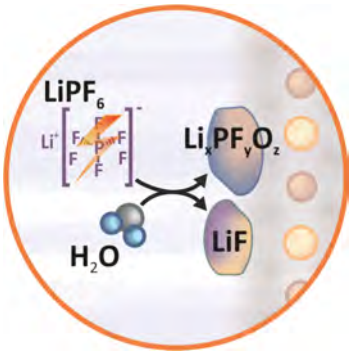

Decomposition of the electrolyte salt, being accelerated by the presence of water.

$$\begin{aligned} 2CH_2CH_2OCO_2 + 2e^- + 2Li^+ &\rightarrow (CH_2OCO_2Li)_2 + C_2H_4 \\ CH_3OCO_2CH_3 + e^- + Li^+ &\rightarrow CH_3OCO_2Li + CH_3^\bullet \end{aligned} \tag{3.2}$$

Since these products are unstable at elevated temperatures, they rather decompose into the more stable Li_2CO_3.[167] Using $LiBF_4$ instead of $LiPF_6$ as electrolyte salt the same polymer species but with different fractions are formed in the CEI, since BF_3, a

decomposition product of the former one, is a stronger initiator of polymerization.[39] It causes higher fractions of carbonate species.[39]

The deposited compounds remain even after prolonged washing of five hours in pure DMC at the cathode surface, thus showing the stability of the deposited layers.[167] However, some P-O species in the CEI like e.g. P_2O_5 are partially soluble, so that the formed layer appears to be not completely stable in the electrolyte. There are slight differences between the deposition products after storage at 100 and 0 % DOD. In the latter case the surface film contains more polymer species.[165,167] The oxidation potential of the electrode is greater in the charged state and therefore enhanced solvent oxidation is expected.[167] Controversy exists concerning the P-O products, since Eriksson et al. reported a lower fraction of these in the charged state, whereas Duncan et al. found a higher portion of $Li_xPF_yO_z$ compared to Li_xPF_y.[165,167]

Decomposition of solvent molecules initiated by the electrolyte salt resulting in the formation of organic species.

The stability of the electrolyte solvents strongly depends on the cathode material. Some release lattice oxygen when charged to higher potentials, which easily oxidizes the carbonate solvents.[174] This catalytic activity for solvent decomposition holds e.g. for Co containing materials due to overlap of the t_{2g} band of Co^{3+}/Co^{4+} and the 2p band at the top of O^{2-}. In consequence, a significant amount of holes is induced into the latter band at high voltages, thus causing loss of oxygen from the electrode lattice. Another factor enhancing the electrolyte decomposition is the formation of unstable structures during delithiation, like e.g. in $Li_{1-x}CoO_2$, which is not stable for $x > 0.5$. However, LNMO and its doped variations are structurally quite stable at high voltages and show excellent compatibility with carbonate electrolytes.[174] According to the results by Xu et al. it can be cycled in these electrolytes up to at least 5.2 V, leading to long cycle life.[174] In contrast to these results, investigations by Lucht et al. show that these electrolytes are in contact with LNMO not stable above 4.5 V.[9]

Comparison between the two common used electrolyte solvents DMC and DEC reveals a more rapid decomposition in the presence of $LiPF_6$ for the latter one.[171] This is explained by the fact, that the nucleophilic attack of fluoride on the α-carbon of alkoxy substitutes during the electrolyte decomposition is favored on primary carbons which are present in DEC over methyl ones like in DMC.[171] Electrolytes containing DMC in addition show better performance at high discharge rates than those based on DEC, since the former electrolyte shows higher ionic conductivity.[174]

b. Transition metal dissolution and CEI components related to this phenomenon

Both storage and cycling at elevated temperatures of 60 °C result in transition metal dissolution from the active material, caused by reactions with acidic species in the solution phase like protons. These are possibly generated in a proton exchange reaction during the electrolyte oxidation. This phenomenon goes along with the formation of λ-MnO_2 according to the following reaction proposed by the group of Aurbach:[67]

$$4LiNi_{0.5}Mn_{1.5}O_4 + 8H^+ \rightarrow 2\lambda - MnO_2 + Mn^{2+} + Ni^{2+} + 4Li^+ + 4H_2O + 2Ni_{0.5}Mn_{1.5}O_4 \quad (3.3)$$

However, these changes rather occur at the surface of the electrode than affecting the volume.[67] Due to the presence of fluorine ions the protons could built HF and formation of MnF_2, NiF_2 and LiF occurs.[175] According to Pieczonka et al. these metal fluorides are stable against HF attack, thus acting as barriers at the cathode/electrolyte interface and retarding transition metal dissolution.[176] Storage time and especially temperature are the main factors affecting the amount of transition metal dissolution.[168] Impact of the temperature is explained by the hydrolysis of the electrolyte salt $LiPF_6$, which occurs at 60 °C.[176] Nickel dissolution seems to be even severe than that of manganese, so that so that after storage for 45 days at 60 °C 1.3 % of manganese and up to 50 % of nickel is lost.[168,176] Pieczonka et al. revealed that the amount of dissolved transition metals from the LNMO electrode increases with its state of charge (SOC).[176] This dependence is possibly caused by the catalytic activity of delitiated λ-MnO_2 towards the electrolyte solvent decomposition which produces H_2O and thus HF.[176] The latter one, as stated already in the last paragraph, enhances the transition metal dissolution.[176] According to the authors the disproportionation of Mn^{3+} with the subsequent dissolution of Mn^{2+} is at least not the main reason for the dissolution of this species. Limiting the lower cut-off voltage during cycling of more than 4.0 V, so that the formation of Mn^{3+} is avoided, do not improve the manganese retention.[176]

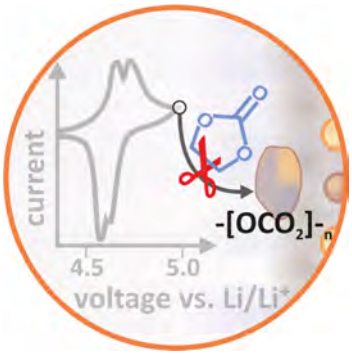

Decomposition of EC at high voltages, resulting in the formation of polymeric species.

The transition metal dissolution can be drastically reduced either by avoiding acidic components like HF in the electrolyte by reduction of the water content and the use of fluorine free electrolyte salt like $LiClO_4$ or by coverage of the electrode particles with basic species like MgO.[20]

c. Special behavior of LNMO

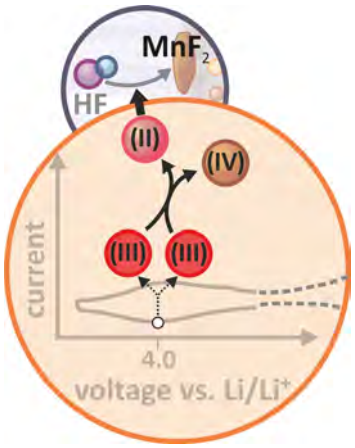

Disproportion of Mn^{3+} to Mn^{4+} and Mn^{2+} with the subsequent dissolution of the latter one in the electrolyte.

In contrast to most other cathode materials, LNMO forms a stable, protecting surface film according to Aurbach et al.[20] The authors emphasize the remarkable stability of this cathode material in $LiPF_6$ containing alkyl carbonate based electrolytes even at 60 °C, despite the fact that their main redox activity lies in the high voltage region of $4.5 - 4.8$ V.[20] Their impedance studies reveal the development of a stable surface layer, which is even pronounced at elevated temperatures. It both protects the cathode material from detrimental reactions with electrolyte and inhibits the pronounced oxidation of solvent molecules. Duncan et al. found in contrast studies on the nickel free material by Edström et al. significant amounts of organic species on the surface of LNMO already after cycling or storage at room temperature, whereas for LMO only a partial, non-protective coverage exists.[165,166] However, to date, the structure of this surface film has not been elucidated.[20] The drastically enhanced stability of LNMO at high temperatures in comparison to the pure, nickel free $LiMn_2O_4$ material is related to two effects: firstly, the average manganese oxidation state in the latter material is 3.5. Thus, there is a significant amount of Mn^{3+} which tends to disproportionate, thereby forming soluble Mn^{2+}. In contrast, in the nickel modified form nearly all manganese ions are in their tetravalent state. Secondly, it is assumed that the presence of nickel in the material makes the oxygen ions more nucleophilic. Therefore, the surface oxygen species nucleophilically attack the electrophilic alkyl carbonate molecules, thereby building up a surface film comprised of ROLi and $ROCO_2Li$ species like in the SEI on the anode.[20] These decomposition layers protect the active material and prevent the transition metal dissolution, but allow lithium ion transport.[20] This mechanism is supported by the fact that $LiNiO_2$ is more reactive towards alcyl carbonates than $LiMn_2O_4$, and by the detection of $ROCO_2Li$ species on the surface of electrodes comprised of the former material.[169]

Results by Ivanova et al. investigating technical LNMO electrodes after soaking for one month at room temperature in EC/DMC solution containing $LiPF_6$ as electrolyte salt show that the exact CEI composition depends both on the particle size of the active material and its crystallographic phase.[62] The authors suggested that different surface products in dependence of particle size reveal that nano-particles decompose $LiPF_6$ more easily to oxofluorides, whereas it adheres on the surface of sub-micrometer particles. Since

the former ones were prepared at a lower temperature of 400 °C they bear some oxygen deficit, which results in the $Fd\overline{3}m$ phase. Thus they contain not only tetravalent, but also trivalent manganese ions. The latter of them might react with the electrolyte salt, which would explain the different surface composition of the spinels with ordered and disordered structure.[62]

d. Full cells and impact of additives on the CEI formation

Aurbach also discussed, whether CEI components on the cathode may be formed at the anode, saturate the solution and finally deposit on the cathode.[177] Results by Duncan et al. reveal that in contrast to half cells, in which a complete coverage of the cathode material occurs after 100 cycles, for full cells only partial coverage of the cathode with organic species is found together with a lower fraction of LiF in the CEI.[165] However, deposition of species originating from the lithium anode could not be the dominant contribution in the CEI formation mechanism. In this case the surface films should be identical independent of the employed cathode material. Aurbach et al. however revealed an enhanced reactivity with the electrolyte for $LiNiO_2$ electrodes in comparison to $LiMn_2O_4$ ones.[169] In consequence, the CEI formed on the former material seems to be thicker. Thus, the cathode material indeed influences the surface layer formation.[169]

In comparison to LNMO half cells using lithium foil as anode, full cells with graphite anodes show severe capacity fading. More than 50 % loss was reported after 100 cycles for C/LNMO cells, whereas no degradation occured in half cells.[178] This discrepancy is presumably caused by the loss of active Li^+ resulting from manganese deposition and reduction on the anode surface:[176]

$$Mn^{2+} + 2LiC_6 \rightarrow Mn + 2Li^+ + \text{graphite} \qquad (3.4)$$

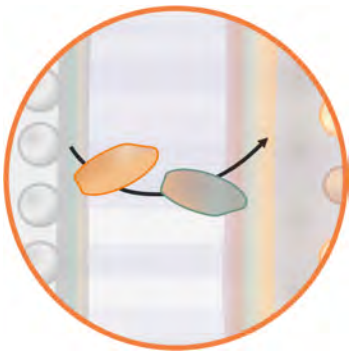

Transport from anode species to and incorporation into the cathode CEI.

Moreover, the reduced manganese metal will further promote the loss of active lithium ions through the formation of thick SEI layers, thus leading to significant capacity fading.[176] This aspect is even more severe for full cells than for those using lithium anodes. In Li/LNMO cells lithium is present in excess, whereas its amount is balanced between both electrodes in C/LNMO cells.[178] Capacity loss is even more severe at higher temperature of 55 °C, partly due to the formation of even thicker SEI layers on the graphite surface with the concomitant consumption of lithium ions. At elevated temperatures a

major side reaction product of EC containing electrolytes is dilithium ethylene dicarbonate $(CH_2OCO_2Li)_2$, forming according to the following reaction:[178]

$$2CH_2CH_2OCO_2 + 2e^- + 2Li^+ \rightarrow (CH_2OCO_2Li)_2 + C_2H_4 \tag{3.5}$$

Since the reaction product is not stable, it decomposes at elevated temperatures, resulting in a more porous SEI layer.[178] Thus, partly bare graphite surfaces are exposed, enabling additional SEI formation and therefore extra loss of lithium ions.[178]

Improvement of the CEI and therefore of the cell performance can by achieved by additives like lithium bisoxalatoborate (LiBOB), which delivers a reduced impedance and a thinner surface film.[179] The oxidation of the additives moreover results in the formation of a protecting surface film of the cathode, thus preventing further electrolyte oxidation.[179] To fulfill this purpose, the additive have to exhibit a lower oxidation potential than the electrolyte solvents, so that they are first oxidized and primarily participate in the CEI formation.[180] Only few percent of additives are considered as sufficient to protect the cathode/electrolyte interface and reduce the self-discharge of the cell.[46]

e. Closing remarks

Whereas bulk studies of cathode materials can be performed quite precisely, the study of decomposition layers at its surface is more difficult, since very thin films may form.[20] Due to its thickness on the nanoscale and the complex composition the number of suitable analytical tools is small. XRD and ICP-OES probe large volumes of the sample under investigation and therefore are not sensitive to thin surface films. Additional difficulties arise, since different molecules show similar signals in infrared (IR) spectroscopy.[181] Even worse, some species are not IR active, which holds e.g. for inorganic salt reduction products like LiF - being not detectable by this technique.[181] Raman spectroscopy has a low depth resolution of about 1 µm which is approximately two orders of magnitude greater than the thickness of the surface films formed on the cathode material.[181]

The composition of the CEI is only accessible by depth profiling using either XPS or SIMS, in which high energetic ion beams like Ar or Cs, respectively, are directed onto the sample to remove material, subsequently interrupted by analytical steps. The sputtering process can affect the sample due to its high energy.[39] For example loss of oxygen followed by the reduction of manganese can be expected.[39] Li_2O may only form due to Ar^+ sputtering out of Li_2CO_3 ($Li_2CO_3 \rightarrow Li_2O + CO_2$) and LiF could be a by-product of argon etching.[39,181] The complex morphology of the surface film adds to the difficulties. In the case of rather stiff polymer electrolytes, there might be voids due to imperfect coverage of the anode material, so that the contact area between electrolyte and

anode is difficult to determine.[158] It moreover changes with temperature, stack pressure and morphology of the native electrode material, thus complicating measurement and interpretation of SEI properties such as conductivity or activation energy for conduction. In any case, there is no alternative to careful multi-method analyses, which offer direct information on the composition of the CEI and SEI.

3.3. SIMS investigation of LiB in literature

This section gives a short overview over the variety of applications of secondary ion mass spectrometry in the analysis of LiB, focusing on LNMO as well as of the SEI/CEI. Despite its outstanding sensitivity for lithium there are only few studies reporting application of SIMS for characterization of battery components. Only a few studies exist and mostly the SEI formed on the anode has been studied. In addition, some investigations dealing with the diffusion of lithium or dopant ions in the electrodes exist.[182,183] In most cases SIMS is not used as main analytical tool, but only to confirm the in-depth homogeneity or the successful coating and doping of an active material.[184–187] Systematic investigations concerning the development of the CEI in dependence of the applied potential, temperature or storage time are very rare.[188,189]

Peled et al. were the first who used ToF-SIMS with 1 µm lateral resolution for the study of SEI on the different planes of highly ordered pyrolytic graphite (HOPG).[190] In this material the layer parallel to the graphene sheets, which is inactive for lithium intercalation, is named basal plane. The one normal to it, across which lithium is incorporated and released, is named as cross-section plane. The SEI formed on the cross-section plane must be a good lithium ion conductor, which not necessarily holds for the basal plane. As a consequence, the compositions of the two planes are expected to be different, which indeed could be confirmed by the authors using SIMS measurements. While the SEI on the basal plane is mainly composed of lithium carbonate and organic polymers, less fractions of the latter species are found in the layer on the cross-section plane, which instead contains higher fractions of LiF and PO_3^- species. Thus, the exchange current density for $LiPF_6$ reduction, which was used as electrolyte salt in this investigation, is much higher at this plane. The SEI thickness was determined using the depth at half signal intensity for several organic and inorganic species. Thereby, values of $0.5 - 2.5$ nm could be measured for the basal plane and about 1.7 to more than 30 nm for the cross-section one, thus being roughly five times thicker on the latter plane.[190] This large difference in thickness is presumably caused by solvent co-intercalation and exfoliation of the graphite on the cross-section plane. However, the reliability of the evaluated SEI thickness is questionable, since the sputtering rate used to transform the sputter time in the corresponding

depth was determined by using a SiO_2/Si sample assuming that this can be transferred to graphite, but both materials show drastic differences in hardness.

The authors also succeeded for the first time in proving the existence of polymers in the SEI by a characteristic sequence of peaks in the SIMS mass spectrum which differ only by one CH_2 group, thus being doubtless assigned to polyolefines.[190] The lateral investigation of the SEI with a resolution of 1 µm revealed its non-homogeneous chemical structure, thus confirming the mosaic-like setup of the SEI with microphases in the range of $1 - 2\,\mu m$. However, despite these interesting results, the presentation of the SIMS results is comparably poor and does not allow to check the reported findings. In particular the quality of the secondary ion images is rather poor. Moreover, no information is given whether the intensity scales in the images at different sample positions are at least for the same mass identical, to allow an estimation of its concentration differences, or whether each single picture was scaled individually to achieve best contrast. Depth profiles mentioned in the paper as well as spectra revealing the presence of polymers in the SEI are not shown. Thus, this study is interesting as a pioneering study, but has serious deficiencies from the technical point of view.

The group of Roling investigated the CEI formed on LNMO thin films by SIMS and determined its thickness to approx. 50 nm.[191] Their results point to an enrichment of organic species and dissolved Mn as well as Ni in its outer part close to the electrolyte.

Yabuuchi et al. examined the surface film formation on lithium excess layered manganese oxide Li_2MnO_3-$LiCo_{1/3}Ni_{1/3}Mn_{1/3}O_2$ (overlithiated high energy-$LiNi_{1/3}Co_{1/3}Mn_{1/3}O_2$ (NCM)) by SIMS.[24] The mass spectra collected after the first and second charge are essentially the same but show clear differences to the one taken in the discharged state. The authors concluded that the surface film formed during discharge of the cell decomposes during its following charging. Whereas in fresh electrodes Mn and Li signals come from the same regions, after discharge to 2.0 V the latter species is also present in other sample areas, thus revealing its presence in the surface film.

The group of Marcus used combined XPS and SIMS measurements to investigate the SEI/CEI formation on several anode and cathode materials.[192–194] Their study of Sn-Co alloy thin film anodes reveal a surface film formation in the first $200 - 260$ s in the depth profile due to the enrichment of C^- and Li^- signals.[193,194] Sn-Co alloy as well as Si anodes reveal a stacked microstructure of the SEI like for Li and graphite anodes, as already reported in the chapter 3.2.1 with organic species predominantly located in its outer part and oxide species in the inner region closer to the electrode.[192,194] SIMS depth profiles moreover reveal an incomplete participation of the Sn-Co alloy electrode in the cycling process, since there is a lithium-rich outer sub-layer and an essentially non-lithiated inner one. This composition gradient is presumably caused by a dense, predominantly of Co

composed region between the two layers, which inhibits the diffusion of Li^+ to inner sample regions, thus decreasing the discharge capacity.[194] They moreover reported an intensity increase of the substrate signal before reaching the film/substrate interface, thus suggesting the presence of pinhole defects and/or cavities in the alloy layer.[194] Different sputter times to reach this film/substrate interface for delithiated and lithiated samples moreover reveal volume shrinkage and expansion, respectively, during cycling.[194] Repeated volume changes result in cracking of the Sn-Co layer evidenced by a higher intensity of the C^- signal in the SIMS depth profile in the film region for the cycled sample in comparison to the pristine one, thus suggesting that the voids are filled with SEI.[194]

SIMS and XPS investigations by the group of Marcus on thin Cr_2O_3 films reveal a dependence of the CEI layer thickness and/or density on the conversion/deconversion reaction, i.e. on the state of charge.[188] The main component in the cathode electrolyte interface is Li_2CO_3, which forms during the first three cycles. They showed an incomplete lithium uptake even for very thin films of only 17 nm in thickness, thus revealing the partition of the oxide into a converted outer and an unconverted inner part. This is caused by the formation of a barrier layer of pure chromium limiting the transport of lithium into the inner region of the electrode.[188]

Myung et al. investigated the formation of protective passivating films on several metals commonly used as current collectors in the LiB by ToF-SIMS.[172] In practice continued corrosion of current collectors occurs due to the decomposition of fluorine containing electrolyte salts with the concomitant formation of HF, which in turn attacks the current collectors. Thus, the formation of thick and compact protective layers on the metal surface are required to ensure durable battery performance and safety. To study the parameters influencing the formation of these layers, the materials under investigation, Al, Cu, Cr, Ni, Fe and stainless steel, were manually scratched to create a new, oxide-free surface, which was exposed to the electrolyte. Afterwards, the newly formed surface layers were analyzed. The SIMS image enabled the resolution of the scratches on the metal surface. The passivation process mainly depends on both the upper cut-off voltage and the used electrolyte salt. Using e.g. $LiPF_6$ and $LiBF_4$ compact and thick protective passive layers were formed, which are highly protective against corrosive electrolytes and thus provide good battery performance even during long-term cycling. In contrast, imide-based electrolytes only built up a non-protective surface film, thus leading to distinct corrosion. Depth profile analysis of the newly deposited films on Al and stainless steel current collectors moreover reveal their stacked setup with an M-F (M = Al, Cr or Fe) compound in its outer region and an M-O one on the inner surface directly on the electrode surface. Severe safety problems arise by the usage of Cu current collectors in overdischarged cells,

because no protective layer on this metal can prevent its dissolution at higher potentials, which subsequently leads to a short-circuit of the cell.

Additional advantage of SIMS is the possibility to determine lithium diffusion profiles, conventionally performed e.g. with energy dispersive X-ray techniques, but due to their limitation on heavier elements not feasible for this light species.[195] Using this benefit, Okumura et al. determined the lithium diffusion coefficient in $LiMn_2O_4$ thin films to $1.23 \cdot 10^{-15}\,m^2/s$ and $6.55 \cdot 10^{-20}\,m^3/s$ for grain boundary and volume diffusion, respectively.[182] Lu and Harris also investigated lithium transport properties in the CEI formed on copper disks.[196] For this purpose, the authors used $LiClO_4$ as electrolyte salt during cycling to built up a CEI. Subsequent diffusion study in this prior formed surface layer occurred by immersion of the electrode in electrolyte using with $^6LiBF_4$ a different electrolyte salt. Their results reveal a CEI thickness of about 20 nm. ^6Li was indeed found in the CEI, leading to the conclusion that lithium is mobile within it. Since the $^6Li^+$:$^7Li^+$ ratio increases for at least 15 min, this process is assumed to be quite slow.[196] However, results are questionable, since the decrease of the boron signal in the beginning of the depth profile is similar for all different times of immersion in the $^6LiBF_4$ containing electrolyte. Thus, this ion either diffuses so fast in the CEI, that already after the shortest immersion time complete penetration occurred, or there are other effects responsible for the apparent enrichment of this ion in the first region like the establishment of the sputter-equilibrium. Depth profiles of a sample being not immersed in the boron containing electrolyte lacks. Therefore, it could not be excluded that this sample possesses a similar trend of the boron signal caused by small impurity contents, that could be detected due to the high sensitivity of the SIMS to even very small amounts. Its sensitivity of boron is in the positive investigation mode even higher than that of lithium.[197] The depth in the depth profiles was only estimated by using the sputter rate in SiO_2, which is questionable since the CEI is to large extend composed of porous organic matter that should be far easier sputtered than the dense silicon oxide.

Pieczonka et al. used SIMS depth profiling to determine the surface composition and transition metal dissolution of technical LNMO electrodes stored for 60 days at 60 °C in electrolyte.[176] According to their results organic and inorganic fragments like C_2H^-, CH^- and PO_3^- showed highest intensities at the electrode surface and decreased to background level after approximately $3-5$ nm. In this region $^6Li^+$ also shows small enrichment. Whereas the Ni^+ signal is constant in this region, the Mn^+ signal increases and reaches its volume value at a depth of about 10 nm, thus showing dissolution of the latter species from the electrode. It was also confirmed by other analytical techniques like XPS.[176] However, using XPS nickel is also clearly depleted from the LNMO surface. The authors explained this discrepancy by the lower sensitivity of the ToF-SIMS to Ni^+ in comparison to Mn^+,

so that the constant value for the former ion may not be meaningful.[176] HF as reason for transition metal dissolution is according to the authors confirmed by the occurrence of LiF, MnF_2 and NiF_2 species, each showing a maximum in intensity within ca. 5 nm of the surface and thus between the organic decomposition products and the LNMO electrode. However, taking into account the very low depths at which these phenomenona occur together with the relatively high roughness of technical LNMO electrodes, these results are again questionable. Enrichment of the decomposition species as well as depletion of manganese at the electrode surface could be caused by establishment of the sputter equilibrium during the first seconds of the depth profile.

Song et al. used SIMS to investigate the influence of the cooling rate of LNMO during its preparation on the transition metal ratio as well as on its electrochemical performance.[63] Slow cooling from 900 °C results in manganese enrichment at the surface, whereas a higher nickel-to-manganese ratio is observed for samples quenched from the same temperature. Since the redox activity of nickel at about 4.7 V is responsible for the electrolyte oxidation and formation of a passivating surface film, reduction of the surface nickel content seems to stabilize the electrochemical performance at elevated temperatures of 55 °C.[63]

Cho et al. used the SIMS to examine the benefit of a polyimide coating on the amount of LiF deposited on the LNMO cathode during cycling.[85] With this protecting film significant lower amount of this rather bad conducting phase was found on the electrode surface. This thus indicates a successful inhibit of surface reactions, which produce byproducts leading to resistive films on the LNMO surface.[85]

Shin et al. used ToF-SIMS depth profiles to study the in-depth distribution of the dopant ions chromium, iron and gallium in LNMO powder and verified their segregation to the electrode surface during post-annealing for 48 h at 700 °C.[183] This stabilizes the cathode/electrolyte interface and minimizes the contact of trivalent manganese with the electrolyte. Thus, its disproportionation reaction with the concomitant dissolution of the divalent form is suppressed.[47] The dopant surface enrichment is beneficial for the electrode performance, since undesired reactions with the electrolyte caused by the nickel redox couple and the subsequent formation of a thicker CEI layer are prevented.[183] However, this surface enrichment is rather questionable since the powder, either compacted on a carbon tape or pelletized, should possess relatively large roughness. Thereby, the in-depth resolution is reduced as will be further discussed in chapter 6.1. The authors just report the sputter time, but gave no information on the corresponding depth. This becomes even more severe, since the enrichment was detected only in the first 20 s of sputter time and therefore very close to the first region in the depth profile, in which the sputter equilibrium is established. Since nickel and manganese show in the first $5 - 15$ s in the doped as well as in the undoped sample decreasing or increasing trends, the extension of the region, in

which the establishment of the sputter equilibrium takes place, should be in this range. This effect could be thus responsible for the enrichment of the dopant ions at least in some measurements. The authors showed no depth profile of a cycled sample, thus offering no proof that the dopant ions reside at the surface, so that their surface enrichment is indeed the reason for the better cycling performance.

In conclusion, in most investigations reported in literature SIMS was not used as main analytical tool, as it delivers no information on the oxidation state of the elements under investigation and is unable to deliver their absolute concentration. Despite the interesting results collected with this method, the inadequate and somehow careless description of the SIMS measurement procedure lowers the value of results. Information concerning the used ion gun energies and crater dimensions is often missing. The data analysis is often not well described and information lacks, whether the shown intensities were normalized to a certain signal like the total ion signal. In many depth profiles only the sputter time is given, but no calculation of the actual depth was reported, so that an estimation of the layer thickness is nearly impossible. Since enrichment of ions building up surface films as well as of dopant ions often occur only in the very first seconds of the depth profile, the results are partially questionable, since in this region the establishment of the sputter equilibrium takes place. Thus, apparent enrichments are possibly only caused by matrix changes and do not necessarily result from actual phenomenons in the sample. Moreover, reported thicknesses of the SEI or CEI are often in the range of $10 - 20\,\mathrm{nm}$. Depending on the measurement conditions and sample roughness, they could be thus in the same order of magnitude like the depth resolution achievable in the SIMS.[14] This points out that SIMS is often used without critical discussion of the method and its potential pitfalls.

4. Sample preparation and basic characterization

This chapter deals with sample preparation and basic characterization of samples, thus setting the basis for the SIMS experiments described in later chapters. It thus entails the preparation of the cathode powder used for thin film deposition, its characterization and first electrochemical measurements to verify its identity. Target preparation required for thin film deposition is also mentioned as well a the cell assembly used for electrochemical investigation of technical LNMO electrodes.

4.1. Powder preparation

The LNMO powder used in this thesis as raw material for the doctor blade electrodes as well as as target in the PLD process was prepared according to a synthesis route already successfully applied in the diploma thesis by Annalena Schlifke at the University of Hamburg.[198] The powder preparation occurred via solid state reaction by mixture of stoichiometric amounts of $Mn(NO_3)_3 \cdot 4H_2O$ (Merck) and $Ni(NO_3)_3 \cdot 6H_2O$ (Merck) together with 5 % excess of Li_2NO_3 (99.995 % purity, Merck). A higher amount of the latter species was added to overcome possible loss of this light element during the high temperature calcination as well as in the PLD process, because light elements like lithium are scattered broarder by the laser pulse, so that a lower amount reach the substrate.[199] The metal nitrates were dissolved in a small amount demineralized water, resulting in a clear, green solution. Solvent removal and drying occured first for 100 h at 80 °C and afterwards for 20 h at 100 °C in air. Subsequent calcination was carried out at 400 °C and 700 °C for 3 h and 5 h in air, respectively, resulting in a brown powder. It was afterwards ground using a ball mill to deliver a fine, homogeneous powder suitable for further application. From SEM investigation, shown in figure 4.1, the average particle size could be estimated to approx. $2 - 10\,\mu m$. Images were recorded using a LEO microscope by Zeiss. It is visible, that the mostly round shaped single particles are composed of smaller, flake-like primary particles, thus having a relatively high surface area.

Formation of the spinel phase was controlled by XRD using an Siemens D500 diffrac-

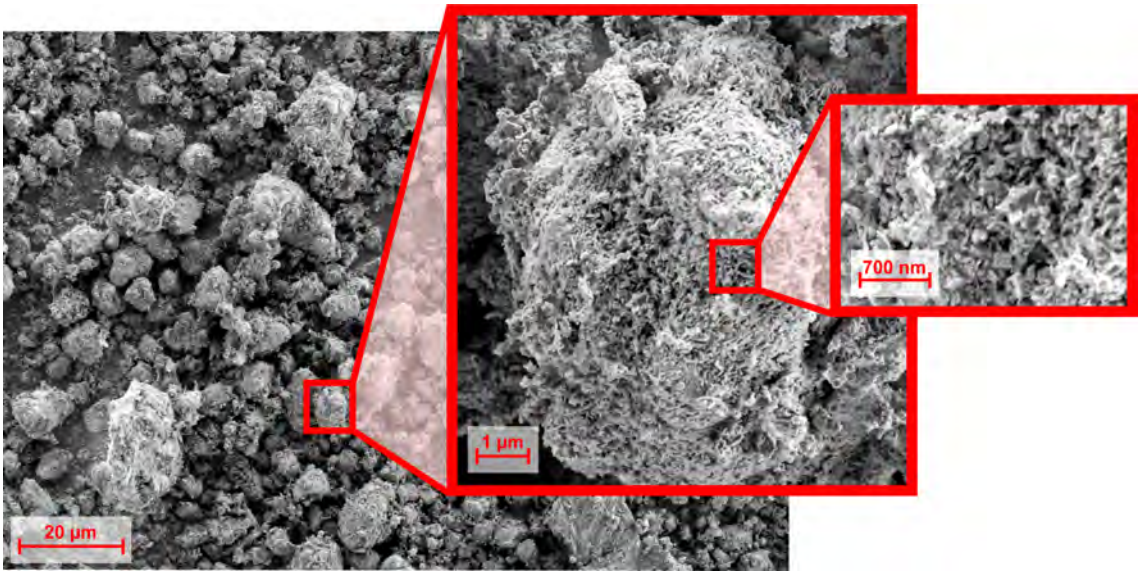

Fig. 4.1.: *SEM image of LNMO powder particles.*

tometer equipped with Cu K_α radiation. From figure 4.2, showing the diffraction pattern of the LNMO powder together with the reflexes of the two crystallographic phases of this material, $Fd\bar{3}m$ and $P4_332$, it can without doubt be indexed to the spinel phase. There is moreover no hint to any impurity phase like NiO or $Li_xNi_{1-x}O$. The reflexes of the two crystallographic phases of LNMO were taken from their particular powder diffraction (PDF) cards, namely 00-032-0581 for $P4_332$ and 01-080-2162 for $Fd\bar{3}m$. Distinction between these two phases by XRD is however rather difficult, since they deliver nearly identical diffraction patterns. Only the absence of the (220) reflex is a sign of the disordered phase.[141] Due to its oxygen deficit is the appearance of this structure often accompanied by the impurity phase NiO. It delivers an additional reflex at approx. $2\Theta = 69°$, which is often by mistake seen as a reflex belonging to the $Fd\bar{3}m$ phase. The ordered structure lacks this reflex, but possesses another reflex at $2\Theta \approx 71°$. Amdouni et al. reported additional minor reflexes for the $P4_332$ phase at 15.3, 39.7, 45.7 and 57.5°.[66] Due to their low intensities, they were not observed in our case. In consequence, distinction between these two phases was only possible by the two reflexes around 70°, each of them being present in only one structure. From figure 4.2 we concluded that the prepared powder shows the oxygen deficit $Fd\bar{3}m$ phase, since it shows only a reflex at $2\Theta = 69°$, but none at $2\Theta \approx 71°$, which is in accordance with the calcination temperature of 700 °C, thus being in the range, where oxygen should be released from the structure. Additional verification was achieved by Rietveld refinement by Prof. H. Ehrenberg (IFW Dresden) using the FULLPROF software, delivering a lattice constant of 8.1710 Å, which is close to the value

of 8.1724 Å reported by Kim et al. for the disordered spinel form, whereas the ordered one possesses distinct smaller one of 8.1663 Å.[60]

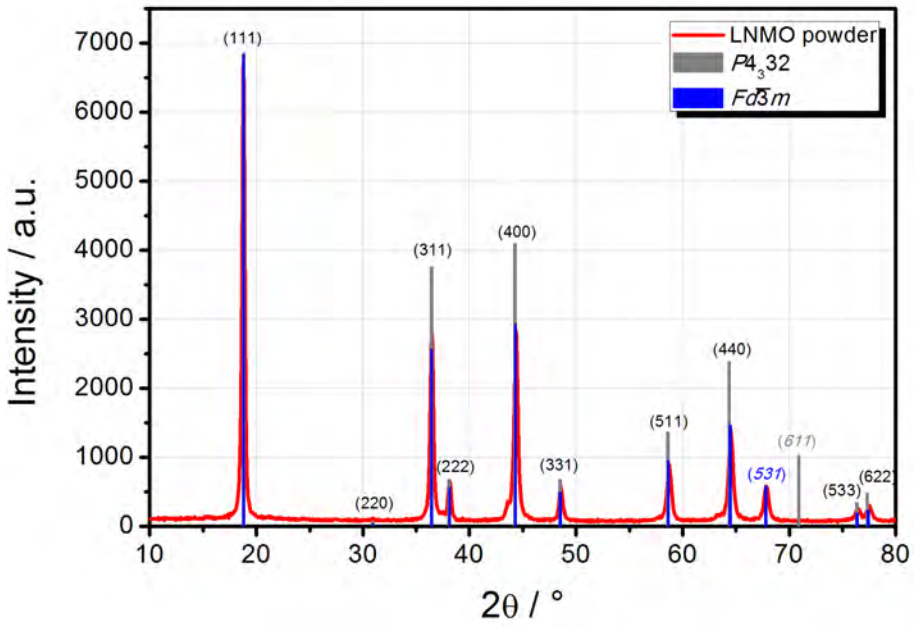

Fig. 4.2.: *XRD of the pristine LNMO powder together with the reflexes of the $P4_332$ and $Fd\bar{3}m$ phases as well as the appendant hkl indices. The indices of the two reflexes being present in only one of the two phases are written in italic.*

Additional characterization with Raman spectroscopy, in which the ordered phase shows additional modes to the five reported for the disordered spinel, and electrochemical methods are consulted to further elucidate the phase present in the prepared powder.[59,200] In CV measurements the absence of any electrochemical activity at 4.0 V vs. Li/Li^+ points to the lack of trivalent manganese in the structure and therefore indicates the presence of the $P4_332$ phase. The Raman spectrum of the pristine powder, recorded using a SENTERRA spectrometer (Bruker), is shown in figure 4.3. It shows five modes in the range of $300 - 700\,cm^{-1}$, which are summarized in table 4.1 together with their assignment to different vibrations.[59,200] Whereas the literature agrees, that the disordered spinel delivers only five Raman modes, differences exist concerning their actual position. The values reported by several groups for LNMO are also reported in this table.

Our own values are found in the expected region. Questionable is, however, whether the pair at $580 - 605\,cm^{-1}$ points to the $P4_332$ phase. According to Oh et al. clear peak splitting in this region, resulting from $T_{2g}^{(3)}$ vibrations, occurs only for the ordered phase, whereas for $Fd\bar{3}m$ just one broad reflex with very small tips was reported. In the Raman spectrum of the $P4_332$ phase, there should be however additional reflexes in the

Tab. 4.1.: *Raman modes of LNMO measured during own investigations as well as values reported in literature and their assignment to different vibrations.*

assignment to vibration	**own measurement**	**Julien et al.**[200]	**Oh et al.**[59]	**Talyosef et al.**[201]
Ni^{2+}-O stretching mode	$403\,cm^{-1}$	$398\,cm^{-1}$	$390\,cm^{-1}$	$407\,cm^{-1}$
	$492\,cm^{-1}$	$498\,cm^{-1}$	$483\,cm^{-1}$	$500\,cm^{-1}$
$T_{2g}^{(3)}$; splitting points to the	$585\,cm^{-1}$	$602\,cm^{-1}$	$582\,cm^{-1}$	$530\,cm^{-1}$
ordered spinel	$605\,cm^{-1}$	-	$588\,cm^{-1}$	$592\,cm^{-1}$
symmetric Mn-O stretching of the MnO_6 octahedra	$634\,cm^{-1}$	$638\,cm^{-1}$, $665\,cm^{-1}$	$623\,cm^{-1}$	$640\,cm^{-1}$

investigated wavelength range at e.g. $387\,cm^{-1}$. Thus, for our own powder the formation of the disordered phase is more likely. This result was also confirmed by CV measurements by the presence of redox activity in the 4 V range, which will be presented in chapter 4.4.

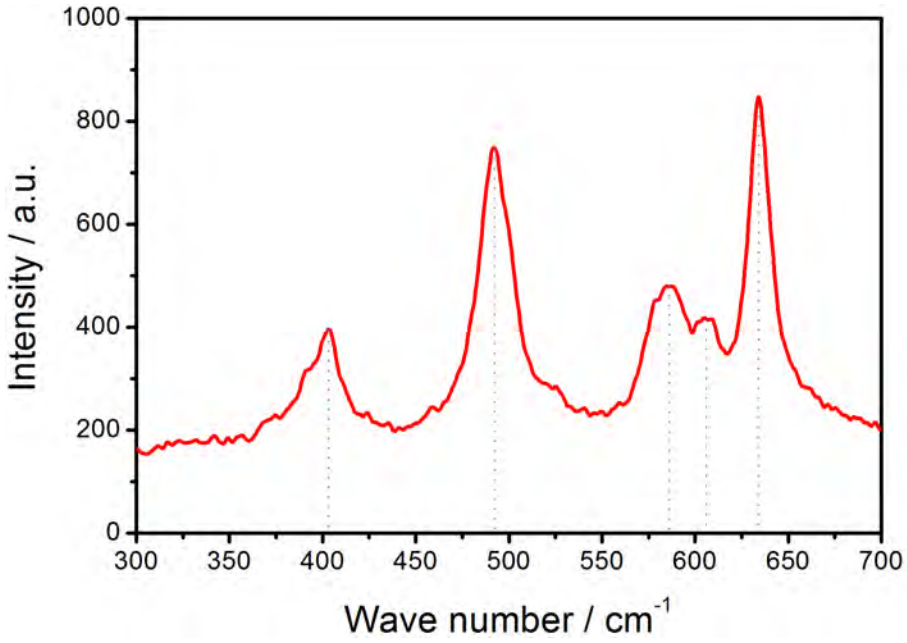

Fig. 4.3.: *Raman spectra of the pristine LNMO powder.*

The chemical composition of the prepared powder was determined by ICP-OES at KIT (thanks to Dr. S. Indris), delivering the atomic fractions and the elemental ratio based on standardization on the nickel content depicted in table 4.2. The results reveal very good agreement with the desired composition of $Li_{1.05}Ni_{0.5}Mn_{1.5}O_4$. Only a negligible deficit in manganese is found. ICP-OES measurements performed at the Schunk Kohlenstofftechnik

GmbH in Heuchelheim (thanks to Dr. J. Metz) revealed a slightly different atomic ratio, resulting in the formula $Li_{0.99}Ni_{0.5}Mn_{1.62}O_{3.68}$, also based on standardization on the nickel content. Here, oxygen content was determined by carries gas hot extraction. In the measurements by Schunk Kohlenstofftechnik GmbH lithium as well as oxygen fractions are reduced and there is more manganese in comparison to nickel found in the powder. The discrepancy between these two measurements could result from different dissolution techniques and probably not the whole material was dissolved.

Tab. 4.2.: *ICP-OES results of the pristine LNMO powder measured at KIT. The calculated ratio based on standardization on the nickel content.*

element	atomic percent	elemental ratio
lithium	15.0	1.06
nickel	7.1	0.50
manganese	21.0	1.48
oxygen	56.9	4.01

4.2. Doctor blade process

For preparation of technical electrodes by the doctor blade process, firstly a so called slurry was prepared. It was afterwards casted by doctor blade over the desired current collector, in most cases a thin metal foil, which is schematically sketched in figure 4.4. The slurry was composed of 70 wt% active material, i.e. LNMO, 10 wt% Super P™Li (TIMCAL, particle size 40 nm) and 20 wt% polyvinylidene fluoride (PVDF) 1013 (Solvay) as binder, which was prior dissolved in N-methyl-2-pyrrolidon (NMP) (Sigma Aldrich). Additional NMP as solvent was added until a honey-like paste was achieved, which was stirred over night to guarantee sufficient homogeneity. As current collector aluminum foil, approx. 20 µm in thickness was used. It was etched in 10 wt% NaOH in demineralized water prior to casting of the slurry to remove the oxygen layer at its surface as well as to roughen it, thus guaranteeing better adhesion of the electrode material even during repeated cycling with volume changes. With about 1/5 of the total electrode material the amount of binder is rather high, while in optimized doctor blade processes only very few percent are needed. In literature in most cases $5 - 10$ % are used.[39,51,165,169] The high amount of binder was needed, since with lower content the electrode material peeled off the current collector.

The slurry was casted over the foil with a thickness of 250 µm and dried in air for about $24 - 48$ h. Afterwards, circles of 12 mm in diameter were punched out and dried in vacuum for 12 h at 120 °C to remove any residual solvent. The finished LNMO electrodes

were subsequently transferred without air contact into an argon filled glovebox (MBraun), where the cell assembling took place. After the final drying step the electrode thickness reduced to about $30 - 40\,\mu m$.

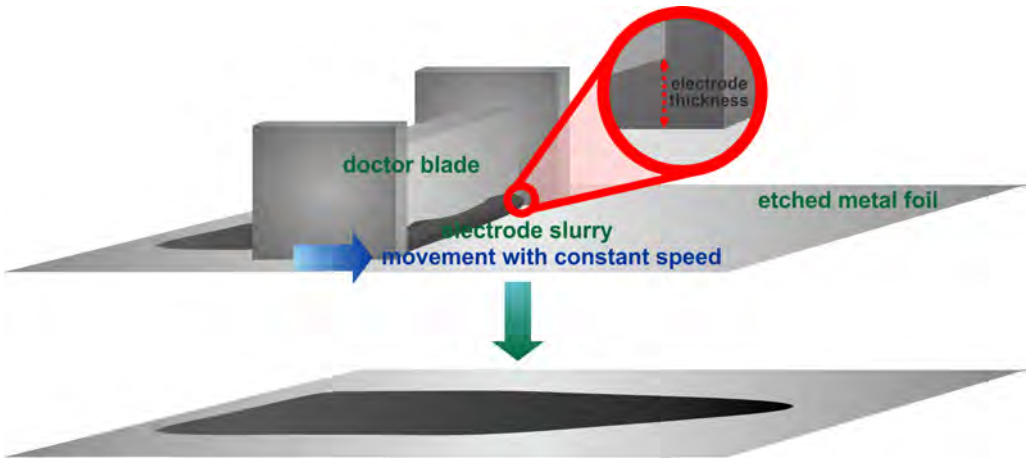

Fig. 4.4.: *Schematic sketch showing the doctor blade process for production of technical electrodes. The electrode slurry is placed in front of the doctor blade, which moves with constant, defined speed over the metal foil. The thickness of the deposited layer is adjusted by variation of the gap between the middle part of the doctor blade and the foil.*

SEM images of a technical LNMO electrode are shown in figure 4.5. It reveals a homogeneous embedding of the greyish particles with $2 - 10\,\mu m$ size in the carbon-binder matrix. The small, globular species represent the conductive carbon and the grey smeared regions result from the binder.

Besides LNMO cathodes also graphite electrodes, later used as anode in full cells, were prepared in the same way also using the doctor blade process. They are composed of 90 wt% SFG-44 (artificial graphite, TIMCAL) and 10 wt% PVDF 1013 with NMP as solvent. The slurry was deposited with a thickness of $120\,\mu m$ on either copper or aluminum foil. Circles of 12 mm in diameter were punched out. The anodes were first dried in air and afterwards for 2 h at 120 °C in vacuum. They were subsequently transferred to an argon filled glove box without air contact. After the final drying step the electrode thickness reduced to about $50\,\mu m$.

4.3. Cell assembly

The cell assembling was performed in an argon filled glovebox to avoid air contact of the lithium foil used as anode and to minimize water content in the cell. As cell housings Swagelok T-shaped cells, that contain also a reference electrode in addition to the working

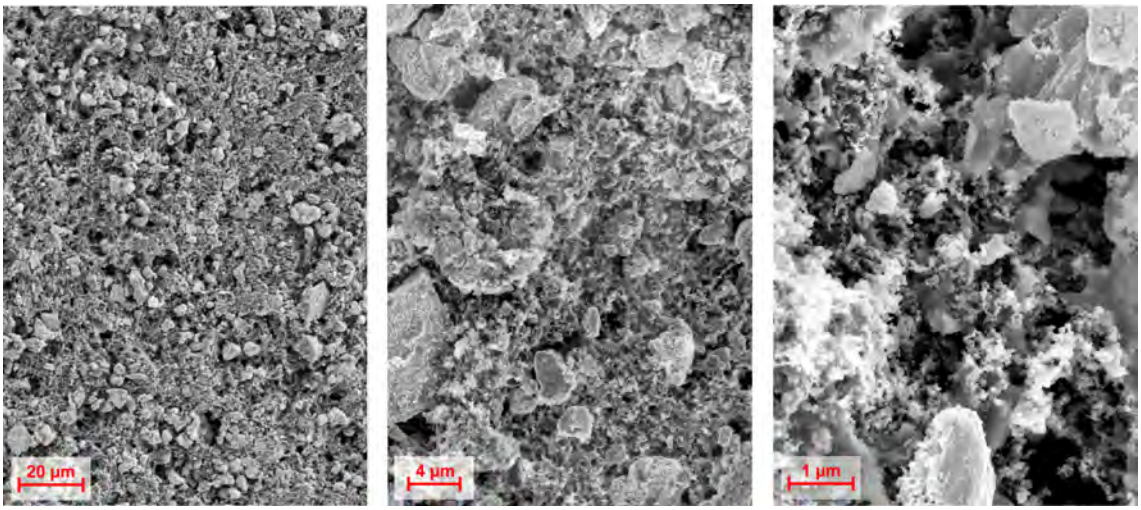

Fig. 4.5.: *SEM images of technical LNMO electrodes, from left to right: overview showing the grayish LNMO particles in a matrix of conductive carbon and binder; image with higher magnification revealing a size of approx.* $2 - 10\,\mu m$ *for the LNMO particles; image of the carbon-binder matrix: the small, globular species represent the conductive carbon and the gray smeared regions result from the binder. In the lower region of the image also a bright shining LNMO particle is visible.*

and counter electrodes, were used. Only in a few experiments I-shaped cells without reference electrode were employed. A schematic sketch of the main parts contained in a T-shaped Swagelok cell is given in figure 4.6. The cell housing is made of stainless steel and has three openings, one for each of the three electrodes and 13 mm in diameter. Its inside is firstly covered with two pieces of insulating Mylar® foil (Du Pont), that prevents electrical contact between the electrodes. First the anode stamp is inserted into the housing and is tightened with a screw nut. On its top the anode is placed, i.e. in case of half cells a piece of lithium foil, prior scratched from both sides to remove the insulating oxide layer on its surface and punched in circles of 12 mm in diameter. On its top three pieces of glass fiber separator (Whatman™, dried for 2 h at 110 °C in vacuum prior to usage), each also 12 mm in diameter, and soaked with 85 µl electrolyte, are inserted. Thereafter, the cathode is placed, followed by a small metal plate guaranteeing homogeneous contact, a spring to apply a constant, reproducible pressure on the cell and the cathode stamp, which is also tightened with a screw nut. In the hole normal to the others first three small pieces of separator, soaked with 15 µl electrolyte are inserted. On top of them a small pin, completely encased with a piece of scratched lithium foil, 10 mm in diameter, is placed as reference electrode. The upper side of the pin is a metal plate, that also guarantees homogeneous contact. On its top another spring and the reference electrode stamp is placed, the latter of them is also tightened with a screw nut. The cell assembled this way is sufficiently gas tight.

The commercial electrolyte LP30 by Merck consisting of 1M $LiPF_6$ in EC/DMC (1:1) was used, since it is reported to be more stable than other commonly used ones containing e.g. DEC instead of DMC as solvent.[171] If not stated otherwise, the cells were stored over night prior to electrochemical experiments to ensure sufficient diffusion of the electrolyte into the porous structure of the electrode, thus reaching a stable performance.

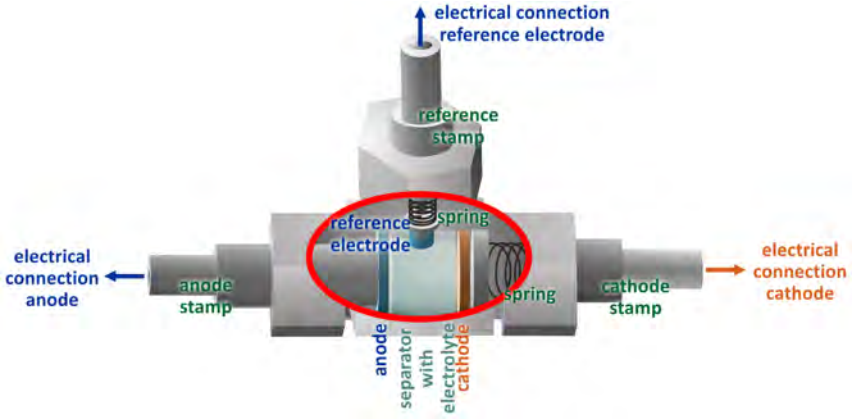

Fig. 4.6.: *Schematic sketch of the main parts contained in a T-shaped Swagelok cell. The cell housing consists of stainless steel and all three stamps are tightened with screw nuts to ensure gas tightness.*

4.4. General electrochemical response of technical LNMO electrodes

CV measurements depicted on the left side in figure 4.7 deliver the expected electrochemical behavior of the material with the two characteristic peaks resulting from the oxidation of nickel at $4.6 - 4.8\,\mathrm{V}$. Besides the main capacity in the high voltage range, there is also a small contribution at about $4.0\,\mathrm{V}$, which results from the Mn^{3+}/Mn^{4+} redox couple. This points to the fact, that in accordance to Raman and XRD investigations prior reported in this chapter the self-made LNMO indeed exists in the $Fd\bar{3}m$ phase. On the right side in figure 4.7 the corresponding constant-current cycling is depicted, showing plateaus at the expected potentials of about $4.0\,\mathrm{V}$ and $4.6 - 4.8\,\mathrm{V}$. In the latter region the two plateaus are rather smeared, presumably due to sluggish kinetics together with the rough surface and different particle sizes of the active material, so that the lengths of the diffusion paths vary greatly. The calculation of the differential capacity as given in figure 4.9 offers more information. Even small features in the cycling curve become visible, clearly revealing the two peaks characteristic for LNMO in the high voltage range.

With $2.9 - 5.0\,\mathrm{V}$ the voltage range for electrochemical investigations was chosen rather

broad, thus ensuring to cover the whole range, in which LNMO is active. Taking into consideration, that the activity of Mn^{3+}/Mn^{4+} lies at approx. 4.0 V, a value of about 3.5 V as lower limit should in principle be low enough, even if some peak shifting due to kinetic limitations is expected. The lower value of 2.9 V was selected, since uptake of excess lithium into LMO takes place at about 3.0 V, so that it could be investigated, whether this reaction also occurs in our electrodes. However, no electrochemical activity was detected at 3.0 V, so that incorporation of excess lithium in this material in contrast to the nickel free one is highly unlikely.

The first cycle is somewhat different in shape than the following. Thus, it is obvious, that during the first (dis)charge slightly different or addition processes like surface film formation on both electrodes take place. The fact, that the current close to 5.0 V does not decrease to the value expected by extrapolation of the baseline in CV measurements, shows that there is a small, but not negligible contribution of the electrolyte oxidation to the current. It is in the first cycle higher than in the subsequent ones, thus again confirming the establishment surface layers on one or both electrodes. The coulometric efficiency, defined as ratio of the discharge by the corresponding charge capacity, reaches however after the first about three cycles a steady value of approx. 95 %. There is still some contribution of parasitic, non-reversible reactions like electrolyte oxidation even in subsequent cycles. This phenomenon will be further discussed in chapter 7.

For some cells, there was a slight increase in capacity found in the first cycles, which is also partially reported in literature.[43] This phenomenon could be caused by two different effects: On the one hand an incomplete wetting of the porous cathode in the beginning of the electrochemical experiment could occur, which improves with time, so that in later cycles more active material is accessed.[43] On the other hand, repeated volume changes by lithium uptake and release could widen the structure of the electrode, so that the electrolyte reaches deeper into the volume of the active material and successively more matter takes part in the redox reaction.

Due to its high potential of 4.7 V vs. Li/Li^+ the definition of the higher cut-off potential during electrochemical testing of LNMO is difficult, since too low values reduce the capacity of the material, whereas at potentials close to 5.0 V the decomposition of carbonate based electrolytes starts, leading to fading of the cell performance. The group of Aurbach stated that a potential of 4.85 V is sufficient to extract the whole capacity of the material and is on the other hand low enough to avoid electrolyte oxidation.[67] According to the authors there are only small capacity losses at cut-off potentials of $4.70 - 4.82$ V, which become significant above 4.85 V. Reduction of the upper cutoff voltage from 5.0 V to 4.85 V for the LNMO cells studied in this thesis, shown in figure 4.8, indeed reduces the capacity fading. In consequence, the lifetime of LNMO cells should be extended. However, since

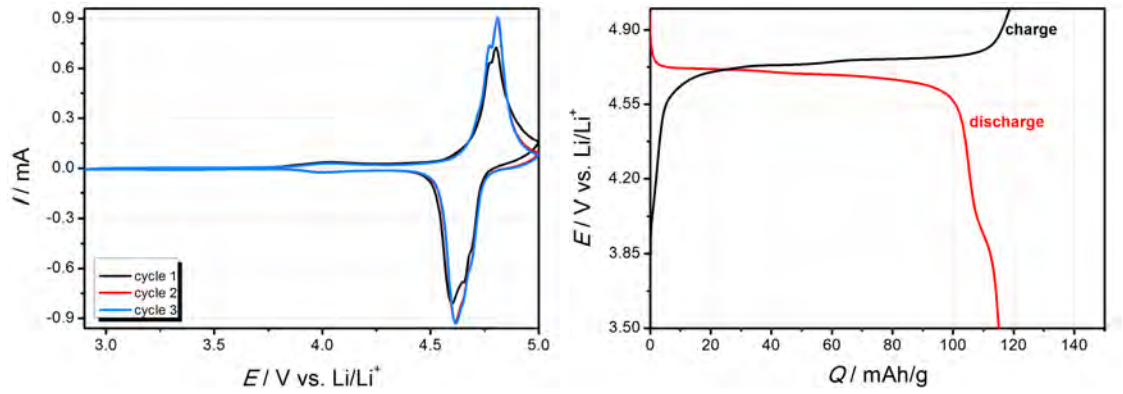

Fig. 4.7.: *CV on the left, recorded with a scan rate of* 0.1 mV/s, *and cc cycling at* 0.5 C *on the right of a LNMO half cell, both measured at room temperature. In the cc measurement for better visibility only the second cycle is shown. In each case LP30 was used as electrolyte.*

the current at the upper cut-off limit is rather high in CV measurements by restriction to 4.85 V, it is questionable if really the whole capacity of the material had been exploited. The coulombic efficiency is with 95 % for both upper cut-off potentials the same. Thus, not only electrolyte oxidation, which should be severe above 4.85 V, but also other irreversible reactions like e.g. loss of active material by transition metal dissolution, deposition of metallic lithium on the anode or simply exfoliation of cathode particles presumably take part.

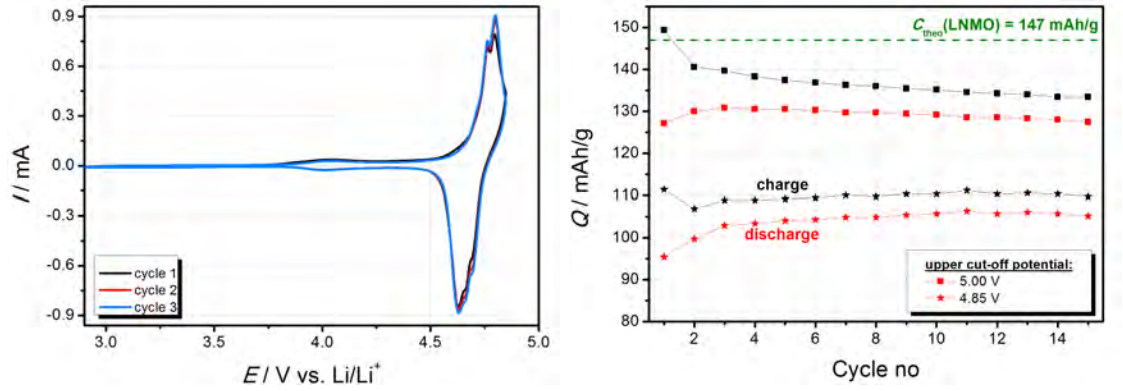

Fig. 4.8.: *CV of a LNMO half cell, setting the upper cut-off potential to* 4.85 V *on the left together with a comparison of the capacity and fading using different higher voltage limits on the right. All measurements were recorded with a scan rate of* 0.1 mV/s *at room temperature and as electrolyte LP30 was used.*

Comparison of the differential capacity calculated from cc cycling data, with CV measurements, which is depicted in figure 4.9, clearly shows the different measurement modes underlying these techniques. Whereas for cc cycling the current increases by lowering the

cycling rate, the opposite holds for the CV measurement, so that with increasing scan speed the peak current also increases. This difference occurs since during cc measurements the potential is only raised if it is insufficient to maintain the selected current, i.e. the active species are depleted in the accessible region. By lowering the current, there is more time for the lithium ions to diffuse in deeper electrode areas, the redox reactions also can take part in these regions and the electrode material could be accessed more completely. During CV measurements the current is higher the smaller the diffusion layer and the fluxes are thus greater, as already stated in chapter 2.5.1. As expected from theory, the peak-to-peak separation ΔE_{pp} increases with cycling speed for cc cycling as well as in CV investigations. Although the scan rate in the latter experiment was even for the fastest measurement lower than during the chronopotentiometry experiment at 1 C, ΔE_{pp} is greater, i.e. there are higher diffusion overpotentials. Thus, the diffusion overpotentials during CV experiments are higher in comparison to cc measurements.

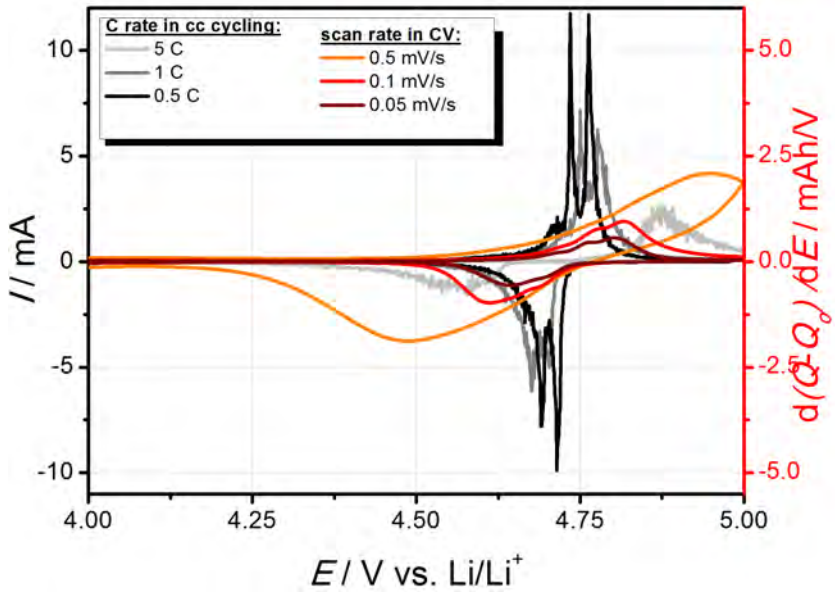

Fig. 4.9.: *Comparison of the current recorded in CV measurements with the differential capacity calculated from cc cycling experiments of the same LNMO half cell at different scan and cycling rates, respectively. The experiments were performed at room temperature, using LP30 as electrolyte. For better visibility, different scaling of the y-axes was used to represent CV and cc data.*

Regarding figure 4.10 is obvious, that the capacity Q of the material is lower than the theoretical value of 147 mAh/g for LNMO, which shows that not the whole material takes part due to kinetic limitations in the electrochemical reaction. This is further confirmed by comparison of the capacity at different scan rates for one cell, also shown in this figure. By lowering the cycling speed the capacity increases, since at lower rates the active species

have more time to diffuse into the electrode particles, so that a more complete access of the cathode takes place. Since the weight of the electrode material as well as that of the current collector vary slightly from one cell to another, the capacity values could however slightly deviate from the reported values.

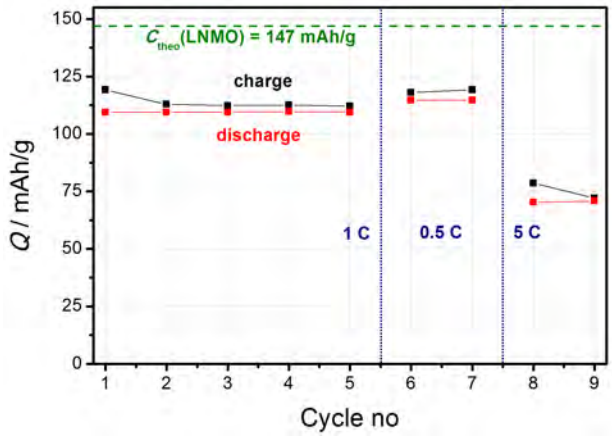

Fig. 4.10.: *cc cycling of a LNMO half cell using LP30 as electrolyte at different C rates of* $0.5 - 5\,\mathrm{C}$ *at room temperature.*

The lithium diffusion coefficient D_{Li} was estimated using equation 2.22 on page 36 for reversible systems. In principle, multiple electron transfer has to be taken into account, resulting in the following equation, where n is the number of electrons transferred:[202]

$$i_p = 0.446 n^{3/2} F A [\mathrm{Li}]_{bulk} \sqrt{\frac{F D_{Li} \nu}{RT}} \tag{4.1}$$

However, assuming that during each peak in CV measurements of LNMO just one electron is transferred, n is set to one. i_p was extracted from the second cycle during CV measurements as exemplarily depicted for one oxidation peak in figure 4.11. The baseline was determined by linear extrapolation of the current gradient at the bottom of the peak. The resulting equation is given in the figure. The second cycle was used for determination of the lithium diffusion coefficient to prevent impact of the CEI formation primarily taking place during the first cycle as well as of cell fading becoming severe in later cycles, which could influence the lithium diffusivity by loss of active lithium. T was set to room temperature of 298 K, the scan rate ν of the experiment was 0.1 mV/s and area A was calculated as $1.31\,\mathrm{cm}^2$. Lithium ion concentration $[\mathrm{Li}]_{bulk}$ in the electrode bulk was estimated to $4.84 \cdot 10^{-3}\,\mathrm{mol/cm}^3$ using the molar mass of LNMO of 182.69 g/mol and the volume of electrode. The volume was calculated using the mass of the electrode, reduced by the amount of binder and conductive carbon, and its volume, which was

estimated using the average height of a dried technical electrode together with its area A. D_{Li} was calculated for the four peaks appearing in the high voltage range related to nickel redox activity during cycling of LNMO electrodes, two during its oxidation and the other two during its reduction. The results are given in table 4.3. The two peaks caused by oxidation and reduction of manganese were not taken into account. They are rather shallow, thus complicating the determination of i_p, and small deviation from the exact baseline would have large impact on this rather low value. Nevertheless, the values are in good agreement, showing an average value of $2 \cdot 10^{-9}\,\mathrm{cm^2/s}$, which is well reproducible using other LNMO half cells. It is also in accordance with those reported in the literature of $10^{-11} - 10^{-9}\,\mathrm{cm^2/s}$.[55–57] The observed value represents an upper limit, since in equation 4.1 area A is estimated using geometric parameters of the electrode, thus assuming zero porosity. The actual surface area is thus distinctly larger, which in turn lowers D_{Li}. A rough estimation of the real surface of the electrode using an average grain size of 6 µm, assuming spherical particles and zero porosity results in a approx. 60 % higher surface area. Estimation of the porosity is virtually impossible, since only the crystallographic density of LNMO, but no density for the composite electrode is reported. Comparison of the crytallographic density of $4.45\,\mathrm{g/cm^3}$ with the value calculated from mass and size of a technical electrode results in a very high porosity of approx. 75 %. Technical electrodes used in commercial batteries show a porosity of about 30 %.[2] Since these are compacted by calenders, the value for the own, uncompacted electrodes appears reasonable. The actual surface area is in consequence approx. seven times higher than the geometric area and D_{Li} reduces to $3.83 \cdot 10^{-11}\,\mathrm{cm^2/s}$. However, this value is still in the range reported in literature for technical LNMO electrodes.

Tab. 4.3.: *Effective lithium diffusion coefficient in technical LNMO electrodes calculated using equation 4.1. The numbers name the peaks depicted in figure 4.11.*

peak no in CV	$\mathbf{D_{Li}}$ **/** $\mathbf{cm^2/s}$
ox_1	$1.55 \cdot 10^{-9}$
ox_2	$2.37 \cdot 10^{-9}$
red_1	$1.56 \cdot 10^{-9}$
red_2	$2.54 \cdot 10^{-9}$

PEIS studies were performed on LNMO technical as well as on thin film electrodes, but are not shown here. They deliver besides confirmation of the studies already reported in literature, no further information about the electrode material or the CEI formation. As also stated in literature, study of the decomposition film formed on the electrodes is in principle possible by this technique.[55,168] The problem is, that always the impedance

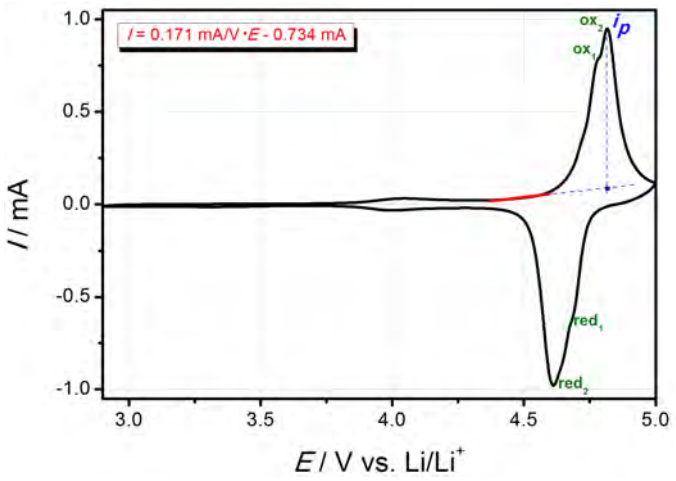

Fig. 4.11.: *Second cycle in CV measurements of a LNMO half cell together with the linear extrapolation of the current gradient at the bottom of the oxidation peak for determination of the baseline and the corresponding equation as well as the resulting peak current i_p. The measurement was performed at room temperature with a scan rate of* 0.1 mV/s *using LP30 as electrolyte. The numbers in the graph are used to name the peaks in table 4.3 for determination of* D_{Li}.

of the whole cell is measured. Thus, that part of the impedance spectra coming from the surface films will be an overlay of contributions from the SEI formed on the anode as well as from the CEI on the cathode, if the time constants of both surface films, i.e. their characteristics, are comparable. In consequence it is unclear, whether the increase in impedance of LNMO half cells measured in own investigations already during its storage points to film formation on both electrodes or only on the lithium anode. For this electrode, SEI formation starts instantaneously upon contact between the electrolyte and the active material.[5,157]

In conclusion, the self-prepared LNMO material works in the expected way and, as can be seen in figure 4.12, constant-current cycling over 300 cycles is in principle possible. However, distinct capacity fading with increasing cycle number is observed so that only approx. one third of the initial capacity could be cycled at the end of this extended experiment. In the literature also high capacity fading is reported. For instance Wang et al. reported that their LNMO cells could release after 500 cycles only approx. 60 % of their initial capacity.[80] Also the amount of binder is too high to compete with optimized cells. Optimization is e.g. possible by longer and more homogeneous stirring to even better mix the active particles with the binder as well as modified, possibly slower drying. The use of a calender that compacts the material by rolling over the prepared electrode sheet, thus intensifying the contact between the electrode particles as well as between the electrode layer and the current collector also could improve the cell performance. As

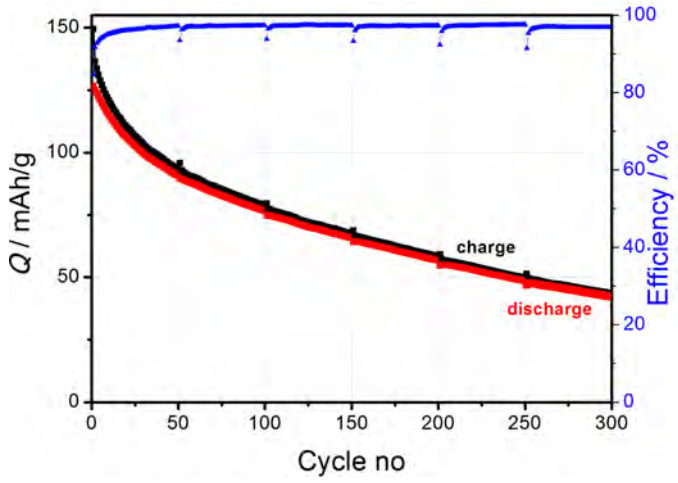

Fig. 4.12.: *Charge and discharge capacities of a LNMO half cell recorded at* 0.5 C *over 300 cycles and room temperature, using LP30 as electrolyte. The coulomb efficiencies are also presented. The small discontinuities occurring every 50th cycle result from interruption of the cycling process to perform other experiments.*

the technical electrodes used in this thesis were only fabricated for fundamental studies in which the volumetric density of the active material is not a key factor, the amount of binder needed not to be optimized. Severe capacity fading was also reported in the literature.[17,27,67,74,85,175] The self-prepared powder shows satisfying performance for the use as precursor for thin film preparation as well as for investigations concerning the CEI formation.

4.5. Target preparation

For PLD pellets, about 0.6 cm in height and $1.0 - 2.5$ cm in diameter were prepared. Wider diameters are beneficial since the same area is less often irradiated during one deposition step, so that segregation within the target is suppressed and the target is consumed more slowly. Using an uniaxial press with a force of approx. 30 kN the powder was firstly compacted in a pressing tool with an inner diameter of 2.5 cm for several hours. For even better densification the formed cylinder was secondly isostatically pressed without mold for about 30 min at a pressure of 2000 bar. The target was afterwards sintered for 2 h at 800 °C in air. This caused a distinct shrinkage, so that the diameter reduced from 2.5 to only about $2.0 - 2.1$ cm.

To study possible segregation or preferred sputtering of the components contained in the LNMO target, its composition was investigated after several PLD depositions by ICP-OES at KIT. Therefore, some material was scratched off that part of the surface, that had been

exposed to the laser spot. The resulting atomic fractions and the corresponding elemental ratio based on standardization to the nickel content is depicted in table 4.4. The results again reveal good agreement with the original composition of $Li_{1.05}Ni_{0.5}Mn_{1.5}O_4$. The light element lithium shows - as expected - a small depletion due to wide spreading by the laser light. The loss of oxygen is even more severe, again presumably caused by spreading together with the low oxygen partial pressure in the atmosphere of the analysis chamber, causing its partial removal from the lattice. Some oxygen depletion could exist already after the sintering step. It was performed at 800 °C and thus in the temperature regime where oxygen, as already reported in chapter 2.2.2, is released from the spinel lattice. However, its deficiency is overcome to a large extent by reoxidation of the thin film during air exposure. Interesting is the loss of manganese, which is only slightly lighter than nickel, so that enhanced depletion due to impact of the laser light is rather questionable. Segregation effects are more likely. However, the ICP-OES results presented so far are normalized based on the nickel content, assuming negligible variations in content of this species, which not necessarily holds. However, normalization on other elements contained in LNMO delivered even greater deviance from the desired ratio. Repeated laser irradiation results - independent of the normalization - in a small depletion of manganese and oxygen, while nickel is slightly enriched at the target surface. ICP-OES analysis on the same target material performed at the Schunk Kohlenstofftechnik GmbH in Heuchelheim revealed a slightly different atomic ratio, but with the same trends observed in comparison with the powder investigation. Thus, manganese is again enriched, while the deficiency in lithium and oxygen is even more severe. The occurrence of the same trends by comparison of the results measured at KIT with that of the Schunk Kohlenstofftechnik GmbH supports the assumption that different dissolution techniques are the reason for the diverging results.

Tab. 4.4.: *ICP-OES results of the LNMO target surface after several PLD depositions measured at KIT. The calculated ratio based on standardization on the nickel content.*

element	**atomic percent**	**elemental ratio**
lithium	15.7	1.02
nickel	7.7	0.50
manganese	21.6	1.40
oxygen	55.0	3.57

In conclusion, prolonged irradiation by the laser light changes the composition of the LNMO target only to a small extent, so that even repeated usage should not significantly alter the composition of the thin films.

5. LNMO model electrodes - preparation and general electrochemical investigation

This chapter deals with the optimization of LNMO thin film cathodes deposited via PLD. These electrodes were specifically optimized to reproduce the electrochemical behavior of technical electrodes while showing a surface as smooth as possible. The search for suitable substrates that fulfill all demands regarding the deposition of smooth thin films that operate in the high voltage regime is also discussed, as well as the cell assembly used for characterization of LNMO thin film electrodes.

5.1. The choice of suitable substrates - roughness vs. electrolyte reactivity

LNMO thin films were deposited on platinum covered YSZ single crystals. Thus, the substrate was no commonly used material system employed for either technical or thin film cathodes in the LiB. Here, often either aluminum or stainless steel foils as well as silicon wafers are used. The Pt/YSZ material combination was selected for two reasons: Firstly, for preparation of thin films with sufficiently smooth surfaces, the roughness of the substrate should be as low as possible. Secondly, the employed substrate should itself not exhibit any electrochemical activity in the investigated voltage range, i.e. at approx. $2.5 - 5.0\,\mathrm{V}$ vs. $\mathrm{Li/Li^+}$ for LNMO to avoid any superposition of the electrochemical response of the substrate with that of the cathode material. The roughness of several materials being commonly employed as current collector is given in figure 5.1, as determined by profilometer (Alpha Step IQ). Calculation of the mean roughness was performed after norm DIN Iso 4287.[203] In the literature often either the arithmetic mean roughness R_a or the squared mean roughness R_q is reported, and both values were calculated and compared. R_a does not allow to distinguish between tips and scratches as well as between different profile forms. A profile with very small, but deep scratches can show approx. the same R_a value like one with distinct smaller roughness, if the net divergence from the baseline is the same.[203] R_q represents the root mean square deviation of the profilometer data and is thus statistically more representative than R_a.[204] R_a and R_q are calculated

according to equation 5.1, where $z(x)$ is the profile function within a single measurement step l_r:[204]

$$R_a = \frac{1}{l_r}\int_0^{l_r} |z(x)|\,dx$$
$$R_q = \sqrt{\frac{1}{l_r}\int_0^{l_r} |z^2(x)|\,dx} \tag{5.1}$$

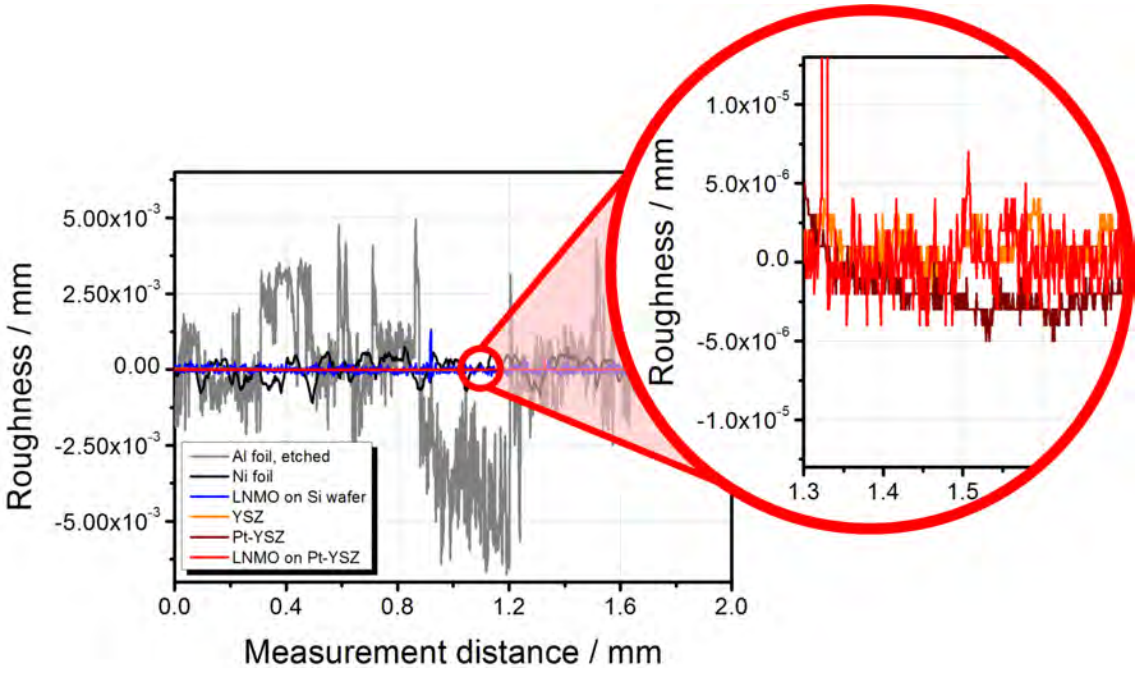

Fig. 5.1.: *Roughness of several materials being commonly used as current collector in the LiB measured with a profilometer. To gain more representative data, a line of* 2 mm *was analyzed for each sample.*

Among them, the etched aluminum foil, the mainly employed current collector for technical cathodes, clearly shows the highest roughness. It is, as obvious from table 5.1, approx. three orders of magnitude higher than that of YSZ single crystals. This is beneficial for the doctor blade process, since the electrode slurry sticks better to the current collector and does not peel off both during solvent evaporation as well as during cycling going along with distinct volume changes. Its high roughness is on the other hand detrimental if the preparation of smooth thin film electrodes is desired, since the surface profile of the substrate sustains also in the deposited layer. The deposited material can, however, fill to some extent the scratches due to residual kinetic energy of the deposited species on the substrate, since reduction of the surface area is energetically favorable. Thereby, the roughness of the prepared sample is lowered. However, this is only possible in a very

restricted range. In consequence, a large initial substrate roughness disables the preparation of thin film electrodes with a low surface roughness in the range of a few nanometers. The accumulation of matter in substrate scratches results in local variation of the film thickness, so that films with poor thickness homogeneity can be prepared. Another disadvantage of aluminum substrates is their low melting point of 660.1 °C.[205] For deposition of electrochemical active LNMO thin films are temperatures of at least 600 °C needed, thus being close to or even higher than the melting point of this material. In consequence, LNMO deposition onto aluminum substrates had to be precluded.

Tab. 5.1.: *Roughness of several materials being commonly employed as current collector, measured by a profilometer, using either R_a or R_q for calculation of the mean roughness. Pt and LNMO on top of the substrates were both deposited by PLD.*

current collector material	R_a / 10^{-3} mm	R_q / 10^{-3} mm
Al foil etched	1.60	2.15
nickel foil	$3.01 \cdot 10^{-1}$	$3.63 \cdot 10^{-1}$
silicon wafer (with LNMO thin film)	$6.51 \cdot 10^{-2}$	$9.35 \cdot 10^{-2}$
YSZ	$5.60 \cdot 10^{-3}$	$8.75 \cdot 10^{-3}$
Pt on YSZ	$2.80 \cdot 10^{-3}$	$3.84 \cdot 10^{-3}$
LNMO on Pt-YSZ	$3.24 \cdot 10^{-3}$	$1.21 \cdot 10^{-2}$

The roughness of the nickel foil and silicon wafers are in the order of hundred and ten nanometers, respectively, and thus still too high for deposition of sufficiently flat thin films. In contrast to this, YSZ single crystals exhibit a roughness of less than ten nanometers, which does not significantly increase by PLD deposition of platinum or LNMO thin films. Due to their deposition the roughness partially even further reduces due to filling of small cavities. The difference between R_a and R_q is obvious from table 5.1. There is no consistent trend, since for one sample one value is higher and for another the other one. This is presumably caused by varying roughness profiles of the samples, which are differently weighted in the two calculations. However, the order of magnitude agrees in both methods.

Investigation of the electrochemical activity in the voltage range used for cycling of LNMO electrodes of commonly employed current collectors together with that of Pt on YSZ single crystals is depicted in figure 5.2. For evaluation of their electrochemical response half cells using Swagelok cell housings with the pure substrates as working electrode, lithium foil as anode and the same amounts of the electrolyte like in common LNMO T-cells reported in chapter 4.3 were used. Nickel foil shows a very high irreversible capacity at about 4.5 V and thus in the range, where the main redox activity of LNMO takes place. This in consequence precludes this metal foil as current collector for this cathode mate-

rial. If the thin films are either not completely dense or if the electrolyte flows around the cathode to the backside of the foil, where no deposition of the electrode material took place, the current coming from the substrate would completely bury the response coming from the cathode. The measured currents rather result from electrolyte oxidation than from lithium deintercalation from the material. In the latter case the reaction should be at least to some extend reversible, so that leastwise small cathodic currents should flow.

Copper foil also shows distinct electrochemical activity in this voltage range. Despite the fact that the resulting current is about two orders of magnitude lower than that of the nickel foil, its magnitude is still in the range achieved with the LNMO thin films, so that a superposition of the response coming from cathode material with that of the current collector will affect the electrochemical response of the thin film electrode to a large extent. In consequence, this material is also not suitable as current collector for cathode materials, but is commonly used on the anode side of the LiB, since it shows no electrochemical reactions in the low voltage range of less than 1.0 V vs. Li/Li^+. In contrast, aluminum foil shows no electrochemical activity in the whole voltage range used for cycling of LNMO half cells, but a minor one in the low voltage range, thus being a suitable current collector for cathodes. As mentioned earlier in this section, its low melting point nevertheless also excludes this material for application in LNMO thin film electrodes.

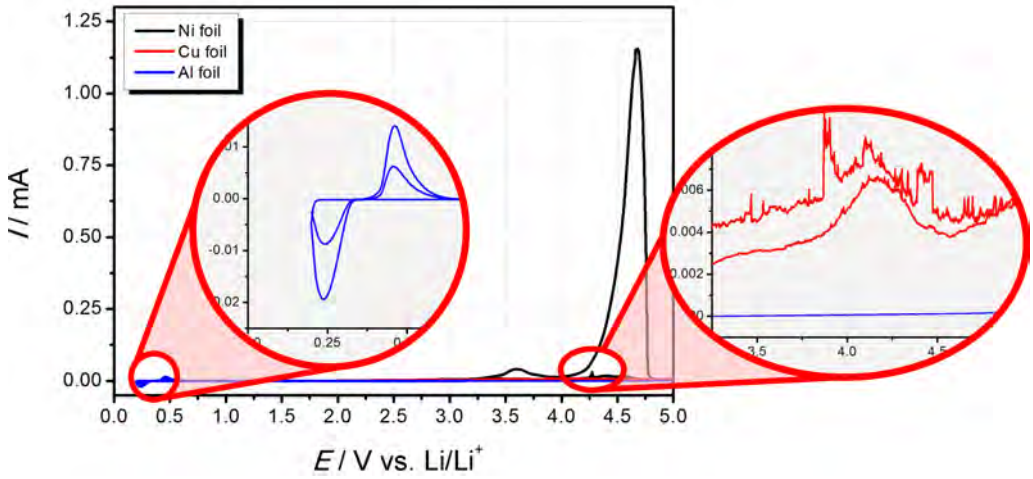

Fig. 5.2.: *CV of half cells employing different metal foils commonly used as current collectors as working electrode using LP30 as electrolyte. The scan rate was set to* 0.1 mV/s *at room temperature.*

Myung et al. also reported reactions between HF, formed by the decomposition of the electrolyte salt in the presence of water, with metal current collectors.[172] They corrode, also they are in principle passivated in alkyl carbonate solutions containing $LiPF_6$ salt

by decomposition products of the solvent molecules. For aluminum, there is down to 0.3 V vs. Li/Li^+ no reaction like the formation of SEI or Li_2O on its surface. Close to 0 V vs. Li/Li^+ Li-Al alloying occurs, being induced by the deposition of dissolved Al^{3+} from the air-formed surface layer on the Al foil.[172] Nickel is stable up to 4.5 V, after which its dissolution begins. Copper current collectors show a large cathodic peak at $1.5 - 3.0$ V, corresponding to the reduction of air-formed copper oxide to metal, reduction of the electrolyte solvent and surface film formation. At 3.6 V in addition oxidation and dissolution of Cu into the electrolyte occurs.[172]

Fortunately the substrate with the lowest roughness, namely Pt on YSZ single crystal, shows only minor electrochemical activity in the high voltage range of about 4.5 V, as depicted in figure 5.3. These results are in accordance with investigations by Wang et al., who found negligible reactivity in this voltage region.[147] The irreversible capacity further reduces after the first cycle, so that afterwards only the unavoidable electrolyte oxidation close to 5.0 V is visible. Thus, possibly protecting surface layers form on Pt during the first charge. The current is lower than or at least in the range of that gained with LNMO thin film electrodes. A possible superposition has thus only minor influence on the signal coming from the cathode material. Since the current at about 5.0 V decreases to nearly zero for the LNMO electrode on Pt-YSZ, it is assumed that the thin film is dense, so that no reaction between the current collector and the electrolyte can take place. Since this film as well as the electrode layer are both deposited only on the surface of the single crystal, which is in contact with the electrolyte, possible diffusion of some electrolyte to its backside should not be severe, because no reactivity between it and YSZ is expected. YSZ is insulating for both electrodes and lithium ions. The current collector leading from the cathode out of the cell is placed on top of the LNMO thin film. Thus, on the backside of the YSZ substrate no reactions can take place.

In conclusion, platinum coated YSZ single crystals turned out as suitable substrates for LNMO thin films regarding the electrochemical stability in the voltage region of interest for this cathode material as well as the surface roughness and temperature stability.

5.2. PLD preparation of LNMO electrodes

LNMO thin films were prepared by pulsed laser deposition using a PLD chamber (PLD surface) equipped with a 248 nm KrF excimer laser (COHERENT) onto with 8 mol% Y_2O_3 doped ZrO_2 (111) oriented single crystals (CrysTec, Germany), 1x1 cm^2 in size and 0.5 mm in thickness. Prior to LNMO deposition, they were covered with platinum as current collector, since the substrate itself is an insulator. The PLD is equipped with a platinum resistance heater as well as an IR laser heater. Both were used during deposition

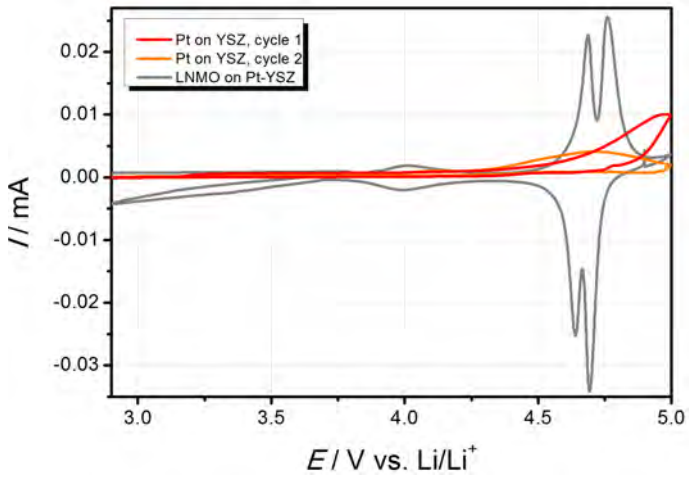

Fig. 5.3.: *CV of a half cell employing a platinum covered YSZ single crystal as working electrode. As electrolyte LP30 was used and the scan rate was set to* 0.1 mV/s *at room temperature. For comparison a CV of a LNMO thin film half cell, using Pt-YSZ as substrate, using the same electrolyte and measurement conditions is also depicted.*
The PLD deposition parameters of the LNMO and Pt thin films are 5000 p*ulses at a laser frequency and fluence of* 5 Hz *and* 3.0 J/cm^2*, respectively, at* 800 °C *in oxygen atmosphere of* 5 Pa *and a target-substrate distance of* 40 mm *for the electrode layer and* 10000 p*ulses at a laser frequency and fluence of* 10 Hz *and* 4.0 J/cm^2*, respectively, at* 400 °C *in argon atmosphere of* 0.3 Pa *and a target-substrate distance of* 40 mm *for the current collector.*

of LNMO thin films, but the latter one delivered better results during depositions at higher temperatures at least for this material, which will be discussed later in this chapter.

5.2.1. Deposition of Pt current collector thin films

The platinum layer, serving as current collector to guarantee homogeneous current distribution in the whole cathode film, was deposited by PLD at relatively low temperature of 400 °C in argon atmosphere of 0.3 Pa. 10000 pulses at a laser frequency and fluence of 10 Hz and 4.0 J/cm^2, respectively, at a target-substrate distance of 40 mm were employed and resulted in a thickness of the current collector of approx. 30 nm as is obvious from the transmission electron microscopy (TEM) image depicted in figure 5.8 below in this chapter. The image was recorded by Dr. F. Berkemeier at the Institute for Material physics at the Westfälische Wilhelms University in Münster. However, since by PLD only very small areas could be homogeneously covered, there exists a thickness gradient from inner to outer sample regions even for these rather small substrates. Thus, the thickness extracted from the TEM image only delivers a rough estimation. Whether the slice cut out for TEM analysis was taken from an inner or an outer area of the electrode, there should be also thinner and thicker parts of the platinum film.

Although the deposition temperature of the platinum current collector was relatively low, no subsequent annealing step was performed to smoothen its surface. The benefit thus gained runs the risk of partial dewetting occurring for this material if being deposited on YSZ single crystals at temperatures of more than about 750 °C. The annealing step thus rather increases the roughness of the current collector thin film and moreover results in incomplete coverage of the substrate. In consequence, the LNMO thin film deposited on top of it is in contact with the Pt film as well as with the bare substrate with their drastically varying electronic conductivity. During electrochemical experiments the cathode is thus presumably rather inhomogeneously accessed with drastically diverging current densities. As a result, this complicates the CEI investigation, since it rather forms in better contacted regions, where the current density should be highest. These regions moreover could lead to failure of the whole cell, since locally high currents promote the formation of lithium dendrites growing from the anode through the separator and finally end up at the cathode surface, thus short-circuiting the cell.

5.2.2. Optimization of LNMO deposition parameters

For PLD deposition of LNMO thin films temperature and oxygen partial pressure $p(O_2)$ are the most important parameters to be adjusted during process optimization.[29,142,146] According to Xia et al. formed below 600 °C no dense, but only flake-like, relatively uneven films. Higher oxygen partial pressures on the one hand reduce the oxygen deficit in the spinel structure. They on the other hand boosts particle formation, since heat dissipation is increased by higher concentration of gas particles, thereby reducing the kinetic energy of the deposited species on the substrate.[29] Lithium deficit occurs at too low background pressures - below 10 Pa in the case of $LiMn_2O_4$ spinel thin films - due to evaporation of lithium oxide from the growing film.[199] Based on these results optimization of the own LNMO thin films was attempted to reproduce the electrochemical behavior of technical electrodes while being as smooth as possible. Besides temperature and oxygen pressure the laser fluence and frequency, the number of pulses and the distance between target and substrate were optimized together. An overview of the adjusted parameters and the range, in which each of them was varied during optimization of the PLD process for deposition of LNMO thin films is given in table 5.2.

Tab. 5.2.: *Adjusted parameters and the range, in which each of them was varied during optimization of the PLD process of LNMO thin films. Distance denotes the distance from target to substrate.*

temperature	$p(O_2)$	fluence	frequency	distance	number of pulses
400 – 1100 °C	5 – 50 Pa	2.3 – 3.5 J/cm^2	5 – 10 Hz	40 – 45 mm	1000 - 5000

Distance between target and substrate; laser frequency and fluence

If the IR laser heater is used in the PLD chamber the lower limit of the distance between target and substrate is 40 mm and no further reduction is possible. Shorter distances are only possible by using the platinum resistance heater. However, this reduced the crystallinity of the thin films and those deposited at higher temperatures were surprisingly electrochemically inactive. This might be caused by the comparably thick sample holder and the resulting inhomogeneous temperature profile. The IR heater allows the use of thin substrate holders with better temperature distribution.

Both the variation of the target-substrate distance and the laser frequency showed only little influence on the film appearance. However, by increasing the laser frequency from 5 to 10 Hz the films show a nearly doubled roughness. The laser fluence had greater influence on the film structure. Best results were gained with an intermediate value of $3.0 - 3.1\,\mathrm{J/cm^2}$. With lower fluence the cubic phase did not form, whereas with higher fluence a more open and rough structure developed. This results presumably from several crystalline regions that grow further during ongoing material deposition. If they encounter each other, small cavities form, since the kinetic energy of the species is insufficient to rearrange larger amounts of material for surface reduction to end up at a relatively smooth surface. The different film morphologies depend on parameters like surface and interface free energies of the substrate and the material to be deposited, lattice mismatch strain between it and the substrate, surface diffusivity, growth rate and layer thickness.[206] In dependence of these values between three different growth regimes can be differentiated concerning epitaxial film growth: Volmer-Weber, Frank-Van-der-Merwe and Stranski-Krastanov growth. Frank-Van-der-Merwe growth is characterized by the nucleation of a new monolayer and its growth to cover the whole substrate, after which nucleation of the next layer starts, i.e. layer-by-layer growth, which results in flat films.[206] Volmer-Weber growth involves the formation of isolated islands on the substrate and their subsequent growth and coalescence. It thus results in a rougher surface. The Stranski-Krastanov growth starts with layer-by-layer growth, but becomes three-dimensional after a certain layer thickness is reached.[206] Defining γ_f and γ_s as the surface energies of the epitaxial layer as well as of the substrate and γ_i as the interface free energy for the film-substrate interface, then $\delta\gamma = \gamma_f + \gamma_s - \gamma_i$ is a measure, which growth mode is observed. If $\delta\gamma < 0$, two-dimensional growth will be the prevalent mechanism, whereas for $\delta\gamma > 0$ a three-dimensional growth will mainly be observed. If the lattice mismatch is small, Frank-Van-der-Merwe growth will be prevalent, while for large mismatch Volmer-Weber growth will occur. An intermediate mismatch will result in Stranski-Krastanov growth.[206] Care has to be taken, that the mismatch between film material and substrate cannot simply be determined by comparison of their lattice parameters. Rotation of the film lattice with respect to the substrate lattice might

result in better congruence. The same holds if one lattice is a multiple of the other, like for example in the Pt-YSZ system. Platinum has with 3.92 Å a distinctly smaller lattice constant as YSZ with 5.15 Å.[207] Epitaxial growth of Pt thin films onto YSZ(111) is nevertheless possible. The lattice constant of YSZ is 3/4 times larger than the lattice constant of platinum, i.e. from every third atom column in the YSZ substrate emerge two columns in the Pt film, with only a small misfit of 1.8 %.[207] For the LNMO thin films studied here the occurrence of small cavities points to three-dimensional, i.e. Volmer-Weber or Stranski-Krastanov growth.

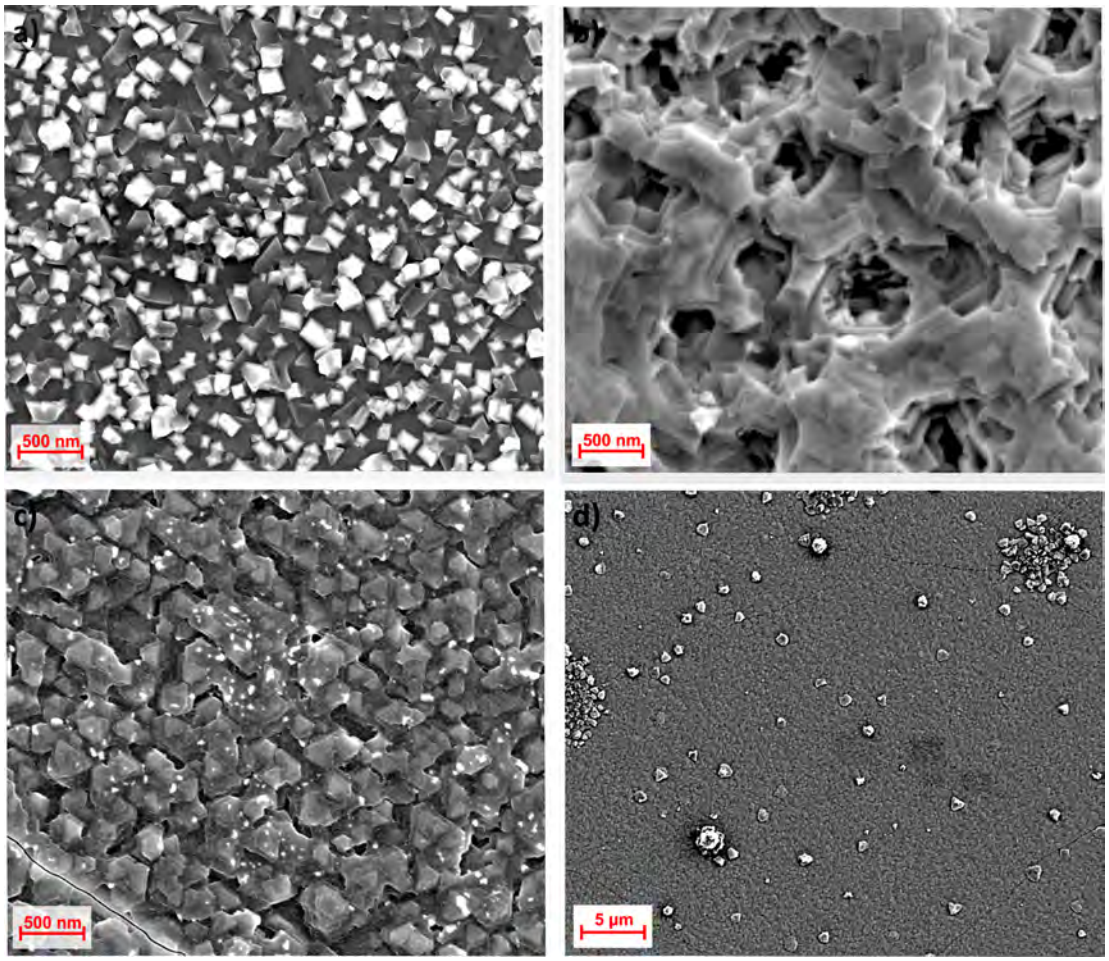

Fig. 5.4.: *SEM images of LNMO thin films deposited by PLD on Pt-YSZ at different oxygen partial pressures of a)* 5 Pa*, b)* 20 Pa *and c)* 50 Pa*; d) offers a wider overview of the film prepared at* 50 Pa*, thus showing the relatively large number of particles on its surface. Besides the oxygen partial pressure all other parameters during the PLD deposition of LNMO were kept constant. The employed deposition parameters are* 5000 p*ulses at a laser frequency and fluence of* 5 Hz *and* 2.3 J/cm^2*, respectively, at* 750 °C *and a target-substrate distance of* 40 mm*. For PLD deposition of Pt current collector films* 10000 p*ulses at a laser frequency and fluence of* 10 Hz *and* 4.0 J/cm^2*, respectively, at* 400 °C *in argon atmosphere of* 0.3 Pa *and a target-substrate distance of* 40 mm *were employed.*

Oxygen partial pressure

Variation of the oxygen partial pressure has, as already stated by Xia et al., a more obvious influence on the film texture, which is depicted in figure 5.4. The lowest one of 5 Pa resulted in the best crystallinity, so that a relatively dense structure with only small holes forms, whereas at intermediate pressures small disconnected crystals formed. At still higher pressures the crystallinity is even more reduced and there is a clear enhancement of undesired particle formation, which is in accordance with results reported by Xia et al.[29] These agglomerations presumably result from the low kinetic energy of the deposited species, caused by more heat dissipation by higher concentration of gas particles. Even partial cracking of the film was detected at higher oxygen partial pressures. Lower pressures than 5 Pa were not investigated to minimize lithium and oxygen sub-stoichiometry in the film with the risk of impurity phases, as reported by Dumont et al.[199]

Substrate temperature and number of pulses

The deposition of electrochemically active LNMO thin films is, in accordance with the results by Xia et al., only possible at temperatures of more than 600 °C.[29] Whereas for lower temperatures of about $600 - 700\,^{\circ}\mathrm{C}$ the crystallites are rather random shaped and oriented, there is a clear development of the cubic phase at higher temperatures, as can be seen in figure 5.5. Usage of even higher temperatures together with the other optimized PLD parameters result in the growth of these domains and at points, where several different oriented ones come together, small cavities form. The films are therefore not ideally flat and show a roughness in the range of 50 nm. Thus, in principle even higher temperatures are needed to provide sufficient kinetic energy for further rearrangement of the deposited species. A temperature increase further than 800 °C, however, results in a partial detachment of the film together with a significant roughness increase in some film areas. This phenomenon could be caused e.g. by different lattice parameters or varying thermal expansion coefficients between substrate and thin film, which result in distinct stress. Thermal expansion coefficients are not available for the cathode material, but for other spinels values of $9 \cdot 10^{-6}\,\mathrm{K}^{-1}$ were reported.[208] These are about $11 - 21\,\%$ lower than the value of $10.1 \cdot 10^{-6}\,\mathrm{K}$ reported for YSZ.[209] This difference thus indeed could be responsible for the partial detachement. There is no report on epitaxial growth of LNMO on Pt. The lattice parameters of LNMO is with 8.1724 Å approx. twice as large as the value of Pt (3.92 Å), resulting in a misfit of 4.2 %.[60,207] This difference in lattice parameters could be overcome for epitaxial layers in the first few monolayers of the deposited material by widening of its lattice parameters, which subsequently reduces in later layers, until the actual distances of the film material are reached. This however results

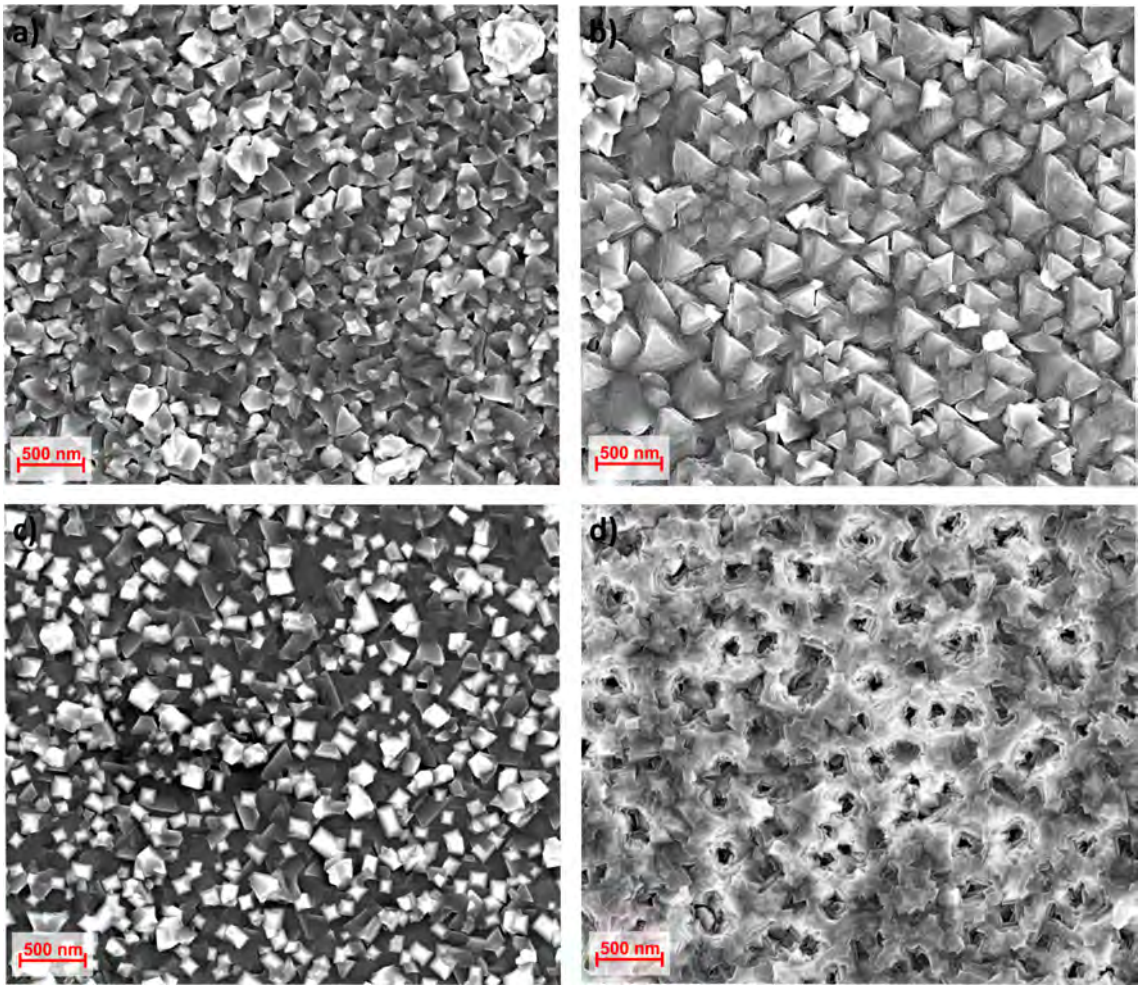

Fig. 5.5.: *SEM images of LNMO thin films deposited by PLD on Pt-YSZ at temperatures of a)* 600 °C, *b)* 700 °C, *c)* 750 °C *and d)* 800 °C. *Besides the temperature all other parameters during the PLD deposition of LNMO were kept constant for images a) - c). Only for d) optimized parameters, written in italic behind the respective standard value if diverging from it, were used. The employed deposition parameters are* 5000 p*ulses at a laser frequency and fluence of* 5 Hz *and* 2.3(*3.0*) J/cm^2, *respectively, at an oxygen pressure of* 20(*5*) Pa *and a target-substrate distance of* 40 mm. *For PLD deposition of Pt current collector films* 10000 p*ulses at a laser frequency and fluence of* 10 Hz *and* 4.0 J/cm^2, *respectively, at* 400 °C *in argon atmosphere of* 0.3 Pa *and a target-substrate distance of* 40 mm *were employed.*

in strains and stresses in the film, possibly even causing in its partial delamination. A detailed investigation of the actual growth of LNMO thin films onto platinum is important to further enlighten thiy system, but beyond the scope of this thesis. However, stresses in the LNMO thin film and in consequence delamination could be by deposition of thinner films. By reduction of the number of pulses and thus the film thickness to 1/5 of the original value, the temperature could be indeed further raised without delamination of

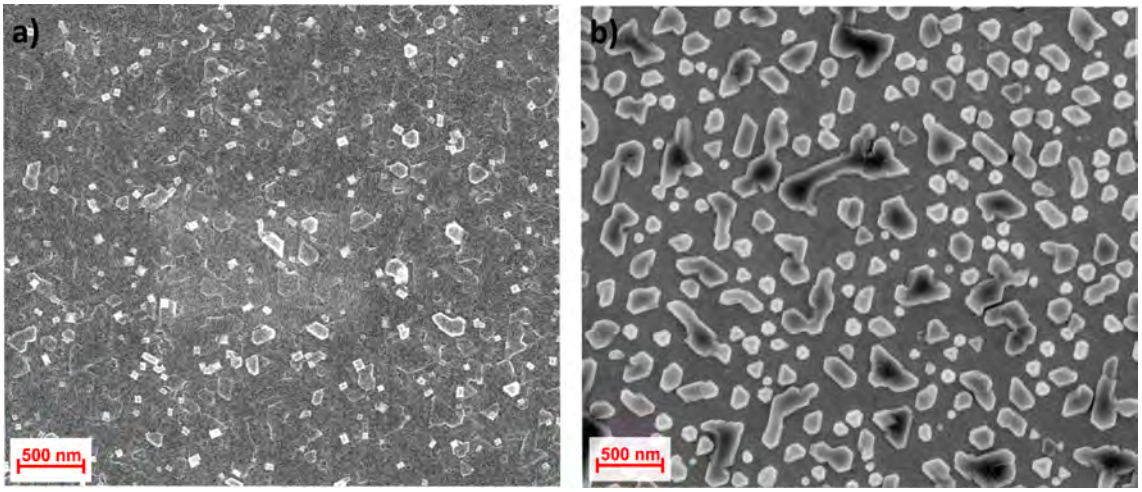

Fig. 5.6.: *SEM images of LNMO thin films deposited by PLD on Pt-YSZ at temperatures of a)* 1000 °C *and b)* 1100 °C. *Besides the temperature all other parameters during the PLD deposition of LNMO were kept constant to guarantee best comparability.*
The employed deposition parameters are 1000 p*ulses at a laser frequency and fluence of* 5 Hz *and* 3.1 J/cm^2*, respectively, at an oxygen pressure of* 5 Pa *and a target-substrate distance of* 40 mm. *For PLD deposition of Pt current collector films* 10000 p*ulses at a laser frequency and fluence of* 10 Hz *and* 4.0 J/cm^2*, respectively, at* 400 °C *in argon atmosphere of* 0.3 Pa *and a target-substrate distance of* 40 mm *were employed.*

the film to 1100 °C. The roughness of the film decreases as expected with further temperature increase from 800 to about 950 – 1000 °C and the small cavities disappear, which is depicted in figure 5.6. Above 1000 °C dewetting of the LNMO thin film occurs. Fang et al. also reported the decomposition of the LNMO spinel phase at this temperature, which is accompanied by structural and morphological degradation.[210] The material thus seems to be unstable at this high temperatures, so that the optimal deposition temperature is around 950 – 1000 °C. The roughness of the deposited films does not significantly vary in this temperature range and seems to be even a bit lower at 950 °C, although the number of small surface crystallites per area is here a bit higher than at 1000 °C. Since low roughness was the main goal during optimization of the PLD parameters for later SIMS measurements, a deposition temperature of 950 °C was used for further thin film preparation. This temperature is also low enough to avoid the risk of dewetting of LNMO.

Optimized PLD parameters

The optimized PLD parameters for deposition of LNMO thin films on Pt-YSZ substrates are summarized in table 5.3. Here also the range in which each parameter was optimized, and its effect are depicted. After optimization a roughnesses of less than 10 nm was reached. From TEM measurements, performed by Dr. F. Berkemeier, a roughness of

only about 6 nm resulted. However, since TEM measurements provide local information, profilometer measurements over a greater region of 2 mm are more representative. Partly values for R_a as low as $3 - 5 \cdot 10^{-6}$ mm are reached and thus, one can consider 10 nm as maximum roughness with the present PLD preparation. A photograph showing the top view of a LNMO thin film electrode is shown in figure 5.7.

Tab. 5.3.: *Optimized parameters for PLD deposition of LNMO thin films on Pt-YSZ. The range, in which the parameter was optimized, and its effect are also depicted.*

parameter	**range**	**effect**	**optimum**
temperature	$400 - 1100\,^{\circ}$C	higher crystallinity and smoother surface with increasing temperature due to higher kinetic energy of the deposited species, thus enabling their diffusion on the substrate, resulting in better oriented films; above 1000 °C dewetting	950 °C
O_2 pressure	5 – 50 Pa	by reduction of the oxygen pressure increased kinetic energy of the deposited particles: less deceleration during flight towards the substrate; lower values bear the risk of impurity phase formation due to significant oxygen loss; best crystallinity at intermediate pressures; at higher values enhanced particle formation	5 Pa
fluence	$2.3 - 3.5\,\mathrm{J/cm^2}$	increased kinetic energy of the deposited species and therefore better crystallinity at higher energies, but favoring local heating of the target during irradiation with the risk of material squirting and droplet formation, resulting in higher roughness	$3.1\,\mathrm{J/cm^2}$
frequency	5 – 10 Hz	roughness increase with higher frequency due to reduced diffusion time of the particles on the substrate surface, so that they are unable to orientate in the from an energetic point of view best position	5 Hz
distance	40 – 45 mm	increase of the distance between target and substrate reduces the kinetic energy of the deposited species due to increased flight time; lower film crystallinity due to reduced energy for diffusion, but prevention of droplet deposition, since the kinetic energy of these comparably rather large particles is insufficient to reach the substrate	40 mm
number of pulses	1000 - 5000	almost linear thickening of the film with increasing number of pulses, resulting in higher and therefore better detectable electrochemical response, but lower tendency for delamination with reduced number of pulses if there is a certain lattice mismatch between substrate and film	1000

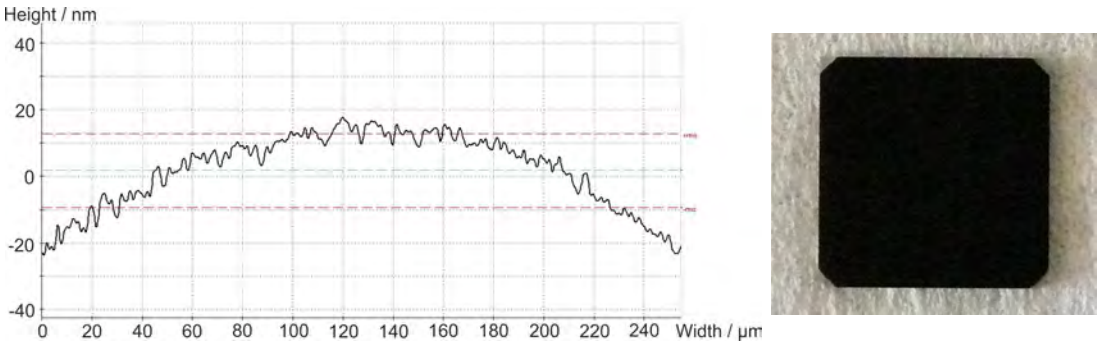

Fig. 5.7.: *Measurement of the surface curvature of a LNMO sample on Pt-YSZ investigated by confocal microscopy on the left together with a photograph showing the top view of a LNMO thin film electrode on the right.*

Due to the directed deposition in the PLD process there are distinct variations in thickness from outer to inner sample regions. Thus, the determination of the thickness of the thin films is not straightforward. This is e.g. obvious from confocal microscopy (PLu neox SENSOFAR 3D Optical Profiler, equipped with software sensoScan 3.2) as depicted in figure 5.7. It shows the surface curvature of a LNMO sample on Pt-YSZ with a height difference of approx. 40 nm measured along an inner sample region of 250 µm and thus over 1/4 of the edge length of the sample. From TEM measurements a thickness of the LNMO layer of $33 - 37$ nm was determined, which is in good accordance with the approx. 40 nm estimated by SIMS depth profiling. Measurement of the sputtered crater was performed either by profilometer or by confocal microscopy. One has to take into account that the crater was sputtered through the whole LNMO as well as through the complete Pt layer and even reached a bit into the YSZ substrate. The correlation between sputter time and measured depth entails thus an averaging of the sputter yields of the three different materials, which not necessarily are comparable. Thus rather hard matter with a low sputter yield is stretched in the depth profile, while soft phases with high sputter yields are seemingly compressed. An image of the SIMS crater investigated by confocal microscopy as well as the SIMS measurement itself is given in figure 5.9. In the depth profile the Pt^-, ZrO^- and YO^- signals, which are used to mark the platinum layer and the YSZ substrate, respectively, show a relatively steep increase over approx. 10 nm. The slightly broadening of the interface region results from the thin film roughness of about 6 nm together with some ion mixing by the sputter gun.

For confirmation that variation of the PLD parameters do not affect the LNMO phase, XRD measurements using either a Siemens D500 or a PANalytical X'PerPRO diffractometer were performed. The resulting diffractogram is depicted exemplarily for one film, deposited using the optimized PLD parameters, in figure 5.10 together with the corre-

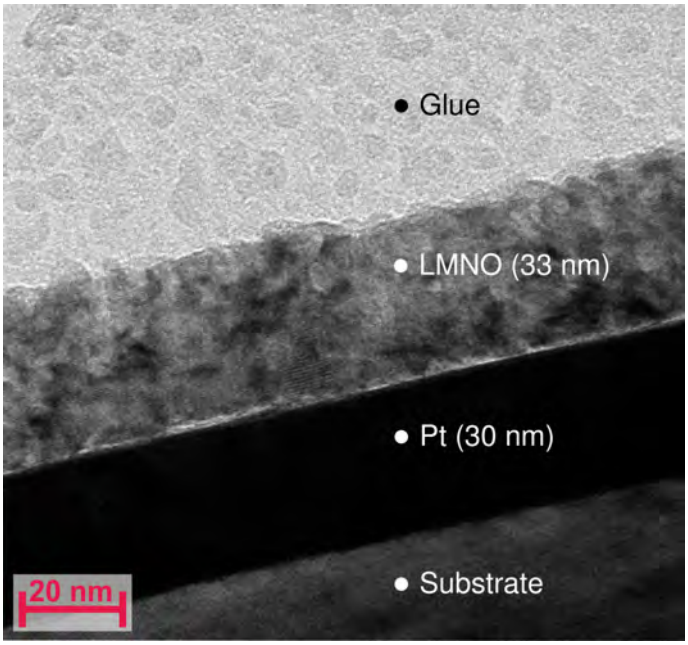

Fig. 5.8.: *TEM of a LNMO thin film electrode deposited by PLD on a platinum covered YSZ single crystal. The employed deposition parameters for the electrode layer are* 1000 p*ulses at a laser frequency and fluence of* 5 Hz *and* 3.1 J/cm^2*, respectively, at* 1000 °C *in oxygen atmosphere of* 5 Pa *and a target-substrate distance of* 40 mm*. For PLD deposition of Pt current collector films* 10000 p*ulses at a laser frequency and fluence of* 10 Hz *and* 4.0 J/cm^2*, respectively, at* 400 °C *in argon atmosphere of* 0.3 Pa *and a target-substrate distance of* 40 mm *were employed. The glue on top of the LNMO layer results from slice preparation prior to TEM measurements.*

sponding hkl indices and the pattern of the pure Pt-YSZ substrate. The most intensive reflexes in the diffraction pattern result from the YSZ single crystal and the Pt current collector thin film. Most reflexes could not be assigned to the cubic Pt structure. According to Prof. G. Beck (University of Augsburg) they might result from tungsten of the filament and K_β radiation. These reflexes are often visible for single crystal samples, since nearly the complete radiation generated by the filament is scattered in high intensity by the sample. However, there are distinct reflexes that are only visible with a LNMO film. Thus, the phase of the electrode material clearly can be indexed to the spinel phase. However, there are only very few reflexes due to preferential orientation of the film. This effect has already been reported in literature.[29] YSZ single crystals are cut along their (111) axis, and LNMO thin films take indeed the same orientation. The (511) and presumably (311) reflex are also visible. This is in accordance with results by Schichtel, who also found (311) orientation in smaller amounts for preferred (111) orientated thin films.[211] For the (311) reflex, there is however also a small contribution from the Pt film. Impurity phases could not be detected.

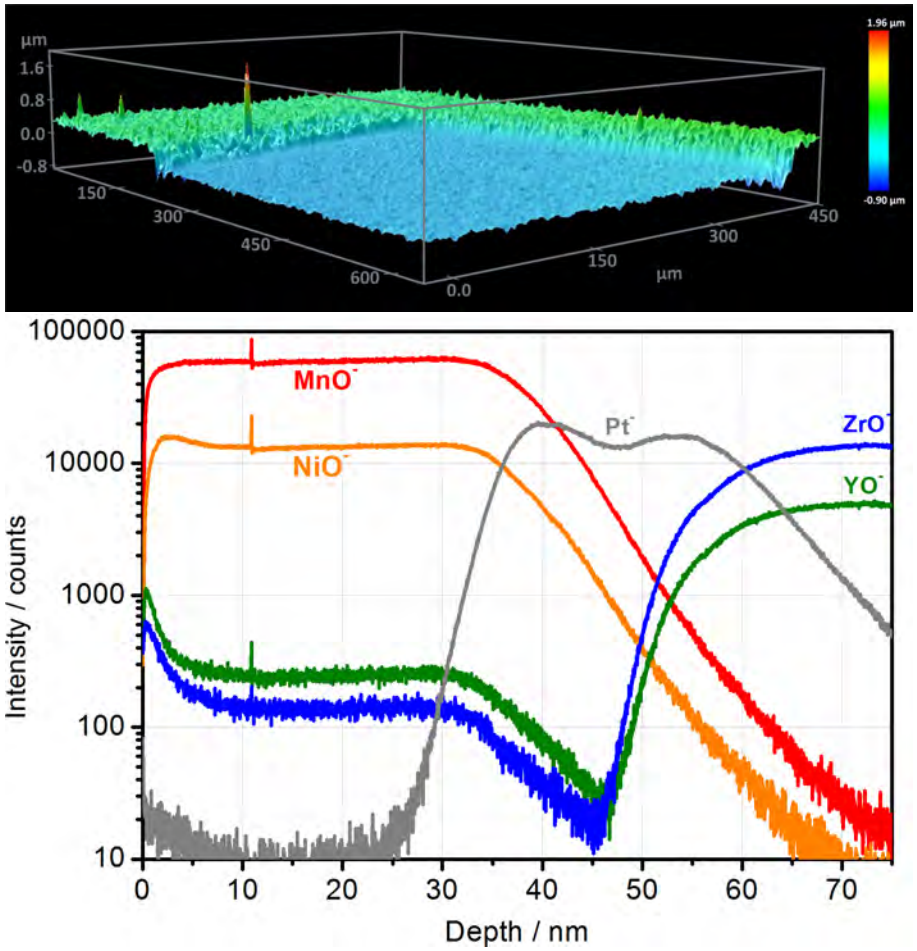

Fig. 5.9.: *Image of the SIMS crater of a LNMO sample on Pt-YSZ as measured by confocal microscope in the upper row as well as the SIMS depth profile itself in the lower row. The color legend in the top picture indicates the height scale.*

5.3. Pouch cell assembly

The YSZ single crystals are cut in squares with an edge length of 1 cm, and they do not fit into the commonly employed Swagelok T-cells with circular inner geometry with an inner diameter of about 12 mm if its interior is covered with Mylar® foil. Thus pouch cells were used, which were assembled in a argon filled glove box. Their geometry is sketched in figure 5.11. They consist of a polymer coated aluminum pouch foil being cut in slices of 4x10 cm^2. It was folded in the middle of the long side to create a small bag. As current collectors aluminum and copper tape (Sumitomo), 5 mm broad, were used for cathode and anode, respectively. Every $7 - 8$ cm these metal stripes are covered with a piece of polymer film. If heated, this film bonds well to the polymer coating of the foil, thus achieving gas tightness

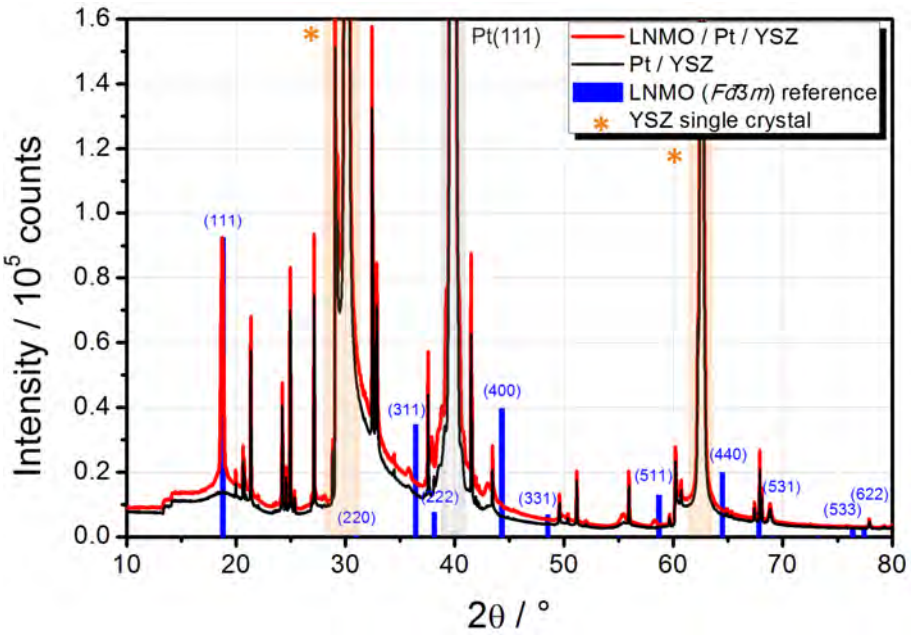

Fig. 5.10.: *XRD of a pristine LNMO thin film deposited by PLD on Pt-YSZ together with the pattern of the pure Pt-YSZ substrate and the $Fd\bar{3}m$ phase as well as the corresponding hkl indices. The deposition parameters of the LNMO and Pt thin films are* 1000 *pulses at a laser frequency and fluence of* 5 Hz *and* 3.1 J/cm^2*, respectively, at* 1000 °C *in oxygen atmosphere of* 5 Pa *and a target-substrate distance of* 40 mm *for the electrode layer and* 10000 *pulses at a laser frequency and fluence of* 10 Hz *and* 4.0 J/cm^2*, respectively, at* 400 °C *in argon atmosphere of* 0.3 Pa *and a target-substrate distance of* 40 mm *for the current collector.*

of the resulting pouch bag also in those regions, where the current collectors leave the bag. One corner of the LNMO thin film was fixed to the Al current collector with adhesive tape, thereby also covering the part of the metal stripe, that might be in contact with the electrolyte. Thus, possible reactions between the current collector and the electrolyte could be excluded. In separate tests was proven, that the adhesive tape does not react in the voltage range used for cycling of the LNMO electrodes. As anode a circular shaped piece of scratched lithium foil, 10 mm in diameter, was employed, which was attached to the Cu current collector by a small slice of lithium foil. Both electrodes were placed in the bend of the pouch foil with their current collectors pointing to opposite sides. Anode and cathode were separated by three pieces of dried Whatman™ separator, each 12 mm in diameter, and soaked with 60 µl LP30 electrolyte. Both sides of the pouch foil, where the current collectors leave the bag, were heat sealed inside the glovebox. The side remaining open was closed by a brace to minimize atmosphere exchange prior to vacuum sealing of the pouch bag, which had to be performed outside the box. The vacuum sealer (Sealervac, by Sealershop) was equipped with an electromagnetic mechanism enabling the opening of

the brace during evacuation. Thus, removal of residual gas from the cell was enabled if the pressure inside the sealing chamber was sufficiently low to protect the cell interior from any air contact. Evacuation of the cell prior to complete sealing is important to minimize any side reactions during cycling. To guarantee homogeneous and reproducible pressure, the pouch bag was pressed between two stiff plates, 5.6x5.6 cm^2 in size, and fixed with two document clamps. Each inner side of the plates was shielded with a piece of flexible rubber plate of the same size to prevent any damage of the pouch cell.

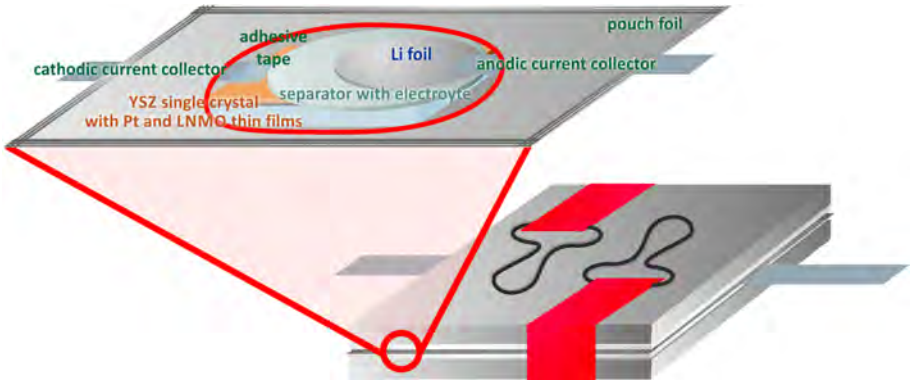

Fig. 5.11.: *Principle setup of a pouch cell containing a LNMO thin film as cathode.*

5.4. General electrochemical response of LNMO thin film electrodes

Using both CV and cc cycling the electrochemical activity of the LNMO thin films was investigated. They delivered the expected behavior with peaks or plateaus at the same position like technical LNMO electrodes, as can be seen in figure 5.12. The thinnest films prepared with only 1000 pulses during the PLD process deliver very shallow plateaus in CP experiments. Here the calculation of the differential capacity is beneficial, as even very small responses are clearly visible. Thus, the expected electrochemical response of the material without any side reaction could be confirmed. By comparison with the peaks in CV measurements, see e.g. figures 4.7 and 5.3, it is obvious that they are more defined for thin film electrodes than for technical electrodes. While for the latter ones the two peaks belonging to the nickel oxidation often merge, there is always a good separation for the thin films. This difference presumably results from their smoother surface without any porosity, so that the reaction takes place only at the surface, while for the technical electrodes deeper sample regions are also accessible, going along with larger diffusion times. This effect thus retards the reaction kinetics with concomitant smearing of the peaks over

a broader voltage region. This phenomenon is presumably even intensified by the fact that the individual particles of technical electrodes are of a size of several µm, i.e. at least one order of magnitude thicker than the thin films. In consequence, lithium diffusion into the particles slows down the charge/discharge kinetics more than diffusion into the thin film.

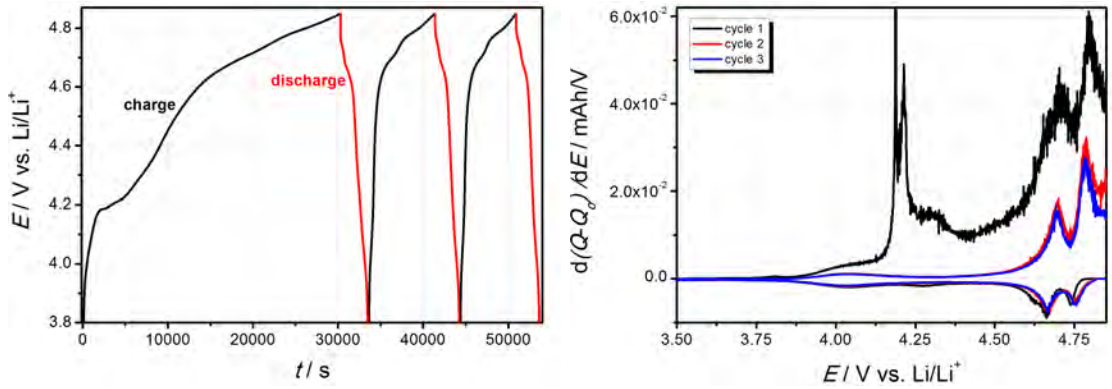

Fig. 5.12.: *cc cycling at approx.* 0.5 C *(corresponding to a current of* 2.044 µA *and a current density of* 2.044 µA/cm^2*) on the left and the corresponding differential capacity on the right of the first three cycles of a LNMO half cell, employing a thin film cathode. The measurement was performed at room temperature and LP30 was used as electrolyte.*
The deposition parameters of the LNMO and Pt thin films are 1000 p*ulses at a laser frequency and fluence of* 5 Hz *and* 3.1 J/cm^2*, respectively, at* 950 °C *in oxygen atmosphere of* 5 Pa *and a target-substrate distance of* 40 mm *for the electrode layer and* 10000 p*ulses at a laser frequency and fluence of* 10 Hz *and* 4.0 J/cm^2*, respectively, at* 400 °C *in argon atmosphere of* 0.3 Pa *and a target-substrate distance of* 40 mm *for the current collector.*

Like for the technical electrodes, the first cycle distinctly differs from the subsequent ones, mainly by an irreversible capacity of $2.8 - 5.0\,\mu Ah/cm^2$ at about 4.2 V and a higher electrolyte oxidation close to 5.0 V. The fact, that the irreversible response in the 4 V range completely diminishes after the first charge, together with the finding that the electrolyte oxidation also levels off in later cycles, again points to the occurrence of slightly different or additional processes like surface film formation on both electrodes taking place during the first cycle. This irreversible capacity will be further discussed in chapter 7.

Calculation of the precise capacity values for the thin film electrodes is virtually impossible. The deposited masses are so low that determination by simply weighting the sample prior and after the deposition process, like it is done for technical electrodes, is not possible. Thus, the film thickness was estimated from TEM or SIMS depth profiling, the size of the substrate and the crystallographic density of LNMO of 4.45 g/cm^3, thereby assuming negligible porosity of the thin film. The latter value was taken from the FindIt software, which entails the Inorganic Crystallographic Structure Data base. The discharge capacity of the thin films was calculated to approx. 112 mAh/g, thus delivering about 76 % of the theoretical capacity of LNMO. This result shows that the thin films cannot compete with

optimized technical electrodes, which reach values very close to the theoretical capacity of 147 mAh/g for LNMO.[212] One reason for the distinctly lower values of the thin films could their smooth surface and dense structure in contrast to the rough and porous morphology of technical electrodes. The electrolyte can thus way better penetrate into the latter electrodes, so that more active material is accessible. Calculation of the time needed for a lithium ion to diffuse through the whole cathode according to the following equation

$$x^2 = 2Dt \tag{5.2}$$

where x is the electrode thickness, i.e. approx. 37 nm for the LNMO thin films, and D_{Li} is the lithium diffusion coefficient, which will be calculated for the own LNMO thin films later in this chapter to $10^{-13} - 10^{-15}$ cm^2, result in a time t of 68 s - 114 min. Thus, the impeded lithium diffusion indeed might be one reason for the reduced capacity of the LNMO thin film cathodes. Another factor might be the charge transfer resistance, i.e. transfer of the ion from the liquid to the solid phase and vice versa, including stripping off of its solvate shell and leaving of the cathode lattice, respectively.[19] Since however the main goal of the thin film optimization was the reduction of the roughness and not the best performance, these values are well acceptable.

Cycling of the thin film half cells over more than 70 cycles was possible. Determination of the capacity loss is rather difficult, since the discharge capacity partly increases during the first cycles, after which its decrease sets in. Thus fading was only calculated between the maximal discharge capacity and its minimal value reached in the 70th cycle. A fading of 18 % is then evaluated, being in the range also seen with technical electrodes. The fact, that the discharge capacity first increases could possibly be attributed to widening of the thin film structure due to repeated volume changes during cycling, thus enabling subsequently easier lithium uptake and release. Crack formation with concomitant surface increase as source of the increase in discharge capacity could be excluded, since in SEM investigations of thin film elctrodes none could be detected, as depicted in figure 5.13. This image also shows, that the complete surface of the cycled electrode is completely covered with smeared decomposition species, i.e. CEI film, on top of which small globular particles are located, so that the bare thin film surface is not visible. Investigation of cycled technical electrodes show similar CEI films.

In figure 5.14 CVs of a LNMO thin film half cell recorded at different scan speeds are depicted. Since a very thin cathode film, deposited with only 2000 pulses, was employed, its electrochemical response is rather small and the electrolyte oxidation close to 5.0 V seems to be more severe. However, it reaches even for the highest scan speed less than 10 µA, thus being distinct lower than the values achieved with technical electrodes. The

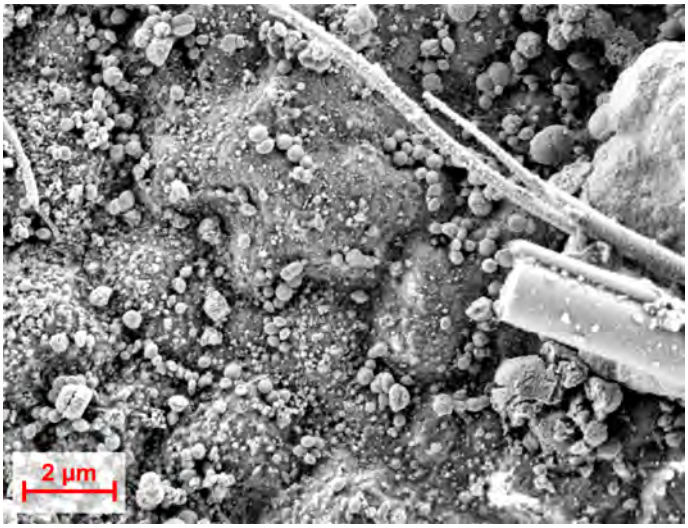

Fig. 5.13.: *SEM image of a cycled LNMO thin film electrode showing the complete coverage of the cathode surface with a smeared CEI film, on top of which small globular particles are located, so that the bare thin film surface could not be detected. The bright shining sticks are residuals from the glass fiber separator.*
The sample was cycled 40 times at room temperature and 60 °C. *The deposition parameters of the LNMO and Pt thin films are* 2000 p*ulses at a laser frequency and fluence of* 5 Hz *and* 3.1 J/cm^2*, respectively, at* 950 °C *in oxygen atmosphere of* 5 Pa *and a target-substrate distance of* 40 mm *for the electrode layer and* 10000 p*ulses at a laser frequency and fluence of* 10 Hz *and* 4.0 J/cm^2*, respectively, at* 400 °C *in argon atmosphere of* 0.3 Pa *and a target-substrate distance of* 40 mm *for the current collector.*

cell nevertheless shows the expected behavior of an electrode controlled by lithium diffusion. Modification of the peak form with scan speed mimics the kinetics of the lithium (de)intercalation at the electrode-electrolyte interface and its diffusion rate in the electrode film.[146] There is an anodic shift and an increase of the oxidation peak with scan speed, which were also reported by Mohamedi et al. for LNMO thin films prepared by electrostatic spray deposition.[140] On the right side of figure 5.14, i_p of the left anodic peak in the high voltage range is depicted for the three different scan rates in figure 5.14 and plotted as function of the scan rate ν and of its square root together with the corresponding linear fits. Since only three points were used for fitting, no non-ambiguous assignment is possible. Taking into account possible errors, i_p might be a linear function of ν as well as of its square root. However, the plot of i_p as function of $\sqrt{\nu}$ probably fits better, thus indicating, as already reported in chapter 2.5.1 diffusion control. In literature a linear dependence of i_p from ν is ascribed to intercalation processes, see e.g. Mohamedi et al. or Frangini et al..[140,213] A closer look to the literature cited by Frangini et al. however showed, that these authors just decided between finite (i_p is proportional to ν) and

semi-finite (i_p is proportional to $\sqrt{\nu}$) diffusion control.[214] Thus the own data probably have to be described by diffusion into semi-finite space.

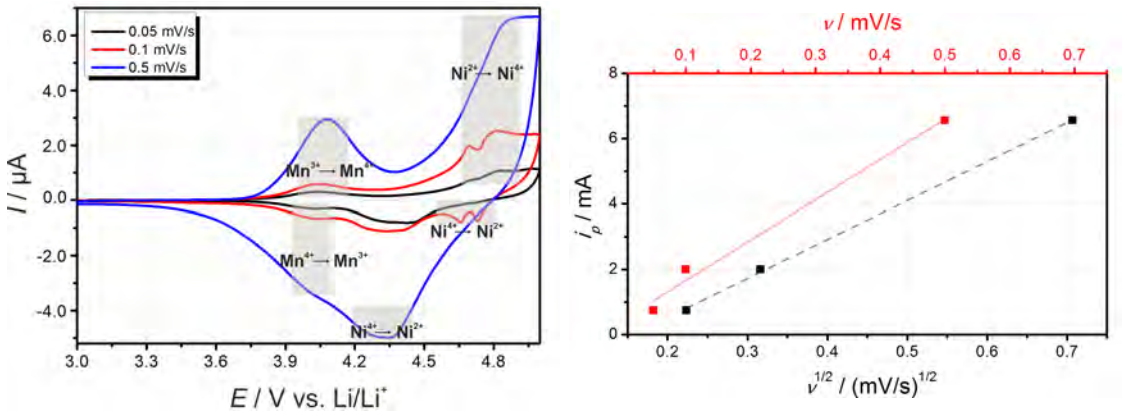

Fig. 5.14.: *CVs of LNMO thin films recorded at different scan speeds on the left together with i_p of the left anodic peak in the high voltage range for the three different scan rates as function of ν or its square root on the right. The corresponding linear fits are also shown. The measurements were performed at room temperature and LP30 was used as electrolyte.*
The deposition parameters of the LNMO and Pt thin films are 2000 p*ulses at a laser frequency and fluence of* 5 Hz *and* 3.1 J/cm^2*, respectively, at* 950 °C *in oxygen atmosphere of* 5 Pa *and a target-substrate distance of* 40 mm *for the electrode layer and* 10000 p*ulses at a laser frequency and fluence of* 10 Hz *and* 4.0 J/cm^2*, respectively, at* 400 °C *in argon atmosphere of* 0.3 Pa *and a target-substrate distance of* 40 mm *for the current collector.*

The lithium diffusion coefficient was evaluated in the same way as reported for the technical electrodes in chapter 4.4, also using the second cycle from CV measurements. Since the mass of the thin film electrodes could not be determined by weighing, the crystallographic density of LNMO was used for calculation of $[\mathrm{Li}]_{bulk}$. This is a good approximation, since the films are rather dense, showing no porosity. The low currents measured especially with the very thin films (deposited with only 1000 - 2000 pulses) were experimentally critical. Small errors in the determination of the baseline have large impact on the resulting D_{Li}. This is probably one reason, why the diffusion coefficients determined for several LNMO thin film cathodes diverge over approx. two orders of magnitude. Higher values are evaluated for thicker films, being prepared with 5000 pulses. The CV of one of these electrodes is depicted in figure 5.15, exemplarily showing the evaluation of i_p together with the baseline and its corresponding equation for the oxidation peaks. It delivered the values of D_{Li} as depicted in table 5.4. The four values are in good accordance and result in an average lithium diffusion coefficient of $2.29 \cdot 10^{-13}\,\mathrm{cm}^2/\mathrm{s}$. Taking also into account the values achieved with thinner LNMO films, D_{Li} is in the range of $10^{-13} - 10^{-15}\,\mathrm{cm}^2/\mathrm{s}$, thus being up to three orders of magnitude lower than that reported in literature by Xia et al. of $10^{-12} - 10^{-10}\,\mathrm{cm}^2/\mathrm{s}$.[29] The PLD films by Xia et al. show a rather flake-like surface

in contrast to the dense, well crystalline one achieved during the own preparation.[29] Therefore, the films by Xia et al. probably had a higher surface area compared to the own ones. Once Xia et al. just used the geometric area from the electrode dimensions for calculation of the lithium diffusion coefficient, their D_{Li} values are overestimated in comparison to the ones obtained here, since the surface area of the present films is closer to the geometric area. This in turn results in lower D_{Li}. The lower values achieved with thinner films could be explained by the impact of the rather stiff substrate, which influences the lattice parameters, as was already discussed in section 5.2.2, and in consequence also the lithium diffusion coefficient in the first monolayers of the deposited material. Thus, thinner films suffer more from its impact.

Tab. 5.4.: *Lithium diffusion coefficient in LNMO thin film electrodes calculated using equation 4.1. The numbers indicate the peaks depicted in figure 5.15.*

peak no in CV	$\mathbf{D_{Li}}$ **/ cm^2/s**
ox_1	$1.52 \cdot 10^{-13}$
ox_2	$1.54 \cdot 10^{-13}$
red_1	$3.72 \cdot 10^{-12}$
red_2	$2.39 \cdot 10^{-13}$

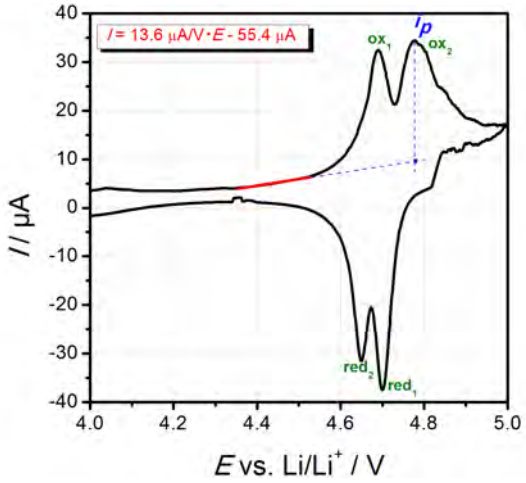

Fig. 5.15.: *Second cycle in CV measurements of a LNMO thin film half cell together with the linear extrapolation of the current gradient at the bottom of the oxidation peak for determination of the baseline and the corresponding equation as well as the resulting peak current i_p. The measurement was performed at room temperature with a scan rate of* 0.1 mV/s *using LP30 as electrolyte. The numbers in the graph are used to name the peaks in table 5.4 for determination of D_{Li}.*

Comparison between the own LNMO thin films and those reported in literature is rather

difficult, since the reported data are in most cases incomplete, and often roughness and/or cycling data are missing. LNMO thin films prepared by PLD by Xia et al. on either stainless steel or silicon wafers delivered a capacity of 122.5 mAh/g, but no roughnesses were reported.[29] From SEM cross-sectional view one can estimate it to be in the range of $100 - 200$ nm.[142] The films were with approx. 500 nm distinctly thicker than the films studied here.

Roughnesses of less than 5 nm were achieved by Konishi et al., who deposited LNMO by PLD on $SrTiO_3$ single crystals, thereby reaching capacities of $80 - 130$ mAh/g.[144] The roughness is thus a bit lower than for the LNMO thin films presented in this thesis, whereas the capacities are comparable to the own values.

Baggetto et al. also did not report any roughness values for their LNMO thin films sputtered on Pt-coated Al_2O_3 substrates, but from SEM and TEM images the films consist of greater agglomerates of smaller particles with a roughness in the range of that prepared by Xia et al.[4] The capacity of about 112 mAh/g compares well with the values obtained in the present study.

LNMO thin films by Wang et al. prepared by PLD on Si, Pt or stainless steel substrates delivered a capacity of approx. 125 mAh/g.[147] Again, no information about their roughness was given, but from SEM images the films consist of either flake-like particles or possess smoother surfaces with high crack density. They thus seem to be higher in roughness than the ones reported here.

Despite the fact, that LNMO thin films prepared by spin coating on LATP or Au substrates deliver hardly any distinct response during CV measurements, according to the authors their discharge capacity reaches 145 mAh/g, i.e. 98 % of the theoretical value.[143] Their roughness is in the range of hundred nanometers. Spin-coated LNMO thin films on Au substrates by Arrebola also delivered a comparably high discharge capacity of up to 130 mAh/g, but show a worm-like surface structure composed of large agglomerates, so that their roughness, although no information were given, is relatively high.

The same holds for the LNMO thin films prepared by electrostatic spray pyrolysis on either stainless steel or silicon wafers by Lafont et al., which also consist of larger aggregates and expose a rather porous structure.[215] They show only very shallow peaks in the CV and deliver discharge capacities of $60 - 106$ mAh/g.

In conclusion, the capacity reached with own thin films in the present study is a bit lower than that reported for most LNMO thin films. The roughness of the own films is distinctly lower than for all published ones, so that the slightly reduced capacity may well be explained with the comparably small surface area. They compete well with the state-of-the-art LNMO thin films. Since the main goal of the film preparation was the reduction of the surface roughness, the slightly reduced capacity is a reasonable compromise.

6. General measurement considerations for CEI investigation by SIMS

This chapters deals with the measurement conditions used for CEI investigation on LNMO thin film electrodes. It furthermore reports the basic results gained with this method and presents the extraction of information about the CEI from these data. In the beginning, difficulties and restrictions inflicted by this analytical method concerning the investigation of thin layers are discussed.

6.1. Difficulties concerning CEI investigation by SIMS

Sample roughness is one very critical parameter during SIMS measurements with depth profiling, since reliable results can only be obtained for sufficiently smooth samples. Too large roughnesses result in an apparently inhomogeneous distribution of the investigated ions, thus implying segregation effects, because the whole area under investigation cannot be optimally focused. As a result from defocused parts less secondary ions reach the detector. This problem can be avoided to some extent by division of the single secondary ion images by the total ion image, which entails the complete mass spectra. It thus displays the same inhomogeneous distribution. This procedure can cause, especially for ions low in concentration, misleading information. An actually inhomogeneous distribution of a secondary ion with high intensity like e.g. fluorine in the negative investigation mode, thus having large impact on the total ion signal, leads to intensity gradients in the images of other ions, which do not exist in reality.

Too large sample roughnesses also result in slightly varying arrival times for secondary ions of the same type coming from different high sample areas, thus leading to (mass) peak broadening. Since some species are only separated by a m/q ratio of less than 0.03, this effect may result in peak overlap. In consequence, the peak area of one of the species also contains counts of another one, causing not only enhanced intensities, but probably also misleading information. The first species is thus apparently also present in regions where signals from the second one emerge, thereby implying a wrong spatial distribution. As an example the SIMS spectra around the phosphorus signal of a relatively

rough separator cycled in a half cell, together with that of a medium-rough technical and a comparably smooth thin film electrode, all three cycled in the same electrolyte, are shown in figure 6.1. Comparison of the peak width clearly demonstrates the effect of different roughness on mass resolution. The group of Marcus also emphasized this problem by comparison of their data achieved on silicon anodes either deposited as planar film or grown as nanowires.[192] The increased roughness for the latter sample distinctly complicated data interpretation.[192] For investigation of geometrically demanding systems like nanowires, they emphasize the usefulness of comparative studies with planar model electrodes to unravel reactions taking place at the electrode/electrolyte interface.[192]

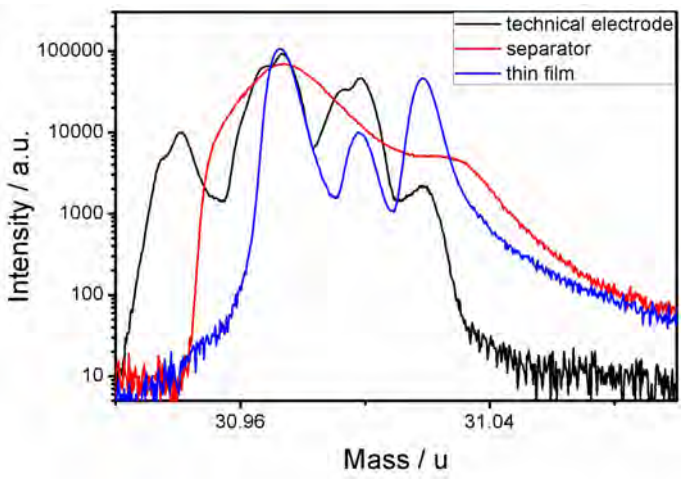

Fig. 6.1.: *SIMS spectra of a separator cycled in a half cell, together with that of a medium-rough technical and a comparably smooth thin film electrode, all three cycled in the same electrolyte. Comparison of the peak width thus clearly demonstrates the effect of different roughness on mass resolution.*

Presence of species with the same nominal mass values in one sample again result in partial overlap of their peaks in the SIMS spectra. To avoid misleading information due to the influence of the first ion in the peak of the second one, care has to be taken during selection of the ions under investigation and the respective peak area. In ambiguous cases several ions of the desired species can be used to verify the observed evolution with depth like e.g. CO_2^- and CO_3^- to monitor carbonate species. Peak separation in mass spectra is improved for small mass values m in order to keep mass resolution given by $\Delta m/m$ constant,[192] so that evaluation of low mass signals is preferred.

Concerning the study of surface film formation during e.g. cycling, an additional problem arises due to sample roughness, since deposition of electrolyte decomposition products may occur preferentially in cavities or pits. This in consequence leads to non-uniform film thickness of the CEI. Using analytical techniques with spatial information on the ions under investigation, in combination with depth profiling, in some regions the bulk material

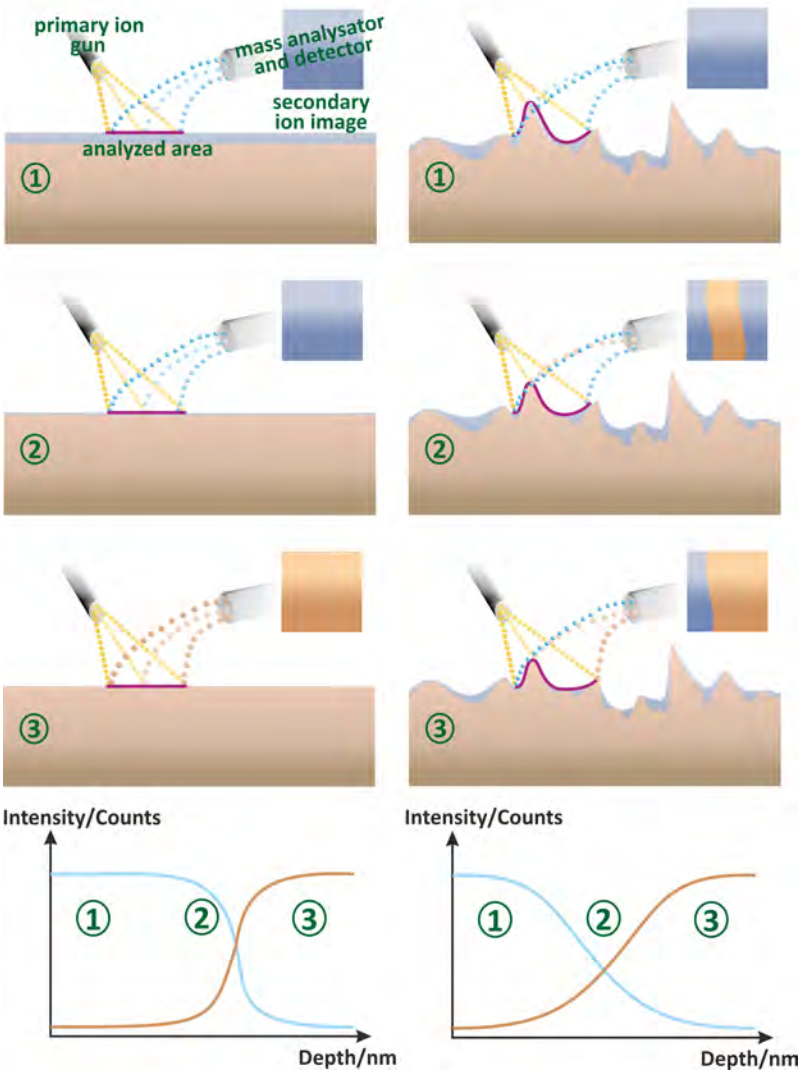

Fig. 6.2.: *Sketch of the influence of varying surface film thicknesses on the SIMS data quality: on the left side three different investigation times together with the corresponding secondary ion image and the depth profile for a flat sample with uniform surface film thickness are sketched. On the right side, the same data for a rough sample with varying surface film thicknesses are presented. The three primary ion beams in each picture represent the raster scanning of this ion gun for investigation of the lateral distribution of the secondary ions.*

is already reached, whereas in others the surface film is still present. This leads to signal mixing and therefore smearing of the depth profile information. The problem is sketched in figure 6.2. This effect is definitely one reason, why the CEI investigation by SIMS with spatial resolution in the $0.2 - 1\,\mu m$ range using technical electrodes is nearly impossible. In own measurements, not depicted here, no decrease of species contained in the surface

layer or increase of those being mainly present in the cathode could be detected due to smearing caused by distinct sample roughness. Thus, no information about the thickness of the CEI or the species present in it could be extracted.

One main drawback of SIMS is the distinct dependence of the secondary ion intensity on the sample matrix. This not only complicates quantification, but since in different matrices diverging ionization probabilities exist for one species, its intensity variation from one material to another during depth profiling not necessarily reflects different concentrations. This problem becomes even more severe at interfaces between two different layers, e.g. a metal and its oxide on top of it. In these regions of abrupt matrix changes, again different ionization probabilities exist compared to the bulk materials. In consequence, apparent enrichment or depletion in this region do not necessarily exist in reality. This aspect was also discussed by the group of Marcus, who detected an lithium enrichment underneath SiO_2 surface layers on Si anodes.[192] They attributed it to a real existing phenomenon, since the intensity rise in this region increased with cycle number, whereas an enrichment solely caused by matrix effects is expected to remain constant.[192] This shows, that a close look to the data gained by SIMS is needed to distinguish measurement artifacts from phenomena really existing in the sample. Comparison of slightly differently treated samples is often helpful, as it can be assumed that their matrices do not vary much. Thus, different gradients found for the same species are likely to be real.

Additional complexity of the analysis arises, since in the first few seconds of the depth profile all ions show either steep increase or decrease due to the surface implantation of sputter ions into the sample matrix. This in consequence affects the ionization probabilities of the species under investigation, as can be seen in figure 6.4. However, after stationary state is reached, i.e. when the same amount of sputter ions is incorporated and removed during a sputter step, the ionization probabilities reach a stationary state and then depth dependent intensities of the different ions reflect their actual content in the sample. The group of Marcus showed, that despite this effect even thin surface films on electrode materials could be investigated, thereby delivering reasonable results that agree with those obtained by XPS.[192,194]

It has also to be kept in mind, that the high energetic ion beams directed onto the sample during e.g. XPS or SIMS depth profiling may generally affect the sample as well as the species present in the surface film.[39] The group of Edström for example reported, that some loss of oxygen connected to the reduction of manganese are expected due to impact of Ar sputter ions, thus complicating the determination of the manganese oxidation state as function of depth.[39] They also mention the preferential sputtering of organic species relative to the surface than inorganic ones, which also could influence the measured concentrations in XPS depth profiles.[39] Li_2O may only form due to Ar^+

sputtering out of Li_2CO_3 ($Li_2CO_3 \rightarrow Li_2O + CO_2$) and argon etching appears to induce LiF formation as well as generation of new P-bonds like P-O and P-P bonds.[181]

One topic of controversial discussion is the sample treatment for cycled electrodes after electrochemical investigation and disassembling in an argon filled glove box. Many researchers wash their samples to remove any residual electrolyte salt from the surface with pure electrolyte solvent, in which the salt is well soluble. However, surface destruction and even partial removal of the surface film cannot be excluded by this procedure. The formation of a thin layer of electrolyte salt on the top of the CEI moreover could reduce the detrimental effect in the first few seconds of the depth profile delivering misleading information due to establishment of the sputter stationary state. This allows better study of the rather thin CEI, which otherwise would be partially buried in intensity variation of the secondary ions simply caused by the latter effect. Washing procedures in literature vary. Some groups simply rinse their samples, whereas the others store them for longer times in the pure solvent, so that a comparison is ambiguous. Investigations by the group of Marcus in addition show that during the washing procedure the electrolyte salt could not be completely removed.[192] In consequence, electrode washing was avoided for most samples in own measurements. Comparison of the depth profiles of a sample prior and after washing show no remarkable differences, as can be seen in figure 6.3. Only species that mainly result from fragments of the electrolyte salt $LiPF_6$ are as expected depleted after washing in the first few nanometers of the depth profile. In conclusion simple washing is assumed to have no distinct impact on the CEI for SIMS depth profiling.

6.2. Experimental setup

For SIMS investigations a ToF-SIMS^5 machine by IonTOF equipped with a bismuth primary ion and a cesium sputter gun for depth profiling was employed. In most SIMS measurements Bi_3^+ cluster ions were used for analysis instead of Bi^+, since the heavier species exert softer impact on the sample. In consequence, especially larger organic molecules, which are presumably present in the CEI, are less fragmented. This enables the extraction of more information about the matter under investigation. The currents of the Bi^+ and Bi_3^+ ion beams were in the range of 1 pA and $0.2 - 0.36$ pA, respectively.

Depending on the primary ion beam focus, the SIMS machine can be operated in several modes, each offering its own advantages and restrictions. By choosing a mode delivering high lateral resolution of about 200 nm, the mass resolution drastically decreases. Employing the mode with the best mass resolution, only a lateral resolution of approx. 2 µm is achieved. The latter one was used, since with the presence of organic species in the sample the number of peaks in the mass spectra drastically increases due to manifold C_xH_y

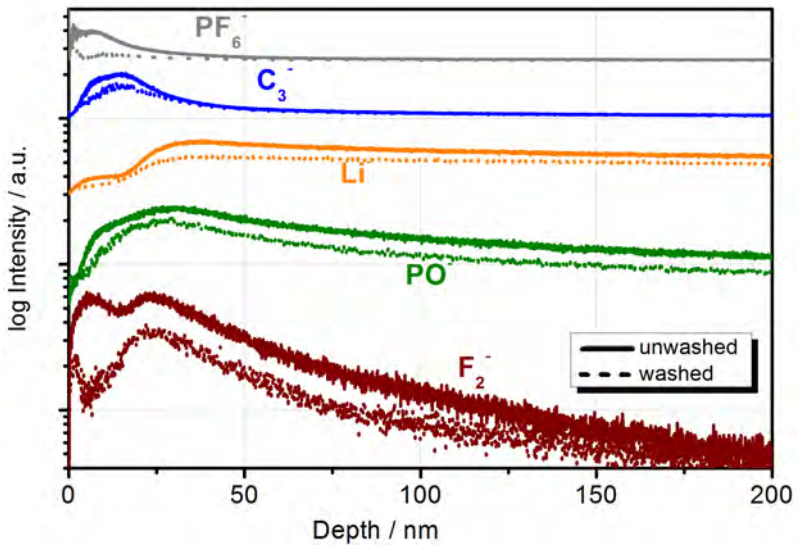

Fig. 6.3.: *SIMS depth profile of a cycled LNMO thin film electrode prior and after washing with pure electrolyte solvent DEC showing selected secondary ion signals present in the CEI, thus revealing only minor influence of the washing procedure on the resulting depth profile. The signals of different species were shifted along the y-axis for better visualization. Cycling was performed at room temperature over 19 cycles and LP30 was used as electrolyte.*

species. The depth resolution is in addition also better using this mode, thus up to 2 nm can be reached. The cesium sputter gun was run at a comparably low energy of 500 eV, thereby guaranteeing low abrasion and in consequence better depth resolution. The latter value was even increased by forming of relatively large sputter crater of $450 - 500\,\mu m^2$. The analysis region was set to $91.1\,\mu m^2$ and placed approx. in the middle of the crater to avoid any crater wall effect.

As discussed in the previous section, the electrodes extracted from cycled cells were not washed prior to SIMS analysis to avoid any modification or destruction of the CEI. For protection of the formed surface films from impact of oxygen and water, air contact was avoided during transport of cycled samples to the SIMS chamber. Therefore, transfer from the argon filled glove box, where disassembling of the cells was performed, to the SIMS chamber occurred in a gas tight box. It was opened in the SIMS ante-chamber not until the pressure was below $3 \cdot 10^{-3}$ Pa.

SIMS investigation of the CEI was performed in the negative mode although metals possess higher ionization probabilities in the positive mode. By employment of the positive mode, there is often an overload of the lithium signal, i.e. more lithium ions reach the detector than can be counted at the same time. In consequence, there is some mistake in its ion intensity and its development with time. Since the distribution of this ion is rather important during investigation of LiB materials, the negative mode was chosen. Its use

bears the same problem for electronegative elements like fluorine and oxygen. This can at least to some extent be overcome by investigation of F_2^- and O_2^- ions, which in a first approximation should show the same behavior like the single atom species. The occurrence of rather implausible species like e.g. F_2^- in the mass spectrum does not necessarily mean that these are indeed present in the sample, but rather form during ejection of secondary ions by impact of the rather high energetic primary ion beams. For achievement of higher intensities in the negative mode, in most cases the metal oxides were analyzed instead of the respective metal, i.e. MnO^- instead of Mn^-. They are more likely to be extracted and accelerated towards the analyzer by application of positive U_{ex} used in this mode.

Since intensities in SIMS depth profiles vary over several orders of magnitude, they are usually reported using a logarithmic scale. Normalization of the data was set aside, since there is no ion that remains completely constant over the whole depth range during profiling. In the total ion signal all ions are entailed, so that variation of one ion high in intensity like fluorine affects the normalized signal of all other ions. This in consequence leads to in-depth variations in the depth profile that do not exist in reality. Since the intensity of the total ion signal is rather high in comparison to most other ones, a small variation in its counts has large impact on that of the ions lower in intensity, thereby resulting in rather saw-toothed profiles. In contrast to this, the bismuth primary ion reaches intensities in the range of most other secondary ions, thus being in principle a suitable signal for normalization. Especially in the beginning of the depth profile, its intensity unfortunately shows distinct increase in most investigations, since firstly more ions are implanted in the sample than ejected. Its signal is thus only stable if approx. the same amount enters the sample than is released during sputtering and analysis, as can be seen in figure 6.4. Since the CEI is mainly located in the first region of the depth profile, the use of the primary ion for normalization would rather result in misleading information than leading to better comparability between different measurements.

Comparison of the MnO^- signal, which should be constant in the bulk of the thin film electrode, shows relatively good agreement for most LNMO samples under investigation, so that samples measured at different days with slightly varying primary ion intensities are relatively well comparable. Since the focus of these investigations was set on the principle buildup and content of the CEI, normalization was set aside to avoid any impact on the in-depth distribution by the species used for normalization.

The number of possible mass interferences reduces with decreasing m/q ratio, since at lower values less ion combinations are possible. This problem holds especially for samples containing organic species like LiB cathodes being cycled in carbonate based electrolytes, due to the large number of peaks resulting from different C-H species. In consequence, during SIMS investigation of the CEI mainly species with low m/q ratio,

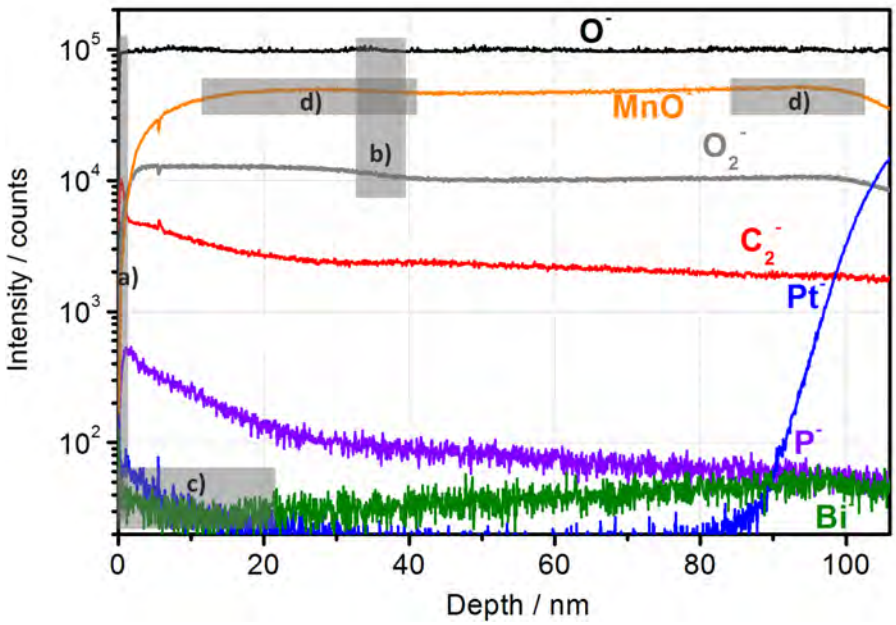

Fig. 6.4.: *SIMS depth profile of a LNMO thin film electrode showing some measurement artifacts during SIMS investigations. a) steep rise/decrease of the signals in the first nm due to establishment of the sputter stationary state; b) due to overload of the O^- signal, the intensity variation in different sample regions is completely lost, whereas it is clearly visible for the O_2^- signal; c) intensity variation of the Bi^- primary ion signal in the beginning of the depth profile, thus ruling it out as suitable signal for normalization; d) apparent enrichment of the MnO^- signal at the CEI/LNMO and the LNMO/Pt interface.*

being characteristic for species present in this surface film, were selected to minimize misleading information due to impact of other species. The evolution with sputter depth of species higher in mass was partially compared to corresponding ones of lower mass, e.g. PO_2 with P, to further verify the results. As already discussed in the last section, interfaces may cause artifacts during SIMS investigations, since the interfacial ionization probabilities vary distinctly from those in the bulk. It is thus often unclear, whether enrichments exist in reality or if they are only artifacts. This can be seen in figure 6.4 for the MnO^- signal, showing apparent enrichment at the CEI/LNMO and the LNMO/Pt interface. Since the CEI is in most cases so thin that interface effects should have large impact on it, its investigation is delicate. This can be overcome by comparison of several samples being only slightly different treated and which matrix should be thus almost the same. This procedure allows the identification of artifacts as well as the extraction of real chemical phenomena.

Another problem is the exact determination of the sputter depth. The craters in cycled samples could often not be detected in the profilometer camera due to increased roughness

of the surface after cycling. In consequence, the sputter yield extracted for one measurable sample was used for calibration of the other depth profiles. This may bear some error, since the different materials present in a cycled LNMO thin film sample are expected to exhibit distinctly varying sputter yields. The rather soft organic matter in the CEI should be easier sputtered than the dense and hard YSZ substrate or the rather compact PLD layers. As a result, the CEI appears thinner in depth profiles stopped in the LNMO layer in comparison to those, where sputtering occurred deeply into the substrate. Also it was tried to stop the depth profiling always in about the same sample depth, i.e. shortly after rise of the Pt signal, some impact could not be excluded. However, even if each depth profile would have been stopped at the same sample depth, the CEI layer would appear thinner than in reality, while the harder sample regions would be stretched. Reason for this effect is the varying sputter yield of the different layers, which were are averaged, thereby delivering misleading thickness information as schematically sketched in figure 6.5. This problem even further complicates for PLD electrodes due to thickness variations in the deposited films arising from the directed deposition during the PLD process. Thus SIMS investigations in inner regions result in thicker LNMO and PLD layers than those performed in outer sample areas. In consequence, comparison of the electrode thickness in several SIMS measurements not necessarily shows, if the used sputter yield delivers reasonable depth values, since the height of the PLD films could almost double in dependence of the location of the measurement. To minimize this effect, it was tried to analyze always inner sample regions. This was not possible for every sample, since separator fibers partially sticked on the electrodes surface. Reliable SIMS investigations are only possible in fiber free areas, which could unfortunately be only found in outer sample regions. Thus, the SIMS measurements do not offer the absolute CEI thickness, but a rough estimate. Comparison between differently treated samples like e.g. by temperature variation during cycling, and averaging over the depth extracted from several equally treated samples nevertheless delivers information about relative variation in CEI thickness in dependence of cycling conditions.

6.3. Making the CEI visible by SIMS

Comparison of the SIMS depth profiles of a cycled and a uncycled, fresh LNMO electrode show distinct differences in the first nanometers, as can be seen in figure 6.6. The MnO^- signal is chosen as indicator for the LNMO electrode, since manganese is the main component besides oxygen. For the fresh electrode this signal steeply rises, thus reaching a constant value, which surely represents the MnO^- bulk value in LNMO thin films, only after about 5 nm. Since all species increase or decrease in this first few nm, it is ascribed

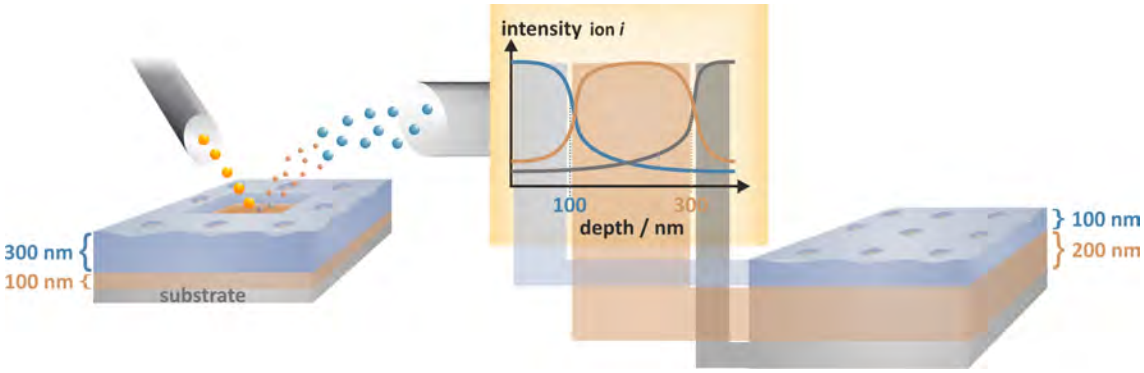

Fig. 6.5.: *Depth profile of materials with different sputter yields, showing their impact on the apparent thicknesses in the resulting graph: the porous, soft layer on top shrinks in the depth profile, while the dense, hard one underneath is stretched, thus delivering wrong thickness information.*

to the establishment of the sputter stationary state. The increase of the MnO^- signal in the cycled electrode occurs in contrast to this over a distinct broader depth, so that the bulk value is first reached at about 50 nm. This region is way too broad to ascribe it to establishment of the sputter stationary state. Other ions in this measurement increase or decrease like in the uncycled sample in the first few nm. The rather slow increase of the MnO^- signal thus leads to the conclusion that the intact electrode material is only reached in deeper regions, and the surface region is composed differently after cycling. This is a first hint to CEI detection via SIMS. For better visualization of the surface species on the cycled electrode the depth axis was shifted to align the point, where the bulk concentration of MnO^- and thus the electrode surface is reached. The NiO^- signal, not shown here, selected as index for the second transition metal in the cathode material, exhibits exactly the same trend for the cycled as well as for the uncycled electrode. This excludes artifacts as reason for the different sloping of the MnO^- signals, but confirms the coverage of the cathode material by deposition products in case of the cycled sample.

After validation that there indeed exists a difference between cycled and fresh LNMO electrodes in the SIMS depth profiling thus pointing to CEI formation, the question arises which species are contained in this surface film. In a first attempt, enriched species were searched in the spectra. There were numerous organic as well as inorganic species like C_xH_y, C_xF_y, P_xF_y, MnF_x, NiF_x, LiF, $LiCO_3$, etc. Thus, the principle CEI components already reported in literature could be indeed detected by their fragments.[20,39,165,166,168] In figure 6.6 the difference between a cycled and a fresh sample is exemplarily depicted for the C_3^- signal together with a graph, in which the depth axis is shifted in the same manner like for the MnO^- signal to better visualize the CEI. An overlay of the MnO^- and C_3^- signals for a cycled as well as a fresh LNMO thin film electrode is also presented.

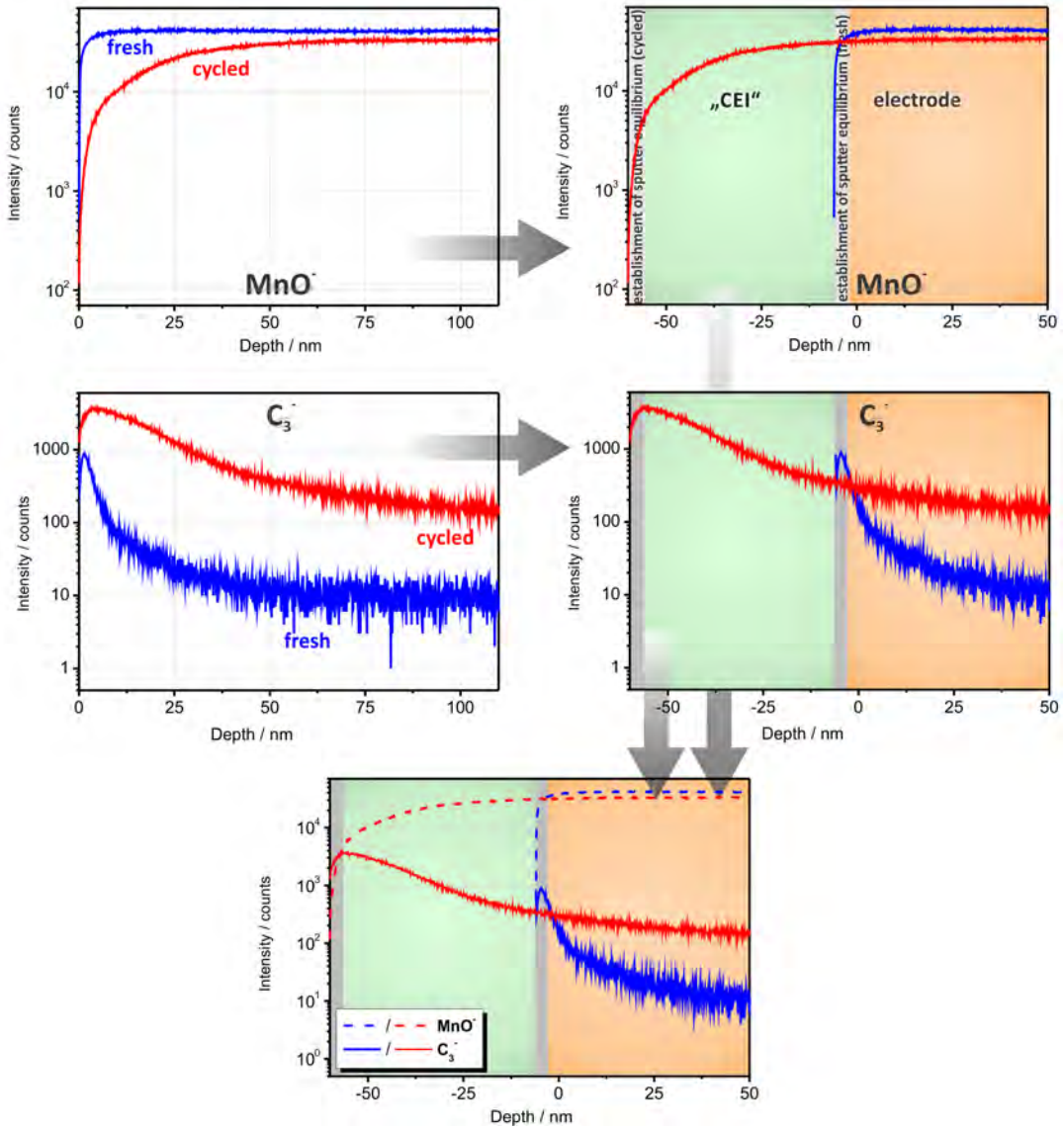

Fig. 6.6.: *From left to right: comparison of the SIMS depth profiles of a cycled and a fresh LNMO thin film electrode showing the MnO^- signal in the upper and the C_3^- one in the lower row; graph with shifted depth axis for better visualization of the surface film formed on the cycled electrode, again depicting MnO^- in the upper and C_3^- in the lower row; depth profile entailing both signals, thus showing the indeed enrichment of C_3^- in the region of the depth profile, where MnO^- is depleted. Both thin film electrodes compared in this graph were deposited with 5000 pulses. Cycling was performed at room temperature over 19 cycles and LP30 was used as electrolyte.*

As already discussed in chapter 2.3 the appearance of secondary ions in the SIMS mass spectrum does not imply, that these species exist exactly in this form in the sample under investigation. One example is the F_2^- ion, that is often recorded in the negative mode instead of the F^- ion, since the latter one is often overloaded. F_2^- is however highly

unlikely to be present in the sample, but forms during secondary ion generation. The same holds for the O^- ion, as can be seen in figure 6.4. Due to overload of its signal, the intensity variation in different sample regions is completely lost, whereas it is clearly visible for the O_2^- signal. Combinations of species from the sample with residual gas molecules are also possible. In consequence care has to be taken, if the detected species in the SIMS spectra are reasonable and if the m/q value indeed result from the expected ion or just from other combinations of secondary ions. Using the high mass resolution mode, already very small differences of more than $m/\Delta m = 9000$ could be resolved with the employed SIMS machine.[216] Confirmation, if the detected species indeed exist in the sample was achieved by checking characteristic mass sequences like C_1^-, C_2^-, C_3^- to verify the presence of polymeric species in the CEI. The P^-, PO^-, PO_2^- species were used for validation of PO_x compounds in the CEI. In figure 6.7 the C_n^- as well as the PO_x^- series are depicted for one LNMO sample. Actually, both sequences are completely present in the sample. The respective maxima of all C_n^- species are moreover at the same position, while those of all PO_x^- ones are located at another depth. This confirms, that the respective fragments indeed emerge from the same location in the CEI. Both aspects thus approve the presence of polymeric and PO_x species in the CEI. The MnO^-, MnO_2^- as well as the Ni^- and NiO^- signals are also presented for confirmation that several species significant for both transition metals in the LNMO cathode exhibit the same profile with rather steep gradient at the same depth. It is thus significant for the definition of the surface of the electrode and the end of the CEI layer.

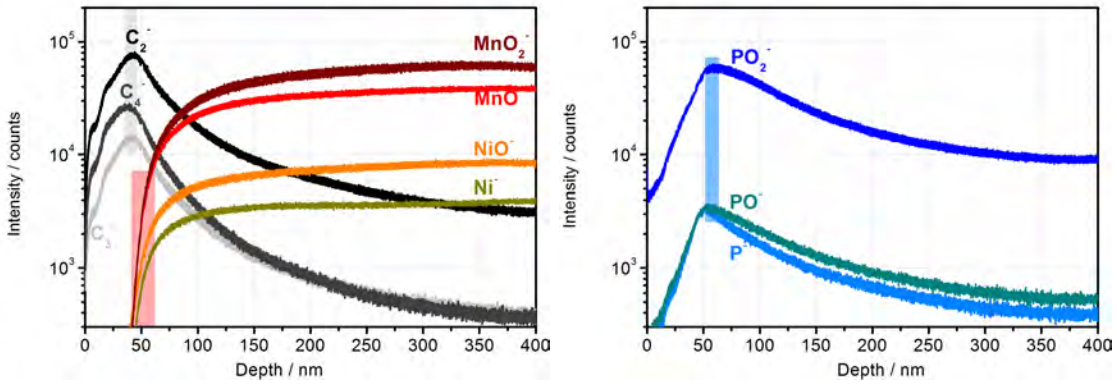

Fig. 6.7.: *SIMS depth profiles of a cycled LNMO thin film electrode showing the C_n (left) and PO_x^- (right) series, which exhibit their respective maxima at the same position. On the left also species significant for both transition metals in the LNMO cathode MnO^-, MnO_2^- as well as Ni^- and NiO^-, are presented. They show the identical, steep increase at the same depth, thus showing the surface of the electrode and the end of the CEI layer. Cycling was performed at room temperature over 19 cycles using LP30 as electrolyte.*

As already mentioned in the last chapter, interfaces are critical during SIMS investi-

gation since often distinctly varying ionization probabilities in comparison to the sample bulk occur there. It is thus questionable, whether maxima in this region indeed point to an enrichment of the respective species, or if it is just an measurement artifact. The CEI is rather thin, so that these effects have to be taken in consideration during evaluation of SIMS measurements. Comparison of cycled samples with uncycled ones, however, show in that region where this surface layer is expected, distinctly different behavior for the species that are assumed to be present in the CEI. Thus, the enrichments are probably real and the disturbing impact of interfaces could be mostly excluded. To verify that the surface film seen as CEI does not just result from residual electrolyte, uncycled samples were dipped into the electrolyte LP30 and afterwards investigated by SIMS. The measurements delivered approx. the same steep increase for the cathode signals as well as a sharp decrease for those significant for the CEI in the first few nanometers of the depth profile like observed for uncycled samples, as can be seen from figure 6.8. This leads to the conclusion, that the detected surface films indeed do not just result from electrolyte residuals, but actually built up due to reactions during cycling.

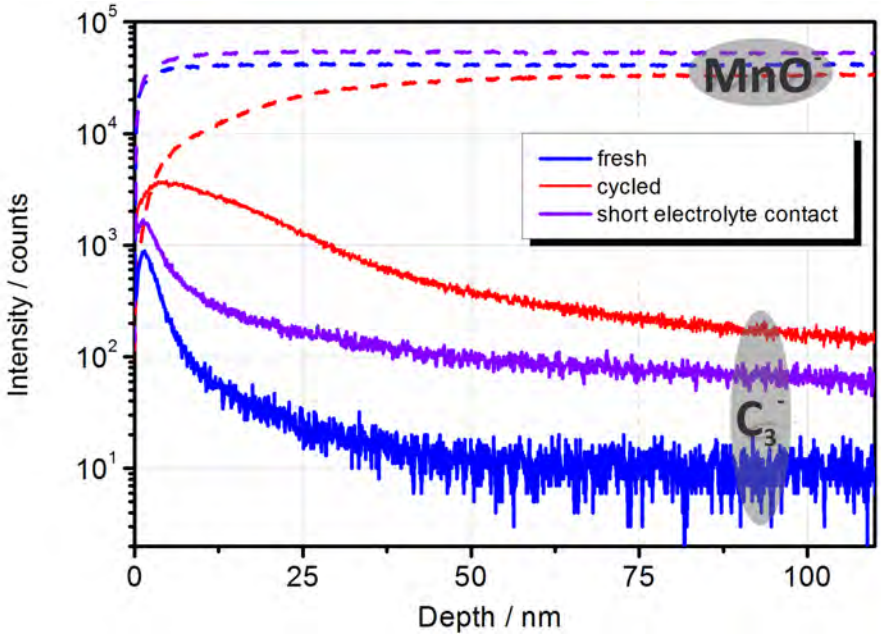

Fig. 6.8.: *Comparison of the SIMS depth profiles of a cycled and a fresh LNMO thin film electrode with an electrode shortly dipped into the electrolyte LP30 showing the MnO^- as well as the C_3^- signals. Cycling was performed at room temperature over 19 cycles and LP30 was used as electrolyte.*

7. Towards greater comprehension of the buildup and composition of the CEI

In this chapter, the results mainly gained by electrochemical and SIMS investigations are summarized and discussed, leading to development of an own model of the CEI formation and composition on LNMO thin film cathodes. The findings are furthermore compared to results reported in literature.

7.1. Electrochemical phenomena related to CEI formation

As already seen from electrochemical investigations of technical as well as thin film LNMO electrodes, two phenomena require deeper investigation. Firstly, the current does not decrease to zero after passage of the second peak relating to the oxidation of nickel in CV or differential capacity plots. There are obviously reactions which do not result from reversible redox reactions of the active material. The stability limit of the used carbonate based electrolyte solvents lies in this voltage range, so that their oxidation is in all likelihood. Thus the question arises, which products are formed and in which way they are further existent in the cell, i.e. if they deposit on one of the electrodes or if they stay solved in the electrolyte.

Secondly, it is obvious that the first cycle significantly differs from the subsequent ones. Here, the currents close to 5.0 V are distinctly higher and there are additional reactions that diminish in the following. These reactions are mainly irreversible, so that lithium storage reactions could be excluded. The fact, that the current at the upper cut-off voltage reduces in subsequent cycles points to the fact, that the reaction products at least to some extent deposit on the electrode surface, thus protecting it. This surface layer prevents direct contact between cathode and electrolyte, thereby suppressing oxidation of the latter species in the following. This however again begs the the question, which reaction products are generated, and of which structure is the formed surface film.

During the first cycle in cc experiments of LNMO thin film electrodes, there is an irreversible capacity at about 4.2 V during oxidation, as can be seen from figure 7.1, which diminishes in subsequent ones. It is therefore presumably attributed to surface

film formation, afterwards hindering direct contact between electrolyte and electrode, so that in further cycles no reactivity between these two matters takes place in this voltage region. This result is in accordance with experiments by Zhang et al., who reported an irreversible capacity at 3.1 V and 3.8 – 4.3 V in the first cycle of $LiMn_2O_4$ half cells using a PC/EC/EMC based electrolyte containing $LiPF_6$ salt.[170] This irreversible capacity observed in own measurements is only visible in constant-current cycling, but not during CV measurements. This difference is surely attributed to the varying cycling conditions, see chapter 2.5.2. It is moreover only visible in cc measurements of LNMO thin film electrodes, but not for technical ones. This not necessarily indicates different reaction mechanisms for the two types of electrodes, but could be caused by the about two orders of magnitude greater currents flowing by use of technical electrodes in comparison to thin film ones. Thus, the irreversible capacity at 4.2 V could be too small and thus is buried in the electrode response.

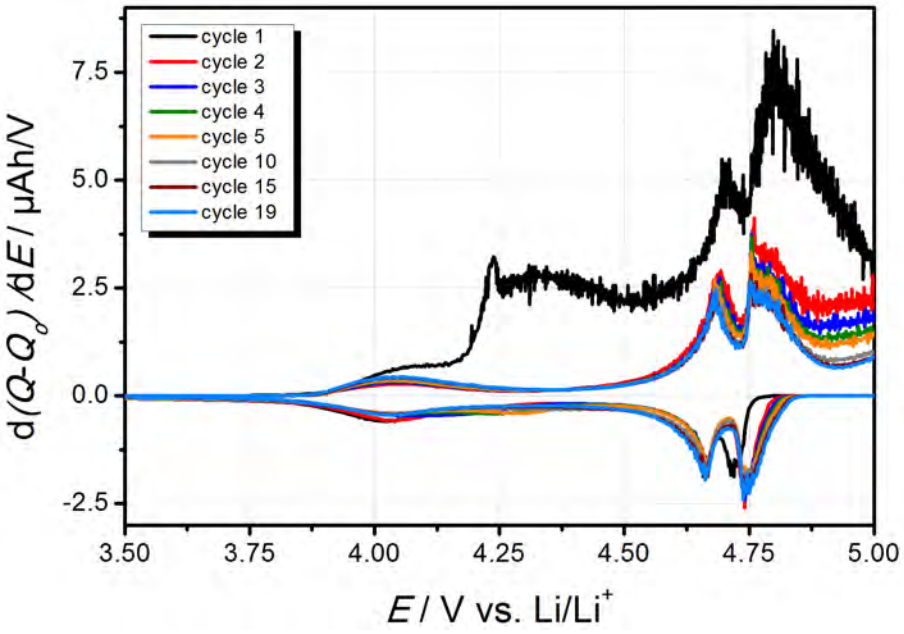

Fig. 7.1.: *Differential capacity of a LNMO half cell, employing a thin film cathode, showing an irreversible capacity at approx.* 4.2 V *during the first cycle. The measurement was performed at room temperature with LP30 as electrolyte.*
The deposition parameters of the LNMO and Pt thin films are 2000 p*ulses at a laser frequency and fluence of* 5 Hz *and* 3.1 J/cm^2*, respectively, at* 950 °C *in oxygen atmosphere of* 5 Pa *and a target-substrate distance of* 40 mm *for the electrode layer and* 10000 p*ulses at a laser frequency and fluence of* 10 Hz *and* 4.0 J/cm^2*, respectively, at* 400 °C *in argon atmosphere of* 0.3 Pa *and a target-substrate distance of* 40 mm *for the current collector.*

After the first few cycles for technical as well as for thin film LNMO electrodes in most cases a stable capacity is reached, as can be seen in figure 7.1. The first one shows

distinct higher charge capacity, i.e. a large irreversible capacity, which reduces during the subsequent three to six cycles, afterwards reaching stable coulombic efficiencies. This also points to formation of surface films on the electrode during the initial cycles, which afterwards protect them, thus preventing direct contact and in consequence reactions between them and the electrolyte. Since the SEI formation on lithium anodes takes place instantaneously upon its contact with electrolyte, surface film formation observed during cycling should mainly occur on the cathode side, i.e. formation of the CEI.[21] The distinct lower current close to 5.0 V due to electrolyte oxidation in later cycles, also visible in figure 7.1, point to the fact, that the formed surface films are dense and stable. This is thus another sign for the effective prevention of side reactions between electrolyte and cathode. The complete coverage of the electrode with CEI species was already obvious from SEM investigations shown in figure 5.13 in chapter 5. This is in accordance with results reported by Aurbach et al., who emphasized the remarkable stability of LNMO cathodes.[20] The authors attributed it to the unique surface chemistry of this cathode material due to presence of nickel in the structure, as already reported in chapter 3.2.[20] The own measurements thus could confirm the special behavior of LNMO electrodes, which is in contrast to other cathode materials. These mainly form porous, non-protective CEI films.[20,166] Wang et al. also reported constant coulombic efficiencies of LNMO half cells after about ten cycles, thus assuming initial CEI formation steps after which the system is stable.[65] The fact that not all own cells showed a stable performance, but that some faded distinctly with time, could be rather attributed to imperfect cell assembling than to formation of different CEI structures. Especially the exact alignment of the cell parts in the bend of the pouch foil, where they are loosely arranged prior to complete sealing, is demanding.

As already reported in chapter 4.4 and also obvious from figure 7.2 the coulometric efficiency reaches after the first cycles a steady value of approx. 95 % for the technical electrodes and approx. $70 - 76$ % for the thin film ones. The comparably low value for thin film electrodes might result from its high surface area in comparison to its small volume, so that there is a large contribution of detrimental surface reactions to the total capacity. The electrochemical reaction is thus not completely reversible, but in each cycle more matter is oxidized than reduced in the following one. This phenomenon is mainly caused by two aspects, namely again electrolyte oxidation, nearly always an irreversible process, or irreversible loss of active matter. Lithium could be either used in the buildup of the SEI/CEI on both electrodes or is trapped in the active material, either in closed channels or, as often reported for the lithium anode, as dendrites.[2] Leaching of both transition metals will be discussed later in this chapter in detail.

While the LNMO half cells work relatively stable at room temperature, thus showing

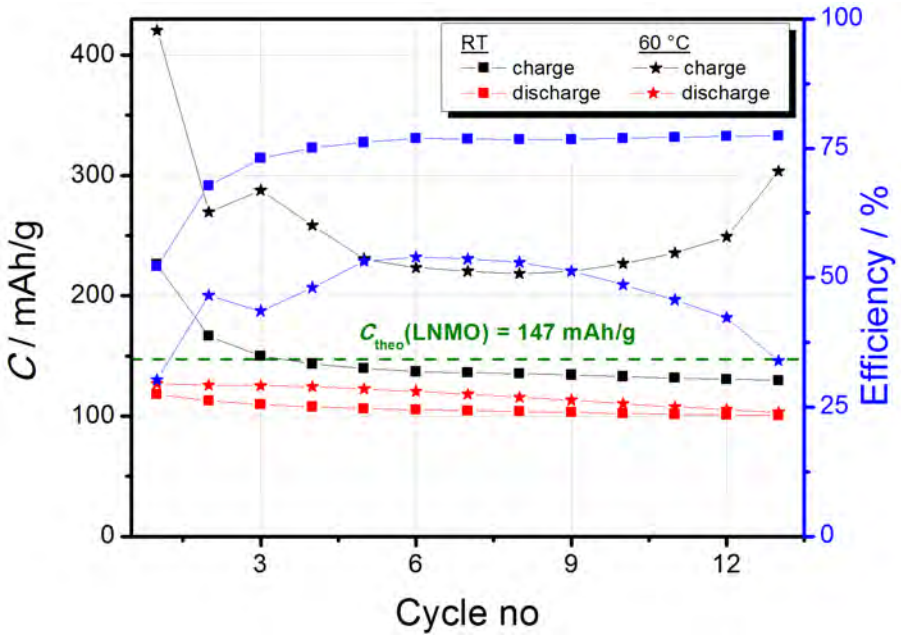

Fig. 7.2.: *Comparison of the charge and discharge capacity of LNMO half cells, employing thin film cathodes, either cycled at room temperature or at* 60 °C. *The respective coulombic efficiencies are also shown. The measurement was performed at a cycling rate of* 3/4 C *with LP30 as electrolyte. The deposition parameters of the LNMO and Pt thin films are* 2000 p*ulses at a laser frequency and fluence of* 5 Hz *and* 3.1 J/cm^2*, respectively, at* 950 °C *in oxygen atmosphere of* 5 Pa *and a target-substrate distance of* 40 mm *for the electrode layer and* 10000 p*ulses at a laser frequency and fluence of* 10 Hz *and* 4.0 J/cm^2*, respectively, at* 400 °C *in argon atmosphere of* 0.3 Pa *and a target-substrate distance of* 40 mm *for the current collector.*

only small losses for most cells, there is a distinct capacity fading at higher temperatures, partially even leading to complete failure of the cell. This is obvious from figure 7.2, showing the charge and discharge capacity vs. the cycle number in cc experiments at room temperature as well as at 60 °C. Remarkable is the distinctly higher charge capacity for the cell cycled at higher temperature, thus pointing to large impact of side reactions like electrolyte oxidation. This is even more severe at higher temperatures as reported in chapter 3.2.2. Capacity losses are also more severe at this temperature. One reason for this effect could be the formation of highly resistive surface films, as was reported by Duncan et al.[165] Another source for this fading could be accelerated transition metal dissolution from the active material at elevated temperatures, caused by acidic byproducts of the oxidation of solution species like protons.[67] This phenomenon was already stated in chapter b and will be discussed on the basis of own results in section 7.7.[67]

7.2. Principle composition of the CEI

As already mentioned in chapter 6.3 species being present in the CEI are identified by maxima in the first region of the depth profile, where those being mainly present in the LNMO electrode like MnO^- and NiO^- are depleted. SIMS measurements thus reveal the presence of organic and inorganic species in this surface layer. Series of C_n^- signals confirm the presence of polymer species. Even C_6^- could be detected. PO_x species point to formation of $Li_zPF_yO_x$ and P_2O_5.[39,165,166,168] A closer look towards this first region shows that the respective maxima shift for different components. Inorganic species are found closer to the electrode surface and organic species are found at the electrolyte side of the CEI. A depth profile magnifying the CEI region and thus the slightly diverging maxima for the respective species is depicted in figure 7.4. A schematic sketch showing the stacked microstructure of the CEI resulting from these measurements is also shown. Depth values of the respective species are determined for at least 15 cycled LNMO thin film electrodes and averaged, thus delivering the approx. depth where these species show their greatest enrichment and thus their main location in the CEI. These are depicted in table 7.1.

Tab. 7.1.: *Stacked structure of the CEI: main appearance of the respective species in depth profiles of LNMO electrodes cycled at room temperature. The values were averaged over at least 15 measurements at different electrodes.*

species	F_2^-	C_3^-	$LiCO_3^-$	PO_2^-	MnF_3^-
depth / nm	16.5	25.0	30.0	46.8	48.3

Depth determination in the presented SIMS measurements is, as already mentioned, not precise, since the sputtered craters could often not be detected during profilometer measurements. The used sputter yields are averaged over the rather organic CEI and the stiffer PLD layers as well as the substrate. The depth values given here are thus only a rough estimation. In consequence, the thickness of the whole CEI layer can also just be estimated, delivering a value of approx. 50 nm. The thickness estimation is based on the rise of the MnO^- signal. TEM investigation of a cycled LNMO thin film electrode, presented in figure 7.3, leads to a value of approx. 45 nm. Keeping in mind local thickness variation of the CEI due to imperfect alignment of cathode and anode with possible divergence in current density, both measurements are in excellent agreement. Thus, the depth calibration of the SIMS measurements appears to be reliable. To best of my knowledge, up to date only the group of Roling reported thickness values for the CEI formed on LNMO electrodes.[191] They determined its thickness also to approx. 50 nm, thus revealing very good comparability to the own measurements.

The shift of the maxima for the different species holds independent of the depth calibration. The first maxima at the electrolyte side of the CEI belong to PF_6^- and F_2^-, which surely result mainly from residual electrolyte salt. Thereafter, organic species like C_n^- are enriched, followed by inorganic PO_x^- ones. In its lower region, thus on the electrode surface, mainly inorganic species resulting from reactions between cathode material and electrolyte salt decomposition species like MF_x^- with M = Mn or Ni and x = 2, 3 are detected. $LiCO_3^-$ could be also detected. It surely points to Li_2CO_3, a species according to literature often present in this surface layer. It is located between the primarily organic and primarily inorganic parts of the CEI. Lithium also shows enrichment in this layer, so that formation of LiF, which appearance is also often reported in literature, is likely.[166] The TEM image in figure 7.3 indicates that the CEI is mostly amorphous. While its lower region close to the cathode is rather dense, its outer parts are more porous. These findings agree with the setup of the SEI, being composed of a dense inorganic layer close to the anode surface and a rather porous structure on top of it.[21,158] TEM investigations moreover reveal no cracks or other destructions of the LNMO thin film after cycling, but still good homogeneity and low roughness with no obvious grain boundaries. This again points to its effective protection by the CEI.

The stacked setup detected during SIMS investigations with more organic species on the electrolyte side of the CEI and rather inorganic ones close to the cathode is reverse to that observed during XPS measurements of LMO cathodes by the group of Edström and Eriksson.[166,167] It is on the other hand the same like that reported for the SEI on the anode.[21,158,194] Results by the group of Roling and Pienczonka et al. also confirm the results achieved during this thesis.[176,191] For the SEI the composition gradient with more inorganic species close to the anode surface and organic ones being situated further away from it is explained by the decreasing chemical potential of lithium along the film.[5] This also should hold for the CEI, so that the setup concluded from the own measurements seems to be more likely than the reverse one reported by the group of Edström and Eriksson. Aurbach et al. stated that polymerization of EC is not blocked by growth of the surface film, because it does not propagate by electron transfer from the cathode material, but by reaction of partially polymerized species with solvent molecules.[169] This also points to location of organic species on the electrolyte side of the CEI. It has to be kept in mind that investigations by the group of Edström and Eriksson were performed on the nickel free material instead of LNMO used in own investigations. Nickel seems to play an important role in the formation of this surface layer. Duncan et al. detected for example significant amounts of organic species on the surface of LNMO already after cycling or storage at room temperature, whereas according to Edström et al. on LMO electrodes only a partial, non-protective coverage exists.[165,166] The contradictory results between

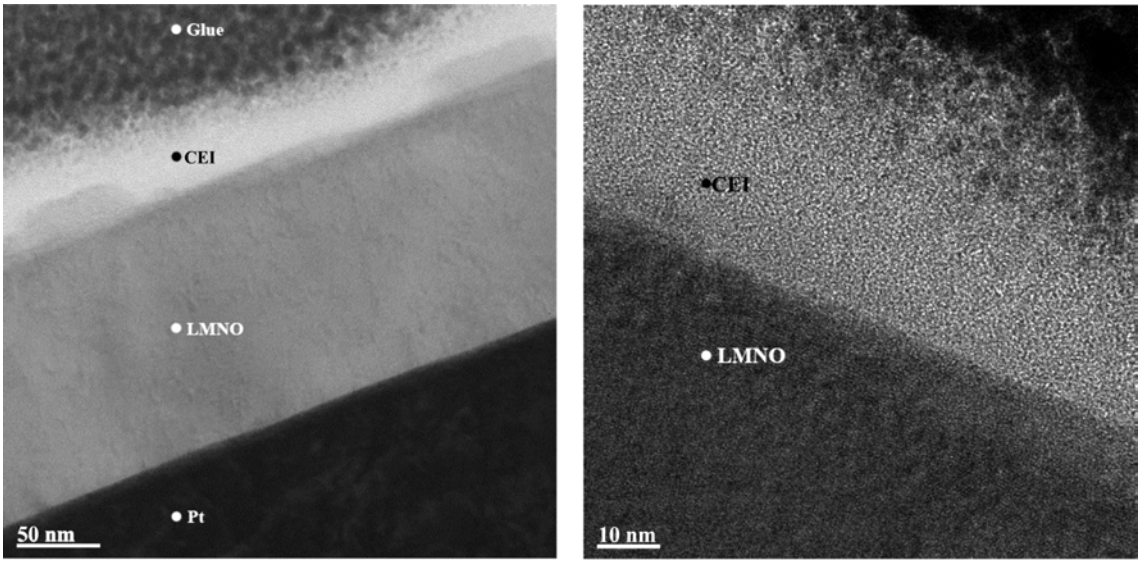

Fig. 7.3.: *TEM images of a cycled LNMO thin film electrode. On the left an overview of the investigated cross-section is given, while on the right an image of higher magnification is presented, thus revealing homogeneity and smoothness of the cathode as well as the porosity of outer CEI parts. The employed deposition parameters for the electrode layer are* 2000 pulses *at a laser frequency and fluence of* 5 Hz *and* 3.1 J/cm^2*, respectively, at* 1000 °C *in oxygen atmosphere of* 5 Pa *and a target-substrate distance of* 40 mm*. For PLD deposition of Pt current collector films* 10000 pulses *at a laser frequency and fluence of* 10 Hz *and* 4.0 J/cm^2*, respectively, at* 400 °C *in argon atmosphere of* 0.3 Pa *and a target-substrate distance of* 40 mm *were employed. The glue on top of the CEI layer results from slice preparation prior to TEM measurements.*

investigations by the group of Edström and Eriksson and own studies concerning the stacked structure of the CEI may thus originate from the different cathode materials used, thereby again pointing to the distinct influence of nickel during formation of this surface film. According to Aurbach et al. the structure of the CEI is to date not known for LNMO electrodes. Thus, the present SIMS studies indeed contribute to better understanding of the CEI formed on the surface of LNMO.

7.3. Influence of SOC, cycling time and temperature on the CEI

In literature, often an impact of the state of charge on the surface layer thickness and composition is reported, being already reviewed in chapter 3.2.2.[165,167,176] Yabuuchi et al. concluded from their SIMS investigations on lithium excess layered manganese oxide Li_2MnO_3-$LiCo_{1/3}Ni_{1/3}Mn_{1/3}O_2$ electrodes that the surface film formed during discharge of the cell decomposes during its following charging. According to Edström et al. the CEI thickens with temperature, storage time and cycle number.[166] For investigation of the influence of different SOCs on the CEI by SIMS LNMO thin film half cells were

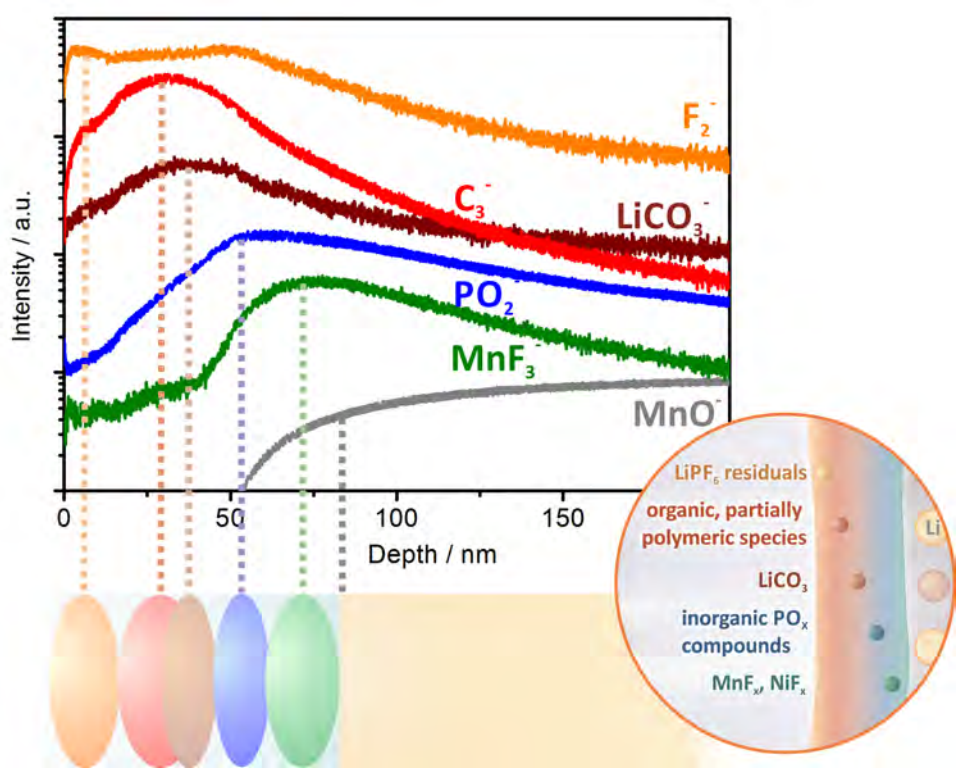

Fig. 7.4.: *SIMS depth profile of a cycled LNMO thin film electrode revealing the stacked structure of the CEI together with a schematic sketch showing its layered setup resulting from these measurements. For better overview, for each respective species only one signal is depicted and the signals were shifted along the y-axis for better visualization. Cycling was performed at room temperature over 19 cycles using LP30 as electrolyte.*

after cycling either completely discharged to 2.9 V or charged to $4.85 - 5.00$ V vs. Li/Li^+ and stored at the respective voltage for longer time. For study of the impact of cycle number on the CEI thickness distinctly longer cycling, i.e. at least three times more cycles than commonly employed for study of these cells, was performed. There is indeed a distinct influence of both the SOC as well as the cycling number on the CEI thickness for most species under investigation. Exact numbers are however difficult to report, since depth calibration distinct influences the measured thickness. Some separator residuals also could affect the resulting depth profile. Thus, areas free of these parts were investigated if possible, but small fibers could be partially not detected in the SIMS camera. Averaging over several investigated cells, at least two for each different treatment, delivers the values depicted in figure 7.5. It summarizes the depth of the maxima of the respective species in SIMS depth profiles for differently treated LNMO thin film half cells. The stacked structure of the CEI is again verified. The CEI thickens both with cycle number and longer storage at varying SOCs. Thereby, it seems to be somewhat thicker in the charged

than in the discharged state, which is in accordance with results by Simmen et al.[217] This is reasonable, since in the charged state the oxidation potential of the electrode is greater, therefore enhancing solvent oxidation.[166] The exact amount of the different species could not be determined by SIMS. Thus, results be Eriksson et al. and Duncan et al., who found different amounts of polymer and $Li_xPF_yO_z$ species in dependence of the SOC unfortunately could not be compared.[165,167] Since the CEI is thicker in the charged state, decomposition of a film formed during discharge and dissolved during the following charge as reported by Yabuuchi et al. can be excluded.[24] Porosity of the film is not detectable by SIMS, but since the irreversible currents distinctly decrease in subsequent cycles, the CEI should to a large extent prevent direct contact between electrolyte and cathode. Thus porosity of the CEI is rather unlikely.

From figure 7.5 it is also obvious, that, in accordance with results by the group of Edström and Eriksson, a temperature increase also leads to distinct CEI thickening.[166,167] This could be one reason for the more intense capacity fading at higher temperatures seen in figure 7.2. Main reason for the CEI growth with temperature will be enhanced reaction kinetics.[165,167]

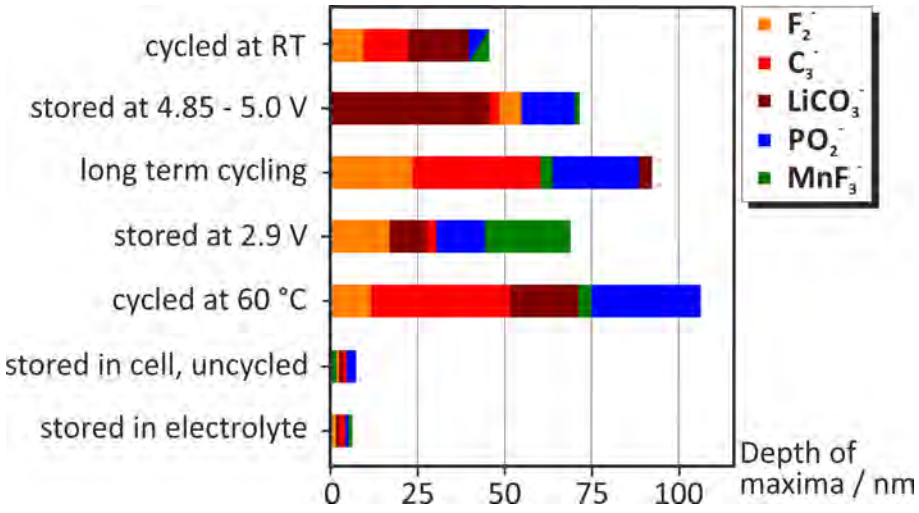

Fig. 7.5.: *Maxima of the respective species in the SIMS depth profile determined for several species present in the CEI after different treatments. Measurements were performed on LNMO thin film half cells using LP30 as electrolyte. Cells stored in the charged and discharged state were previously cycled.*

7.4. CEI formation during storage

Still under discussion is the question, whether CEI formation takes already place during storage, or whether cycling. For investigation of this aspect, fresh LNMO electrodes were either immersed in pure electrolyte or stored assembled in a half cell, but not cycled, for several days. Subsequent SIMS analysis revealed the formation of a very thin, CEI like surface film for both treatments, as also visible in figure 7.5. An interesting difference to cycled LNMO cells is however the absence of longer chained polymeric species, as obvious from figure 7.6. While the C_2^- signal exhibits the expected "hump" in the depth profile, it diminishes with increasing chain length, so that for C_6^- only the sharp decrease in the beginning of the depth profile due to establishment of the sputter equilibrium is visible, but no clear enrichment in the CEI. This leads to the conclusion that higher potentials are indeed needed for the formation of longer chained polymer species or that these at least accelerate their buildup. Similar results were also reported by the group of Edström and Eriksson, who detected essentially identical surface films for both electrochemical cycled and stored films at a given temperature.[39,166,167] Therefore, the reactions occurring at the cathode surface seem to be of chemical and/or electrochemical origin and take place both under storage and cycling. According to them minimal differences between both treatments occur, since the kinetics for the surface film formation may be more favorable during cycling due to enhanced mass transport in the electrolyte.[167]

These results fit very well to those reported by Wu et al., who investigated LNMO electrodes after cycling or storage at 60 °C in a carbonate based electrolyte using $LiPF_6$ as conductive salt by TEM.[218] After storage in electrolyte as well as after cycling the LNMO particles are covered with an amorphous thin film, which is after storage distinctly thinner than after cycling. According to the authors, the new substances on the surface of LNMO are products of thermal electrolyte decomposition as well as reactions between electrolyte and cathode.[218]

7.5. Ionic liquid based electrolyte

Besides half cells using common carbonate based electrolytes, also cells employing an ionic liquid as electrolyte solvent were fabricated. Employment of the latter electrolyte is beneficial with respect to *in situ* studies, since these show in contrast to carbonate based ones negligible vapor pressure. This enables *in situ* studies in analysis chambers working at UHV as it is required for XPS and SIMS. While $10 - 15$ wt% LiTFSI in BMP-TFSI (IoLiTec) as ionic liquid based electrolyte properly worked for technical electrodes, it did not deliver the expected electrochemical response of LNMO for thin film electrodes. How-

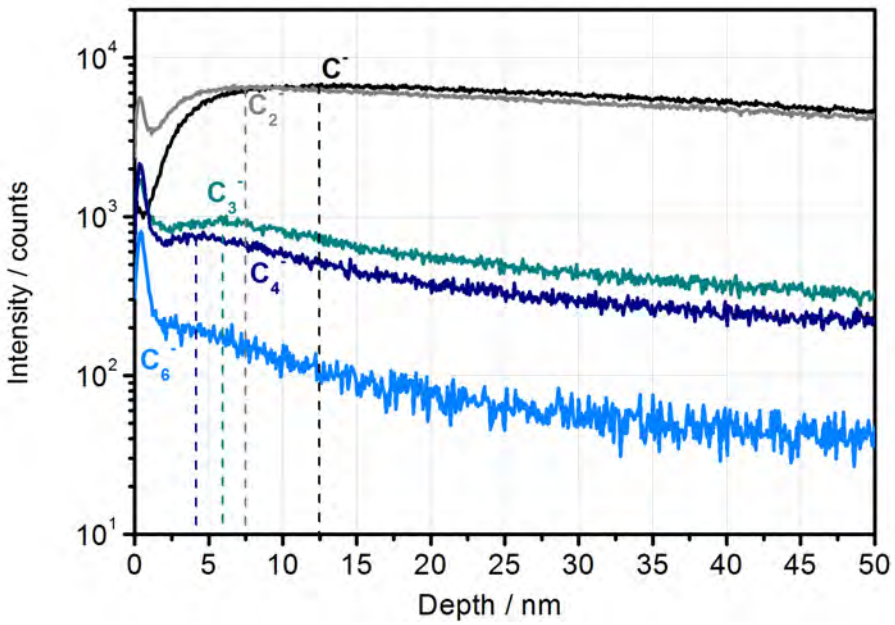

Fig. 7.6.: *SIMS depth profile of a LNMO thin film sample stored for one week in LP30 electrolyte inside an argon filled glovebox at room temperature showing the maxima of the different C_x^- species if present in the measurement.*

ever, by replacement of the electrolyte salt LiTFSI with the commonly employed $LiPF_6$, the thin film half cells also could be charged and discharged in the expected way. This is surprisingly, since the viscosity of the ionic liquid containing the latter electrolyte salt is higher than that containing LiTFSI, so that worse cell performance is expected. It is generally still under discussion, whether ionic liquid based electrolytes form an interface film between electrolyte and electrode like that observed in liquid carbonate based electrolytes. $LiPF_6$ appears to be responsible for establishment of CEI like surface films. It decomposes easier than LiTFSI, e.g. due to presence of water in the cell, subsequently initiating other decomposition reactions of for instance the electrolyte solvents. In SIMS depth profiles of cycled LNMO thin film half cells using ionic liquid with either LiTFSI or $LiPF_6$ as electrolyte, there is indeed a distinct difference visible. With $LiPF_6$ a CEI like that observed for carbonate based electrolytes established, but none formed if LiTFSI was empolyed, as obvious from figure 7.7.

On the left side of figure 7.8 the electrochemical response of technical LNMO half cells using either $10 - 15\,\mathrm{wt}\%$ LiTFSI in BMP-TFSI or LP30 as electrolyte were compared. On the right side of this figure, the same comparison is depicted for LNMO thin film half cells. Here $LiPF_6$ in BMP-TFSI was used as ionic liquid. For technical electrodes the capacity of the ionic liquid containing cell is distinctly lower than that employing the carbonate based

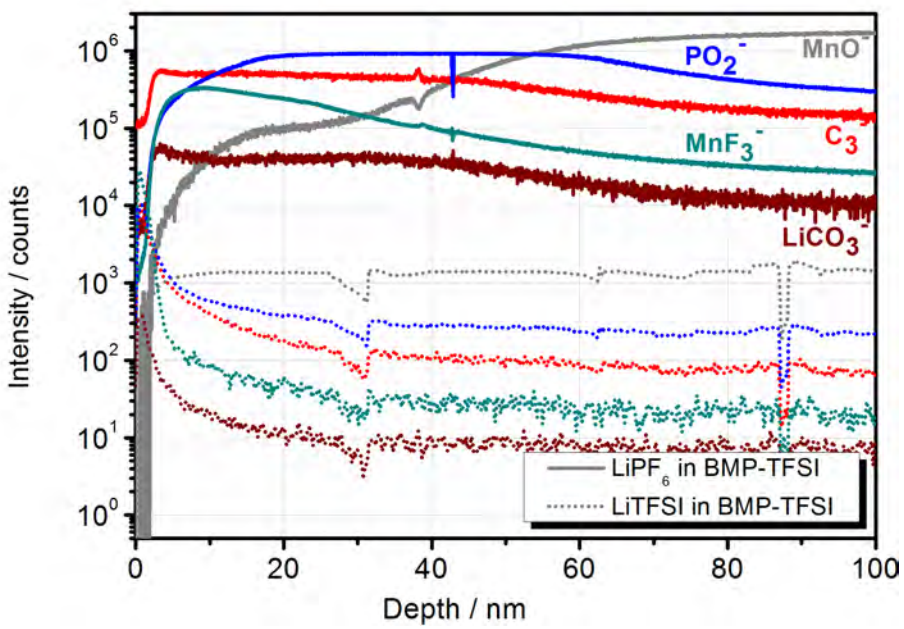

Fig. 7.7.: *SIMS depth profile comparing the CEI formed on LNMO thin film cathodes by usage of LiTFSI in BMP-TFSI or $LiPF_6$ in BMP-TFSI as ionic liquid based electrolyte. Both cells were prior to SIMS investigation cycled at room temperature.*

electrolyte and the peaks in the CV are distinctly broader. Both effects are mainly caused by the higher viscosity of the ionic liquid due to which lithium diffusion into the electrode as well as its extraction from it is slower. In consequence, less of the active material in deeper regions of the electrode is accessed. This explains, why capacity reduction and peak broading are both less severe if an ionic liquid based electrolyte is compared to a carbonate based one in contact with thin film electrodes. For this type of electrodes, the electrolyte is only in contact with its rather smooth surface, so that slower ion kinetics in the electrode have less impact on the cell performance. In conclusion, ionic liquids show slightly worse performance than carbonate based electrolytes in the case of thin film electrodes. All features typical for LNMO electrodes during electrochemical experiments are observed, which reveals the stability of all cell parts in this electrolyte. Thus, ionic liquids turn out to be suitable for *in situ* experiments using LNMO cathodes, specially at least BMP-TFSI turns out as suitable. By employment of $LiPF_6$ as electrolyte salt in ionic liquid based electrolytes CEI like surface films form.

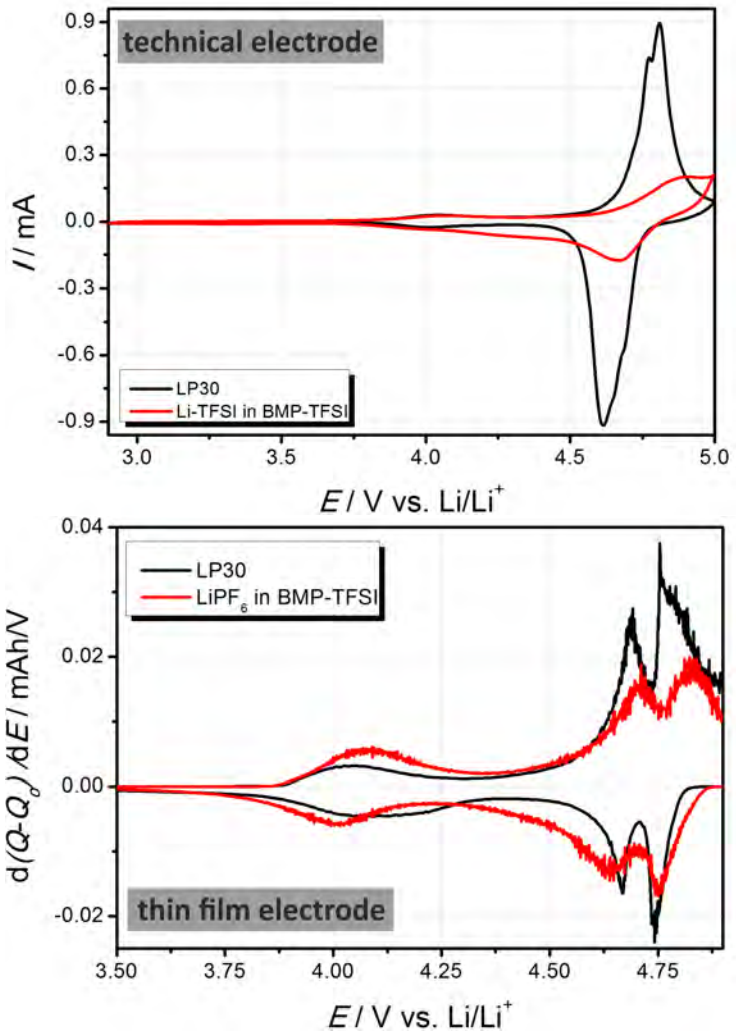

Fig. 7.8.: *Comparison of the electrochemical response of technical as well as thin film LNMO half cells using either LP30 or ionic liquid based electrolytes. In the upper row the CVs of technical LNMO half cells employing either LP30 or the ionic liquid* $10-15\,\mathrm{wt\%}$ *LiTFSI in BMP-TFSI at room temperature, each recorded with a scan rate of* $0.1\,\mathrm{mV/s}$*, are depicted. For both cells the second cycle is presented. In the lower row the differential capacities of LNMO thin film electrodes using either LP30 or* $10\,\mathrm{wt\%}$ *$LiPF_6$ in BMP-TFSI at room temperature are shown. For both cells the third cycle is presented. In the thin film cell cycled with LP30 a smaller cathode was used, i.e. the amount of active mass was lower in comparison to the thin film cell using BMP-TFSI. Thus, the response of the cell using LP30 was scaled to deliver comparable differential capacities.*
The thin film electrodes were deposited on Pt-YSZ. The deposition parameters of the LNMO and Pt thin films are 2000/5000 p*ulses at a laser frequency and fluence of* $5\,\mathrm{Hz}$ *and* $3.1\,\mathrm{J/cm^2}$*, respectively, at* $950/1000\,^{\circ}\mathrm{C}$ *in oxygen atmosphere of* $5\,\mathrm{Pa}$ *and a target-substrate distance of* $40\,\mathrm{mm}$ *for the LNMO and* 10000 p*ulses at a laser frequency and fluence of* $10\,\mathrm{Hz}$ *and* $4.0\,\mathrm{J/cm^2}$*, respectively, at* $400\,^{\circ}\mathrm{C}$ *in argon atmosphere of* $0.3\,\mathrm{Pa}$ *and a target-substrate distance of* $40\,\mathrm{mm}$ *for Pt.*

7.6. Cycling in full cells

LNMO full cells, using graphite instead of lithium as anode, suffer from severe capacity fading, as already mentioned in chapter 3.2.2, so that more than 50 % loss was reported after 100 cycles.[178] This degradation is presumably caused by loss of active Li^+, which is more severe for full than for half cells. Whereas in the latter case lithium is present in excess in the cell, in full cells its amount is balanced between both electrodes.[176,178] Own technical LNMO-graphite full cells indeed show drastic capacity fading, as obvious from figure 7.9, so that only 43 % of the inital discharge capacity is observed already after 15 CV cycles. LNMO thin film cells suffered even more, so that cycling was hardly possible and results are not depicted here. Partially rising the voltage to the upper cut-off limit of 5.0 V succeeded, but very large irreversible capacities were observed and hardly any response from the active material. Therefore, the current appears to be nearly completely consumed by side reactions like electrolyte oxidation. Thus, formation of rather thick CEI layer is likely, as will be confirmed by SIMS investigations later in this section.

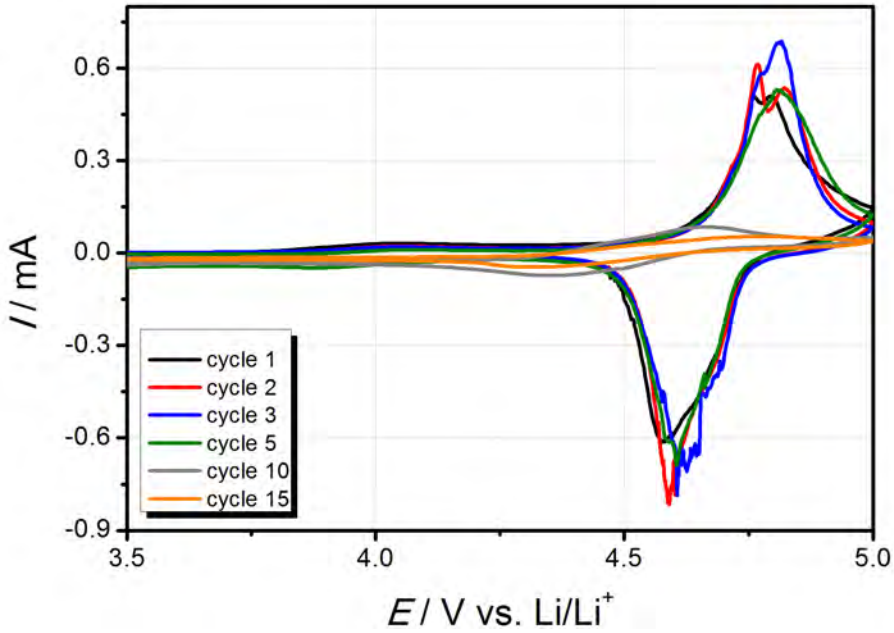

Fig. 7.9.: *CV of a LNMO-graphite full cell, recorded with a scan rate of* 0.1 mV/s *at room temperature. As electrolyte LP30 was used employing a technical LNMO electrode as cathode.*

An additional problem arises by the use of full cells in combination with high-voltage materials like LNMO, since the copper foil commonly employed as current collector for anode materials is unstable in the cathode is operated in the high voltage range, as was already discussed in chapter 5. It shows such strong reactivity that only after few cycles

hole formation is visible through the whole current collector, leading to complete failure of the cell already after three cycles. According to Myung et al. no protective layer forms on this metal which prevents its dissolution at higher potentials.[172] This subsequently leads to a short-circuit of the cell. To overcome this problem, aluminum foil, being stable in the high voltage range, was instead used as current collector. The employment of this material enables cycling of full cells over more than 35 cycles, as obvious from figure 7.10. This graph highlights another interesting fact. By increasing the lower cut-off voltage from 2.9 V to 4.4 V vs. Li/Li^+, the capacity on the one hand reduces as expected since the manganese redox couple is not accessed, but on the other hand the irreversible capacity reduces drastically. The cycling stability thus increases, so that almost no fading is visible. This leads to the conclusion that detrimental reactions take place also at lower potentials and not only in the high voltage range of more than 4.8 V. Main reason for this fading could be the Jahn-Teller distortion of the trivalent manganese, that forms at about 4.0 V, thus leading to mechanical stress and eventually to partial delamination of the electrode. Since this ion tends to disproportionate into the tetra- and divalent form with the latter one being soluble in the electrolyte, its occurrence could result in loss of active material.

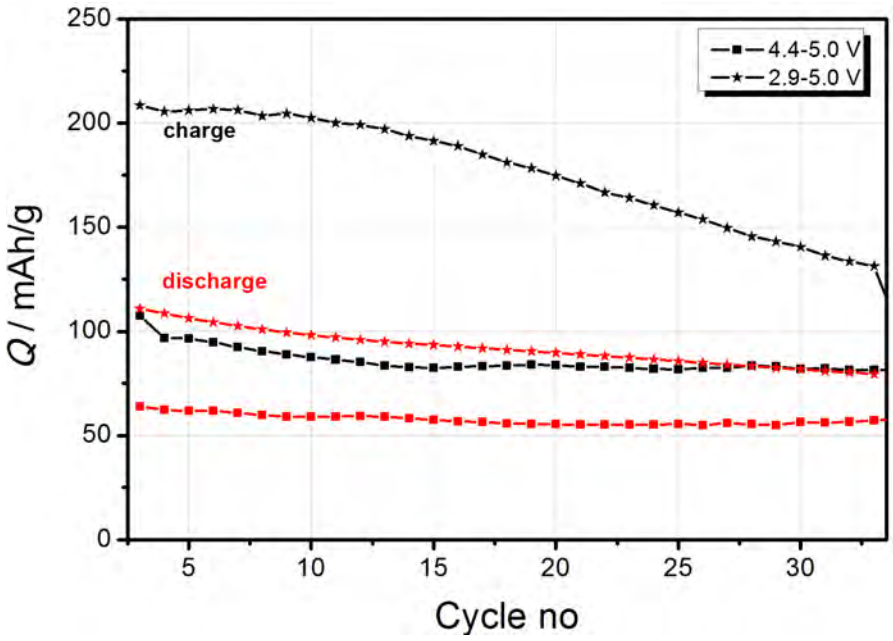

Fig. 7.10.: *Comparison of the charge and discharge capacities of LNMO-graphite full cells by variation of the lower cut-off voltage, recorded at C/2 and room temperature. As electrolyte LP30 was used. C rate was calculated on the basis of the cathode weight, since only this electrode contains active lithium prior to cycling.*

SIMS investigations performed on LNMO thin film full cells revealed the formation

of an CEI like surface film. The C_n^+ signals appear as rather broad. This could point to drastic electrolyte oxidation on the one hand. This was already assumed from cycling data, where partially no charging was possible, but distinct currents flow at lower voltages. On the other hand, transfer of species from the graphite anode might occur: This is rather likely during longer cycling with repeated volume changes, leading to delamination of outer, distant anode parts. However, it has to be kept in mind that the cells did not run successfully. Thus, further discussion is set aside at this point.

Cycling in full cells did not only result in distinct capacity fading, but even leads to destruction of the spinel phase, as obvious from figure 7.11, showing the diffraction pattern of a fresh technical LNMO electrode together with the XRD pattern of cathodes cycled either in half or full cells. The XRD pattern of the pure aluminum foil, onto which the electrodes were deposited by doctor blade and the reflexes of the $Fd\bar{3}m$ phases as well as the corresponding hkl indices are also depicted for comparison. XRD measurements were performed using a PANalytical EMPYREAN diffractometer. While the LNMO cathode cycled in a half cell still clearly shows the reflexes of the spinel phase, they completely disappeared after employment in a full cell, and instead new ones emerged. The phase transformation could be induced by lithium loss, which is present in excess in half cells with lithium anodes. The newly formed reflexes could not be indexed to the rock salt phase. The exact reaction mechanism occurring during cycling in full cells requires further investigation. The use of thicker thin film cathodes might result in cells which could be cycled. In this case probably not the whole lithium of the cathode will be consumed during SEI/CEI formation on both electrodes.

7.7. Transition metal dissolution from LNMO cathodes and their impact on CEI and SEI

Transition metal dissolution is one main reason for the capacity fading of LNMO cells, since the transition metal ions are not only lost at the cathode, but eventually redeposit on the anode, resulting there in a thicker and therefore more resistive SEI. For evaluation of the metal loss from the cathode, separators, prior cycled in LNMO thin film half cells, thus containing residual electrolyte, were analyzed by ICP-OES by Dr. H. Sommer at BASF SE. The resulting values for differently treated cells are presented in table 7.2 together with those of a separator only soaked in electrolyte. This technique is sensitive for trace amounts of 1 ppm. Taking into account the weight of a typical separator of about 15 mg, these values are fully reliable and the error should be as low as 0.15 ng. While no detectable amounts of both transition metals could be found in the fresh separator as expected, relatively large amounts were detected after cycling. The content of nickel is even higher than that

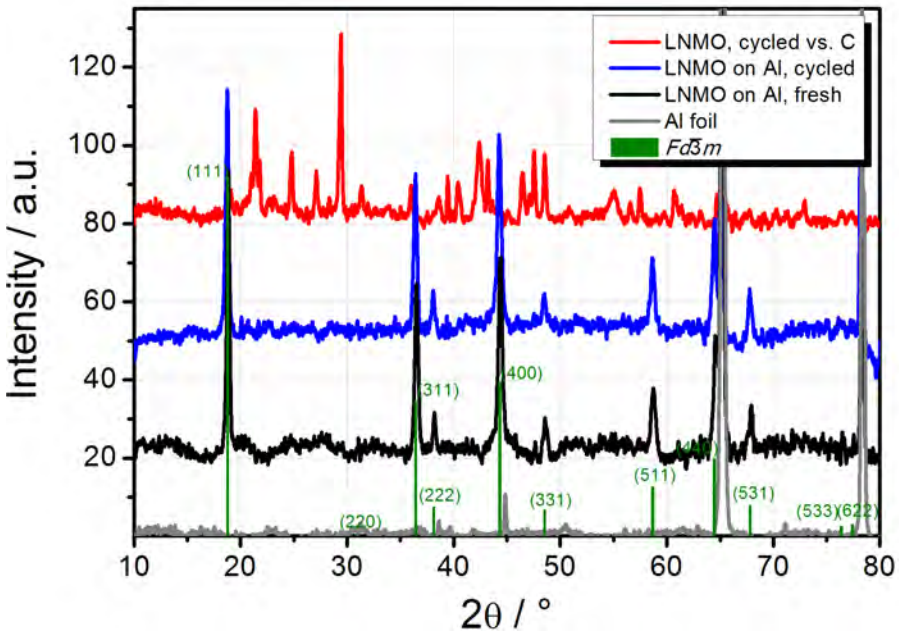

Fig. 7.11.: *XRD of a fresh technical LNMO electrode together with those of cathodes cycled either in half or full cells. The XRD pattern of the pure aluminum foil, onto which the electrodes were deposited by doctor blade and the reflexes of the Fd$\bar{3}$m phases as well as the corresponding hkl indices are also depicted. Background subtraction was performed using X'Pert Plus software.*

of manganese, although the content of the latter species in LNMO is three times higher in comparison to nickel. In literature mainly the dissolution of manganese is discussed as consequence of the Mn^{3+} disproportion, while that of nickel is not discussed. However, if the dissolution of both transition metals is investigated, the dissolution of nickel is often found to be higher in comparison to that of manganese, thus agreeing with our own results.[168,176] According to Aurbach et al. up to 50 % of the initial nickel content is lost after storage for 45 days at 60 °C.[168] Nevertheless, the dissolved amounts of both species are rather high in our own measurements. Unfortunately, no absolute values could be given, since determination of their amounts initially contained in the thin films is rather difficult and leads to large experimental errors. Partial delamination of complete thin film parts due to repeated volume changes during cycling could not be excluded. The latter effect however cannot be a major reason for the presence of the transition metals in the separator, since their ratio should then reflect their stoichiometry in LNMO, i.e. Mn:Ni = 3 : 1. This leads to the conclusion, that other mechanisms are mainly responsible for their dissolution. By rising the lower cut-off voltage to 4.4 V, thereby cutting the range where Mn^{3+} is formed with the risk of disproportionation and subsequent dissolution of Mn^{2+}, the amounts of both transition metals in the separator distinctly reduce. While

this is reasonable for manganese, reduction of nickel dissolution is somewhat surprising. The stronger leaching of this species by cycling over the full voltage range of 2.9 – 5.0 V is probably mainly caused by the higher temperature of 60 °C used in this measurement. In contrast to this, cycling between 4.4 – 5.0 V occurred at room temperature. In reference measurements with cycling between 2.9 – 5.0 V at room temperature, not presented here, the Ni:Mn ratio is not significantly higher than expected from the stoichiometry in LNMO. In contrast to this, cycling over the same range at 60 °C resulted in leaching of three times more nickel than manganese. According to Aurbach et al., temperature is one main factor affecting transition metal dissolution.[168] Its impact is explained by increased hydrolysis of the electrolyte salt $LiPF_6$ occurring at 60 °C.[176]

Tab. 7.2.: *Transition metal content in the separator after cycling in LNMO thin film half cells at varying cycling conditions measured by ICP-OES. LP30 was used as electrolyte. As reference a fresh separator, soaked in pure electrolyte was used.*

treatment	**nickel**	**manganese**
fresh	<1 µg	<1 µg
2.9 – 5.0 V, 60 °C	79 µg	15 µg
4.4 – 5.0 V, room temperature	1.5 µg	<1 µg

Hong et al. also used ICP-OES measurements to quantify the transition metal content in the separator after cycling.[219] In contrast to own studies the content of manganese dissolved in the electrolyte and therefore in the separator was twice as high as expected from the ratio of the two transition metals nickel and manganese in the cathode material.[219]

To obtain information on the transition metal conctent in the anode, X-ray absorption near edge spectroscopy (XANES) investigations were performed using synchrotron radiation at the DESY in Hamburg as well as the AKNA in Karlsruhe in cooperation with U. Fittschen, M. Menzel and U. Bösenberg. X-ray absorption spectroscopy at the K-edges of transition metals delivers information about the electronic and local structure of the system under investigation like oxidation state of the chemical species, their site symmetries and covalent bond strength.[220] The penetration depth of these K-edge X-rays is in the order of micrometers from the surface due to its relatively high energy of several thousands of electron volts, thus probing the volume of the sample.[220] In contrast to this, the study of the transition metal L-edges delivers surface information from depths of less than 100 Å due to distinctly lower energy of only several 100 eV.[220] In literature, X-ray absorption spectroscopy is often applied in *in situ* studies, since no UHV is required during measurements.[34,221] Radiation instead of ions or electrons is used as probe, thus no enlargement of the mean free path by UHV conditions is required.

In own measurements technical LNMO electrodes, cycled in half- as well as in full cells were investigated, since thin film electrodes hardly could be cycled in full cells. The low amount of cathode material in comparison to the large substrate for this type of electrode further complicate their analysis using X-rays. To prevent any impact of the atmosphere, the cells were disassembled in an argon filled glove box and vacuum sealed in transparent foils. For imaging of the cross-sectional area, the electrodes were bisected prior to sealing.

3D imaging of a graphite anode after cycling in full cells shows distinct amounts of both transition metals on its surface as well as in its volume, as obvious from figure 7.12. The measurement was performed at the FLUO beamline at ANKA, having a spatial resolution of 10x10x10 μm^3. K_α-lines were employed for the analysis of all elements. For determination of the amounts of transition metals incorporated into the graphite anode and thus leached from the cathode, the electrode was dissolved in HNO_3 using microwave assisted dissolution and afterwards analyzed by graphite furnace atomic absorption spectrometry as well as by total reflection X-ray fluorescence. Whereas the pristine anode contained no detectable amounts of manganese or nickel, in the cycled one about 4 % of both transition metals, referred to the original contents present in the LNMO cathode, were detected. This again proves distinct transition metal dissolution from the cathode, which afterwards migrate trough the electrolyte towards the anode. Pieczonka et al. also found the same amounts of both transition metals on the surface of the anode at 100 % SOC.[176] Minor amounts of gallium were detected in the aluminum current collector, which was used for its indication in the 3D image.[222] While its detection is very sensitive, the direct analysis of Al was not possible due to its high response level.[222] Surprisingly also small amounts of copper were detected on cycled anodes. This element is not present in the employed contacts, but trace amounts of Cu are present in Al alloys, so that it is possibly leached from the current collectors and accumulated at the anode surface during cycling. In comparison to nickel and manganese its amounts were very low. There are, however, distinct differences in the distribution of copper in comparison to Mn and Ni at the anode. While the latter two species are located in pore-like features all over the anode bulk, copper is only present in plaques on the surface. One possible explanation for this diverging behavior is that copper is readily reduced at the electrode surface, whereas the other two transition metal ions show reduction at lower potentials on the graphite and are transported deeply into the pores.[222]

2D scans over the cross-sectional surface of LNMO cathodes cycled in half cells were recorded at beam line P06 at PetraIII at the DESY in Hamburg to study the influence of the SOC on the oxidation state and distribution of the two transition metals. Comparison of the XANES spectra show that deviation between the charged and discharged species is large around 8340 and 8353 eV, so that 2D scans were recorded at these energies to monitor

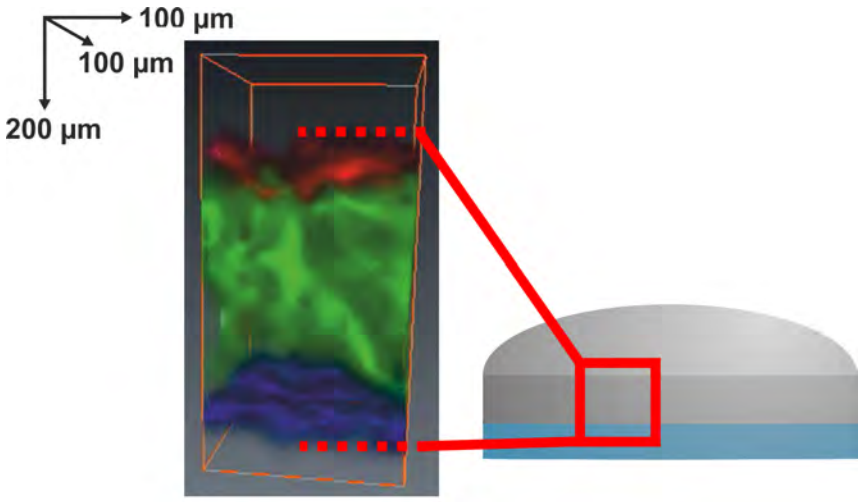

Fig. 7.12.: *3D cross-sectional XANES measurement of the elemental distribution in a graphite anode cycled in a full cell using LNMO as cathode. Kα-lines were employed for determination of all elements. Ga (presented in blue) is contained in trace amounts in the aluminum current collector, thus being employed for its indication in the image. Ni (green) and Mn show very good correlation, so that only the former one is presented. Copper is shown in red.*

spatial distribution of the different species. For better contrast, the scans at both energies were related, thereby expecting a value of about 1.9 for the discharged electrode, i.e. Ni^{2+}, and approx. 4.3 for the charged one ($Ni^{3+/4+}$). The images depicted in figure 7.13 indicate relatively homogeneous charge and discharge. Nevertheless, there are less efficiently cycled regions, i.e. lower amounts of $Ni^{3+/4+}$ for the charged and less Ni^{2+} for the discharged one, close to the current collector especially for the charged electrode. This leads to the conclusion, that not the whole electrode is accessed during cycling. The migration of Li^+ into and out of the cathode during discharge and charge, respectively, determines the rate of these processes.[223] Thus, they do not reach lower electrode regions close to the current collector during the finite time that allows diffusion during CV measurements as well as during cc cycling with higher C rates. These measurements show a bit higher Mn:Ni ratio close to the electrolyte side of the cathode in comparison to that near the current collector, thus pointing to migration effects. It also indicates, that nickel is a bit more leached into the electrolyte. Measurement artifacts like regions of different absorption due to varying elemental concentration and density, however, have to be kept in mind. But further data analysis points to negligible influence.[223]

The measurements presented in this section show distinct dissolution of both transition metals, which seems to be even more severe for nickel. This not only leads to loss of active material on the cathode side of the LiB, but since their redeposition on the anode was proven, they also impact the anode. They can be there incorporated in the SEI, thus

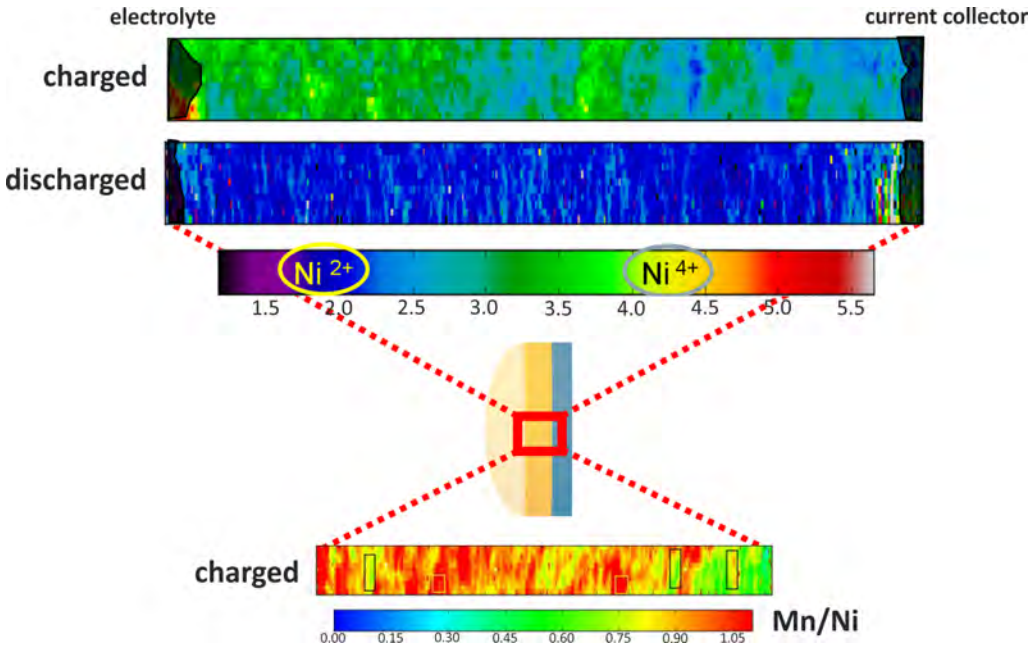

Fig. 7.13.: *2D cross-sectional scan of a charged as well as of a discharged LNMO electrode, each cycled in a half cell showing the distribution of the nickel oxidation state. For the charged electrode also the transition metal ratio is presented.*

leading to further lithium loss and the formation of even thicker and in consequence more resistive surface films. This further reduces cell capacity, which was also reported by Kim et al. and Pieczonka et al.[176,178]

7.8. Discussion regarding data quality & reliability of the LNMO thin film model system

To the best of the knowledge of the author, there are only very few SIMS studies dealing with the CEI formation on the cathode side of LiB.[85,176,188,191,196] Investigations by Lu and Harris dealt with films formed on copper disks, mainly concerning the lithium diffusivity in the CEI.[196] Copper was used to eliminate insertion, thus allowing to focus on transport between electrolyte and CEI as well as within the CEI. Investigation by Cho et al. concentrated on the benefit of a polyimide coating on the amount of LiF deposited on LNMO cathodes during cycling.[85] The group of Marcus studied CEI formation on thin Cr_2O_3 films.[188] Thus, only Pieczonka et al. and the group of Roling studied the CEI composition employing LNMO cathodes in detail.[176,191] However, Pieczonka et al. investigated only technical electrodes, so that the comparison with our own measurements is interesting. Keeping in mind the distinct roughness of those electrodes, it is however ques-

tionable, how the CEI thickness in the range of $3-10\,\mathrm{nm}$ could be resolved. Pieczonka et al. used a $30\,\mathrm{kV}$ Au^+ ion source for both sputtering and analysis, thereby employing a analysis and sputter area of $(50\,\mu\mathrm{m})^2$ and $(200\,\mu\mathrm{m})^2$, respectively. For depth calibration, they used the erosion rate determined for SiO_2, thus assuming the same sputter yields for this rather dense and hard phase and the porous and chemically "Soft" CEI. This procedure appears clearly not adequate. This assumption should lead to underestimation of the CEI thickness. The erosion rate given by Pieczonka et al. is with $0.1\,\mathrm{nm/s}$ a bit higher than that determined for our own CEI investigations. Taking the higher sputter yield in less dense, organic matter into account, it should be even higher, so that our own in-depth resolution appears to be somewhat higher. The group of Roling investigated LNMO thin films deposited by spin coating onto Au-coated stainless steel.[191] They delivered no information about sample roughness, but from AFM images it seems to be in the range of $70\,\mathrm{nm}$, thus being nearly one order of magnitude higher than for the own thin films. They used Bi^+ primary ion gun like in the own investigations, but employed an O_2^+ sputter gun, scanning over an area of $(300\,\mu\mathrm{m})^2$ and delivering a current around $200\,\mathrm{nA}$. Since in own measurements a sputter current of approx. $30-60\,\mathrm{nA}$ was employed, the own in-depth resolution seems to be a bit higher. Crater depth was measured like during the own investigations by profilometer.

The group of Marcus also employed a Bi^+ primary ion source delivering a current of $1.4-1.8\,\mathrm{pA}$ over an analyzing area of $(100\,\mu\mathrm{m})^2$.[188,192–194] The energy of the Cs^+ sputter gun was in the range of $250\,\mathrm{eV}$ - $2\,\mathrm{keV}$, resulting in a $25-100\,\mathrm{nA}$ target current eroding a $(250\,\mu\mathrm{m})^2$ - $(300\,\mu\mathrm{m})^2$ area.[188,192–194] Since in the own measurements a sputter ion energy of $500\,\mathrm{eV}$, but a greater sputter crater of in most cases $(450\,\mu\mathrm{m})^2$ was used, the in-depth resolution of the interface film in our own measurements is even improved compared to Marcus' experiments. Before transfered to the SIMS chamber, the samples of Marcus had in contrast to own measurements, in most investigations short air contact. This might have caused partial oxidation of the surface film and thus changed its composition. Often only the sputter time, but not the actual depth was reported in depth profiles, so that the thickness of the different layers cannot be estimated. Variations in sputter currents due to measurements at different days were also not taken into consideration. At least for the sputter gun used in our own investigations the current varied between $30-60\,\mathrm{nA}$, i.e. it could almost double. This results one the one hand from aging of the ion gun and on the other hand from imperfect focus of the ion beam. Thus it is unclear from the report, how the SEI thickness formed on Sn-Co alloys was estimated to approx. $10\,\mathrm{nm}$.[193] For Cr_2O_3 cathodes the sputter yield and thus the depth information was estimated by taking the sputter ion current into consideration, the total sputtering yield of metallic chromium given by the Ion-Spec software of the SIMS machine, the charge of the sputtering particle,

the atomic density of the sputtered material and the dimensions of the scanned area.[188] This procedure results in a sixfold higher sputter yield compared to the one determined by taking into account the external measurement of the thickness of the chromium oxide, thus being rather ambiguous. The application of this method is limited to well known materials, but not suitable for e.g. LNMO, since parameters like the sputtering yield lack for this compound in the SIMS software.

In conclusion, the own SIMS data concerning CEI investigation are considered as reliable and well comparable to others reported in literature. In comparison, the in-depth resolution appears to be even improved.

According to Ivanova et al.[62] the electrode particle size influences the CEI, see chapter 3.2. This challenges the comparability of results achieved on thin film model systems with those on technical electrodes, since dimensions of the two systems are completely different. A comparison of the data gained by Pieczonka et al. on technical electrodes with own measurements is of particular interest. Pieczonka et al. determined the CEI thickness to about $10 - 15\,\mathrm{nm}$ after storage for 60 days at $60\,^{\circ}\mathrm{C}$. Data of cycled electrodes are unfortunately not reported, so that comparison to thicknesses determined in own measurements is impossible. For the CEI of stored electrodes, however, about the same values were determined, thus pointing to a comparable CEI thickness. The authors also found enrichment of PO_3^-, C_2H^- and MnF_3^- as well as NiF_3^- in the surface layer, thus again revealing good agreement between results achieved on technical and thin film LNMO cathodes. The authors did not report the stacked setup of the CEI. Investigation of this composition gradient is from their data due to the small CEI thickness rather difficult. However, small shift between the maxima of organic and inorganic species points to the same composition gradient also observed for thin film LNMO electrodes in own measurements. Results by the group of Roling also point to a stacked setup of the CEI with more organic species on its electrolyte side.[191] They authors determined its thickness to approx. $50\,\mathrm{nm}$.

Unfortunately, the group of Roling and Pieczonka et al. report only a few SIMS measurements, but those presented point to relatively good comparability between each other as wells as to the own data regarding both CEI thickness and composition. This leads to the conclusion, that LNMO thin films are indeed a good model for a more detailed CEI investigation, thereby allowing to some extent transfer of the results to electrodes employed in commercial cells. This only holds for the behavior of the pure cathode material. It has to be kept in mind, that technical electrodes contain non-negligible amounts of conductive carbon and binder besides the active material. These also might react with the electrolyte and its decomposition products. Electrochemical investigations deliver almost identical responses for both types of electrodes, so that large impact of side reactions between additives and other cell parts could be excluded in the present case. For further clarification

both types of electrodes should be cycled and investigated under identical conditions, thus revealing even small differences. Due to their large roughness, resolution of the CEI on technical electrodes by SIMS will always be poorer in comparison to thin film electrodes. Thus, detailed investigation of this surface layer requires thin film electrodes and technical electrodes mainly serve as comparison, that the overall features are the same.

7.9. Model of CEI formation

The data achieved with mainly SIMS and electrochemical investigations lead to the following model for the CEI formation on LNMO electrodes, which is in good accordance with results reported so far in literature for LNMO as well as LMO electrodes. It even complete these, and according to Aurbach et al. the structure of this surface film was not yet clarified for the nickel containing manganese spinel.[20]

In accordance with literature the CEI on LNMO thin film electrodes is composed of organic, partially polymeric as well as of inorganic species Li_2CO_3, $Li_zPF_yO_x$, P_2O_5 and MF_x with M = Mn, Ni.[20,39,165,166,168] It exhibits a stacked structure like the SEI on the anode with primary organic species on its electrolyte side and inorganic phases close to the electrode surface. However, this sequence is reverse to that reported by the group of Edström and Eriksson on the nickel free manganese spinel.[166,167] Results by the group of Roling and Pieczonka et al. on LNMO electrodes nevertheless also result in the same composition gradient found in own measurements.[176] Thus, the discrepancy to the results by the group of Edström and Eriksson may simply be caused by the presence of nickel.

The first cycle in electrochemical measurements looks quite different than subsequent ones and shows an irreversible capacity at about 4.2 V, a distinctly higher current in the high voltage range and a lower coulombic efficiency, thus showing a large contribution of side reactions. This leads to the conclusion that the CEI formation mainly takes place during the first cycle and afterwards prevents to a large extent reactions between cathode and electrolyte. Stable coulombic efficiencies are reached after about three to six cycles, so that minor CEI formation also occurs during a few later cycles. Afterwards, charge and discharge capacities remain rather stable, thus showing effective protection. Irreversible capacities between 3.8 and 4.3 V vs. Li/Li^+ were also observed by Zhang et al. using $LiMn_2O_4$ electrodes, attributing them to electrochemical oxidation of the electrolyte solvents, since carbonates can be oxidized already at potentials as low as 2.1 V vs. Li/Li^+. Above 3.5 V its rate of oxidation substantially increases.[170] From SEM images complete coverage of the electrode with this surface layer is obvious. The distinct decrease of the current close to 5.0 V during electrochemical measurements with cycle number due to electrolyte oxidation also points to effective protection of the cathode and prevention

of reactions between electrolyte and active material. The complete coverage of the cathode surface already at room temperature is in accordance with results by Duncan et al., also achieved on LNMO electrodes.[165] It however contradicts findings by Edström et al., who reported only partial covering at this temperature for the nickel free spinel.[166] This highlights the remarkable capability of LNMO to form stable and protective surface layers, which do not hold for most other cathode materials.[20] However, in accordance with literature, the CEI thickens with cycle number as well as storage time.[166]

Determination of the exact CEI thickness is rather difficult using SIMS due to varying sputter yields over the crater depth sputtered during depth profiling through the CEI, the LNMO thin film and a bit into the Pt layer. However, a rough estimation delivers a CEI thickness of about 50 nm for electrodes cycled at room temperature, being in good agreement with the 45 nm determined by TEM. The measurement of the CEI thickness in dependence of the SOC reveals a bit thicker surface layer in the charged (stored at $4.85 - 5.0\,\mathrm{V}$) than in the discharged (stored at 2.9 V) state, presumably resulting from enhanced electrolyte oxidation in the high voltage range. In accordance with literature the CEI also thickens with temperature, with enhanced reaction kinetics as main reason for this effect rather than promotion of new reactions.[165,167]

Presence of organic species in the CEI results from decomposition of the electrolyte solvent molecules DMC and EC. Thereby, oxidation of the latter molecule is assumed to be the main source for formation of polymer components, because it is more likely to be oxidized at the positive electrode due to its in comparison to DMC higher dielectric constant.[9,173] PF_6^- anions will be thus preferentially solvated by this species.[173] By application of a positive potential, these anions and with them the EC molecules will enrich in the double layer at the cathode, where their oxidation occurs. Moreover, due to its higher polarity, EC will be the preferred target of electrophilic and nucleophilic attacks by contaminants in the electrolyte.[173] According to Aurbach et al. the polymerization of EC is not blocked by the growth of the CEI, as it does not propagate by electron transfer from the cathode, but by the reaction of partially polymerized species with solvent molecules.[169] Thus, no direct electrode contact is needed, which again makes the observed microstructure with more organic species at the electrolyte side of the CEI more likely. Polymerization of EC occurs according to the following equation:[165–167]

$$2n(CH_2CH_2)OCO_2 \rightarrow \text{-}[(CH_2CH_2O)_x\text{-}/\text{-}(CH_2CH_2OCO_2)_y]\text{-}_n + nxCO_2 \tag{7.1}$$

EC decomposition is for instance initiated by strong Lewis acids like e.g. PF_5, formed by the decomposition of the electrolyte salt $LiPF_6$ according to the following reaction:[39,166,167]

$$\begin{aligned} \mathrm{LiPF_6(sol.)} &\rightarrow \mathrm{LiF(s) + PF_5(g)} \\ \mathrm{PF_5(g) + H_2O(l)} &\rightarrow \mathrm{2HF(sol.) + POF_3(g)} \\ \mathrm{2POF_3(g) + 3Li_2O(s)} &\rightarrow \mathrm{P_2O_5(s) + 6LiF(s)} \end{aligned} \tag{7.2}$$

P_2O_5 may further react with Li_2O and LiF:

$$\begin{aligned} \mathrm{1/2P_2O_5(s) + 3/2Li_2O(s)} &\rightarrow \mathrm{Li_3PO_4(s)} \\ \mathrm{1/2P_2O_5(s) + 1/2Li_2O(s) + LiF(s)} &\rightarrow \mathrm{Li_2PFO_3(s)} \end{aligned} \tag{7.3}$$

The commonly used electrolyte salt $LiPF_6$ shows poor temperature stability. Its decomposition reaction takes already place at $60 - 85\,^{\circ}\mathrm{C}$.[171] The presence of water even accelerates this process either at temperatures of more than $40\,^{\circ}\mathrm{C}$ or at potentials higher than 4.0 V vs. Li/Li^+. Thereby, HF is formed, which reacts with the cathode, thus creating new water molecules. Thereby, decomposition of the electrolyte salt proceeds, until the water molecules completely disappear.[172] Decomposition of the electrolyte salt moreover results in the presence of inorganic species like $Li_zPF_yO_x$ and P_2O_5 in the CEI.

The presence of carbonates in the CEI also results from decomposition of EC and DMC according to the following equation; since the formed products are unstable at elevated temperatures, they rather transform into the more stable Li_2CO_3:[167]

$$\begin{aligned} \mathrm{2CH_2CH_2OCO_2 + 2}e^- + \mathrm{2Li^+} &\rightarrow \mathrm{(CH_2OCO_2Li)_2 + C_2H_4} \\ \mathrm{CH_3OCO_2CH_3} + e^- + \mathrm{Li^+} &\rightarrow \mathrm{CH_3OCO_2Li + CH_3^\bullet} \end{aligned} \tag{7.4}$$

LNMO electrodes suffer from distinct transition metal dissolution into the electrolyte, which finally end up at the anode. This leaching in consequence results not only in capacity fading due to loss of active material, but also impacts the anode side of the LiB, possibly leading to thicker SEI films with subsequent loss of active lithium and the formation of more resistive surface films, also being reported by Pieczonka et al.[176] This is one explanation, why LNMO full cells show drastic capacity fading, since in these lithium is not present in excess in contrast to half cells. Due to presence of fluorine ions, for instance from electrolyte salt decomposition, HF forms. It in turn could react with the cathode material, thus leading to formation of MF_x with M = Mn, Ni species in the CEI according to the following equation (modified from Aurbach et al.[67]):

$$\mathrm{4LiNi_{0.5}Mn_{1.5}O_4 + 8HF} \rightarrow \mathrm{2}\lambda\mathrm{-MnO_2 + MnF_2 + NiF_2 + 4LiF + 4H_2O + 2Ni_{0.5}Mn_{1.5}O_4} \tag{7.5}$$

In accordance with results by Pieczonka et al. and Aurbach et al. the dissolution of

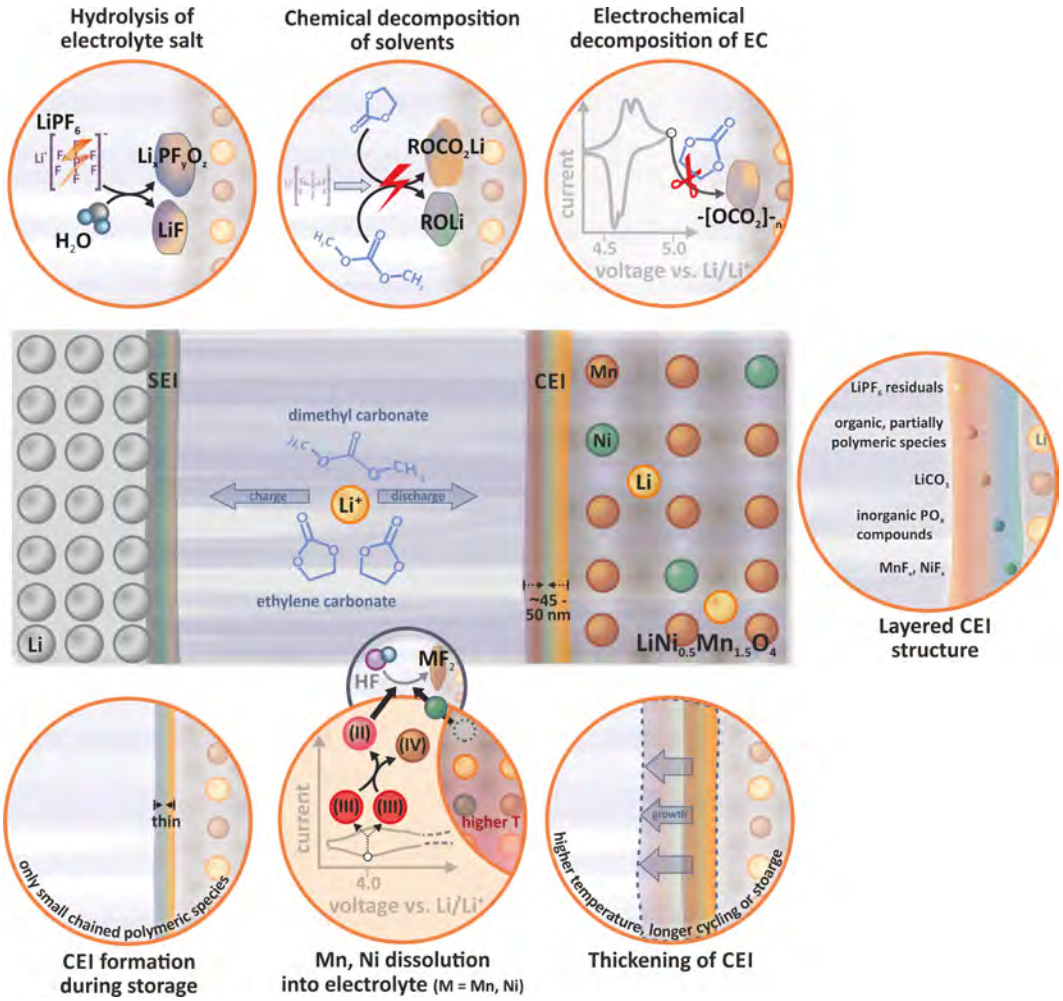

Fig. 7.14.: *Summary of the results collected by SIMS and electrochemical investigation concerning the CEI setup on LNMO electrodes. In the upper row the formation of species in the CEI due to electrolyte salt and solvent decomposition is sketched and on the right side its stacked microstructure is presented. In the lower row the impact of different treatments on the CEI thickness and composition as well as CEI species due to transition metal dissolution are depicted.*

nickel is even more severe than that of manganese.[67,176] Rising the lower cut-off-voltage above 4.0 V, where formation of Mn^{3+} occurs, tending to disproportion with subsequent dissolution of Mn^{2+}, as well as temperature reduction from 60 °C to room temperature distinctly lowers their leaching. Impact of the temperature is explained by hydrolysis of the electrolyte salt $LiPF_6$, occurring at 60 °C.[176]

Participation of SEI species from the anode in the setup of the CEI, as reported by Aurbach et al., could yet not been proven with the analytical techniques available.[177] Cycling was mainly performed using lithium and only in minor cases graphite anodes

were used. There are however several other components in the cell, that also contain lithium and carbonaceous species like the electrolyte salt and solvents. Thus, there are manifold explanations for the occurrence of both elements in the CEI and their origin from the anode or its SEI could not be verified. Evidence for a transport from the anode side could for example be gained with *in situ* techniques, enabling the time resolved monitoring of the location of these species in the cell.

CEI formation takes not only place during cycling, but already during storage of LNMO electrodes assembled in uncycled cells or in pure electrolyte. This phenomenon was also reported by the group of Edström and Eriksson, who detected essentially identical surface films for both electrochemical cycled and stored films at a given temperature.[39,166,167] According to them, only minimal differences between both treatments exist, since the kinetics for the surface film formation may be more favorable during cycling due to enhanced mass transport in the electrolyte.[167] The own measurements agree with these findings, since the CEI films after storage are distinctly thinner in comparison to that observed on cycled electrodes. They also lack in longer chained polymer species, thus also pointing to slower kinetics during mere storage.

A summary of the model mainly gained by SIMS and electrochemical investigation concerning the CEI setup on LNMO electrodes is given in figure 7.14. In this image only results gained in own measurements are depicted. To date a detailed CEI investigation on LNMO thin films completely lacks. Only a few studies dealt with the composition and formation mechanism of the surface film on technical LNMO electrodes.[67,165,168,176] Its buildup of organic and inorganic species was reported as well as a variation of its composition with temperature, SOC and storage.[67,165,168] Dissolution of both transition metals was detected.[67,168,176] Investigations e.g. on the nickel free counterpart helped to complete the model.[117,166,167] However, studies often investigated just one aspect in detail, like e.g. transition metal dissolution, operation at varying cycling conditions or storage. Impact of varying cathode materials, not only the difference between LNMO and LMO, but also slightly different preparation or investigation methods thus has to be kept in mind regarding the CEI model sketched so far in literature. This study analyzes a larger variety of different influences and factors on the CEI formation under the same investigation conditions for - as far as possible - identical samples, thus minimizing parasitic effects. This results in a more complete and more reliable picture of this surface film. To the best of the knowledge of the author the stacked microstructure of the CEI was not investigated before in detail on this cathode material; CEI thickness was previously only reported by the group of Roling.[191] The results presented in this thesis reveal that a number of parameters like temperature and cycle number, storage time prior and after cycling at different SOCs influence the CEI. The exact cell setup also may impact it, since imperfect

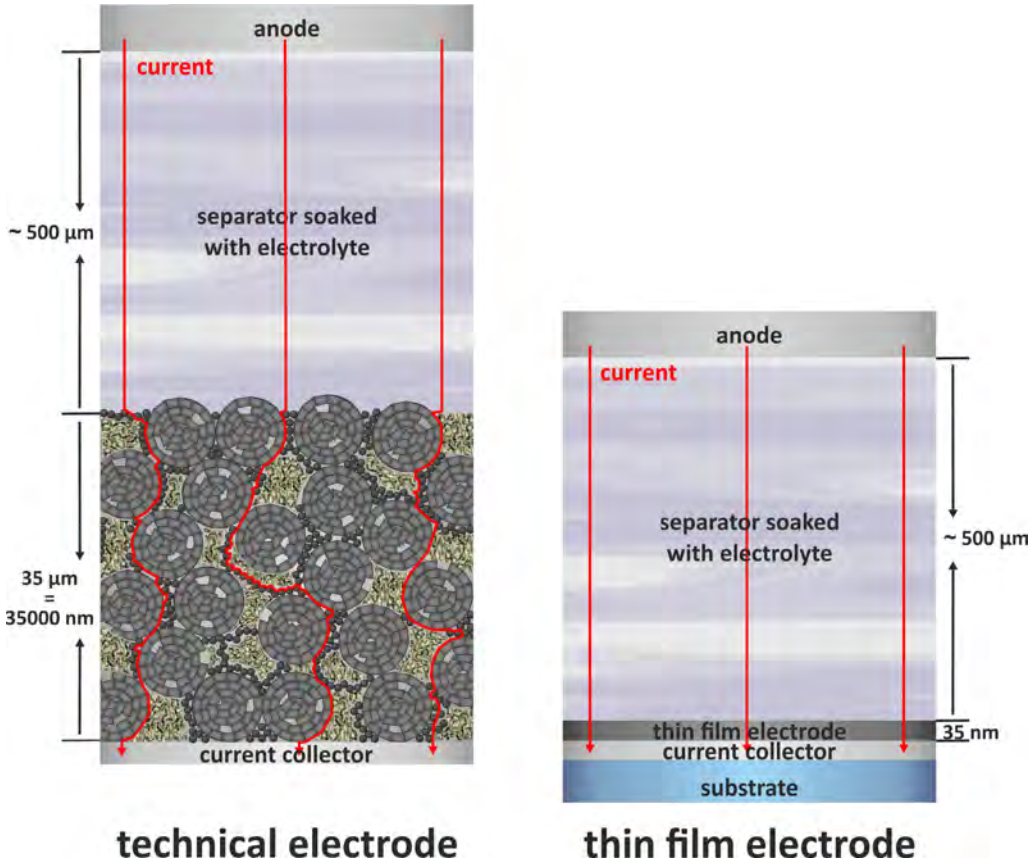

Fig. 7.15.: *Schematic sketch comparing technical and thin film electrodes with respect to parameters like dimensions, structure as well as composition and current density. Due to distinct difference between the dimensions of technical and thin film electrode as well as the electrolyte, the graphic only tries to visualize the differences, but delivers no exact scale.*

alignment of anode and cathode may result in local differences in current densities and thus in varying CEI thicknesses. Different deposition conditions of the thin films cause varying roughnesses, which could affect the apparent CEI thickness during SIMS measurements. Since only an average sputter yield is available, depth profiles sputtered to diverging sample depths, i.e. stopping short after the rather soft CEI with high sputter yield vs. sputtering deeply into the hard substrate, also should result in varying CEI thicknesses. In consequence, in further studies care has to be taken, that sample and cell preparation as well as cycling and measurement conditions are reproduced as well as possible to exclude parasitic effects. Thus, even tiny differences should be detectable, resulting in a more detailed picture of the CEI.

Despite the promising results achieved with the thin films investigated in this thesis, question of its reliability as suitable model system for technical electrodes remains. In

figure 7.15 technical and thin film electrodes are compared. Due to their rough and porous structure the surface of technical electrodes is distinctly larger than than of thin film electrodes. They contain besides the active material also conductive carbon and binder, thus further complicating the calculation of the actual surface. However, taking in consideration, that the LNMO particles - having a size in the low µm range - are composed of primary particles of approx. 100 nm, their actual size and geometry is comparable to the dimensions of the thin films. Thus, on a microscopic scale both types of electrodes show better conformity as expected from their macroscopic appearance. However, the comparability of the current densities for both types of electrodes is questionable. While it can be easily calculated for thin film electrodes due to their simple geometry, it is rather difficult for technical electrodes. Assuming spherical particles, at the connection points between them, the current densities are very high, while they are in other regions distinctly lower. The locally very high densities might result in higher reactivity in these regions, thus promoting additional reaction products. A detailed calculation is beyond the scope of this thesis, but is necessary for a detailed study of eventual differences between technical and thin film electrodes. The thickness of technical electrodes is approx. two to three orders of magnitude higher in comparison to thin film electrodes. In consequence the electrolyte volume is distinctly larger with respect to the active electrode mass for the thin films. Thus, more active material can dissolve in the electrolyte. This might explain the large amounts of transition metal ions which dissolved from the thin films during cycling. For better comparison between technical and thin film electrodes in future investigations the electrolyte volume should be scaled to the actual active electrode mass. The use of cells scaled this way together with modified thin film electrodes which contain also some binder and conductive carbon would on the one hand complicate the system concerning CEI investigation, but on the other hand would mimic the features of technical electrodes even better.

8. Conclusion and outlook

This thesis reports on the investigation of the cathode electrolyte interface formed on LNMO electrodes. This high voltage cathode material was chosen due to its unique surface chemistry caused by presence of nickel in the lattice, resulting in higher nucleophily of the oxygen ions.[20] The surface oxygen species thus nucleophilically attack the electrophilic alkyl carbonate molecules, thereby building up a rather stable and protective surface film.[20] Since SIMS was employed as main characterization tool, requiring flat surfaces for reliable investigations, LNMO thin films were prepared by PLD. Using platinum covered YSZ single crystals, by adjusting the deposition parameters, roughnesses of less than 10 nm could be established. Main improvement was achieved by variation of the temperature and the oxygen partial pressure. Since deposition at temperatures of more than 800 °C resulted in partial delamination of the electrode layer if thicker LNMO films were deposited, the pulse number had to be reduced to prevent greater stresses in the deposited films. Thereby, successful deposition at temperatures as high as $950 - 1000$ °C was possible, delivering smooth, well crystalline films about 40 nm in thickness showing the cubic spinel structure.

Lowering the electrode thickness unfortunately also the capacity reduces, thus complicating the electrochemical investigation of the thin films. The characteristic features of the LNMO were hardly detectable both during CV as well as during CP measurements, due to very small currents. This problem was overcome by calculation of the differential capacity out of the cc data, allowing to identify even very tinny electrochemical responses. Thus, successful cycling of the thin films in half cells using common carbonate based electrolyte could be confirmed. The films thereby showed the response characteristic for (technical) LNMO electrodes without any visible side reactions, thus emphasizing its suitability as model system.

Employing SIMS depth profiling with a depth resolution of about 2 nm, the structure and composition of the CEI formed on this electrode material was eludicated. The CEI model presented so far in literature has been completed. To the best of the knowledge of the author, SIMS investigations of the CEI on LNMO electrodes were only performed by Pieczonka et al., who studied technical LNMO electrodes and the group of Roling, who investigated thin film electrodes. However, they reported no detailed investigation of the

CEI. Comparison of the results by the group of Roling and Pieczonka et al. with own data proved the reliability of the LNMO thin film electrodes as suitable model systems for CEI investigation, thus allowing at least to some extent the transfer of the results to electrodes employed in commercial cells.

SIMS investigations revealed a stacked microstructure of the CEI similar to the composition gradient of the SEI on the anode with more organic species on its electrolyte side and more inorganic ones close the the electrode. Although the CEI appears as rather dense in SEM and electrochemical investigations, its thickness increases with cycling number and storage time, thus showing only an incomplete prevention of the reactivity between cathode and electrolyte. However, distinct reduction of the current due to electrolyte oxidation in the high voltage range after the first cycle, in which main CEI formation took place, points to relatively effective protection. The thickness of the CEI also increases with temperature, presumably mainly caused by enhanced kinetics and increased degradation of the electrolyte salt $LiPF_6$, thus initiating further decomposition reactions. Storage in electrolyte and assembly in an uncycled cell already results in formation of a thin CEI.

Despite the promising results achieved with the thin films investigated in this thesis, some doubts about its reliability as suitable model system of technical electrodes remains. Although at first glance the CEI investigation of LNMO thin film electrodes reveals good agreement with those on technical electrodes, some problems remain unresolved, like e.g. the complete failure of full cells employing LNMO thin film cathodes. Possibly the limited fraction of lithium is completely consumed by CEI/SEI buildup during the first charge. This appears to be reasonable in view of the large irreversible capacity observed during electrochemical measurements. The lithium ions are thus trapped and cannot participate in (dis)charge reactions, leading to failure of the cell. This effect is less pronounced for full cells employing technical electrodes, since they contain much more lithium than the about three orders of magnitude thinner thin films investigated for this thesis. To overcome this "gap" to technical electrodes, also observed e.g. in heterogeneous catalysis ("materials gap" or "pressure gap" by transfer of results gained on simplified, clean systems under UHV conditions to commercial catalysts employed at ambient pressure[15]), the use of modified thin film systems is required. These should be thicker, not ideally flat and should even contain some percent of binder and conductive carbon at the expense of simplicity and depth resolution during analysis. This "compromise" hopefully entails to some extent features from both types of electrodes, i.e. sufficient flatness for reliable analysis from the thin films and composition as well as structure with some roughness and porosity of technical electrodes.

Like technical LNMO electrodes, thin films suffer from distinct dissolution of both transition metals, being for nickel even severe than for manganese. This results not only in

loss of active material but they travel through the electrolyte and reach the anode, as proven by XANES measurements. They might also be incorporated in the anode SEI, going along with additional lithium loss and formation of even thicker and more resistive SEI films. To overcome this problem, "artificial" CEI layers, which should protect leaching of the cathode material and even better prevent reactions between it and the electrolyte should be tested in further investigations. Another aspect in ongoing experiments is the establishment of a measurement setup for *in situ* SIMS investigations. Both topics will be sketched in the following and some preliminary experiments will be briefly reported as part of an outlook.

8.1. *In situ* SIMS study of the CEI builtup

Of special interest during *in situ* SIMS investigations is the first charge. It shows distinct differences to the subsequent ones, that are assigned to CEI formation, like for instance the irreversible capacity around 4.2 V. Using an *in situ* SIMS measurement coupled with electrochemical investigations, stepwise charging interrupted by SIMS analysis could be performed, thus possibly enabling a relation between the irreversible features in the electrochemical measurement to the appearance of different species in the CEI. Performance of the same experiment *ex situ* is rather time consuming and afflicted with errors, since the cell has to be disassembled in a glovebox after each charging step, transferred to the SIMS and after the analysis reassembled in a cell for further cycling. It has to be kept in mind that repeated exchange of anode and electrolyte may strongly impact the CEI setup. Moreover, best comparability between the single measurements should be reached, if always approx. the same area is analyzed to avoid influence of different contacted areas on the CEI thickness. In regions further away from the cathode current collector or in those, not perfectly aligned to the anode possibly lower currents flow. It is, however, rather difficult to relocate the same position in the SIMS machine once the sample was removed from the sample holder. These problems could only be overcome during *in situ* studies. They nevertheless bear other difficulties like suitable cell geometries and the vapor pressure of the electrolyte. The vapor pressure of common carbonate based electrolytes is much too high for its use in UHV chambers, whereas that of ionic liquids is low enough. Fortunately, cycling with ionic liquid based electrolytes using $LiPF_6$ as conductive salt succeed for thin film electrodes and CEI formation was proven using SIMS.

In principle, a horizontal cell setup as well as a vertical, stacked one, both schematically sketched in figure 8.1, are possible. In the former geometry one electrode is placed on the left and the other on the right side of the cell, separated by a small region of electrolyte. In contrast, in the stacked setup the anode is located on top, followed by a very thin separator

soaked with electrolyte and underneath the thin film cathode is placed. Realization of the horizontal setup is difficult, since the electrolyte gap has to be small for flow of sufficiently high currents. In addition only the upper side of the cathode could be investigated, that is hardly wetted with electrolyte, and the main current and thus CEI formation should occur at the side facing the anode. Moreover, using this setup only the SIMS imaging modus with its drastically reduced lateral resolution of maximal 200 nm, but no depth profiling, could be performed. Taking in mind the extension of the CEI of only about $45 - 50$ nm, it surely will not be properly resolved. The stacked cell setup thus seems to be more suitable. The anode should be shifted a bit aside from the center of the cathode. Thus sputtering does not have to be performed through the former electrode during depth profiling to reach the cathode/electrolyte interface. Thereby, current distribution will not be optimal, but if the cathode current collector is placed at the opposite side of the cathode, at least some contribution - and therefore CEI formation - also should occur in the region close to the edge of the anode.

To avoid splashing of the liquid electrolyte during depth profiling, it should be frozen during the analysis and defrosted for further cycling. This is possible in the SIMS chamber with a special sample holder equipped with a copper cooling tip and a heating plate, thus allowing fast cooling and heating. It it equipped with a thermocouple and two electric contacts, enabling cycling inside the SIMS chamber. This sample holder was already successful employed during quasi *in situ* study of solid oxide fuel cell cathodes.[224] First measurements were already performed on LNMO thin film half cells and charging inside the SIMS chamber indeed succeeded. Instead of the commonly used Whatman™ separator a Cellgard® one was employed, since it is distinctly thinner (10 µm) and smoother, thus minimizing the sputter time to reach the separator/cathode interface. Assuming typical erosion rates achieved during SIMS depth profiling of approx. 1 µm/h, it is anyhow too thick to perform measurements in an acceptable time. Thus, the search for even thinner separators is required. Cycling tests using cells without separator, instead employing a thin teflon ring filled with electrolyte for physical separation of cathode and anode, however did not work up to date for technical as well as for thin film LNMO cathodes. Nevertheless, in first measurements using a Cellgard® separator, depth profiling succeeded without any obvious problems. Due to large time consumption of these measurements, it was however stopped before the separator/cathode interface was reached, but could be used as proof of principle. By performing these measurements in the proposed way, eventually also the diffusion coefficients of manganese and nickel through the electrolyte towards the anode could be determined.

Although LNMO thin film electrodes turned out as suitable model for principle CEI investigations, comparison to technical electrodes is sometimes desirable. Due to the

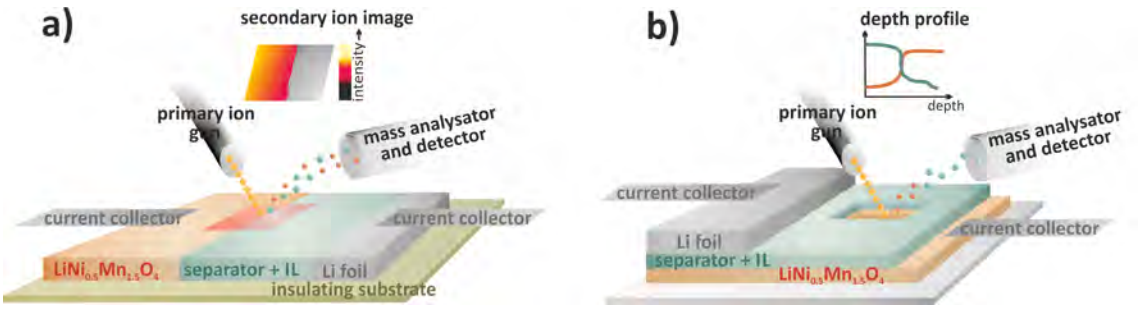

Fig. 8.1.: *Schematic sketch of cell designs for in situ SIMS measurements: a) horizontal, b) vertical setup.*

large roughness of technical electrodes, resulting in rather smeared depth profiles, resolution of the CEI on technical electrodes did not succeed yet. Using principle component analysis (PCA), a reduction of the topographic influences on the secondary ion image is possible.[103,225] This hopefully enables analysis of these rough electrodes in future.

In situ XANES experiments have been proven as quite useful. The principal measurement setup and equipment are well available. These measurements enable the study of the distribution of both transition metals not only in the cathode, but in the whole cell. Thereby, hopefully their exact dissolution and migration process will be resolved, i.e. at which potentials are they preferentially leached. Does lowering the higher cut-off limit during cycling or rather rising of the lower one reduce their dissolution? How many cycles are needed for their transfer through the complete cell to end up at the anode?

8.2. Artificial CEI for protection of the cathode

As obvious from chapter 7.7 LNMO thin film as well as technical cathodes suffer from distinct transition metal dissolution into the electrolyte.[168,176] By coating of the active material, this effect can be suppressed to a large extent. In the literature mainly metal oxides, like for instance Al_2O_3 and TiO, are successfully applied to mostly technical electrodes.[84,86] The question arises, if these coatings completely cover the whole cathode particle, thus shielding it from direct electrolyte contact, or whether they are rather spread over the cathode surface as small particles. They thus act not as physical barrier, but protect the cathode rather by catching reactive species initiating transition metal dissolution like HF.[8,89] The latter aspect seems to hold for LTO.[89] Distinct longer cycle life and reduced capacity fading was achieved with LTO coated separators in LNMO-graphite full cells.[226] Benefit of this electroactive separator is its capability to scavenge electrolyte decomposition products formed at LNMO cathodes due to their high electrochemical potential, as well as Mn^{2+}. These species are presumably reduced at the separator surface.

Its employment indeed results in distinct reduction of the manganese content on the anode. Due to its lithium conductivity LiPON is also interesting as protection layer.[69] It not only reduces the manganese dissolution, but also improves both rate performance and capacity retention. This coating is assumed to slow down the resistance increase at the cathode/electrolyte interface by forming a slightly thinner reaction product layer on the cathode surface compared to the uncoated one.[69]

In first tests, LNMO thin film cathodes were coated with thin TiO_2, LTO and Al_2O_3 by PLD, as well a by LiPON, sputter deposited at the University of Münster by T. Gallasch. The thickness of the sputtered layer was rather high with about $100 - 200\,nm$, while that of the PLD films is thinner. The exact thickness determination, however, as already mentioned in chapter 5, was rather difficult, thus being not in detail studied during these first experiments. Deposition parameters of the PLD coatings are reported in table 8.1.

Tab. 8.1.: *Parameters for PLD deposition of different coatings onto LNMO thin films.*

coating	temperature	background gas	fluence	frequency	distance	pulse no.
TiO_2	800 °C	0.3 Pa Ar	$3.0\,J/cm^2$	10 Hz	70 mm	2000
LTO	650 °C	30 Pa O_2	$3.0\,J/cm^2$	10 Hz	45 mm	500
Al_2O_3	30 °C	20 Pa O_2	$4.0\,J/cm^2$	5 Hz	40 mm	3000

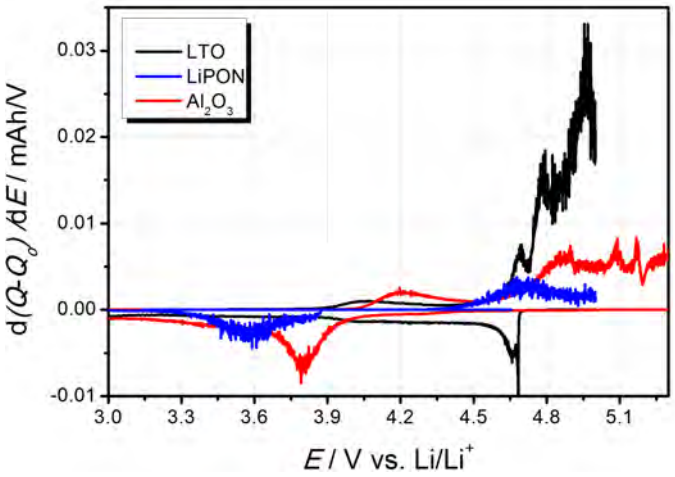

Fig. 8.2.: *Differential capacity of different coatings on LNMO thin film electrodes. cc cycling was performed at room temperature in half cells. LiPON was sputtered, while LTO and Al_2O_3 were deposited by PLD. Deposition parameter of the latter two coatings are depicted in table 8.1.*

While no electrochemical response from LNMO was detected at all using TiO_2 as coating, application of the other three led to cyclable cells, as can be seen in figure 8.2. Also cycling over more than 20 cycles was possible, the achieved capacities are rather small and

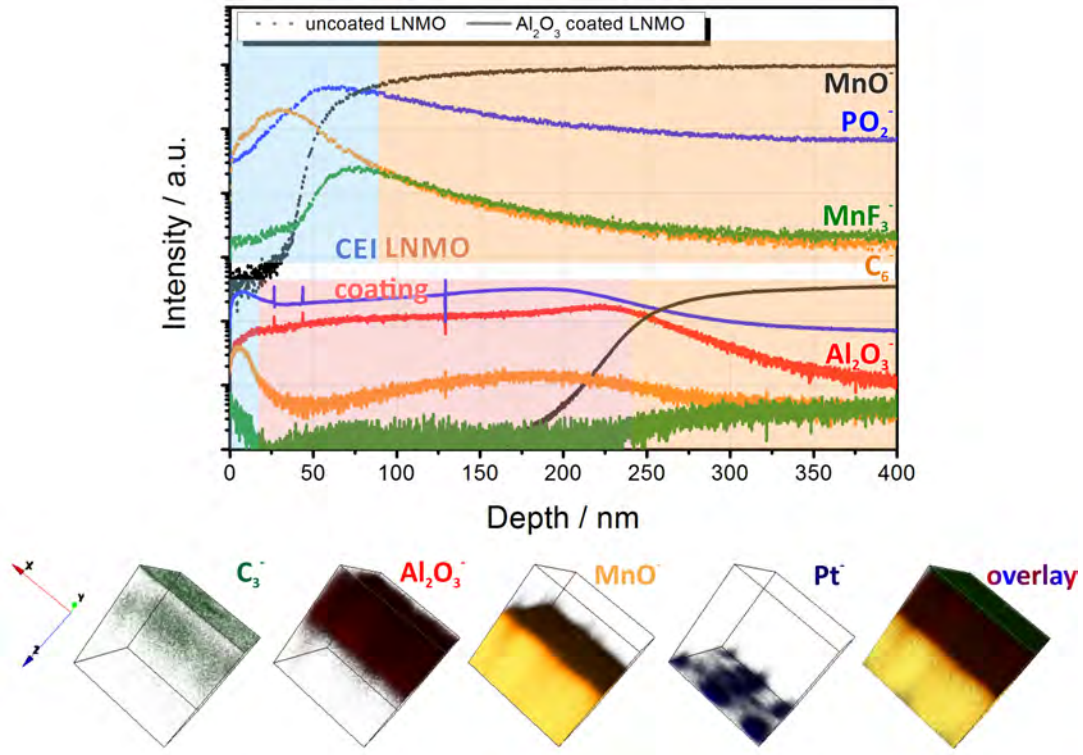

Fig. 8.3.: *SIMS depth profiles comparing the CEI thickness of Al_2O_3 coated and uncoated LNMO thin film half cells is shown in the upper row. In the lower one, a three dimensional visualization of the depth profile data of the coated sample is given. Thereby, C_3^- represents the CEI, $Al_2O_3^-$ the coating, MnO^- the LNMO electrode and Pt^- the current collector. Both cells were cycled at room temperature. The coating was prepared by PLD, the deposition parameters are listed in table 8.1. In the depth profile, the intensities of the coated and the uncoated sample were shifted along the intensity axis for better visualization.*

all three coatings show distinct over-voltages due to slower lithium diffusion kinetics in the coating. Both disadvantages could be to some extent reduced by application of thinner coatings, which then bears the risk of incomplete coverage.

A SIMS depth profile after cycling of a LNMO thin film half cell covered with an Al_2O_3 protection layer revealed a somewhat thinner CEI in comparison to uncoated electrodes cycled under the same conditions, as can be seen in figure 8.3. Thus, reactions between cathode and electrolyte appear to be sufficiently prevented. In conclusion, coatings indeed seem to be a promising way to extend the cycle life of LNMO based cells.

SEM images of the LTO and Al_2O_3 coatings prior and after cycling are depicted in figure 8.4. Both fresh protection films show a complete coverage of the LNMO thin film electrode. However, some cracks are visible for the LTO coating. After cycling, the surface of the Al_2O_3 protection film is also cracked, while none are visible for the LTO coating,

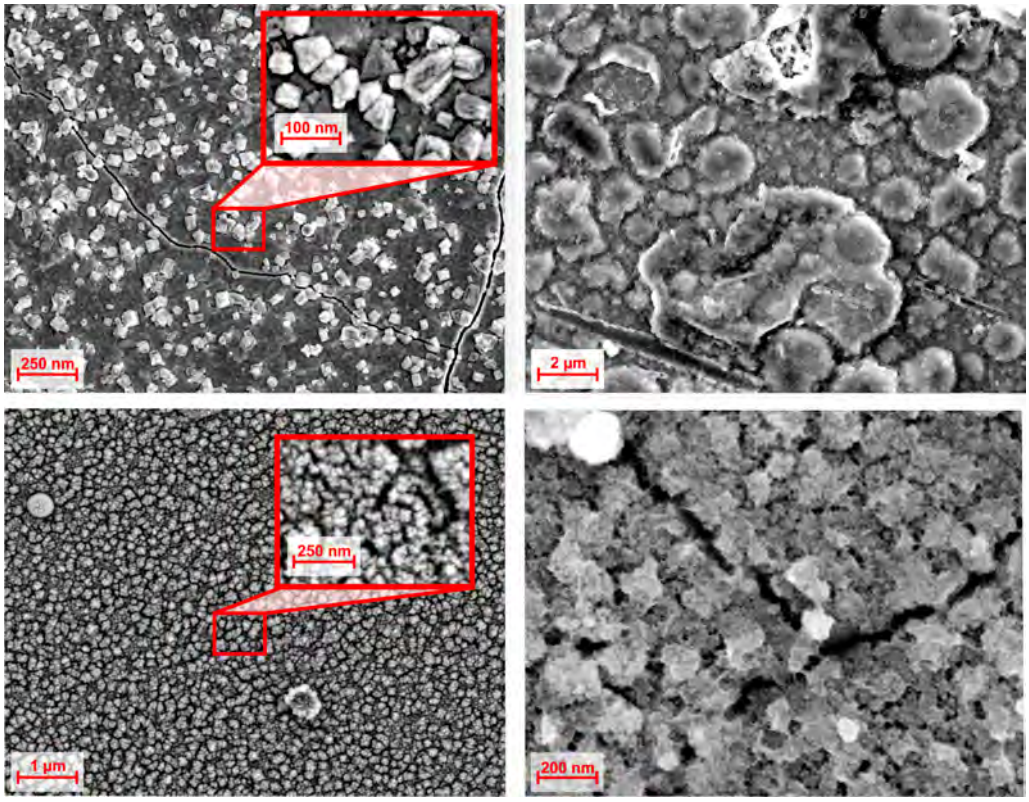

Fig. 8.4.: *SEM images of different coatings on LNMO thin films electrodes deposited by PLD on the left prior and on the right after cycling: In the upper row LTO coating is presented and in the lower one Al_2O_3 protection layer. The deposition parameters of the coatings are listened in table 8.1.*

thus leading to the conclusion, that the ones formed during PLD preparation are filled by reaction products. Question thus rises, whether the lithium ions indeed diffuse through the protection layer, of if they reach the LNMO electrode only through cracks. The exact protection mechanism of the coatings thus need further detailed investigation. Using atomic layer deposition (ALD), the deposition of dense coatings of only a few monolayers is possible. This allows better thickness control than by application of the PLD process. The preparation of even thinner, dense films should be possible, that hopefully do not crack during cycling. They should be thin enough, that the lattice misfit between coating and LNMO is overcome like it was observed during preparation of the LNMO thin film electrodes on Pt-YSZ substrates reported in chapter 5.2. By employment of coatings prepared by this technique, hopefully the question concerning the minimum coating thickness will be answered. Investigations also should reveal, whether the formation of a dense layer is indeed needed for prevention of transition metal dissolution and electrolyte oxidation or if dispersed nano-particles are sufficient for this task.

9. Bibliography

[1] N. M. Hagh, F Cosandey, S Rangan, R Bartynski, G. G. Amatucci, "Electrochemical Performance of Acid-Treated Nanostructured $LiMn_{1.5}Ni_{0.5}O_{4-\delta}$ Spinel at Elevated Temperature", *J. Electrochem. Soc.* **2010**, *157*, A305–A319.

[2] M Winter, R. J. Brodd, "What are batteries, fuel cells, and supercapacitors?", *Chem. Rev.* **2004**, *104*, 4245–4269.

[3] J Vetter, P Novak, M. R. Wagner, C Veit, K. C. Moller, J. O. Besenhard, M Winter, M Wohlfahrt-Mehrens, C Vogler, A Hammouche, "Ageing mechanisms in lithium-ion batteries", *J. Power Sources* **2005**, *147*, 269–281.

[4] L. Baggetto, R. R. Unocic, N. J. Dudney, G. M. Veith, "Fabrication and characterization of Li-Mn-Ni-O sputtered thin film high voltage cathodes for Li-ion batteries", *J. Power Sources* **2012**, *211*, 108–118.

[5] K. Xu, "Electrolytes and Interphasial Chemistry in Li Ion Devices", *Energies* **2010**, *3*, 135–154.

[6] A. Yoshino, "Die Geburt der Lithiumionen-Batterie", *Angew. Chemie* **2012**, *124*, 5898–5900.

[7] A. Deb, U. Bergmann, S. P. Cramer, E. J. Cairns, "In situ X-ray absorption spectroscopic study of $Li_{1.05}Ni_{0.35}Co_{0.25}Mn_{0.4}O_2$ cathode material coated with $LiCoO_2$", *J. Electrochem. Soc.* **2007**, *154*, A534–A541.

[8] M.-K. Song, S. Park, F. M. Alamgir, J. Cho, M. Liu, "Nanostructured electrodes for lithium-ion and lithium-air batteries: the latest developments, challenges, and perspectives", *Mater. Sci. Eng. R* **2011**, *72*, 203–252.

[9] L. Yang, B. Ravdel, B. L. Lucht, "Electrolyte Reactions with the Surface of High Voltage $LiNi_{0.5}Mn_{1.5}O_4$ Cathodes for Lithium-Ion Batteries", *Electrochem. Solid-State Lett.* **2010**, *13*, A95–A97.

[10] K. Bullis, Volt's Battery Capacity Could Double, **2011**, http://www.technologyreview.com/news/422360/volts-battery-capacity-could-double/.

[11] S. Fletcher, GM's New Battery Chemistry? It's Already In the Chevy Volt, **2011**, http://www.popsci.com/cars/article/2011-01/gm\%E2\%80\%99s-new-battery-chemistry-it\%E2\%80\%99s-already-chevy-volt.

[12] G. Jeong, Y.-U. Kim, H. Kim, Y.-J. Kim, H.-J. Sohn, "Prospective materials and applications for Li secondary batteries", *Energy Environ. Sci.* **2011**, *4*, 1986–2002.

[13] S. Laubach, S. Laubach, P. C. Schmidt, D. Ensling, S. Schmid, W. Jaegermann, A. Thissen, K. Nikolowski, H. Ehrenberg, "Changes in the crystal and electronic structure of $LiCoO_2$ and $LiNiO_2$ upon Li intercalation and de-intercalation", *Phys. Chem. Chem. Phys.* **2009**, *11*, 3278–3289.

[14] R. A. De Souza, M. Martin, "Secondary ion mass spectrometry (SIMS) - a powerful tool for studying mass transport over various length scales", *Phys. status solidi* **2007**, *4*, 1785 –1801.

[15] H. J. Freund, H Kuhlenbeck, J Libuda, G Rupprechter, M Baumer, H Hamann, “Bridging the pressure and materials gaps between catalysis and surface science: clean and modified oxide surfaces”, *Top. Catal.* **2001**, *15*, 201–209.

[16] H. Xia, L. Lu, M. O. Lai, “Li diffusion in $LiNi_{0.5}Mn_{0.5}O_2$ thin film electrodes prepared by pulsed laser deposition”, *Electrochim. Acta* **2009**, *54*, 5986–5991.

[17] C. M. Julien, A Mauger, “Review of 5-V electrodes for Li-ion batteries: status and trends”, *Ionics* **2013**, *19*, 951–988.

[18] D. Linden, T. B. Reddy, *Handbook of Batteries 3rd ed.* McGraw-Hill, New York, **2002**.

[19] G. Wedler, H.-J. Freund, *Lehrbuch der Physikalischen Chemie - Sechste, vollstaendig ueberarbeitete und aktualisierte Auflage*, Wiley-VCH, Weinheim, **2012**.

[20] D. Aurbach, B. Markovsky, G. Salitra, E. Markevich, Y. Talyossef, M. Koltypin, L. Nazar, B. Ellis, D. Kovacheva, “Review on electrode-electrolyte solution interactions, related to cathode materials for Li-ion batteries”, *J. Power Sources* **2007**, *165*, 491–499.

[21] M Winter, J. O. Besenhard, M. E. Spahr, P Novak, “Insertion electrode materials for rechargeable lithium batteries”, *Adv. Mater.* **1998**, *10*, 725–763.

[22] M. Winter, J. O. Besenhard, “Wiederaufladbare Batterien”, *ChiuZ* **1999**, *33*, 252–266.

[23] L. J. Fu, H Liu, C Li, Y. P. Wu, E Rahm, R Holze, H. Q. Wu, “Electrode materials for lithium secondary batteries prepared by sol-gel methods”, *Prog. Mater. Sci.* **2005**, *50*, 881–928.

[24] N. Yabuuchi, K. Yoshii, S.-T. Myung, I. Nakai, S. Komaba, “Detailed Studies of a High-Capacity Electrode Material for Rechargeable Batteries, Li_2MnO_3-$LiCo_{1/3}Ni_{1/3}Mn_{1/3}O_2$”, *J. Am. Chem. Soc.* **2011**, *133*, 4404–4419.

[25] B. L. Ellis, K. T. Lee, L. F. Nazar, “Positive Electrode Materials for Li-Ion and Li-Batteries”, *Chem. Mater.* **2010**, *22*, 691–714.

[26] D Aurbach, “Review of selected electrode-solution interactions which determine the performance of Li and Li ion batteries”, *J. Power Sources* **2000**, *89*, 206–218.

[27] R Santhanam, B Rambabu, “Research progress in high voltage spinel $LiNi_{0.5}Mn_{1.5}O_4$ material”, *J. Power Sources* **2010**, *195*, 5442–5451.

[28] A. Patil, V. Patil, D. W. Shin, J.-W. Choi, D.-S. Paik, S.-J. Yoon, “Issue and challenges facing rechargeable thin film lithium batteries”, *Mater. Res. Bull.* **2008**, *43*, 1913–1942.

[29] H. Xia, L. Lu, “Li diffusion in spinel $LiNi_{0.5}Mn_{1.5}O_4$ thin films prepared by pulsed laser deposition”, *Phys. Scripta* **2007**, *T129*, 43–48.

[30] J. B. Goodenough, K.-S. Park, “The Li-Ion Rechargeable Battery: A Perspective”, *J. Am. Chem. Soc.* **2013**, *135*, 1167–1176.

[31] Q.-H. Wu, "Photoelectron Spectroscopy of Intercalation Phases: Na and Li in V_2O_5 Thin Films and $LiMn_2O_4$", PhD thesis, Darmstadt University of Technology, **2003**.

[32] T Ohzuku, M Kitagawa, T Hirai, “Electrochemistra of manganese-dioxide in lithium nonaqueous cell .3. X-ray diffractional study on the reduction of spinel-related manganese-dioxide”, *J. Electrochem. Soc.* **1990**, *137*, 769–775.

[33] H Bjoerk, J. E. Dabkowska, T Greedan, G. T, T. J. O, “$(Li_{0.91}Mn_{0.09})Mn_2O_4$”, *Acta Crystallogr. C* **2001**, *C57*, 331–332.

[34] N.-E. Sung, Y.-K. Sun, S.-K. Kim, M.-S. Jang, "In situ XAFS study of the effect of dopants in $Li_{1+x}Ni_{(1-3x)/2}Mn_{(3+x)/2}O_4$, ($0 \leq x \leq 1/3$), a Li-ion battery cathode material", *J. Electrochem. Soc.* **2008**, *155*, A845–A850.

[35] J. Huheey, E. Keiter, R. Keiter, *Anorganische Chemie - Prinzipien von Struktur und Reaktivitaet*, de Gruyter, New York.

[36] K. Y. Chung, W. S. Yoon, K. B. Kim, X. Q. Yang, S. M. Oh, "Suppression of structural fatigue by doping in spinel electrode probed by in situ bending beam method", *J. Electrochem. Soc.* **2004**, *151*, A484–A492.

[37] C. Daniel, J. O. Besenhard, *Handbook of Battery Materials*, Wiley-VCH Verlag GmBH & Co. KGaA, Weinheim, **2011**.

[38] R. J. Gummow, A de Kock, M. M. Thackeray, "Improved capacity retention in rechargeable 4 V lithium/lithium-manganese oxide (spinel) cells", *Solid State Ionics* **1994**, *69*, 59–67.

[39] T Eriksson, A. M. Andersson, A. G. Bishop, C Gejke, T Gustafsson, J. O. Thomas, "Surface analysis of $LiMn_2O_4$ electrodes in carbonate-based electrolytes", *J. Electrochem. Soc.* **2002**, *149*, A69–A78.

[40] J. C. Hunter, "Preparation of a new crystal form of manganese-dioxide - lambda-MnO_2", *J. Solid State Chem.* **1981**, *39*, 142–147.

[41] R Alcantara, M Jaraba, P Lavela, J. L. Tirado, "Optimizing preparation conditions for 5 V electrode performance, and structural changes in $Li_{1-x}Ni_{0.5}Mn_{1.5}O_4$ spinel", *Electrochim. Acta* **2002**, *47*, 1829–1835.

[42] S Mukerjee, X. Q. Yang, X Sun, S. J. Lee, J McBreen, Y Ein-Eli, "In situ synchrotron X-ray studies on copper-nickel 5 V Mn oxide spinel cathodes for Li-ion batteries", *Electrochim. Acta* **2004**, *49*, 3373–3382.

[43] T.-F. Yi, X.-G. Hu, "Preparation and characterization of sub-micro $LiNi_{0.5-x}Mn_{1.5-x}O_4$ for 5V cathode materials synthesized by an ultrasonic-assisted co-precipitation method", *J. Power Sources* **2007**, *167*, 185–191.

[44] Q. Zhong, A. Bonakdarpour, M. Zhang, Y. Gao, J. R. Dahn, "Synthesis and Electrochemistry of $LiNi_xMn_{2-x}O_4$", *J. Electrochem. Soc.* **1997**, *144*, 205–213.

[45] K Amine, H Tukamoto, H Yasuda, Y Fujita, "Preparation and electrochemical investigation of $LiMn_{2-x}Me_xO_4$ (Me : Ni, Fe, and $x = 0.5$, 1) cathode materials for secondary lithium batteries", *J. Power Sources* **1997**, *68*, 604–608.

[46] S. Patoux, L. Daniel, C. Bourbon, H. Lignier, C. Pagano, F. Le Cras, S. Jouanneau, S. Martinet, "High voltage spinel oxides for Li-ion batteries: From the material research to the application", *J. Power Sources* **2009**, *189*, 344–352.

[47] D. W. Shin, A. Manthiram, "Surface-segregated, high-voltage spinel $LiMn_{1.5}Ni_{0.42}Ga_{0.08}O_4$ cathodes with superior high-temperature cyclability for lithium-ion batteries", *Electrochem. Commun.* **2011**, *13*, 1213–1216.

[48] Y. J. Lee, C. Eng, C. P. Grey, "^{6}Li Magic Angle Spinning NMR Study of the Cathode Material $LiNi_xMn_{2-x}O_4$: The Effect of Ni Doping on the Local Structure during Charging", *J. Electrochem. Soc.* **2001**, *148*, A249–A257.

[49] G. Liu, Q. Lu, W. Lei, "Synthesis and Electrochemical Performance of $LiNi_xMn_{2-x}O_4$ Spinel as Cathode Material for Lithium Ion Batteries", *Rare Met. Mater. Eng.* **2006**, *35*, 299–302.

[50] M. G. Lazarraga, L Pascual, H Gadjov, D Kovacheva, K Petrov, J. M. Amarilla, R. M. Rojas, M. A. Martin-Luengo, J. M. Rojo, "Nanosize $LiNiMn_{2-y}O_4$ ($0 < y \leq 0.5$) spinels synthesized by a sucrose-aided combustion method. Characterization and electrochemical performance", *J. Mater. Chem.* **2004**, *14*, 1640–1647.

[51] A. Bhaskar, N. N. Bramnik, A. Senyshyn, H. Fuess, H. Ehrenberg, "Synthesis, Characterization, and Comparison of Electrochemical Properties of $LiM_{0.5}Mn_{1.5}O_4$ (M = Fe, Co, Ni) at Different Temperatures", *J. Electrochem. Soc.* **2010**, *157*, A689–A695.

[52] Y. Ting-Feng, Z. Yan-Rong, Z. Rong-Sun, H. Xin-Guo, "Electronic Structure of Ni-doped Spinel $LiMn_2O_4$ Cathode Material for Lithium Ion Battery", *Chin. J. Inorg. Chem.* **2008**, *24*, 1576–1581.

[53] J. Shu, T.-F. Yi, M. Shui, Y. Wang, R.-S. Zhu, X.-F. Chu, F. Huang, D. Xu, L. Hou, "Comparison of electronic property and structural stability of $LiMn_2O_4$ and $LiNi_{0.5}Mn_{1.5}O_4$ as cathode materials for lithium-ion batteries", *Comp. Mater. Sci.* **2010**, *50*, 776–779.

[54] K Ariyoshi, Y Iwakoshi, N Nakayama, T Ohzuku, "Topotactic two-phase reactions of $Li[Ni_{1/2}Mn_{3/2}]O_4$ ($P4_332$) in nonaqueous lithium cells", *J. Electrochem. Soc.* **2004**, *151*, A296–A303.

[55] T.-F. Yi, C.-Y. Li, Y.-R. Zhu, R.-S. Zhu, J Shu, "Electrochemical Intercalation Kinetics of Lithium Ions for Spinel $LiNi_{0.5}Mn_{1.5}O_4$ Cathode Material", *Russ. J. Electrochem.* **2010**, *46*, 227–232.

[56] X Fang, N Ding, X. Y. Feng, Y Lu, C. H. Chen, "Study of $LiNi_{0.5}Mn_{1.5}O_4$ synthesized via a chloride-ammonia co-precipitation method: Electrochemical performance, diffusion coefficient and capacity loss mechanism", *Electrochim. Acta* **2009**, *54*, 7471–7475.

[57] X. Ma, B. Kang, G. Ceder, "High Rate Micron-Sized Ordered $LiNi_{0.5}Mn_{1.5}O_4$", *J. Electrochem. Soc.* **2010**, *157*, A925–A931.

[58] D Guyomard, J. M. Tarascon, "The carbon $Li_{1+x}Mn_2O_4$ system", *Solid State Ionics* **1994**, *69*, 222–237.

[59] S. H. Oh, K. Y. Chung, S. H. Jeon, C. S. Kim, W. I. Cho, B. W. Cho, "Structural and electrochemical investigations on the $LiNi_{0.5-x}Mn_{1.5-y}M_{x+y}O_4$ (M = Cr, Al, Zr) compound for 5 V cathode material", *J. Alloy. Compd.* **2009**, *469*, 244–250.

[60] M. G. Kim, J. Cho, "Reversible and High-Capacity Nanostructured Electrode Materials for Li-Ion Batteries", *Adv. Funct. Mater.* **2009**, *19*, 1497–1514.

[61] Y.-C. Jin, C.-Y. Lin, J.-G. Duh, "Improving rate capability of high potential $LiNi_{0.5}Mn_{1.5}O_{4-x}$ cathode materials via increasing oxygen non-stoichiometries", *Electrochim. Acta* **2012**, *69*, 45–50.

[62] S. Ivanova, E. Zhecheva, R. Stoyanova, D. Nihtianova, S. Wegner, P. Tzvetkova, S. Simova, "High-Voltage $LiNi_{1/2}Mn_{3/2}O_4$ Spinel: Cationic Order and Particle Size Distribution", *J. Phys. Chem. C* **2011**, *115*, 25170–25182.

[63] J. Song, D. W. Shin, Y. Lu, C. D. Amos, A. Manthiram, J. B. Goodenough, "Role of Oxygen Vacancies on the Performance of $Li[Ni_{0.5-x}Mn_{1.5+x}]O_4$ (x = 0, 0.05, and 0.08) Spinel Cathodes for Lithium-Ion Batteries", *Chem. Mater.* **2012**, *24*, 3101–3109.

[64] E. Lee, K. A. Persson, "Revealing the coupled cation interactions behind the electrochemical profile of $Li_xNi_{0.5}Mn_{1.5}O_4$", *Energy Environ. Sci.* **2012**, *5*, 6047–6051.

[65] L. Wang, H. Li, X. Huang, E. Baudrin, "A comparative study of $Fd\bar{3}m$ and $P4_332$ $LiNi_{0.5}Mn_{1.5}O_4$", *Solid State Ionics* **2011**, *193*, 32–38.

[66] N Amdouni, K Zaghib, F Gendron, A Mauger, C. M. Julien, "Structure and insertion properties of disordered and ordered $LiNi_{0.5}Mn_{1.5}O_4$ spinels prepared by wet chemistry", *Ionics* **2006**, *12*, 117–126.

[67] Y Talyosef, B Markovsky, G Salitra, D Aurbach, H. J. Kim, S Choi, "The study of $LiNi_{0.5}Mn_{1.5}O_4$ 5 V cathodes for Li-ion batteries", *J. Power Sources* **2005**, *146*, 664–669.

[68] Y Terada, K Yasaka, F Nishikawa, T Konishi, M Yoshio, I Nakai, "In situ XAFS analysis of $Li(Mn,M)_2O_4$ (M = Cr, Co, Ni) 5 V cathode materials for lithium-ion secondary batteries", *J. Solid State Chem.* **2001**, *156*, 286–291.

[69] Y. Kim, N. J. Dudney, M. Chi, S. K. Martha, J. Nanda, G. M. Veith, C. Liang, "A Perspective on Coatings to Stabilize High-Voltage Cathodes: $LiMn_{1.5}Ni_{0.5}O_4$ with Sub-Nanometer Lipon Cycled with $LiPF_6$ Electrolyte", *J. Electrochem. Soc.* **2013**, *160*, A3113–A3125.

[70] K. M. Shaju, G. V. S. Rao, B. V. R. Chowdari, "Performance of layered $Li(Ni_{1/3}Co_{1/3}Mn_{1/3})O_2$ as cathode for Li-ion batteries", *Electrochim. Acta* **2002**, *48*, 145–151.

[71] K Takahashi, M Saitoh, M Sano, M Fujita, K Kifune, "Electrochemical and structural properties of a 4.7 V-class $LiNi_{0.5}Mn_{1.5}O_4$ positive electrode material prepared with a self-reaction method", *J. Electrochem. Soc.* **2004**, *151*, A173–A177.

[72] D Pasero, N Reeves, V Pralong, A. R. West, "Oxygen nonstoichiometry and phase transitions in $LiMn_{1.5}Ni_{0.5}O_{4-delta}$", *J. Electrochem. Soc.* **2008**, *155*, A282–A291.

[73] J. Cabana, M. Casas-Cabanas, F. O. Omenya, N. A. Chernova, D. Zeng, M. S. Whittingham, C. P. Grey, "Composition-Structure Relationships in the Li-Ion Battery Electrode Material $LiNi_{0.5}Mn_{1.5}O_4$", *Chem. Mater.* **2012**, *24*, 2952–2964.

[74] T.-F. Yi, Y. Xie, M.-F. Ye, L.-J. Jiang, R.-S. Zhu, Y.-R. Zhu, "Recent developments in the doping of $LiNi_{0.5}Mn_{1.5}O_4$ cathode material for 5 V lithium-ion batteries", *Ionics* **2011**, *17*, 383–389.

[75] G. Q. Liu, L Wen, X Wang, B. Y. Ma, "Effect of the impurity $Li_xNi_{1-x}O$ on the electrochemical properties of 5 V cathode material $LiNi_{0.5}Mn_{1.5}O_4$", *J. Alloy. Compd.* **2011**, *509*, 9377–9381.

[76] S. H. Oh, S. H. Jeon, W. I. Cho, C. S. Kim, B. W. Cho, "Synthesis and characterization of the metal-doped high-voltage spinel $LiNi_{0.5}Mn_{1.5}O_4$ by mechanochemical process", *J. Alloy. Compd.* **2008**, *452*, 389–396.

[77] M. Aklalouch, J. Manuel Amarilla, R. M. Rojas, I. Saadoune, J. Maria Rojo, "Sub-micrometric $LiCr_{0.2}Ni_{0.4}Mn_{1.4}O_4$ spinel as 5 V-cathode material exhibiting huge rate capability at 25 and 55 degrees C", *Electrochem. Commun.* **2010**, *12*, 548–552.

[78] Y. Kadoma, S. Sato, K. Ui, N. Kumagai, "Synthesis and Electrochemical Properties of $LiNi_{0.5-x}Mn_{1.5-x}M_2O_4$ (M = Al, Cr) Cathode Materials Prepared by PVA Method", *Electrochemistry* **2010**, *78*, 658–661.

[79] F. G. B. Ooms, E. M. Kelder, J Schoonman, M Wagemaker, F. M. Mulder, "High-voltage $LiMg_{delta}Ni_{0.5-delta}Mn_{1.5}O_4$ spinels for Li-ion batteries", *Solid State Ionics* **2002**, *152*, 143–153.

[80] H. Wang, H. Xia, M. O. Lai, L. Lu, "Enhancements of rate capability and cyclic performance of spinel $LiNi_{0.5}Mn_{1.5}O_4$ by trace Ru-doping", *Electrochem. Commun.* **2009**, *11*, 1539–1542.

[81] J. Liu, A. Manthiram, "Understanding the Improved Electrochemical Performances of Fe-Substituted 5 V Spinel Cathode $LiMn_{1.5}Ni_{0.5}O_4$", *J. Phys. Chem. C* **2009**, *113*, 15073–15079.

[82] M Lin, S. H. Wang, Z. L. Gong, X. K. Huang, Y Yang, "A Strategy to Improve Cyclic Performance of $LiNi_{0.5}Mn_{1.5}O_4$ in a Wide Voltage Region by Ti-Doping", *J. Electrochem. Soc.* **2013**, *160*, A3036–A3040.

[83] T. Noguchi, I. Yamazaki, T. Numata, M. Shirakata, "Effect of Bi oxide surface treatment on 5 V spinel $LiNi_{0.5}Mn_{1.5-x}Ti_xO_4$", *J. Power Sources* **2007**, *174*, 359–365.

[84] L. Baggetto, N. J. Dudney, G. M. Veith, "Surface chemistry of metal oxide coated lithium manganese nickel oxide thin film cathodes studied by XPS", *Electrochim. Acta* **2013**, *90*, 135–147.

[85] J.-H. Cho, J.-H. Park, M.-H. Lee, H.-K. Song, S.-Y. Lee, "A polymer electrolyte-skinned active material strategy toward high-voltage lithium ion batteries: a polyimide-coated $LiNi_{0.5}Mn_{1.5}O_4$ spinel cathode material case", *Energy Environ. Sci.* **2012**, *5*, 7124–7131.

[86] X. Hao, B. M. Bartlett, "Improving the Electrochemical Stability of the High-Voltage Li-Ion Battery Cathode $LiNi_{0.5}Mn_{1.5}O_4$ by Titanate-Based Surface Modification", *J. Electrochem. Soc.* **2013**, *160*, A3162–A3170.

[87] J. Y. Shi, C.-W. Yi, K. Kim, "Improved electrochemical performance of $AlPO_4$-coated $LiMn_{1.5}Ni_{0.5}O_4$ electrode for lithium-ion batteries", *J. Power Sources* **2010**, *195*, 6860–6866.

[88] D. Liu, Y. Bai, S. Zhao, W. Zhang, "Improved cycling performance of 5 V spinel $LiMn_{1.5}Ni_{0.5}O_4$ by amorphous $FePO_4$ coating", *J. Power Sources* **2012**, *219*, 333–338.

[89] Y.-R. Zhu, T.-F. Yi, R.-S. Zhu, A.-N. Zhou, "Increased cycling stability of $Li_4Ti_5O_{12}$-coated $LiMn_{1.5}Ni_{0.5}O_4$ as cathode material for lithium-ion batteries", *Ceram. Int.* **2013**, *39*, 3087–3094.

[90] X. Fang, M. Ge, J. Rong, C. Zhou, "Graphene-oxide-coated $LiNi_{0.5}Mn_{1.5}O_4$ as high voltage cathode for lithium ion batteries with high energy density and long cycle life", *J. Mater. Chem. A* **2013**, *1*, 4083–4088.

[91] J. Gao, J. Li, C. Jiang, C. Wan, "Controlled Preparation and Characterization of Spherical $LiNi_{0.5}Mn_{1.5}O_4$ Cathode Material for Lithium-Ion Batteries", *J. Electrochem. Soc.* **2010**, *157*, A899–A902.

[92] S. Qiang, L. Xin-hai, W. Zhi-xing, J. Yong, "Synthesis and electrochemical performance of 5V spinel $LiNi_{0.5}Mn_{1.5}O_4$ prepared by solid-state reaction", *T. Nonferr. Metal. Soc.* **2009**, *19*, 176–181.

[93] Y. Sun, Y. Yang, H. Zhan, H. Shao, Y. Zhou, "Synthesis of high power type $LiMn_{1.5}Ni_{0.5}O_4$ by optimizing its preparation conditions", *J. Power Sources* **2010**, *195*, 4322–4326.

[94] M. Jo, Y.-K. Lee, K. M. Kim, J. Cho, "Nanoparticle-Nanorod Core-Shell $LiNi_{0.5}Mn_{1.5}O_4$ Spinel Cathodes with High Energy Density for Li-Ion Batteries", *J. Electrochem. Soc.* **2010**, *157*, A841–A845.

[95] F. Wei-Feng, Q. Mei-Zhen, P. Gong-Chang, Y. Zuo-Long, "Electrochemical Properties of $LiNi_{0.5}Mn_{1.5}O_4$ as 5 V Cathode Materials Synthesized through Self-Combustion Reaction(SCR)", *Chin. J. Inorg. Chem.* **2009**, *25*, 124–128.

[96] X. Zhang, J. Liu, H. Yu, G. Yang, J. Wang, Z. Yu, H. Xie, R. Wang, "Enhanced electrochemical performances of $LiNi_{0.5}Mn_{1.5}O_4$ spinel via ethylene glycol-assisted synthesis", *Electrochim. Acta* **2010**, *55*, 2414–2417.

[97] D. Ke-Hua, M. Jing, Z. Yu-Chun, "High Rate Capability of 5 V $LiNi_{0.5}Mn_{1.5}O_4$ Cathode Materials Synthesized via a Gel-Combustion Method", *Acta Phys-Chim Sin.* **2010**, *26*, 2130–2134.

[98] J. C. Arrebola, A Caballero, L Hernan, J Morales, "Improving the performance of lithium-ion batteries by using spinel nanoparticles", *J. Nanomater.* **2008**.

[99] J. C. Arrebola, A Caballero, L Hernan, J Morales, "Expanding the rate capabilities of the $LiNi_{0.5}Mn_{1.5}O_4$ spinel by exploiting the synergistic effect between nano and microparticles", *Electrochem. Solid-State Lett.* **2005**, *8*, A641–A645.

[100] L. Xiao, Y. Zhao, Y. Yang, X. Ai, H. Yang, Y. Cao, "Electrochemical properties of nano-crystalline $LiNi_{0.5}Mn_{1.5}O_4$ synthesized by polymer-pyrolysis method", *J. Solid State Electr.* **2008**, *12*, 687–691.

[101] R. A. De Souza, M. Martin, "Secondary Ion Mass Spectrometry - SIMS", *Bunsen-Magazin* **2007**, *5*, 109–120.

[102] J. C. Vickerman, B. David, *TOF-SIMS: Materials Analysis by Mass Spectrometry, 2^{nd} Edition*, IM Publications LLP and SurfaceSpectra Limited, Manchester, **2013**.

[103] R. N. S. Sodhi, "Time-of-flight secondary ion mass spectrometry (TOF-SIMS): versatility in chemical and imaging surface analysis", *Analyst* **2004**, *129*, 483–487.

[104] G. Hinterndorfer, "Simulationssoftware fuer ein Sekundaerionen-Flugzeit-Massenspektrometer zur Untersuchung von Kometenstaub", Technische Universitaet Wien, Diplomarbeit, **2001**.

[105] K. M. Shaju, P. G. Bruce, "Nano-$LiNi_{0.5}Mn_{1.5}O_4$ spinel: a high power electrode for Li-ion batteries", *Dalt. Trans.* **2008**, 5471–5475.

[106] H Mai, W Pompe, "Manufacture and characterization of soft-X-ray mirrors by laser ablation", *Appl. Surf. Sci.* **1992**, *54*, 215–226.

[107] D. B. Chrisey, G. K. Hubler, *Pulsed Laser Deposition of Thin Films*, John Wiles & Sons, New York, **1994**.

[108] D Beckel, A Bieberle-Huetter, A Harvey, A Infortuna, U. P. Muecke, M Prestat, J. L. M. Rupp, L. J. Gauckler, "Thin films for micro solid oxide fuel cells", *J. Power Sources* **2007**, *173*, 325–345.

[109] M. J. Schoning, Y. G. Mourzina, J Schubert, W Zander, A Legin, Y. G. Vlasov, H Luth, "Pulsed Laser Deposition - An Innovative Technique for Preparing Inorganic Thin Films", *Electroanalysis* **2001**, *13*, 727–732.

[110] C Belouet, "Thin film growth by the pulsed laser assisted deposition technique", *Appl. Surf. Sci.* **1996**, *96-8*, 630–642.

[111] L. Guan, D. Zhang, X. Li, Z. Li, "Role of pulse repetition rate in film growth of pulsed laser deposition", *Nucl. Instrum. Methods* **2008**, *266*, 57–62.

[112] T. D. Bennett, C. P. Grigoropoulos, D. J. Krajnovich, "Near-threshold laser sputtering of gold", *J. Appl. Phys.* **1995**, *77*, 849–864.

[113] R Castro-Rodriguez, D. R. Coronado, A Iribarren, B. E. Watts, F Leccabue, J. L. Pena, "Correlation between target-substrate distance and oxygen pressure in pulsed laser deposition of complex oxide thin films", *Appl. Phys. A-Mater* **2005**, *81*, 1503–1507.

[114] D. Ende, K.-M. Mangold, "Impedanzspektroskopie", *ChiuZ* **1993**, *27*, 134–140.

[115] R. G. Compton, C. E. Banks, *Understanding Voltammetry - 2nd ed.* Imperial College Press, London, **2011**.

[116] A. J. Bard, L. R. Faulkner, *Electrochemical Methods: Fundamentals and Applications - 2nd ed.* John Wiles & Sons Inc., Hoboken, NJ, **2001**.

[117] T Eriksson, A. K. Hjelm, G Lindbergh, T Gustafsson, "Kinetic study of $LiMn_2O_4$ cathodes by in situ XRD with constant-current cycling and potential stepping", *J. Electrochem. Soc.* **2002**, *149*, A1164–A1170.

[118] M. M. Thackeray, "Manganese oxides for lithium batteries", *Prog. Solid State Ch.* **1997**, *25*, 1–71.

[119] M. D. Levi, K Gamolsky, D Aurbach, U Heider, R Oesten, "Determination of the Li ion chemical diffusion coefficient for the topotactic solid-state reactions occurring via a two-phase or single-phase solid solution pathway", *J. Electroanal. Chem.* **1999**, *477*, 32–40.

[120] D Ensling, A Thissen, Y Gassenbauer, A Klein, W Jaegermann, "In-situ preparation and analysis functional oxides", *Adv. Eng. Mater.* **2005**, *7*, 945–949.

[121] D. Ensling, A. Thissen, W. Jaegermann, "On the formation of lithium oxides and carbonates on Li metal electrodes in comparison to $LiCoO_2$ surface phases investigated by photoelectron spectroscopy", *Appl. Surf. Sci.*, 2517–2523.

[122] P. J. Bouwman, B. A. Boukamp, H. J. M. Bouwmeester, P. H. L. Notten, "Structure-related intercalation behaviour of $LiCoO_2$ films", *Solid State Ionics* **2002**, *152*, 181–188.

[123] F Sauvage, E Baudrin, L Laffont, J. M. Tarascon, "Origin of electrochemical reactivity enhancement of post-annealed $LiFePO_4$ thin films: Preparation of heterosite-type $FePO_4$", *Solid State Ionics* **2007**, *178*, 145–152.

[124] N Imanishi, K Kanamura, Z Takehara, "Synthesis of MoS_2 thin-film by chemical vapor-deposition method and discharge characteristics as a cathode of the lithium secondary battery", *J. Electrochem. Soc.* **1992**, *139*, 2082–2087.

[125] J. Park, S. Kalnaus, S. Han, Y. K. Lee, G. B. Less, N. J. Dudney, C. Daniel, A. M. Sastry, "In situ atomic force microscopy studies on lithium (de)intercalation-induced morphology changes in Li_xCoO_2 micro-machined thin film electrodes", *J. Power Sources* **2013**, *222*, 417–425.

[126] K. Tang, X. Yu, J. Sun, H. Li, X. Huang, "Kinetic analysis on $LiFePO_4$ thin films by CV, GITT, and EIS", *Electrochim. Acta* **2011**, *56*, 4869–4875.

[127] H Kozuka, M Hirano, "Radiative striations and surface roughness of alkoxide-derived spin coating films", *J. Sol-Gel Sci. Techn.* **2000**, *19*, 501–504.

[128] R Dewi, N. I. Baa'yah, I. A. Talib, "The effect of spin coating rate on the microstructure, grain size, surface roughness and thickness of $Ba_{0.6}Sr_{0.4}TiO_3$ thin film prepared by the sol-gel process", *Mater. Sci.* **2007**, *25*, 657–662.

[129] Y Yu, J. L. Shui, Y Jin, C. H. Chen, "Electrochemical performance of nano-SiO_2 modified $LiCoO_2$ thin films fabricated by electrostatic spray deposition (ESD)", *Electrochim. Acta* **2006**, *51*, 3292–3296.

[130] F Simmen, M Horisberger, B Seyfang, T Lippert, P Novak, M Doebeli, M Mallepell, C. W. Schneider, A Wokaun, "Glassy carbon - A promising substrate material for pulsed laser deposition of thin $Li_{1+x}Mn_2O_{4-delta}$ electrodes", *Appl. Surf. Sci.* **2011**, *257*, 5347–5353.

[131] M. Hirayama, H. Ido, K. Kim, W. Cho, K. Tamura, J. Mizuki, R. Kanno, "Dynamic Structural Changes at $LiMn_2O_4$/Electrolyte Interface during Lithium Battery Reaction", *J. Am. Chem. Soc.*, 15268–15276.

[132] F Lantelme, A Mantoux, H Groult, D Lincot, "Analysis of a phase transition process controlled by diffusion, application to lithium insertion into V_2O_5", *Electrochim. Acta* **2002**, *47*, 3927–3938.

[133] H. Yim, W. Y. Kong, Y. C. Kim, S.-J. Yoon, J.-W. Choi, "Electrochemical properties of $Li[Li_{0.2}Mn_{0.54}Co_{0.13}Ni_{0.13}]O_2$ cathode thin film by RF sputtering for all-solid-state lithium battery", *J. Solid State Chem.* **2012**, *196*, 288–292.

[134] V. Boovaragavan, V. Ramadesigan, M. V. Panchagnula, V. R. Subramanian, "Continuum Representation for Simulating Discrete Events of Battery Operation", *J. Electrochem. Soc.* **2010**, *157*, A98–A104.

[135] Y. Zheng, S. Taminato, K. Suzuki, M. Hirayama, R. Kanno, "Fabrication and lithium intercalation properties of epitaxial Li_2RuO_3 thin films", *Thin Solid Films* **2012**, *520*, 4889–4893.

[136] K. A. Striebel, C. Z. Deng, S. J. Wen, E. J. Cairns, "Electrochemical behavior of $LiMn_2O_4$ and $LiCoO_2$ thin films produced with pulsed laser deposition", *J. Electrochem. Soc.* **1996**, *143*, 1821–1827.

[137] T. Matsumura, N. Imanishi, A. Hirano, N. Sonoyama, Y. Takeda, "Electrochemical performances for preferred oriented PLD thin-film electrodes of $LiNi_{0.8}Co_{0.2}O_2$, $LiFePO_4$ and $LiMn_2O_4$", *Solid State Ionics* **2008**, *179*, 2011–2015.

[138] A. K. Hjelm, G Lindbergh, "Experimental and theoretical analysis of $LiMn_2O_4$ cathodes for use in rechargeable lithium batteries by electrochemical impedance spectroscopy (EIS)", *Electrochim. Acta* **2002**, *47*, 1747–1759.

[139] P. J. Bouwman, B. A. Boukamp, H. J. M. Bouwmeester, P. H. L. Notten, "Influence of diffusion plane orientation on electrochemical properties of thin film $LiCoO_2$ electrodes", *J. Electrochem. Soc.* **2002**, *149*, A699–A709.

[140] M Mohamedi, A Makino, K Dokko, T Itoh, I Uchida, "Electrochemical investigation of $LiNi_{0.5}Mn_{1.5}O_4$ thin film intercalation electrodes", *Electrochim. Acta* **2002**, *48*, 79–84.

[141] J. C. Arrebola, A. Caballero, L. Hernan, M. Melero, J. Morales, E. R. Castellon, "Electrochemical properties of $LiNi_{0.5}Mn_{1.5}O_4$ films prepared by spin-coating deposition", *J. Power Sources* **2006**, *162*, 606–613.

[142] H Xia, Y. S. Meng, L Lu, G Ceder, "Electrochemical properties of nonstoichiometric $LiNi_{0.5}Mn_{1.5}O_{4-delta}$ thin-film electrodes prepared by pulsed laser deposition", *J. Electrochem. Soc.* **2007**, *154*, A737–A743.

[143] K. Hoshina, K. Yoshima, M. Kotobuki, K. Kanamura, "Fabrication of $LiNi_{0.5}Mn_{1.5}O_4$ thin film cathode by PVP sol-gel process and its application of all-solid-state lithium ion batteries using $Li_{1+x}Al_xTi_{2-x}(PO_4)_3$ solid electrolyte", *Solid State Ionics* **2012**, *209*, 30–35.

[144] H. Konishi, K. Suzuki, S. Taminato, K. Kim, S. Kim, J. Lim, M. Hirayama, R. Kanno, "Structure and electrochemical properties of $LiNi_{0.5}Mn_{1.5}O_4$ epitaxial thin film electrodes", *J. Power Sources* **2014**, *246*, 365–370.

[145] H. Kawaura, D. Takamatsu, S. Mori, Y. Orikasa, H. Sugaya, H. Murayama, K. Nakanishi, H. Tanida, Y. Koyama, H. Arai, Y. Uchimoto, Z. Ogumi, "High potential durability of $LiNi_{0.5}Mn_{1.5}O_4$ electrodes studied by surface sensitive X-ray absorption spectroscopy", *J. Power Sources* **2014**, *245*, 816–821.

[146] H. Xia, L. Lu, "Li diffusion in spinel $LiNi_{0.5}Mn_{1.5}O_4$ thin films prepared by pulsed laser deposition", *Phys. Scripta* **2007**, *T129*, 43–48.

[147] L. Wang, H. Li, M. Courty, X. Huang, E. Baudrin, "Preparation and characterization of $LiNi_{0.5}Mn_{1.5}O_{4-delta}$ thin films taking advantage of correlations with powder samples behavior", *J. Power Sources* **2013**, *232*, 165–172.

[148] Y. Wang, G. Yang, Z. Yang, L. Zhang, M. Fu, H. Long, Z. Li, Y. Huang, P. Lu, "High power and capacity of $LiNi_{0.5}Mn_{1.5}O_4$ thin films cathodes prepared by pulsed laser deposition", *Electrochim. Acta* **2013**, *102*, 416–422.

[149] M. A. McArthur, S Trussler, J. R. Dahn, "In Situ Investigations of SEI Layer Growth on Electrode Materials for Lithium-Ion Batteries Using Spectroscopic Ellipsometry", *J. Electrochem. Soc.* **2012**, *159*, A198–A207.

[150] K Dokko, M Mohamedi, N Anzue, T Itoh, I Uchida, "In situ Raman spectroscopic studies of $LiNi_xMn_{2-x}O_4$ thin film cathode materials for lithium ion secondary batteries", *J. Mater. Chem.* **2002**, *12*, 3688–3693.

[151] M. Matsui, K. Dokko, K. Kanamura, "Surface Layer Formation and Stripping Process on $LiMn_2O_4$ and $LiNi_{1/2}Mn_{3/2}O_4$ Thin Film Electrodes", *J. Electrochem. Soc.* **2010**, *157*, A121–A129.

[152] J. L. Lei, L. J. Li, R Kostecki, R Muller, F McLarnon, "Characterization of SEI layers on $LiMn_2O_4$ cathodes with in situ spectroscopic ellipsometry", *J. Electrochem. Soc.* **2005**, *152*, A774–A777.

[153] P. Mukherjee, A. Lagutchev, D. D. Dlott, "In Situ Probing of Solid-Electrolyte Interfaces with Nonlinear Coherent Vibrational Spectroscopy", *J. Electrochem. Soc.* **2012**, *159*, A244–A252.

[154] T. Doi, M. Inaba, H. Tsuchiya, S.-K. Jeong, Y. Iriyama, T. Abe, Z. Ogumi, "Electrochemical AFM study of $LiMn_2O_4$ thin film electrodes exposed to elevated temperatures", *J. Power Sources* **2008**, *180*, 539–545.

[155] M. Hirayama, N. Sonoyama, T. Abe, M. Minoura, M. Ito, D. Mori, A. Yamada, R. Kanno, T. Terashima, M. Takano, K. Tamura, J. Mizuki, "Characterization of electrode/electrolyte interface for lithium batteries using in situ synchrotron X-ray reflectometry - A new experimental technique for $LiCoO_2$ model electrode", *J. Power Sources* **2007**, *168*, 493–500.

[156] A Thissen, D Ensling, M Liberatore, Q. H. Wu, F. J. F. Madrigal, M. S. Bhuvaneswari, R Hunger, W Jaegermann, "Experimental routes to in situ characterization of the electronic structure and chemical composition of cathode materials for lithium ion batteries during lithium intercalation and deintercalation using photoelectron spectroscopy and related techniques", *Ionics* **2009**, *15*, 393–403.

[157] E Peled, "The electrochemical-behavior of alkali and alkaline-earth metals in non-aqueous battery systems - the solid electrolyte interphase model", *J. Electrochem. Soc.* **1979**, *126*, 2047–2051.

[158] E Peled, D Golodnitsky, G Ardel, V Eshkenazy, "The SEI model - application to lithium polymer electrolyte batteries", *Electrochim. Acta* **1995**, *40*, 2197–2204.

[159] E Peled, D Golodnitsky, G Ardel, "Advanced model for solid electrolyte interphase electrodes in liquid and polymer electrolytes", *J. Electrochem. Soc.* **1997**, *144*, L208–L210.

[160] S. Dalavi, M. Xu, B. Ravdel, L. Zhou, B. L. Lucht, "Nonflammable Electrolytes for Lithium-Ion Batteries Containing Dimethyl Methylphosphonate", *J. Electrochem. Soc.* **2010**, *157*, A1113–A1120.

[161] H. Takahara, H. Miyauchi, M. Tabuchi, T. Nakamura, "Elemental Distribution Analysis of $LiFePO_4$/Graphite Cells Studied with Glow Discharge Optical Emission Spectroscopy (GD-OES)", *J. Electrochem. Soc.* **2013**, *160*, A272–A278.

[162] D Aurbach, B Markovsky, A Shechter, Y EinEli, H Cohen, "A comparative study of synthetic graphite and Li electrodes in electrolyte solutions based on ethylene carbonate dimethyl carbonate mixtures", *J. Electrochem. Soc.* **1996**, *143*, 3809–3820.

[163] K Kanamura, H Tomura, S Shiraishi, Z. I. Takehara, "XPS analysis of lithium surfaces following immersion in various solvents containing $LiBF_4$", *J. Electrochem. Soc.* **1995**, *142*, 340–347.

[164] L Martin, H Martinez, M Ulldemolins, B Pecquenard, F Le Cras, "Evolution of the Si electrode/electrolyte interface in lithium batteries characterized by XPS and AFM techniques: The influence of vinylene carbonate additive", *Solid State Ionics* **2012**, *215*, 36–44.

[165] H. Duncan, D. Duguay, Y. Abu-Lebdeh, I. J. Davidson, "Study of the $LiMn_{1.5}Ni_{0.5}O_4$/Electrolyte Interface at Room Temperature and 60 degrees C", *J. Electrochem. Soc.* **2011**, *158*, A537–A545.

[166] K Edstrom, T Gustafsson, J. O. Thomas, "The cathode-electrolyte interface in the Li-ion battery", *Electrochim. Acta* **2004**, *50*, 397–403.

[167] T Eriksson, A. M. Andersson, C Gejke, T Gustafsson, J. O. Thomas, "Influence of temperature on the interface chemistry of $Li_xMn_2O_4$ electrodes", *Langmuir* **2002**, *18*, 3609–3619.

[168] D. Aurbach, B. Markovsky, Y. Talyossef, G. Salitra, H.-J. Kim, S. Choi, "Studies of cycling behavior, ageing, and interfacial reactions of $LiNi_{0.5}Mn_{1.5}O_4$ and carbon electrodes for lithium-ion 5-V cells", *J. Power Sources* **2006**, *162*, 780–789.

[169] D Aurbach, K Gamolsky, B Markovsky, G Salitra, Y Gofer, U Heider, R Oesten, M Schmidt, "The study of surface phenomena related to electrochemical lithium intercalation into Li_xMO_y host materials (M = Ni, Mn)", *J. Electrochem. Soc.* **2000**, *147*, 1322–1331.

[170] S. S. Zhang, K Xu, T. R. Jow, "Understanding formation of solid electrolyte interface film on $LiMn_2O_4$ electrode", *J. Electrochem. Soc.* **2002**, *149*, A1521–A1526.

[171] B Ravdel, K. M. Abraham, R Gitzendanner, J DiCarlo, B Lucht, C Campion, "Thermal stability of lithium-ion battery electrolytes", *J. Power Sources* **2003**, *119*, 805–810.

[172] S.-T. Myung, Y. Hitoshi, Y.-K. Sun, "Electrochemical behavior and passivation of current collectors in lithium-ion batteries", *J. Mater. Chem.* **2011**, *21*, 9891–9911.

[173] F Joho, P Novak, "SNIFTIRS investigation of the oxidative decomposition of organic-carbonate-based electrolytes for lithium-ion cells", *Electrochim. Acta* **2000**, *45*, 3589–3599.

[174] W. Xu, X. Chen, F. Ding, J. Xiao, D. Wang, A. Pan, J. Zheng, X. S. Li, A. B. Padmaperuma, J.-G. Zhang, "Reinvestigation on the state-of-the-art nonaqueous carbonate electrolytes for 5 V Li-ion battery applications", *J. Power Sources* **2012**, *213*, 304–316.

[175] X. Wu, X. Li, Z. Wang, H. Guo, P. Yue, "Capacity fading reason of $LiNi_{0.5}Mn_{1.5}O_4$ with commercial electrolyte", *Ionics* **2013**, *19*, 379–383.

[176] N. P. W. Pieczonka, Z. Liu, P. Lu, K. L. Olson, J. Moote, B. R. Powell, J.-H. Kim, "Understanding Transition-Metal Dissolution Behavior in $LiNi_{0.5}Mn_{1.5}O_4$ High-Voltage Spinel for Lithium Ion Batteries", *J. Phys. Chem. C* **2013**, *117*, 15947–15957.

[177] D Aurbach, M. D. Levi, E Levi, H Teller, B Markovsky, G Salitra, U Heider, L Heider, "Common electroanalytical behavior of Li intercalation processes into graphite and transition metal oxides", *J. Electrochem. Soc.* **1998**, *145*, 3024–3034.

[178] J.-H. Kim, N. P. W. Pieczonka, Z. Li, Y. Wu, S. Harris, B. R. Powell, "Understanding the capacity fading mechanism in $LiNi_{0.5}Mn_{1.5}O_4$/graphite Li-ion batteries", *Electrochim. Acta* **2013**, *90*, 556–562.

[179] L. Yang, T. Markmaitree, B. L. Lucht, "Inorganic additives for passivation of high voltage cathode materials", *J. Power Sources* **2011**, *196*, 2251–2254.

[180] X. Zuo, C. Fan, X. Xiao, J. Liu, J. Nan, "High-voltage performance of $LiCoO_2$/graphite batteries with methylene methanedisulfonate as electrolyte additive", *J. Power Sources* **2012**, *219*, 94–99.

[181] K Edstrom, M Herstedt, D. P. Abraham, "A new look at the solid electrolyte interphase on graphite anodes in Li-ion batteries", *J. Power Sources* **2006**, *153*, 380–384.

[182] T. Okumura, T. Fukutsuka, Y. Uchimoto, N. Sakai, K. Yamaji, H. Yokokawa, "Determination of lithium ion diffusion in lithium-manganese-oxide-spinel thin films by secondary-ion mass spectrometry", *J. Power Sources* **2009**, *189*, 643–645.

[183] D. W. Shin, C. A. Bridges, A. Huq, M. P. Paranthaman, A. Manthiram, "Role of Cation Ordering and Surface Segregation in High-Voltage Spinel $LiMn_{1.5}Ni_{0.5-x}M_xO_4$ (M = Cr, Fe, and Ga) Cathodes for Lithium-Ion Batteries", *Chem. Mater.* **2012**, *24*, 3720–3731.

[184] V Yufit, D Golodnitsky, L Burstein, M Nathan, E Peled, "X-ray photoelectron spectroscopy and Time-Of-Flight secondary ion mass spectroscopy studies of electrodeposited molybdenum oxysulfide cathodes for lithium and lithium-ion microbatteries", *J. Solid State Electr.* **2008**, *12*, 273–285.

[185] M. Minakshi, "Improved performance of Bi_2O_3-doped MnO_2 cathode on rechargeability in LiOH aqueous cell", *J. Solid State Electr.* **2009**, *13*, 1209–1214.

[186] H. J. Kweon, J Park, J Seo, G Kim, B Jung, H. S. Lim, "Effects of metal oxide coatings on the thermal stability and electrical performance of $LiCoCO_2$ in a Li-ion cell", *J. Power Sources* **2004**, *126*, 156–162.

[187] H Ota, T Akai, H Namita, S Yamaguchi, M Nomura, "XAFS and TOF-SIMS analysis of SEI layers on electrodes", *J. Power Sources* **2003**, *119*, 567–571.

[188] J.-T. Li, V. Maurice, J. Swiatowska-Mrowiecka, A. Seyeux, S. Zanna, L. Klein, S.-G. Sun, P. Marcus, "XPS, time-of-flight-SIMS and polarization modulation IRRAS study of Cr_2O_3 thin film materials as anode for lithium ion battery", *Electrochim. Acta* **2009**, *54*, 3700–3707.

[189] J. Swiatowska-Mrowiecka, F. Martin, V. Maurice, S. Zanna, L. Klein, J. Castle, P. Marcus, "The distribution of lithium intercalated in V_2O_5 thin films studied by XPS and ToF-SIMS", *Electrochim. Acta* **2008**, *53*, 4257–4266.

[190] E Peled, D. B. Tow, A Merson, A Gladkich, L Burstein, D Golodnitsky, "Composition, depth profiles and lateral distribution of materials in the SEI built on HOPG-TOF SIMS and XPS studies", *J. Power Sources* **2001**, *97-8*, 52–57.

[191] M Gellert, K. I. Gries, J Zakel, A Ott, S Spannenberger, C Yada, F Rosciano, K Volz, B Roling, "$LiNi_{0.5}Mn_{1.5}O_4$ Thin-Film Cathodes on Gold-Coated Stainless Steel Substrates: Formation of Interlayers and Electrochemical Properties", *Electrochim. Acta* **2014**, *133*, 146–152.

[192] C. Pereira-Nabais, J. Swiatowska, A. Chagnes, F. Ozanam, A. Gohier, P. Tran-Van, C.-S. Cojocaru, M. Cassir, P. Marcus, "Interphase chemistry of Si electrodes used as anodes in Li-ion batteries", *Appl. Surf. Sci.* **2013**, *266*, 5–16.

[193] J.-T. Li, J. Swiatowska, V. Maurice, A. Seyeux, L. Huang, S.-G. Sun, P. Marcus, "XPS and ToF-SIMS Study of Electrode Processes on Sn-Ni Alloy Anodes for Li-Ion Batteries", *J. Phys. Chem. C* **2011**, *115*, 7012–7018.

[194] J.-T. Li, J. Swiatowska, A. Seyeux, L. Huang, V. Maurice, S.-G. Sun, P. Marcus, "XPS and ToF-SIMS study of Sn-Co alloy thin films as anode for lithium ion battery", *J. Power Sources* **2010**, *195*, 8251–8257.

[195] N Thorne, A Dubus, J. M. Lang, F Degreve, P Meyer, "SIMS determination of the surface lithium depletion zone in Al-Li alloys by quantitative image-analysis", *J. Phys.* **1987**, *48*, 521–526.

[196] P. Lu, S. J. Harris, "Lithium transport within the solid electrolyte interphase", *Electrochem. Commun.* **2011**, *13*, 1035–1037.

[197] N. Volbers, "Sekundaerionenmassenspektrometrie an Zinkoxid", PhD thesis, Justus-Liebig-Universitaet Giessen.

[198] A. Schlifke, "Synthese und Charakterisierung ternaerer und Quarternaerer mesoporoeser Metalloxide", Diplomarbeit (personal communication), Universitaet Hamburg, **2010**.

[199] T Dumont, T Lippert, M Dobeli, H Grimmer, J Ufheil, P Novak, A Wursig, U Vogt, A Wokaun, "Influence of experimental parameter on the Li-content of $LiMn_2O_4$ electrodes produced by pulsed laser deposition", *Appl. Surf. Sci.* **2006**, *252*, 4902–4906.

[200] C. M. Julien, F Gendron, A Amdouni, A Massot, "Lattice vibrations of materials for lithium rechargeable batteries. VI: Ordered spinels", *Mater. Sci. Eng. B-Solid* **2006**, *130*, 41–48.

[201] Y. Talyosef, B. Markovsky, R. Lavi, G. Salitra, D. Aurbach, D. Kovacheva, M. Gorova, E. Zhecheva, R. Stoyanova, "Comparing the behavior of nano- and microsized particles of $LiMn_{1.5}Ni_{0.5}O_4$ spinel as cathode materials for Li-ion batteries", *J. Electrochem. Soc.* **2007**, *154*, A682–A691.

[202] M. D. Chung, J. H. Seo, X. C. Zhang, A. M. Sastry, "Implementing Realistic Geometry and Measured Diffusion Coefficients into Single Particle Electrode Modeling Based on Experiments with Single $LiMn_2O_4$ Spinel Particles", *J. Electrochem. Soc.* **2011**, *158*, A371–A378.

[203] R. Volk, *Rauheitsmessung - Theorie und Praxis*, Beuth Verlag GmbH, Berlin, **2005**.

[204] A. W. Momber, R.-R. Schulz, *Handbuch der Oberflaechenbearbeitung Beton - Bearbeitung - Eigenschaften - Pruefung*, Birkhaeuser Verlag, Basel, **2006**.

[205] G. I. Kanel, S. V. Razorenov, K Baumung, J Singer, "Dynamic yield and tensile strength of aluminum single crystals at temperatures up to the melting point", *J. Appl. Phys.* **2001**, *90*, 136–143.

[206] J. E. Ayers, *Heteroepitaxy of Semiconductors: Theory, Growth, and Characterization*, Taylor & Francis Group, Boca Raton, Florida, USA, **2007**.

[207] G. Beck, H. Fischer, E. Mutoro, V. Srot, K. Petrikowski, E. Tchernychova, M. Wuttig, M. Ruehle, B. Luerssen, J. Janek, "Epitaxial Pt(111) thin film electrodes on YSZ(111) and YSZ(100) - Preparation and characterisation", *Solid State Ionics* **2007**, *178*, 327–337.

[208] A. Petric, H. Ling, "Electrical conductivity and thermal expansion of spinels at elevated temperatures", *J. Am. Ceram. Soc.* **2007**, *90*, 1515–1520.

[209] "Thermal expansion coefficient of yttria stabilized zirconia for various yttria contents ", *Solid State Ionics* **2005**, *176*, 613 –619.

[210] H. S. Fang, Z. X. Wang, X. H. Li, Z. L. Yin, H. J. Guo, W. J. Peng, "Synthesis and characterization of high capacity $LiNi_{0.5}Mn_{1.5}O_4$ using Li_2CO_3, NiO and electrolytic MnO_2", *Chin. J. Inorg. Chem.* **2006**, *22*, 311–315.

[211] N. Schichtel, "Misfit Induced Elastic Strain at Interfaces and its Impact on Ionic Conductivity", PhD thesis, Justus-Liebig-Universitaet Giessen.

[212] G. Q. Liu, L Wen, Y. M. Liu, "Spinel $LiNi_{0.5}Mn_{1.5}O_4$ and its derivatives as cathodes for high-voltage Li-ion batteries", *J. Solid State Electr.* **2010**, *14*, 2191–2202.

[213] S Frangini, M Carewska, S Passerini, S Scaccia, "Intercalation behavior of $LiCoO_2$ electrodes in aqueous alkaline electrolytes by microparticle cyclic voltammetry", *J. New Mat. Elect. Syst.* **2001**, *4*, 83–88.

[214] S Waki, K Dokko, T Itoh, M Nishizawa, T Abe, I Uchida, "High-Speed voltammetry of Mn-doped $LiCoO_2$ using a microelectrode technique", *J. Solid State Electr.* **2000**, *4*, 205–209.

[215] U. Lafont, A. Anastasopol, E. Garcia-Tamayo, E. Kelder, "Electrostatic spray pyrolysis of $LiNi_{0.5}Mn_{1.5}O_4$ films for 3D Li-ion microbatteries", *Thin Solid Films* **2012**, *520*, 3464–3471.

[216] ION-TOF, TOF.SIMS^5 Performance Specifications, Website, **2003**.

[217] F Simmen, A Foelske-Schmitz, P Verma, M Horisberger, T. Lippert, P Novak, C. W. Schneider, A Wokaun, "Surface layer formation on $Li_{1+x}Mn_2O_{4-delta}$ thin film electrodes during electrochemical cycling", *Electrochim. Acta* **2011**, *56*, 8539–8544.

[218] X. Wu, X. Li, Z. Wang, H. Guo, J. Wang, P. Yue, "Comprehensive reinvestigation on the initial coulombic efficiency and capacity fading mechanism of $LiNi_{0.5}Mn_{1.5}O_4$ at low rate and elevated temperature", *J. Solid State Electr.* **2013**, *17*, 1029–1038.

[219] J. Hong, H.-D. Lim, M. Lee, S.-W. Kim, H. Kim, S.-T. Oh, G.-C. Chung, K. Kang, "Critical Role of Oxygen Evolved from Layered Li-Excess Metal Oxides in Lithium Rechargeable Batteries", *Chem. Mater.* **2012**, *24*, 2692–2697.

[220] M. G. Kim, H. J. Shin, J. H. Kim, S. H. Park, Y. K. Sun, "XAS investigation of inhomogeneous metal-oxygen bond covalency in bulk and surface for charge compensation in li-ion battery cathode $Li[Ni_{1/3}Co_{1/3}Mn_{1/3}]O_2$ material", *J. Electrochem. Soc.* **2005**, *152*, A1320–A1328.

[221] H. Arai, K. Sato, Y. Orikasa, H. Murayama, I. Takahashi, Y. Koyama, Y. Uchimoto, Z. Ogumi, "Phase transition kinetics of $LiNi_{0.5}Mn_{1.5}O_4$ electrodes studied by in situ X-ray absorption near-edge structure and X-ray diffraction analysis", *J. Mater. Chem. A* **2013**, *1*, 10442–10449.

[222] U. E. A. Fittschen, U. Boesenberg, M. Falk, R. Simon, M. Menzel, B. Jache, J. Janek, "3D Imaging of elemental deposition of Mn, Ni and Cu on the graphite anode in cycled $LiNi_{0.5}Mn_{1.5}O_4$ /graphite full cells", **2013**.

[223] U. E. A. Fittschen, U. Boesenberg, M. Falk, M. Menzel, Schlifke Annalena, M. Froeba, J. Janeck, "Visualisatin of the Ni oxidation state in $LiNi_{0.5}Mn_{1.5}O_4$ Li-ion battery cathodes at different cycle states: pristine, discharged, after quick charging and slow charging", **2013**.

[224] M. Falk, "Elektrochemische und spektrometrische Untersuchungen von SOFC-Modellelektroden", Master thesis (personal communication, Justus-Liebig University Giessen, **2010**.

[225] M. C. Biesinger, P. Y. Paepegaey, N. S. McIntyre, R. R. Harbottle, N. O. Petersent, "Principal component analysis of TOF-SIMS images of organic monolayers", *Anal. Chem.* **2002**, *74*, 5711–5716.

[226] K. W. Leitner, H Wolf, A Garsuch, F Chesneau, M Schulz-Dobrick, "Electroactive separator for high voltage graphite/$LiNi_{0.5}Mn_{1.5}O_4$ lithium ion batteries", *J. Power Sources* **2013**, *244*, 548–551.

10. Danksagung

Prof. Dr. Jürgen Janek danke ich für die Möglichkeit, mich mit diesem interessanten Thema befassen zu dürfen, sowie für die gute Betreuung.

Dr. Joachim Sann danke ich für die freundliche Betreuung, hilfreiche Diskussionen über Material- sowie Messparameter und Layoutfragen.

Bei Dr. Bjoern Luerssen möchte ich mich für die sehr nette und geduldige Unterstütung bei der grafischen Gestaltung meiner Arbeit danken.

Ich danke auch allen Mitgliedern der AG Janek für die angenehme Arbeitsatmosphäre und die Unterstützung bei allen Fragen und Problemen. Besonderer Dank gilt Alexander Braun, Martin Busche, Matthias Kleine-Boymann und Dr. Marcus Rohnke für die Hilfe bei PLD- SIMS- oder Messsoftware-Problemen sowie Ljerka Majdandzic für viele kleine, aber wichtige Dinge.

Last but not least danke ich meiner Familie, allen voran meinen Eltern Charlotte und Erich Falk sowie meinem Freund Christian Länger. Danke für die vielen schönen Ablenkungen, Aufmunterungen und den Trost, wenn scheinbar gar nichts mehr ging!